



Universidade de Brasília – UnB  
Instituto de Geociências  
Programa de Pós-Graduação em Geologia

**EVOLUÇÃO CRUSTAL DO LIMITE ORIENTAL DA FAIXA PARAGUAI:  
SIGNIFICADO TECTÔNICO DA GRANITOGÊNESE DE HIGH Ba-Sr E  
SUAS ROCHAS HOSPEDEIRAS**

**CRUSTAL EVOLUTION OF THE EASTERN BOUNDARY OF  
PARAGUAY BELT: TECTONIC SIGNIFICANCE OF THE HIGH Ba-Sr  
GRANITOGENESIS AND THEIR HOST ROCKS**

Amanda Figueiredo Granja Dorilêo Leite

**TESE DE DOUTORADO Nº 182**

Brasília, DF

Novembro de 2021



Universidade de Brasília – UnB  
Instituto de Geociências  
Programa de Pós-Graduação em Geologia

**EVOLUÇÃO CRUSTAL DO LIMITE ORIENTAL DA FAIXA  
PARAGUAI: SIGNIFICADO TECTÔNICO DA GRANITOGÊNESE DE  
HIGH BA-SR E SUAS ROCHAS HOSPEDEIRAS**

Amanda Figueiredo Granja Dorilêo Leite

**TESE DE DOUTORADO Nº 182**

**Orientador:** Prof. Dr. Reinhardt Adolfo Fuck (UnB);

**Co-orientador:** Prof. Dr. Elton Luiz Dantas (UnB);

**Co-orientador:** Prof. Dr. Amarildo Salina Ruiz (UFMT).

**Banca Examinadora:**

Prof. Dr. Reinhardt Adolfo Fuck (Orientador);

Prof<sup>a</sup>. Dr<sup>a</sup>. Natalia Hauser (Interno);

Prof<sup>a</sup>. Dr<sup>a</sup>. Mônica da Costa Pereira Lavalle Heilbron (UERJ);

Prof. Dr. Jean Michel Lafon (UFPA);

Prof. Dr. Federico Alberto Cuadro Jiménez (Suplente interno).

Brasília, DF, novembro de 2021

Ficha catalográfica elaborada automaticamente,  
com os dados fornecidos pelo(a) autor(a)

FL533e Figueiredo Granja Dorilêo Leite, Amanda  
Evolução crustal do limite oriental da Faixa Paraguai:  
significado tectônico da granitogênese de high Ba-Sr e suas  
rochas hospedeiras / Amanda Figueiredo Granja Dorilêo  
Leite; orientador Reinhardt Adolf Fuck; co-orientador  
Elton Luiz Dantas. -- Brasília, 2021.  
233 p.

Tese (Doutorado - Doutorado em Geologia) -- Universidade  
de Brasília, 2021.

1. Gondwana Ocidental. 2. Faixa Paraguai. 3. Granitoides  
de alto Ba-Sr. 4. Proveniência Sedimentar. 5. Evolução  
Crustal. I. Fuck, Reinhardt Adolf, orient. II. Dantas,  
Elton Luiz, co-orient. III. Título.

*Dedicado a Jeanine e Carlos, aqueles que me ensinaram  
que tudo aquilo que podemos sonhar, conseguimos realizar.*

## AGRADECIMENTOS

O presente trabalho foi realizado com apoio da Coordenação de Aperfeiçoamento de Pessoal de Nível Superior - Brasil (CAPES) - Código de Financiamento 001. Agradeço ao suporte financeiro que me foi oferecido pela CAPES e o Instituto Nacional de Ciência e Tecnologia – Estudos Tectônicos (INCT - ET).

Agradeço a minha família, por todo apoio e carinho, ofertando-me palavras sábias nos momentos de fragilidade. Aos meus pais e à minha irmã, por serem a minha base, por me passarem uma visão otimista da vida, sendo essenciais na minha caminhada até aqui. Ao meu companheiro de vida, por todo apoio e amor, e por me mostrar sempre uma visão mais justa do mundo. Vocês que me motivaram, quando eu já não tinha mais força, que me inspiraram e foram exemplos para continuar nessa jornada.

Sou grata às pessoas que colaboraram, de alguma forma, com a troca de conhecimento, com todo o tipo de ajuda que generosamente me ofereceram nesses quase quatro anos de trabalho. Aos professores Amarildo, Fuck e Elton, pela dedicação e tempo destinado às correções e orientações. Estendo os agradecimentos a todos os professores que passaram pelo meu caminho nas universidades federais que frequentei, por todo conhecimento destinado a mim. À equipe do Laboratório de Geocronologia da UnB pelo suporte fornecido. Ao professor Patrick Monié da *Geosciences Montpellier* pelo acolhimento no seu laboratório e por ter lutado junto comigo pela realização das análises  $^{40}\text{Ar}/^{39}\text{Ar}$ .

E obrigada Deus, e a qualquer nome que se possa dar a essa energia e/ou ligação quântica que possa existir nesse mundo, por nunca ter soltado da minha mão nos momentos.

## SUMÁRIO

|  |           |
|--|-----------|
| LISTA DE FIGURAS .....   | ii        |
| LISTA DE TABELAS .....   | xi        |
| RESUMO.....  | 18        |
| ABSTRACT.....  | 18        |
| <b>1. INTRODUÇÃO.....</b>  | <b>20</b> |
| 1.1. Apresentação do tema .....  | 20        |
| 1.2. Relevância e objetivos da tese.....   | 22        |
| 1.3. Localização e vias de acesso.....   | 25        |
| 1.4. Estrutura da tese.....  | 26        |
| <b>2. REFERENCIAL TEÓRICO E REVISÃO BIBLIOGRÁFICA.....</b>                       | <b>28</b> |
| 2.1. A evolução do magmatismo terrestre .....                                    | 28        |
| 2.2. O supercontinente Gondwana e suas fases finais de fechamento .....          | 32        |
| 2.3. O Lineamento Transbrasiliano-Kandi e a Tectônica strik-slip.....            | 41        |
| <b>3. MATERIAIS E MÉTODOS .....</b>  | <b>45</b> |
| 3.1. Etapa Pré-Campo .....   | 45        |
| 3.2. Etapa de amostragem .....   | 45        |
| 3.3. Etapa de preparação de amostras .....                                       | 46        |
| 3.4. Análises Petrográficas .....  | 46        |
| 3.5. Análises Litoquímicas.....  | 47        |
| 3.6. Análises Geocronológicas e geoquímica isotópica .....                       | 47        |
| <b>4. ARTIGO 1 .....</b>   | <b>52</b> |
| 4.1. INTRODUCTION .....  | 54        |
| 4.2. GEOLOGICAL SETTING .....  | 57        |
| 4.3. MATERIALS AND METHODS .....   | 62        |
| 4.4. RESULTS .....   | 64        |
| 4.4.1. <i>Geology and Petrography</i> .....                                      | 64        |
| 4.4.1.1. <i>The qz-monzodiorite/granodiorite suite</i> .....                     | 66        |
| 4.4.1.2. <i>The monzogranite suite</i> .....                                     | 68        |
| 4.4.2. <i>Lithochemical Data</i> .....   | 69        |
| 4.4.3. <i>Zircon U-Pb Geochronology</i> .....                                    | 78        |
| 4.4.3.1. <i>The qz-monzodiorite/granodiorite suite</i> .....                     | 87        |
| 4.4.3.2. <i>The monzogranite suite</i> .....                                     | 90        |
| 4.4.4. <i>Sm-Nd isotope data of whole-rock samples</i> .....                     | 91        |
| 4.5. DISCUSSION .....  | 93        |
| 4.5.1. <i>Interpretation of U-Pb data</i> .....                                  | 93        |
| 4.5.1.1. <i>Magma temperatures</i> .....   | 94        |
| 4.5.2. <i>Type of Magmatism</i> .....  | 95        |
| 4.5.3. <i>Petrogenesis of the qz-monzodiorite/granodiorite suite</i> .....       | 100       |
| 4.5.3.1. <i>The qz-monzodiorite facies: evidence of appinitic affinity</i> ..... | 101       |
| 4.5.3.2. <i>Cogeneticity of qz-monzodioritic and granodioritic rocks</i> .....   | 101       |

|          |  |     |
|----------|--|-----|
| 4.5.4.   | <i>Petrogenesis of the monzogranite suite</i> .....        | 103 |
| 4.5.5.   | <i>Tectonic interpretations</i> .....                      | 105 |
| 4.5.5.1. | <i>The qz-monzodiorite/granodiorite suite</i> .....        | 106 |
| 4.5.5.2. | <i>The monzogranite suite</i> .....                        | 108 |
| 4.5.6.   | <i>Sanukitoids and high Ba-Sr connections</i> .....        | 109 |
| 4.6.     | <b>CONCLUSION</b> .....                                    | 113 |
|          | <b>REFERENCES</b> .....                                    | 114 |
|          | <b>ANEXOS ARTIGO 1</b> .....                               | 125 |
| 5.       | <b>ARTIGO 2</b> .....                                      | 133 |
|          | <b>ABSTRACT</b> .....                                      | 134 |
| 5.1.     | <b>INTRODUCTION</b> .....                                  | 135 |
| 5.2.     | <b>GEOLOGICAL SETTING</b> .....                            | 137 |
| 5.3.     | <b>MATERIALS AND METHODS</b> .....                         | 143 |
| 5.4.     | <b>RESULTS</b> .....                                       | 146 |
| 5.4.1.   | <i>Field observations and Petrography</i> .....            | 146 |
| 5.4.2.   | <i>U-Pb geochronology of detrital zircon grains</i> .....  | 150 |
| 5.4.3.   | <i>Sm-Nd isotope data of whole-rock samples</i> .....      | 173 |
| 5.4.4.   | <i><sup>40</sup>Ar/<sup>39</sup>Ar data</i> .....          | 174 |
| 5.5.     | <b>DISCUSSION</b> .....                                    | 176 |
| 5.5.1.   | <i>Age of sedimentation and depositional setting</i> ..... | 176 |
| 5.5.2.   | <i>Most probable source areas</i> .....                    | 179 |
| 5.5.3.   | <i>Record of thermal conditions</i> .....                  | 181 |
| 5.5.3.1. | <i>Constraining an igneous cooling</i> .....               | 182 |
| 5.5.3.2. | <i>Country rocks metamorphic evolution</i> .....           | 184 |
| 5.5.4.   | <i>Evolution of the Paraguay Belt</i> .....                | 186 |
| 5.5.5.   | <i>West Gondwana assembly at Cambrian times</i> .....      | 190 |
| 5.6.     | <b>CONCLUSION</b> .....                                    | 193 |
|          | <b>REFERENCE</b> .....                                     | 195 |
|          | <b>ANEXOS ARTIGO 2</b> .....                               | 209 |
|          | <b>Supplementary Table 5.1</b> .....                       | 209 |
| 6.       | <b>CONSIDERAÇÕES FINAIS</b> .....                          | 215 |
| 7.       | <b>REFERÊNCIAS</b> .....                                   | 218 |

## LISTA DE FIGURAS

- Figura 1.1** – Mapa de localização e vias de acesso à área de pesquisa, localizada a aproximadamente 47 km do município de Barra do Garças - MT, divisa com Goiás..26
- Figura 2.1** – Mapa da configuração do supercontinente em 500 Ma (extraído de Schmitt et al., 2018). .....33
- Figura 2.2** – Configuração do Gondwana mostrando a distribuição dos orógenos tardios (extraído de Zhao et al. 2018). .....37
- Figura 2.3** - Esquema tectônico ilustrando os principais blocos e cinturões orogênicos na América do Sul e África, incluindo a localização da região de fechamento do orógeno West Gondwana (extraído de Oriolo et al., 2017). .....39
- Figura 2.4** - Localização do Lineamento Transbrasiliano (LTB) no contexto das grandes unidades geológicas da América do Sul. O retângulo vermelho representa a área de estudo (Modificado de Fairhead e Maus, 2003; Ramos et al., 2010). .....42
- Figure 2.5** - Modelo tectônico proposto para o Gondwana Ocidental no fim do Neoproterozoico a partir de dados paleomagnéticos (extraído de Trindade *et al.*, 2006)..... 35
- Figure 4.1**– Geological and geotectonic context of the study area: (A) geotectonic context of the formation of the Tocantins Province during the Brasiliano Orogeny. Cratons are shown in dark gray. AM: Amazonian, WA: West Africa; CO: Congo; SF: São Francisco; KA: Kalahari; RP: Rio de la Plata; PP: Paranapanema; RA: Rio Apa. The red rectangle refers to the investigated region in the context of the Brasiliano Pan-African Orogeny (modified from Vaughan and Pankhurst, 2008); (B) location of the Tocantins Province in the Brazilian territory. The red rectangle comprises the Paraguay Belt shown in (C) Simplified geological map of the Paraguay Belt and Brasília Belt (modified after



Ruiz et al., 2010; Pimentel et al., 2000). Red numbers related to the respective granitic intrusions in the Paraguay Belt: 1- Araguaiana; 2- Lajinha; 3- São Vicente; 4- Sonora; 5- Coxim; 6- Rio Negro; 7- Taboco; (D) simplified geological map of the study area. ....58

**Figure 4.2** – Geological map of the study area (modified from CPRM, 2017). MS – monzogranite suite; QMF – qz-monzodiorite facies; GF - granodiorite facies. ....65

**Figure 4.3-** Petrographic aspects of the investigated rocks: (A) QAP classification diagram of Streckeisen (1974) showing CIPW normative compositions for the studied rocks. Evolutionary trend for magmatic series of Lameyre and Bowden (1982); (B) hand specimen of quartz monzodiorite showing porphyritic texture and very fine- to fine-grained, dark greenish-grey matrix; (C) photomicrograph of quartz monzodiorite showing porphyritic to glomeroporphyritic texture and very fine-grained matrix mainly formed of plagioclase. Augite is enveloped by hornblende rims; (D) granodiorite sample showing weak foliation resulting from the orientation of mafic minerals; (E) photomicrograph of granodiorite showing discrete orientation, formed of plagioclase, hornblende, biotite, titanite and opaque minerals; (F) hand specimen of monzogranite showing porphyritic texture, in which pinkish K-feldspar phenocrysts stand out from a dark-grey matrix of plagioclase, quartz and biotite; (G) photomicrograph of monzogranite showing inequigranular, xenomorphic texture and graphic intergrowth. Photomicrographs taken under crossed polarizers. Mineral abbreviations are after Whitney and Evans (2010). ....67

**Figure 4.4** - The continuous and dotted lines correspond to studies related to high Ba-Sr magmatism used for comparison. Distribution of representative analytical points of the investigated magmatism in the diagrams: (A) Na<sub>2</sub>O+K<sub>2</sub>O-CaO versus SiO<sub>2</sub> proposed by Frost et al. (2001); (B) AFM diagram of Irvine and Baragar (1971); (C)

FeOtot/(FeOtot+MgO) versus SiO<sub>2</sub> proposed by Frost et al. (2001); (D) A/CNK versus A/NK by Maniar and Picolli (1989); (E) K<sub>2</sub>O versus SiO<sub>2</sub> of Peccerillo and Taylor (1976).....75

**Figure 4.5**– Harker diagrams with the distribution of major elements (in ppm) data. Each rock mineralogical composition allows qualitative assessment of possible crystal fractionation and the major elements distribution set up pathways which is represented by vectors from parental appinite to granodiorite. Mineral abbreviations are after Whitney and Evans (2010).....76

**Figure 4.6** – (A) harker diagrams with the distribution of some trace elements (in ppm) data; (B) selected bivariant trace element diagrams for studied suites. Mineral abbreviations are after Whitney and Evans (2010). .....77

**Figure 4.7** - Rare earth elements patterns of the investigated rocks, normalized to the chondritic values of Evensen (1978), compared to high Ba-Sr granites (Fowler et al., 2008) and to monzogranite values of Matok Pluton (Laurent et al., 2014b). .....77

**Figure 4.8** – Multi-element distribution patterns of analyzed samples normalized to primitive mantle values (Thompson, 1982), compared to high Ba-Sr granites (Fowler et al., 2001) and to monzogranite values of Matok Pluton (Laurent et al., 2014b). .....78

**Figure 4.9**- U-Pb geochronological diagrams for the qz-monzodiorite facies, sample AL08. The spots of 30 μm are represented as white circles. (A) Distribution of all the 44 U–Pb data in the Wetherill Concordia Diagram; (B) U-Pb concordant isotope analyses of sample AL08 from the qz-monzodiorite facies with BSE images of zircon grain ZR12 showing upper intercept of 1035 ± 120 Ma; (C) concordia diagram (557±5.7 Ma) for the U-Pb analysis and CL image of representative zircon ZR20 and ZR1. ....88

**Figure 4.10** – U-Pb geochronological diagrams for the granodiorite facies, sample AL01. The spots of 30 μm are represented as white circles. (A) Distribution of all 51 U–Pb data in

the Wetherill Concordia Diagram; (B) U-Pb isotope analysis of sample AL01 from the granodiorite facies with upper intercept age of  $719 \pm 80$  Ma; (C) concordia diagram ( $554 \pm 2.9$  Ma) for the U-Pb analysis and CL images of representative ZR19 and ZR45 zircon grains. ....90

**Figure 4.11-** U-Pb geochronological diagrams for the monzogranite, sample AL27. The spots of  $30 \mu\text{m}$  are represented as white circles. (A) Distribution of 47 U-Pb data in the Wetherill Concordia Diagram; (B) U-Pb concordant isotope analyses of monzogranite sample AL27; CL images of zircon grains showing upper intercept ages older than  $527 \pm 86$  Ma; (C) concordia diagram ( $515 \pm 3.6$  Ma) for the U-Pb analyses and CL images of representative zircon grains ZR06N, ZR24 and ZR5. ....91

**Figure 4.12** – Age (Ga) vs.  $\epsilon_{\text{Nd}}$  diagram for samples from the studied high Ba-Sr intrusions. For comparison, values from the Neoproterozoic granitic province of the Paraguay Belt are also plotted. Data from Ferreira (2009), Godoy et al., (2010) and Pinho (2001). ..92

**Figure 4.13** - (A) Discrimination diagram for high Ba-Sr intrusions (Tarney and Jones, 1994); (B) Sr/Y versus Y proposed by Fowler et al. (2008); (C) Th/Yb vs. Nb/Yb diagram proposed by Pearce and Peate (1995), with the boundary between felsic igneous rocks from oceanic and continental arcs adapted from Condie and Kröner (2013); (D) Ba/La vs. Th/Yb proposed by Woodhead et al. (2001); (E) Rb versus Ta+Yb of Pearce et al. (1984), modified by Pearce et al. (1996); (F) FeOt/MgO versus Zr + Nb + Ce + Y proposed by Whalen et al. (1987). ....99

**Figure 4.14** - Schematic model for the evolution of the investigated high Ba–Sr intrusions and the generation of two contrasting groups at post-collisional scenario. See text for discussions. (A) new accretion stage with onset at ca. 590 Ma; (B) late- to post-collisional stage with the petrogenetic model for the older suite: 1) lithospheric mantle enriched by subducted slab-derived fluid and/or melt; 2) mafic magma rich in LREE

and LILE derived from partial melting of the enriched lithospheric mantle; 3) magma mixing between the mafic magma from the enriched lithospheric mantle and the silicic magma from partial melting of the overlying lower crust, that has been passing through degrees of crystal fractionation to generate the older suite; (C) transitional to within-plate stage which generated the younger suite: 1) metasomatized lithospheric mantle; 2) magma rich in LREE, LILE and some HFSE derived from partial melting of enriched lithospheric mantle and asthenospheric OIB-affinity component; 3) hybridized magma and differentiation at the mechanical boundary level to form the hybridized granitic signature. CC – Continental crust; OC – Oceanic crust; SCLM – Subcontinental lithospheric mantle; TBL – Transbrasiliano Lineament. .... 108

**Figure 4.15** - Distribution of representative analytical points of the studied rocks in the diagrams proposed by Laurent et al. (2014a): (A) ternary diagram  $((\text{Na}_2\text{O}/\text{K}_2\text{O}) - 2 * \text{A}/\text{CNK} (\text{molar } \text{Al}_2\text{O}_3/[\text{CaO} + \text{Na}_2\text{O} + \text{K}_2\text{O}]) - 2 * [(\text{FeOt} + \text{MgO}) \text{ wt.} \% * (\text{Sr} + \text{Ba}) \text{ wt.} \%] = \text{FMSB})$  of sanukitoids and high-K anatectic granites; (B) ternary diagram  $\text{Al}_2\text{O}_3/(\text{FeOt} + \text{MgO}) - 3 * \text{CaO} - 5 * (\text{K}_2\text{O}/\text{Na}_2\text{O})$ ; (C) Plots of incompatible element contents (Sr+Ba) plotted as a function of FeOt+MgO (wt.%) concentrations. .... 112

**Figure 5.1** - Geological sketch of the study area: (A) geotectonic context of the formation of the Tocantins Province during the Brasiliano Orogeny. Cratons are shown in dark gray (modified from Vaughan and Pankhurst, 2008); (B) location of the Tocantins Province in the Brazilian territory; (C) simplified geological map of the Paraguay Belt (modified from Ruiz et al., 2010). Red polygons indicate geochronologically different portions of the Paraguay Belt. Black letters in Region 2 indicate previous investigations in the upper Cuiabá Group (Mata-Mata unit): a- Pelosi (2017); b- Vasconcelos (2018); c- phyllite samples - McGee et al. (2018); (D) simplified geological map of the investigated area

(modified from CPRM, 2017). Corrigir na legenda: Post-tectonic granites; Jacadigo and Boqui groups; Granulite terrains; falta arco magmático de C e D; Granite-gneiss .... 139

**Figure 5.2** - Schematic model illustrating the stratigraphic column of the northern segment of the Cuiabá Group (modified after Manoel et al. 2020). The unit numbers correspond to the subunits of Luz et al. (1980). The syn-rift formations are composed of the units 1 and 2: intercalated pelites and carbon-rich pelites, marbles and metagreywacke; The passive margin formations comprise the units 3 to 8. Unit 3 and 5: metaconglomerates, metarenites and graded phyllites, meta-arkose and quartzite; Unit 4: metadiamicrites (Engenho Facies) and psammitic to pelitic metarhythmites with dropstones (Cangas Facies); Units 6, 7 and 8: phyllites, metadiamicrites, quartzites (Mata-Mata Facies) and marbles (Guia Facies). The ages (Ma) represent U-Pb detrital zircon ages of each unit, the youngest concordant age of which is interpreted as maximum depositional age: (a) Babinski et al., (2018); (b) Batalha (2017); (c) Pelosi (2017); (d) Vasconcelos (2018).  
..... 141

**Figure 5.3** - Geological map of the study area (modified from CPRM, 2017). Colored dots indicate the samples localities. Circled numbers refer to granitoids: 1 – monzogranite (Leite et al., 2021); 2- granodiorite and quartz-monzodiorite (Leite et al., 2021); 3- Macacos syenogranite (Seer, 1987); 4- Serra Negra syenogranite (Guimarães, 2012); 5- Indaiá tonalite (CPRM, 2017). See text for details. .... 147

**Figure 5.4** – (A) macroscopic field aspect of the laminated structure, that corresponds to bedding planes and compositional variation and rhythmic alternation between quartzite and phyllite (B) photomicrography of muscovite-chlorite phyllite with foliations highlighted and layers of polycrystalline quartz intercalated with mica; (C) photomicrography of muscovite-biotite schist. Oriented and metamorphic mica reach up to the biotite zone – sample AL019; (D) photomicrography of the quartzite portion of

polycrystalline quartz and well-marked open folds; (E) photomicrography of schist with cordierite and sillimanite – sample AL06; (F) hand specimen of dark-colored fine to medium-grained schist – sample AL06. Mineral abbreviations are after Whitney and Evans (2010). Pt= perthite. .... 148

**Figure 5.5** – (A) photograph of open fold with deformation phases highlighted; (B) photograph of the preserved axial planes of the D1, resulting in relict axial planes S1 foliation overprinted by TBL; (C) outcrop photograph representing the TLB trend in the rocks and the rotated porphyroclasts with sigmoidal structures; (D) photomicrography showing mylonitic foliation with rotated quartz phenoclast – sample AL18. .... 149

**Figure 5.6** – Backscattered images of some representative grains from the analyzed samples. U-Pb measurement spots are indicated in white circles with 30 μm. See text for details. .... 169

**Figure 5.7** - (A) weighted mean average plot of 104 analyzed concordant grains of sample AL18; (B) probability density diagrams showing  $^{206}\text{Pb}/^{238}\text{U}$  age spectra of the concordant analyzed grains of the sample AL18; (C) weighted mean average plot of 64 analyzed concordant grains of sample AL06; (D) probability density diagrams showing  $^{206}\text{Pb}/^{238}\text{U}$  age spectra of the concordant analyzed grains of the sample AL06. .... 171

**Figure 5.8** - Distribution of probability density diagrams using weighted mean average calculation of samples AL11 and AL31. Some of the analyses were automatically rejected during the Concordia age plotting. (A) weighted mean average plot of 104 analyzed concordant grains of sample AL11; (B) probability density diagrams showing  $^{206}\text{Pb}/^{238}\text{U}$  age spectra of the concordant analyzed grains of the sample AL11; (C) weighted mean average plot of 64 analyzed concordant grains of sample AL31; (D)

|   |     |
|---|-----|
| probability density diagrams showing $^{206}\text{Pb}/^{238}\text{U}$ age spectra of the concordant analyzed grains of the sample AL31. ....  | 172 |
| <b>Figure 5.9</b> - Sm-Nd plots for metasedimentary rocks of the studied rocks in comparison with Nd values of likely source areas of the nearby Goiás Magmatic Arc, Paraguay Belt and Brasília Belt. See text for details. ....  | 174 |
| <b>Figure 5.10</b> – (A) Hand specimen of granodiorite highlighting the weak schistosity marked by oriented mafic minerals. The plutonic body was emplaced in the investigated metasedimentary rocks and the analyzed biotite grains presented orientation parallel to the Transbrasiliano Lineament trend; (B) result of the Ar-Ar analyses performed on biotite and respective plateau ages segments of age spectra; (C) photomicrograph of mica schist, highlighting a muscovite porphyroblast; (D) result of the Ar-Ar analyses performed on white micas and respective plateau (and pseudo-plateau) ages segments of age spectra. .... | 176 |
| <b>Figure 5.11</b> – Distribution of the youngest dated grains, which vary between 600 and 512 Ma. ....   | 177 |
| <b>Figure 5.12</b> – (A) summary plot of variation of the difference between the measured crystallization age for a detrital zircon grain and the depositional age of the succession in which it occurs, based on cumulative proportion curves of Cawood et al. (2012) for the four samples of this study. A: convergent basins (red field); B: collisional basins (blue field); C: extensional basins (green field); (B) plot of cumulative proportion as function of different curves related to foreland data from five locations established by Cawood et al. (2012). ....  | 179 |
| <b>Figure 5.13</b> - P-T-t schematic illustration of the cooling path evolution of sample AL01 (granodiorite pluton). ....  | 183 |

**Figure 5.14** – Histogram illustrating the probability density of different regions of the Cuiabá Group, Paraguay Belt: (A) provenance age pattern of rocks considered as typical Cuiabá Group in the core of the Paraguay Belt (Baixada Cuiabana); (B) provenance age pattern of the southern sector of the Cuiabá Group; (C) provenance age pattern of the studied sector of the Paraguay Belt. .... 188



## LISTA DE TABELAS

|   |  |
|---|--|
| <b>Table 4.1</b> – Summary of U-Pb, Sm-Nd and tectonic environment data available in the literature on Neoproterozoic magmatism of the Paraguay Belt. ....                                | 59                                     |
| <b>Table 4.2</b> – Results of the whole rock geochemical analyses of the investigated rocks. ....   | 69                                     |
| <b>Table 4.3</b> - Data of U-Pb analyses performed through LA-ICP-MS on zircon from the investigated magmatism. ....  | 79                                     |
| <b>Table 4.4</b> - Sm-Nd isotope results. ....  | 92                                     |
| <b>Table 4.5</b> – Worldwide documented appinitic rocks associated to high Ba-Sr magmatism generated at the end of the Proterozoic and beginning of the Phanerozoic. ....                 | 96                                     |
| <b>Table 5.1</b> – Maximum depositional ages and summary of tectonic interpretations from the U-Pb detrital zircon data in the center-south portion of the Paraguay Belt (Region 2). .... | <b>Erreur !<br/>Signet non défini.</b> |
| <b>Table 5.2</b> – Summary of the deformation phases in the investigated area. ....   | 150                                    |
| <b>Table 5.3</b> - Descrição .....  |  |
| <b>Table 5.4</b> – Sm-Nd analytical data for the metasedimentary rocks. ....  | 173                                    |
| <b>Table 5.5</b> – Summary of Ar-Ar data available in the Araguaia, Paraguay and Pampean belts, along the Clymene Ocean corridor. ....  | 184                                    |
| <b>Table 5.6</b> – Evidence of Clymene Ocean existence and/or closure in the Paraguay Belt. ....  | 190                                    |

|  |     |
|--|-----|
| <b>Supplementary Table 4.1</b> – U-Pb general conditions at Laboratory of Geochronology and Isotope Geochemistry of the Universidade de Brasília - UnB. .... | 125 |
| <b>Supplementary Table 4.2</b> - Data of U-Pb analyses performed through LA-ICP-MS on zircon from 91500.....   | 128 |
| <b>Supplementary Table 4.3</b> - Calculation of zircon saturation temperatures ( $T_{Zr.sat.C}$ ) of the Zr concentrations for both suites. ....             | 132 |

**RESUMO**

As faixas móveis mais recentes da Plataforma Sul-Americana correspondem a regiões que registram intensa atividade tectônica, formadas durante a Orogenia Brasileira. A Província Tocantins é considerada um mosaico composto pelas Faixas móveis Paraguai, Araguaia e Brasília, geradas entre os crátons Amazônico e São Francisco. Esta tese de doutorado busca contribuir na compreensão da evolução geotectônica da região oriental da Faixa Paraguai a partir do estudo de granitóides e rochas metassedimentares encaixantes. A região de estudo é localizada quase nas imediações do contato com o Lineamento Transbrasiliano (LTB), que faz limite com o Arco Magmático Arenópolis, Faixa Brasília. A área de interesse é constituída por sequência supracrustal metamorfisada em fácies xisto verde e por corpos graníticos pouco estudados, tipicamente associados ao magmatismo neoproterozoico da Faixa Paraguai. Parte das rochas estudadas apresentam deformação superimposta transcorrente, relacionada evolução do Sistema Direcional do Lineamento Transbrasiliano. Os granitóides estudados compreendem duas suítes que cristalizaram com aproximadamente 40 Ma de diferença entre si. Ambas as suítes apresentam elevados teores de Ba (~1430 ppm), Sr (~800 ppm), K<sub>2</sub>O (~4 wt%), LREE e LILE. Os valores negativos de  $\epsilon_{Nd}(T)$  (-6,32 e -6,65), associados a conteúdos elevados de elementos incompatíveis, indicam evolução a partir da fusão parcial do magma derivado do manto, que foi previamente metassomatizado por fluidos vindos da placa subductante. Foram obtidas idades de cristalização de  $557 \pm 5,7$  Ma e  $554 \pm 2,9$  Ma para a suíte mais antiga, que apresenta caráter cálcio-alcálico e alto K. Esta suíte evoluiu de magma apinitico com alto conteúdo de Cr, V e Ni, derivado do manto, para magma contemporâneo granodiorítico a partir de cristalização fracionada acompanhada de pequena contaminação crustal. A suíte mais nova, de  $515 \pm 3,6$  Ma, é representada por monzogranitos isotópicos de alto K e concentração elevada de alguns HFSE, mostrando afinidade álcali-cálcica. O modelo petrológico proposto para as duas suítes baseia-se no mecanismo de *slab break-off* e posterior delaminação litosférica após

40 Ma. O estudo de proveniência sedimentar foi aplicado nas rochas metassedimentares encaixantes dos granitoides. A utilização de zircão detrítico com a aplicação do método U-Pb permitiu estabelecer espectro de idades distribuídas desde o fim do Ediacarano até o Arqueano, sendo ~60% dos grãos analisados são derivados de fontes ediacarano-criogenianas. A idade máxima de deposição da bacia é definida em ca. 594 Ma, limitada pelos pico principal de zircões mais jovens. O caráter sin-orogênico da bacia é definido pelo fato de que mais de 50% dos grãos apresentam idades próximas da idade máxima de sedimentação da bacia. O maior pico de idades U-Pb de zircão é registrado em torno de 620 Ma, indicando um evento de sedimentação sin-colisional relacionado à atividade de um arco magmático contemporâneo à deposição. O desenvolvimento dessa margem ativa teria acontecido após ca. 620 Ma e se encerrado em 594 Ma com a deposição da bacia. A idade  $^{40}\text{Ar}$ - $^{39}\text{Ar}$  de  $536\pm 4$  Ma obtida para o metamorfismo das rochas encaixantes indica a continuação da temperatura de aproximadamente 400 °C até o Cambriano. Pode-se sugerir também a presença de alguns plutons que não afloram na área que causou o aquecimento da área neste período. A taxa rápida de 25°C/Myr indica a taxa de resfriamento do pluton granodiorítico, associação às falhas transcorrentes relacionadas ao Lineamento Transbrasiliano. Os dados geoquímicos e geocronológicos U-Pb do magmatismo e de zircão detrítico, associado ao contexto tectônico e metamórfico, indicam que a evolução da porção central do Gondwana Oriental ultrapassou os 600 Ma e, possivelmente, um oceano mais jovem foi consumido, o Oceano Clymene.

**Palavras-chave:** Gondwana Ocidental; Faixa Paraguai; Granitoides de alto Ba-Sr; Petrogênese; Proveniência Sedimentar; Evolução Crustal.

**ABSTRACT**

The youngest mobile belts of the South-American Platform correspond to regions that record intense tectonic activity and were formed during the Brasiliano Orogeny. The Tocantins Province is a mosaic composed of three mobile belts located between the Amazonian and São Francisco cratons. This Ph.D. thesis presents the advance of the studies regarding the geotectonic evolution of the eastern region of the Paraguay Belt, located almost on its limit with the Arenópolis Magmatic Arc of the Brasília Belt. The study area is composed of a supracrustal sequence metamorphosed to the greenschist facies and granitic bodies associated with the Neoproterozoic magmatism of the Paraguay Belt. Superimposed deformation was produced by transcurrent faults related to the Transbrasiliano Lineament (LTB). The granitoids of the study area belong to two suites that crystallized with an approximately 40 Ma age difference from one another. Both suites present high Ba (~1430 ppm), Sr (~800 ppm), K<sub>2</sub>O (~4 wt%), LREE and LILE contents. Negative  $\epsilon_{Nd}(T)$  values (-6.32 and -6.65 respectively) associated with high incompatible-element contents indicate magmatic evolution from partial melting of a previously metasomatized mantle by fluids coming from a subducting plate. Crystallization ages of  $557 \pm 5.7$  Ma and  $554 \pm 2.9$  Ma were obtained for the older, high-K, calc-alkaline suite. This suite evolved from a mantle-derived, appinitic magma with high Cr, V, and Ni contents to a coeval granodioritic magma via fractional crystallization accompanied by minor crustal contamination. The younger suite of  $515 \pm 3.6$  Ma of age is represented by high-K monzogranites with high concentrations of some HFSE, indicating alkali-calcic affinity. The petrologic model proposed for both hybrid suites is based on the slab break-off mechanism followed by lithospheric delamination after 40 Ma. Sedimentary provenance of the metasedimentary rocks that host the granitoid bodies was investigated. Detrital zircon U-Pb geochronology helped establish an age spectrum from the beginning of the Cambrian to the Archean, in which ~60% of the zircon grains derived from Ediacaran-Cryogenian sources. The

maximum deposition age is defined at ca. 594 Ma, constrained by the main peak youngest zircon grains. The syn-orogenic character of the sedimentary basin is inferred by the fact that the ages obtained for more than 50% of the grains are close to the maximum sedimentation age obtained for the basin. The highest zircon U-Pb age peak is recorded around 620 Ma, indicating a syn-collisional sedimentation event related to the activity of a magmatic arc coeval to deposition. The development of this active margin may have taken place after ca. 620 Ma and ended at ca. 594 Ma. The  $^{40}\text{Ar}$ - $^{39}\text{Ar}$  age of  $536 \pm 1.83$  Ma obtained for the metamorphism of the host rocks indicates the maintenance of a temperature of approximately 400 °C until the Cambrian or may indicate the presence of plutons that not cropped out, yielding the heating in the area. A 25°C/Myr cooling rate is estimated for the granodioritic magma – the fast magma emplacement takes place possibly associated with transcurrent faults related to the Transbrasiliano Lineament. The assembly of the data presented here highlight the fact that the study area was a tectonically active region from the late Ediacaran to the beginning of the Cambrian. The geochronological U-Pb data from detrital zircon and magmatic rocks, associated to the tectonic and metamorphic context, indicate that the evolution of the central portion of West Gondwana has overtaken 600 Ma. Possibly, a younger ocean was consumed for generation of this rocks, the Clymene Ocean.

**Keywords:** West Gondwana; Paraguay Belt; High Ba-Sr granitoids; Petrogenesis; Sedimentary Provenance; Crustal Evolution.

## 1. INTRODUÇÃO

### 1.1. Apresentação do tema

As causas e relações entre as mudanças que ocorreram no planeta durante a Era Neoproterozoica (1000-540 Ma) têm sido abordadas em muitas pesquisas interdisciplinares (Stern, 1994). Extensas zonas de cisalhamento transpressionais e cinturões móveis com volumoso magmatismo orogênico foram eventos marcantes que se consolidaram nas fases finais de importantes orogênias neoproterozoicas (Unrug, 1992; Meert, 2001; Cordani *et al.*, 2013). O entendimento da paleogeografia e tectônica da Plataforma Sul-Americana baseia-se no esclarecimento de fases de amálgama do Gondwana, último grande evento que registra formação de cadeias de montanhas e fechamento de bacias oceânicas e intracontinentais no final do Pré-Cambriano. A aglutinação do Supercontinente Pannotia-Gondwana originou-se no Neoproterozoico durante a Orogenia Brasileira-Pan-Africana (Kennedy, 1964; Kröner, 1984, Rogers, 1996, Meert, 1999 entre outros), que amalgamou os grandes crátons Amazônico, São Francisco-Congo, Kalahari, Rio de la Plata, metacraton do Sahara e outros pequenos fragmentos crustais.

Em visão geral de Gondwana, algumas peças constituintes foram posteriormente aglutinadas ao longo de colisões diacrônicas no final do Neoproterozóico e início Fanerozóico (~575-480 Ma). Esse intervalo é caracterizado por abundante consumo de litosfera oceânica em todos os sectores do supercontinente, visto que a distribuição global de zircão detrítico datados em 600–500 Ma são recorrentes nos terrenos de toda extensão do supercontinente Gondwana (Kennedy, 1964; Meert, 1999, 2001; Veevers, 2004; Meert e Lieberman, 2008; Meredith *et al.*, 2017). A fase final de aglutinação de Gondwana Ocidental é tradicionalmente registrada pelos eventos colisionais gerados pela aproximação dos crátons Amazônico, São Francisco-Congo,

Rio de la Plata e do Bloco Paranapanema, que indicam o fechamento do grande oceano Goiás-Farusiano até 620 Ma (Kröner e Cordani, 2003; Cordani *et al.*, 2009, 2013; Della Giustina *et al.*, 2009, 2011). Porém, um outro modelo de evolução vem sendo apresentado e a integração de dados paleomagnéticos do Gondwana Ocidental e diversos eventos tectono-termiais cronocorrelatos entre as Faixas Araguaia, Paraguai e Pampeana, sugerem o fechamento de oceano cambriano denominado de Clymene (Trindade *et al.*, 2003, 2006; Tohver *et al.*, 2010, 2012; Tohver e Trindade, 2014).

No contexto de aglutinação de supercontinentes, margens continentais passivas se tornam margens ativas, originando faixas móveis. A Província Tocantins é formada por um conjunto de blocos tectônicos agregados durante a Orogenia Brasileira, formando extenso mosaico orogênico no centro do Brasil. A Faixa Paraguai constitui parte dessa rede de orógenos neoproterozoicos e é alvo de diversos questionamentos a respeito da evolução geotectônica e paleogeográfica do Gondwana Ocidental.

A área foco do presente trabalho situa-se no limite leste da Faixa Paraguai, onde o Lineamento Transbrasiliano (LTB) separa o extremo leste da Faixa Paraguai da extensão meridional do Arco Magmático de Goiás, da Faixa Brasília. O LTB é entendido como uma megafeição continental resultante de deslocamentos laterais, durante e/ou após a colisão envolvendo massas continentais como os crátons Amazônico, São Francisco-Congo, Rio de La Plata e o bloco Paranapanema (Pimentel e Fuck, 1992; Fuck *et al.*, 2013).

O presente trabalho busca evidências a partir de dados geoquímicos e isotópicos/geocronológicos do magmatismo e de rochas supracrustais expostas em uma área muito pouco estudada, situada na região limítrofe da Faixa Paraguai com o Arco Magmático Arenópolis, da Faixa Brasília. Os dados apresentados buscam contribuir para a compreensão da evolução geotectônica da Faixa Paraguai, e assim, melhorar o entendimento da fase final de



aglutinação do Gondwana Ocidental. A integração dos elementos obtidos permitiu analisar de forma ampla o cenário tectônico que gerou as rochas investigadas e assim, correlacioná-lo com a possível existência de oceano mais recente no centro do Gondwana Ocidental.

## 1.2.Relevância e objetivos da tese

Muitos trabalhos têm sido desenvolvidos para esclarecer a história do amálgama de Gondwana (Stern, 1994; Meert, 2001, 2003; Collins e Pisarevsky, 2005; Pisarevsky *et al.*, 2008; Schmitt *et al.*, 2018), incorporando evidências de eventos colisionais a partir de dados estruturais, termais, magmáticos, geocronológicos e deformacionais entre pequenos continentes durante o Neoproterozoico. Indícios sobre a existência de oceano de idade ediacarana a cambriana tem sido sugerida, cuja destruição gerou rochas orogênicas no fim do Neoproterozoico, implicando em importantes discussões tectônicas sobre a amalgamação da porção oeste do supercontinente Gondwana. Neste sentido, a região do extremo leste da Faixa Paraguai constitui um objeto ideal para o estudo da presença desse tipo de eventos evolucionais tardios no Gondwana Ocidental.

A área foco deste trabalho é constituída por sequência supracrustal tipicamente descrita como pertencente ao Grupo Cuiabá, zona interna da Faixa Paraguai, e por intrusões graníticas (Seer, 1985; Seer e Nilson, 1985). Não há dados geocronológicos e geoquímicos disponíveis para essas rochas, que permitam definir idade e ambiente geotectônico e relacioná-las com a geologia regional da Faixa Paraguai e/ou da Província Tocantins. Logo, por falta de dados, tem-se uma área que é pouco considerada quando é abordada a evolução Brasileira, não havendo consenso sobre a origem das rochas aflorantes. Seer (1985) atribui a unidade ao Grupo Cuiabá e CPRM (2017) a define como prolongamento da Sequência Metavulcano-sedimentar Nova

Xavantina, exposta a norte da região de estudo. Além disso, trabalhos iniciais identificaram os corpos intrusivos estudados e sugeriram que a gênese destes corpos seria possivelmente correlacionada com o evento magmático neoproterozoico descrito na Faixa Paraguai (Seer, 1985; Seer e Nilson, 1985; Godoy *et al.*, 2007, 2010).

A leste da área investigada, as rochas estudadas apresentam deformação superimposta pelas falhas transcorrentes associadas ao Lineamento Transbrasiliano (LTB). A zona de descontinuidade transcorrente na região de Bom Jardim de Goiás é exposta em sua fase rúptil-dúctil e nomeada como Lineamento Serra Negra (Curto *et al.*, 2014, 2015). Tendo em vista a grande relevância do Lineamento Transbrasiliano na história geológica de estabilização da Província Tocantins, torna-se de extremo interesse científico melhor compreensão do seu papel na estruturação termal e deformacional nos terrenos que são afetados pela mega-estrutura continental, e assim entender a possível associação com o magmatismo aparentemente influenciado pela acomodação do TLB e suas falhas interconectadas.

O presente trabalho visa contribuir para o avanço do conhecimento sobre a evolução tectônica da região central da Província Tocantins e elucidação da evolução crustal neoproterozoica tardia do Gondwana Ocidental. Este estudo se mostra relevante, principalmente, em termos de registro de material juvenil adicionado à crosta continental durante os eventos finais de aglutinação. Este registro pode ser detectado a partir de métodos como geoquímica de rocha total e geoquímica isotópica, podendo desvendar processos episódicos de extração de material juvenil e assim, indicar processos geodinâmicos para a área de estudo. Ademais, a utilização do método U-Pb em zircão detrítico permite definir a idade de formação da bacia a partir das idades dos grãos mais jovens e detectar possíveis áreas fontes. Estudos isotópicos com foco em análise de proveniência sedimentar é comumente utilizado para definir a idade máxima de deposição, que ocorre necessariamente após a cristalização do grão em terrenos já consolidados.

Assim, este trabalho tem como objetivos gerais: (i) caracterização de duas suites magmáticas cristalizadas com 40 Ma de diferença entre si; (ii) compreensão da história evolucionária das rochas metassedimentares encaixantes das intrusões. Para tanto, dois artigos de cunho geotectônico são apresentados, com os seguintes objetivos específicos:

- **Artigo 1:** O foco do artigo é a definição da idade de cristalização das rochas ígneas e estabelecer a fonte (mantélica ou fusão parcial de crosta continental preexistente?), assim como definir padrões de cristalização fracionada. O estabelecimento de origem e evolução do magma contribui para a elucidação do ambiente tectônico de geração dessas rochas, assim como dos principais processos petrogenéticos e geodinâmicos. Um dos objetivos específicos consiste em compreender a contribuição do Lineamento Transbrasileiro para a evolução e a colocação dos corpos graníticos, assim como sugerir o papel dos magmatismos de high Ba-Sr na aglutinação neoproterozoica tardia dos terrenos envolvidos na estabilização do Gondwana Ocidental.

- **Artigo 2:** O objetivo geral do artigo é compreender os dados de proveniência sedimentar de um orógeno neoproterozoico, assim como adicionar novos dados referentes à região investigada, antes não estudada com a aplicação do método U-Pb em zircão detrítico. Sabe-se que bacias desenvolvidas em ambiente colisional tendem a apresentar maiores conteúdos de idades próximas à deposicional, com variações por volta de 50% dos grãos com idades até 150 Ma mais antigas que a idade deposicional, refletindo magmatismo pré a sin-colisional de terrenos acrescidos ao orógeno. O objetivo principal é a associação de dados isotópicos U-Pb e Ar-Ar para a elucidação da história evolutiva das rochas metassedimentares, definindo idade de deposição, idade de metamorfismo/deformação e taxa de resfriamento.

### 1.3. Localização e vias de acesso

A área de estudo localiza-se no limite entre os estados de Mato Grosso e Goiás, englobando as cidades de Torixoréu, em Mato Grosso e Baliza e Bom Jardim de Goiás, em Goiás, abrangendo parte da folha SE.22-V-B (Iporá – CPRM, 2017). O acesso, partindo de Cuiabá-MT (Figura 1.1), foi feito pela BR-251 por 68 km até a cidade de Chapada dos Guimarães, por mais 58 km até o trevo que liga a MT-344 para chegar em Campo Verde (12 km a partir do Trevo). A partir de Primavera do Leste, é necessário percorrer a BR-070 por 324 km passando por General Carneiro e Barra do Garças. Desta última cidade até Bom Jardim de Goiás trafega-se mais 47 km pela BR-158. Para chegar à cidade de Baliza-GO, percorre-se 42 km a partir de Bom Jardim de Goiás pela GO-421. O trajeto todo totaliza 580 km de Cuiabá até a área de estudo.

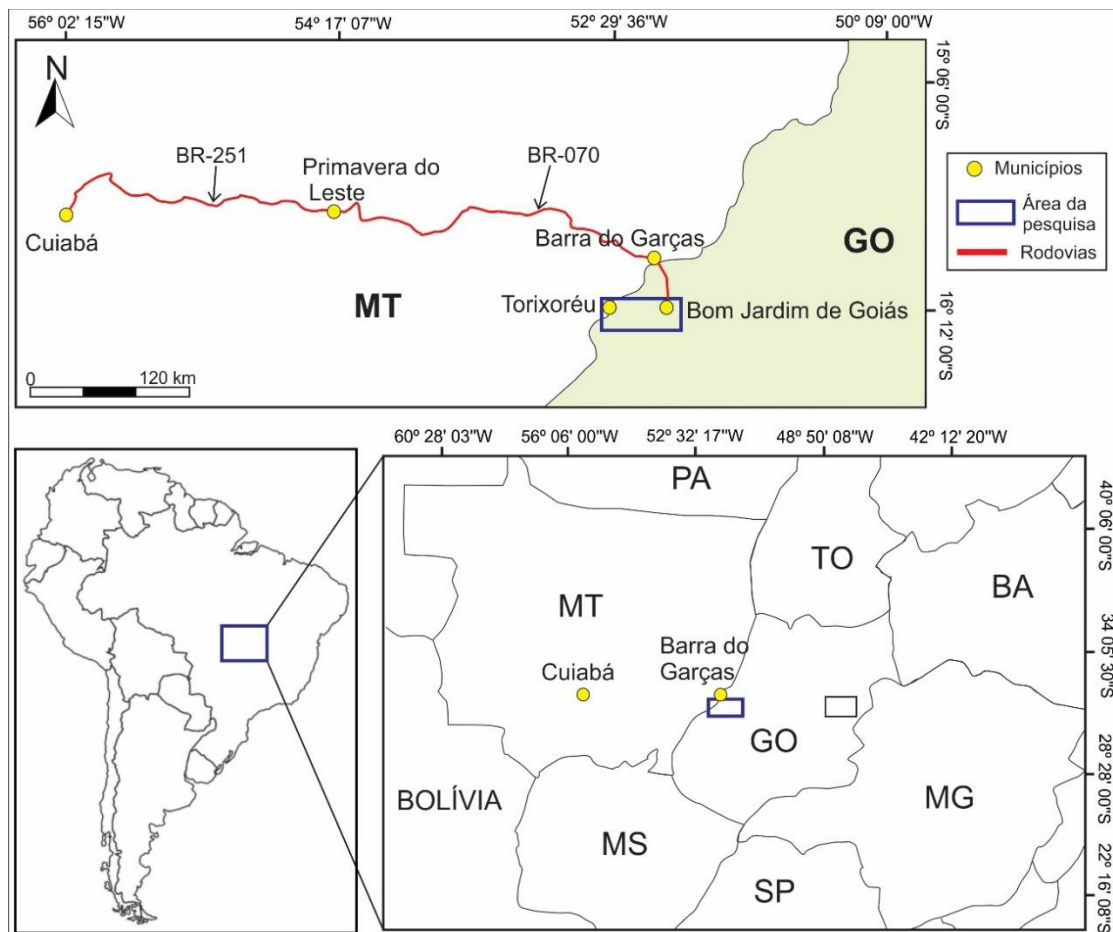


**Figura 1.1** – Mapa de localização e vias de acesso à área de pesquisa, localizada a aproximadamente 47 km do município de Barra do Garças - MT, divisa com o estado de Goiás.

#### 1.4. Estrutura da tese

A tese encontra-se organizada em sete (7) Capítulos. Após este tópico introdutório do capítulo 1, segue-se revisão teórica no capítulo 2, que trata de questões relativas à formação das principais ideias quanto a orogênese e formação de supercontinentes, com foco no Gondwana, assim como evolução de ambientes tectônicos pós-colisionais e magmatismos associados. Os materiais e métodos utilizados durante o doutorado são apresentados no Capítulo 3, incluindo preparação pré-campo e etapas laboratoriais.

Os capítulos 4 e 5 apresentam os resultados obtidos em forma de dois artigos científicos, sendo o primeiro publicado e o segundo submetido:

- 1) O Capítulo 4 contém o artigo aceito para publicação no periódico *Lithos* do mês de junho de 2021, intitulado: *Appinitic and high Ba–Sr magmatism in central Brazil: Insights into the late accretion stage of West Gondwana.*
- 2) O capítulo 5 compreende o artigo submetido recentemente (outubro de 2021) ao periódico *Gondwana Research*, O artigo é intitulado: *Tectonic significance of the early-Cambrian syn-orogenic basin in the easternmost portion of Paraguay Belt, Tocantins Province, central Brazil.*

O Capítulo 6 expõe as considerações finais dessa tese, incluindo a síntese conclusiva da a partir dos dados apresentados nos dois artigos, destacando a história evolutiva integrada da região de estudo em relação ao Gondwana Ocidental.

Finalmente, o Capítulo 7 contém as referências bibliográficas utilizadas nos capítulos 1 a 3 desta Tese.

## 2. REFERENCIAL TEÓRICO E REVISÃO BIBLIOGRÁFICA

O registo de crescimento continental permanece sendo tópico de discussões, pois os processos orogênicos conduzem frequentemente a reciclagem significativa do material continental. No sentido de contextualizar o que será discutido nos artigos científicos apresentados nos capítulos seguintes, este tópico apresenta revisão geral das principais temáticas envolvidas ao longo do doutorado. Será apresentada visão geral sobre a evolução do magmatismo ao longo da história tectônica da terra e o significado do magmatismo de alto Ba-Sr moderno e suas correlações com os sanukitoides de 2.5 Ga. Conceitos de formação de orógenos, assim como as principais características que definem a formação do supercontinente Gondwana também serão comentados. Além disso, o último tópico aborda conceitos sobre o Lineamento Transbrasiliano no Gondwana. Os principais trabalhos consultados acerca do tema da tese estão inseridos no corpo do texto e as referências estão inclusas no último tópico da tese (capítulo 7).

### 2.1.A evolução do magmatismo terrestre

Como pioneiro no assunto, Wilson (1966) apresentou a Teoria da Tectônica de Placas, expondo-a como proposta para explicar os processos de deriva continental e expansão dos fundos oceânicos. Gastil (1960) desenvolveu a ideia de que os processos ocorrem de forma episódica e não contínua. Atualmente, há consenso de que as massas da terra se amalgamam quase periodicamente em supercontinentes, interpretados como super-placas rígidas, marcadas essencialmente por limites tectônicos ativos e exibindo pequenas interações internas de litosfera-manto (Nance *et al.*, 2014; Pastor-Gálan *et al.*, 2018). Os limites tectônicos são identificados graças às assinaturas e características marcantes das rochas geradas durante as orogenias. A investigação das orogenias

colisionais e acrescionárias se mostra, portanto, de extrema importância uma vez que são a chave das configurações de antigos continentes e supercontinentes (Hoffman, 1989).

A formação e ruptura de supercontinentes são fortemente ligadas às mudanças globais de nível do mar, ciclos biogênicos, mudanças climáticas, sedimentação de margens continentais, grandes províncias ígneas, circulação do manto profundo, assim como dinâmica do núcleo exterior e campo magnético da terra (Rogers, 1996; Meert, 1999). A formação de supercontinentes ocorre associada a crescimento da crosta terrestre, visto que os principais processos geológicos ocorrem em margens convergentes. Os picos de idades de grãos detríticos de zircão apontam excelentes correlações com a formação dos continentes, refletindo a preservação de rochas juvenis e crustais retrabalhadas durante as orogenias (Cawood *et al.*, 2007, 2012; Pereira *et al.*, 2021).

Crescimento e evolução da crosta continental através do tempo geológico resultam de equilíbrio entre a extração magmática do material juvenil do manto e o retorno do material continental ao manto por meio da subducção de sedimentos, erosão por subducção e/ou delaminação (Laurent *et al.*, 2014; Moyen *et al.*, 2017). A assinatura geoquímica de rochas ígneas pode ser considerada como indicador útil de reciclagem da crosta continental no manto litosférico subcontinental durante as diferentes fases do processo de subducção. Este processo registra diferentes condições de fusão parcial e de anatexia crustal em ambiente tectônico sin-a pós-colisional, contribuindo para a evolução do planeta terra.

A evolução do registro magmático da Terra evolui do Arqueano até os tempos modernos como reflexo de seu resfriamento e da evolução dos processos tectonomagmáticos (Moyen e Laurent, 2017 e referências contidas). Granitoides representam a crosta continental recém-formada, e evoluíram de TTGs arqueanos, formados por fusão parcial direta da crosta máfica, passando por sanukitoides e rochas relacionadas ao Neoarqueano e Paleoproterozóico que



carregam a assinatura de uma cunha de manto primitiva, e finalmente, para granodioritos e granitos com composições de magma de arco (os equivalentes plutônicos de BADR – basalto–andesito–dacito–riolito; Martin, 1987, 1988, 1993, 1999; Martin *et al.*, 2005; Moyen e Martin, 2012). Muitas questões fundamentais permanecem em aberto quando fala-se sobre processos tectonomagmáticos da Terra, o crescimento da crosta continental e a transição para a tectônica dirigida por subducção. Algumas questões podem ainda serem abordadas com uma compreensão mais completa dos tempos e proporções da gênese do magma granitoide.

Há consenso que o mecanismo terrestre de formação de magmatismo atual da Terra é associado a um modelo de geração de rochas diferente daquele inferido para o Arqueano. A diferença aponta para mudança importante em determinados aspectos do funcionamento das placas tectônicas. Durante o Arqueano, o processo de fusão de crosta oceânica subductada em profundidade rasa gerava importantes volumes de TTG, que formaram a grande maioria das crostas continentais juvenis antigas (Martin, 1985; Martin *et al.*, 2005, 2009). A diminuição progressiva da taxa de produção de magmas TTGs resultou em aumento eficiente no processo de hibridização na cunha do manto e diminuição na fusão direta da placa subductante descendente (Martin, 1993, 1999). Este processo marca o momento em que o fluxo de calor terrestre era alto o bastante para induzir a desidratação da crosta oceânica, mas suficientemente baixo para gerar pouca quantidade de fusão parcial da placa subductante. O produto é então inteiramente consumido por processos de hibridização na cunha de manto sobrejacente (Martin, 1993; Martin *et al.*, 2005; Moyen e Martin, 2012).

Os sanukitoides, além de apresentar características transitórias em termos de idade, também são intermediários em termos de composição química entre as séries de TTGs arqueanos e granitóides tidos como modernos (que ocorrem após 2.5 Ga). Tipicamente, a assinatura dos elementos traços dos exemplos mundiais os aproximam de TTGs, enquanto sua composição em elementos principais (principalmente  $K_2O$  e  $Na_2O$ ) está claramente mais

próxima dos granitóides cálcio-alcálicos pós-arqueanos (Martin *et al.*, 2005). Stern *et al.* (1989) mostraram que é física e quimicamente impossível gerar magmas com as assinaturas de elementos traços de sanukitoides por fusão parcial de peridotito não enriquecido, que apresente composição idêntica ao manto primitivo, por exemplo. Assim, a fonte é claramente manto enriquecido, resultante de interação entre peridotito, por um lado, e um componente rico em elementos incompatíveis por outro lado (Shireye e Hanson, 1984; Martin, 1988; Stern *et al.*, 1989; Stern e Hanson, 1991). Outros trabalhos também atestam alterações das assinaturas geoquímicas de rochas magmáticas após 2.5 Ga, indicando transição entre a geração de magma tipo TTG e geração de magmatismo do tipo sanukitoide (Stern e Hanson, 1991; Steverson *et al.*, 1999; Martin *et al.*, 2009). Com isso, o período de transição entre Arqueano e Paleoproterozoico foi consagrado como marco para o mecanismo global de geração de rochas, em que parte da crosta continental juvenil moderna é gerada em subducção pela fusão parcial da cunha de manto, cuja composição foi previamente modificada por fluidos liberados por desidratação das placas subductadas (Moyen e Martin, 2012).

Os granitos de alto Ba-Sr correspondem a distinto grupo de rochas que são consideradas ter sido formadas em ambientes de subducção com significativa entrada de material mantélico (Tarney e Jones, 1994). A conexão genética entre os sanukitoides e granitoides de alto Ba-Sr é uma discussão recente sobre a relação entre mecanismo de crescimento da crosta continental registrados em 2.5 Ma e em tempos modernos (Fowler e Rollinson, 2012). O persistente padrão geoquímico registrado nos granitoides de alto Ba-Sr revelam significativa similaridade com aqueles descritos para os sanukitoides arqueanos após 2.5 Ma. Portanto, é proposto que a formação dos dois grupos de rocha, mesmo que distantes na história da Terra, podem ser associados pelos mesmos processos tectonomagmáticos e pela reincidência dos mecanismos que permitem a ocorrência de tal assinatura híbrida (Heilimo *et al.*, 2010; Fowler e Rollinson, 2012). A fonte mais provável corresponde a manto enriquecido, como um peridotito, e por outro

lado, a um componente rico em elementos incompatíveis (Shirey & Hanson, 1984; Stern et al., 1989; Stern & Hanson, 1991).

Os estudos sobre a ocorrência dos magmas de alto Ba-Sr no Fanerozoico indicam eventos metassomáticos e contextos geodinâmicos específicos na tectônica recente, como o mecanismo de *slab break-off* e a consequente subida da astenosfera em ambientes de subducção e/ou subducção tardia (Tarney e Jones, 1994; Fowler *et al.*, 2001, 2008; Fowler e Rollinson, 2012). A ocorrência de rochas com esse tipo de assinatura geoquímica pode ser utilizada como indicador de reciclagem da crosta continental no manto litosférico subcontinental durante as fases finais do processo de subducção. Por fim, este processo registra diferentes condições de fusão parcial e de anatexia crustal no cenário sin- a pós-colisional, contribuindo para a evolução do planeta terra até os tempos Phanerozoicos.

## 2.2.O supercontinente Gondwana e suas fases finais de fechamento

A formação de supercontinentes é comumente explicada pela coalescência de numerosos fragmentos continentais ao longo de suturas formadas pelo fechamento de bacias oceânicas (Unrug, 1992; Pastor-Gálan *et al.*, 2018). Hoffman (1991) sugeriu pela primeira vez que a fragmentação do supercontinente Rodínia envolveu peças continentais se afastando de Laurentia e colidindo para formar Gondwana. O supercontinente Gondwana foi o produto de eventos convergentes diacrônicos durante o Neoproterozoico, que tiveram sua fase final de aglutinação no começo do Paleozoico (Collins & Pisarevsky, 2005; Meert & Lieberman, 2008; Schmitt *et al.*, 2018). Pisarevsky *et al.* (2008) indicam que a dinâmica de montagem completa desse supercontinente abrangeu o intervalo de tempo entre 900 e 500 Ma. O início da formação se deu a partir da aglutinação de duas massas continentais na porção Ocidental (África-América do Sul) e na Oriental (Índia-Austrália-Antártica), ao longo do cinturão Moçambique

(McWilliams e McElhinny, 1980; McWilliams, 1981; Stern, 1994; Figura 1). Este argumento foi baseado na extensão deste cinturão a norte, no escudo Arabian-Nubian e a partir disso, ocorreram as orogêneses neoproterozoicas entre os fragmentos cratônicos (Harris, 1994). Diversos outros pequenos fragmentos também seriam incorporados à Ásia, Europa e América do Norte (Schmitt *et al.*, 2018; Figura 2.1).

Gondwana at ca. 500 Ma

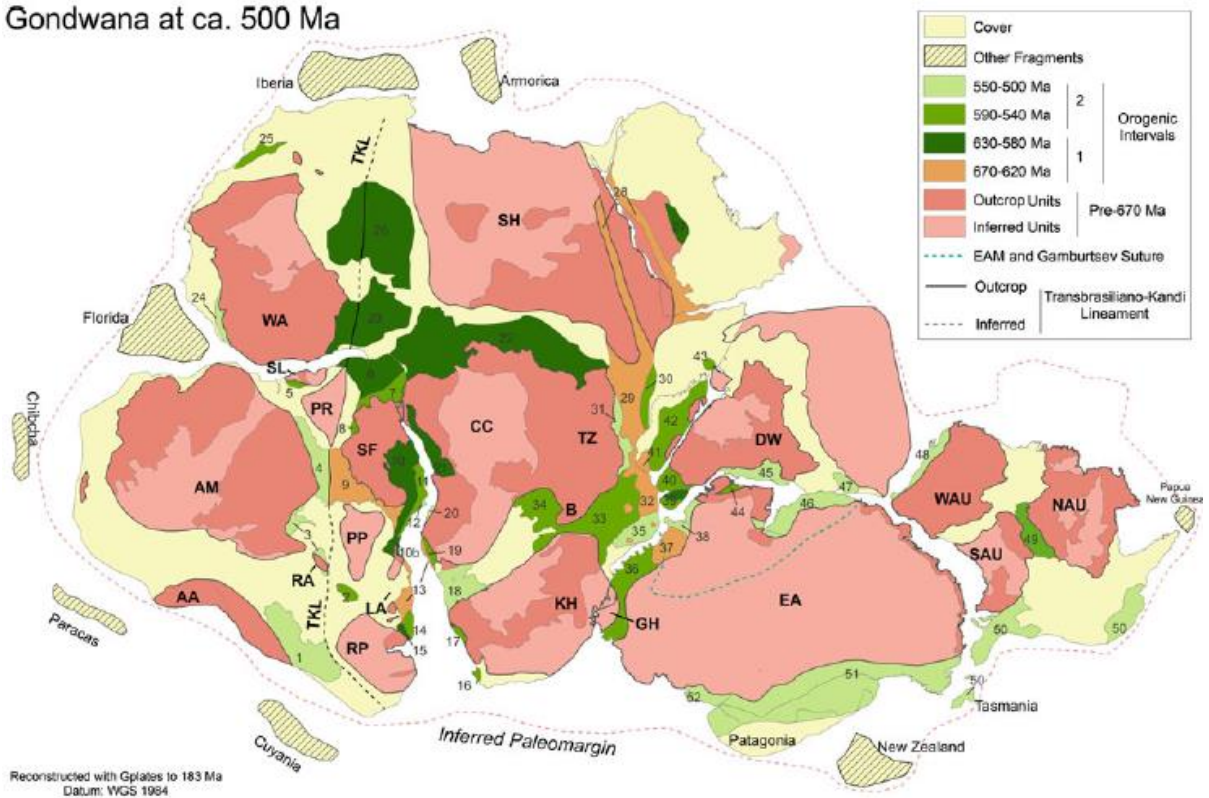


Figura 2.1 – Mapa da configuração do supercontinente há 500 Ma (extraído de Schmitt *et al.*, 2018).

O nome Gondwana foi sugerido para denominar uma sequência de rochas sedimentares não marinhas. O nome proveio de uma antiga tribo aborígine, que se acredita ter habitado na parte central da Índia, onde estas rochas foram encontradas (Melicott e Blandford, 1879). O intervalo de tempo exato da montagem do Gondwana sobrepõe o período de rápida diversificação de vida no planeta Terra e segue intervalo de resfriamento global em evento de *Snowball Earth* (Meert & Torsvik, 2003; Valentine, 2002). Muitos modelos têm sido

gerados para a montagem e melhor compreensão desse supercontinente, cuja primeira ideia surgiu com observações de padrões de distribuição de sedimentos glaciais, fósseis de plantas e outras características do Permo-Carbonífero (Danziel, 1975). A partir disso, estabeleceu-se que o Gondwana teve muitos processos de acreção no Pre-Cambriano e a sua fragmentação da grande Pangea se deu no Mesozoico tardio (Danziel, 1975; Meert, 1999; Cawood *et al.*, 2005).

Dois estágios principais de amálgama são indicados por Schmitt *et al.* (2018) no Gondwana, entre 670 e 575 Ma e entre 575 e 480 Ma, representando os períodos de colisões mais abundantes em todos os setores. O primeiro estágio gerou cerca de 40 orógenos e o mais novo, cerca de 15 faixas móveis. O período mais longo de amálgama foi entre 670 e 480 Ma (Schmitt *et al.*, 2016, 2018), no qual diversos oceanos foram consumidos para a formação do supercontinente Gondwana (Moçambique, Adamastor, Goiás-Farusiano) e outros foram abertos (Iapetus, Paleo-Asian, Tornquist) entre os continentes Laurentia, Baltica, Siberia, Gondwana e outros blocos cratônicos (Meert, 2001; Meert & Torsvik, 2003; Collins & Pisarevsky, 2005; Li *et al.*, 2008).

Os orógenos finais do Gondwana, também chamados de “orógenos internos” (como Búzios, Damara, Saldania, Paraguai, Araguaia, Malagasy, entre outros), se desenvolveram inicialmente devido às configurações convergentes das margens recém-formadas, influenciando os “orógenos externos” eocambrianos-ordovicianos (a exemplo do Pampeano, Ross, Delamerian, Bhimphedian; Rapela *et al.*, 1998, 2011; Schmitt *et al.*, 2004). Há diversas interpretações sobre a natureza dos orógenos finais do Gondwana. Uma das hipóteses é de que são produto do fechamento de largo oceano, culminando com a agregação de vários paleocontinentes distantes entre si (Oceano Clymene, Tohver *et al.*, 2010, 2012; Oceano Adamastor, Heilbron *et al.*, 2008; Oceano Moçambique, Stern, 1994; Boger & Miller, 2004). Outro ponto de vista sugere que esses orógenos foram produtos de rifteamentos intracontinentais e inversão de bacias entre blocos que nunca foram distantes (Cinturão

Araguaia, Cordani *et al.*, 2013; Cinturão Damara, Nascimento *et al.*, 2017; Cinturão Ribeira, Meira *et al.*, 2015).

Em uma visão geral, algumas peças constituintes de Supercontinente Gondwana foram acrescidas tardiamente ao longo de colisões diacrônicas no final do Neoproterozóico e início do Cambriano (575-480 Ma; Meert, 2001). Este intervalo é caracterizado por abundante de consumo tardio de oceanos em todos os setores, assim como por ampla reativação tectono-térmica anteriormente afetadas pelas orogênias acrecionárias, colisionais ou intracontinentais neoproterozoicas (Kennedy, 1964; Meert, 2001; Meredith *et al.*, 2017; Schmitt *et al.*, 2018). No Gondwana Oriental, registra-se neste período a Orogenia Kuunga (Figura 2.2; Meert *et al.*, 2003), em que margens convergentes evoluem de forma contemporânea à aproximação dos blocos da Índia, Austrália e Mawson, implicando no fechamento do oceano Mawson entre 570 e 500 Ma e na geração de extenso arco magmático (Meert *et al.*, 2003; Collin & Pisarevsky, 2005).

Já o orógeno Damara, na Namíbia, reflete a convergência dos crátons Rio de La Plata, Congo e Kalahari e consiste na junção tríplice de três cinturões móveis, Damara Kaoko e Gariep (Hoffman *et al.*, 1994). O maior período de aproximação dos blocos foi entre 655 e 600 Ma, com o fechamento final do Oceano Adamastor em 540 Ma (Gray *et al.*, 2008). O Cinturão Damara foi limitado ao intervalo 570-500 Ma, com grande metamorfismo e magmatismo em torno de 540-530 Ma e intrusões pós-cinematias de granitos tipo A entre 495 e 486 Ma (McDermott *et al.*, 2000; Frimmel *et al.*, 2011; Goscombe *et al.*, 2007, 2017). A Faixa Móvel Kaoko contém intrusões pós-tectônicas entre 535 e 505 Ma (Goscombe *et al.*, 2007) e o cinturão Gariep, os granitos pós-orogênicos registrados entre 547 e 529 Ma (Frimmel & Frank, 1998). A parte ocidental do Cinturão de Kaoko na África, definida como Coastal Terrain e tomada como um domínio exótico, aglutinado tardiamente ao orógeno já consolidado (Goscombe *et al.*, 2005, 2017).

O período de aglutinação entre o Ediacarano e Cambriano é também vastamente registado no Gondwana Ocidental, tal como as rochas metamórficas descritas em fase de subducção tardia no domínio oriental do Cinturão Ribeira, Orógeno Búzios, que se desenvolveu relacionado a uma colisão continental em 570-520 Ma (Schmitt *et al.*, 2004, 2008; Faleiros *et al.*, 2011). No Orógeno Araçuaí, a Formação de Salinas representa um conjunto de rochas sedimentares acumuladas até 551 Ma e é interpretada como uma bacia remanescente formada em cenário de sin-colisão (Castro *et al.*, 2020).

Os eventos por volta de 500 Ma, demoninados de Pampeano-Ross-Delamariano, correspondem a um dos exemplos de orógenos tardios (Rapela *et al.*, 1998). As atividades tectônicas tardias seriam relacionadas com extensão nos estágios finais da montagem do Gondwana, produto do colapso orogênico e/ou reflexo da orogenia Pampeano-Ross-Delamariano, sendo os orógenos resultantes classificados também como paleozoicos (Figura 2.2; Rapela *et al.*, 1998; Cordani *et al.*, 2009; 2013; Zhao *et al.*, 2018). O padrão e período de colisão dos orógenos formados no fim do Gondwana indicam que as causas de fechamento de muitas bacias e desenvolvimento de arco magmático ocorreram até o começo do Ediacarano, e podem, em muitos casos, serem considerados como registros da sutura final do Supercontinente Gondwana.

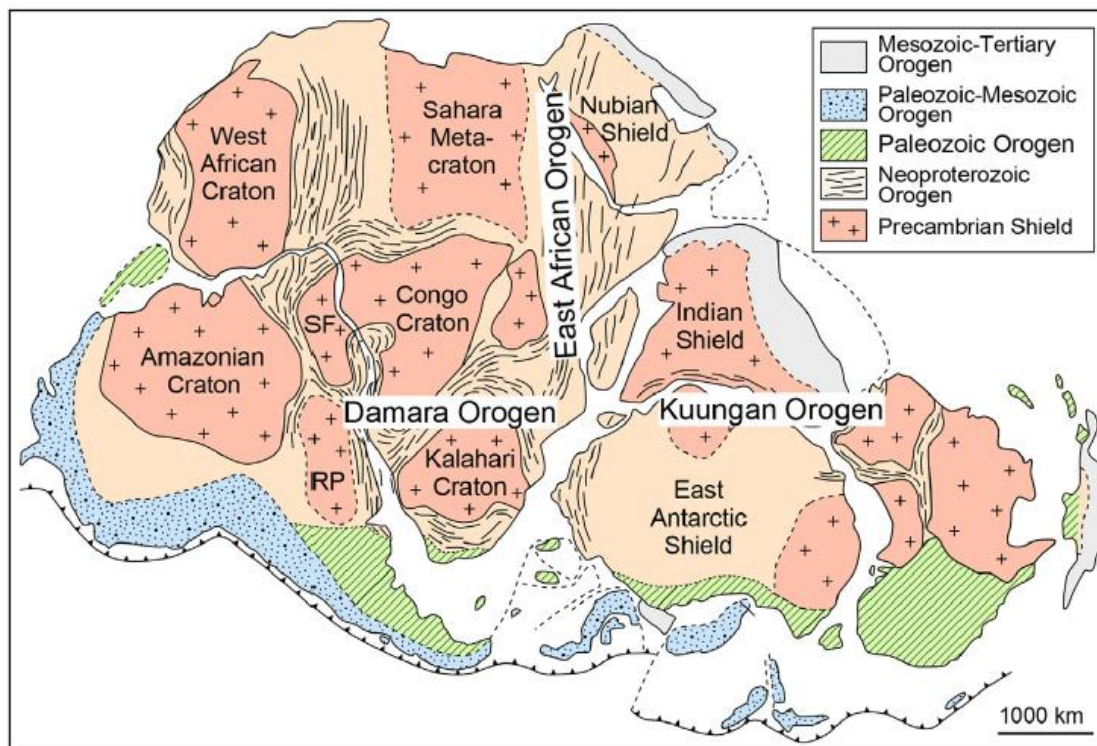


**Figura 2.2** – Configuração de Gondwana mostrando a distribuição dos orógenos tardios (extraído de Zhao *et al.* 2018).

### **Amalgamação do Gondwana Ocidental.**

O período de aumento de crescimento crustal no Gondwana Ocidental resultou da adição de crosta continental juvenil ao longo de margens convergentes (Condie, 2001; Kröner & Cordani, 2003). O amálgama do Gondwana Ocidental foi contemporâneo ao último evento de fragmentação de Rodínia, relacionado com a abertura do Oceano Ipetus, em 610-600 Ma (Cawood *et al.*, 2001, 2007; Li *et al.* 2008). O Gondwana Ocidental é marcado pela colisão entre os crátons Rio de La Plata, Congo-São Francisco, África Ocidental e Amazônico por volta de 630-600 Ma, configurando a instalação dos orógenos da Orogenia Brasileira-Pan-Africana (Figura 2.3; Oriolo *et al.*, 2017).

A colisão brasileira no Continente Sul-Americano ocorreu em diversos eventos diacrônicos, que evoluíram relacionados a processos de fechamento de oceanos e colisões



continentais, resultando nos sistemas orogênicos neoproterozoicos Mantiqueira, Tocantins e Borborema (Hasui *et al.*, 1980; Hasui, 2010). O evento compressional de maior expressão envolveu a aglutinação do Cráton São Francisco e o Maciço de Goiás entre 670 e 620 Ma (Pimentel and Fuck, 1987), possibilitando o fechamento do grande oceano Goiás-Farusiano (Kröner & Cordani, 2003; Cordani *et al.*, 2009, 2013). O fechamento do oceano Goiás-Pharusiano, por volta de 620 Ma, é registrado pelas rochas relacionadas à evento de subducção ao longo dos orógenos e pela ocorrência de unidades oceânicas (Ganade de Araujo *et al.*, 2014). A existência de mar epicontinental ediacarano ao longo das margens dos crátons Amazônico e Rio de la Plata, representado pelos grupos Corumbá e Arroyo del Soldado (Gaucher *et al.*, 2003), depositados em bacia de antepaís, indicam o fechamento do oceano Goiás-Farusiano.

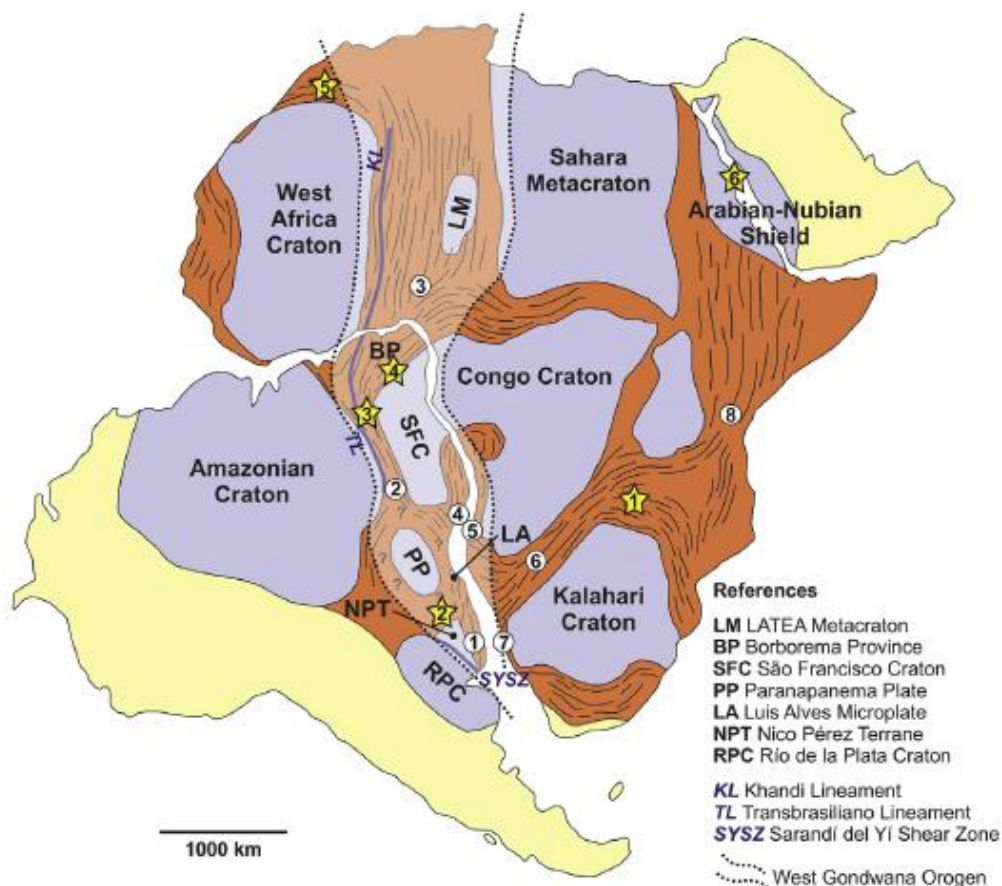


**Figura 2.3** - Esquema tectônico ilustrando os principais blocos e cinturões orogênicos na América do Sul e África, incluindo a localização da região de fechamento do orógeno West Gondwana (extraído de Oriolo *et al.*, 2017). As marcações em amarelo correspondem aos principais pontos de aglutinação.

A existência de oceano separando um bloco a oeste (Laurentia), composto pelos crátons Amazônicos, Oeste Africano e Pampia, de um bloco a leste, composto pelos crátons/terrenos localizados a leste do Cráton Amazônico é um tema amplamente discutido. A existência do Oceano Clymene é apontada por autores que afirmam que esses dois conjuntos de terrenos teriam colidido no intervalo de 550-525 Ma, como produto da orogênese Pampeana-Araguaia (Meert, 2003; Trindade *et al.*, 2003; Trindade *et al.*, 2006. Tohver *et al.*, 2012). Trindade *et al.* (2006) sugerem que o bloco Amazônico-Pampeano só colidiu com o proto-Gondwana no início do Cambriano, formando extensa zona de sutura composta pelos cinturões orogênicos Araguaia, Paraguai e Pampeano (Figura 2.4). Esta proposta destaca características que apontam evidências contrárias ao modelo anterior, visto que os eventos tardios não seriam mais interpretados como de caráter locais, mas sim como representantes da principal orogênese que modelou o Gondwana Ocidental.

O trabalho que iniciaram as discussões da existência do Oceano Clymene se baseou em dados paleomagnéticos das rochas pós-glaciais do Grupo Araras, setor norte da Faixa Paraguai (Trindade *et al.*, 2003). Os dados obtidos apontam que durante a deformação das rochas carbonáticas, estimada como ocorrida entre 550 e 525 Ma, o Cráton Amazônico e a plataforma cratônica relacionada à deposição desses sedimentos cratônicos, estava em baixas latitudes (Trindade *et al.*, 2003). Esta posição seria diferente daquelas dos blocos a leste no mesmo período, que, segundo os modelos de reconstrução estavam em altas latitudes nesse período (Morel, 1981; D'Agrella Filho *et al.*, 1998). Portanto, as massas continentais localizadas a leste do Craton Amazônico, representadas pelos crátons São Francisco-Congo, Kalahari e Rio de La Plata, já estavam reunidas no período entre 550 e 525 Ma, porém em posição polar e conseqüentemente distantes do Cráton Amazônico, em posição subequatorial (Figura 2.4; Trindade *et al.*, 2003, 2006).

Posteriormente, Tohver *et al.* (2010, 2012) corroboram o modelo com dados paleomagnéticos e geocronológicos que indicam o fechamento do Oceano Clymene.

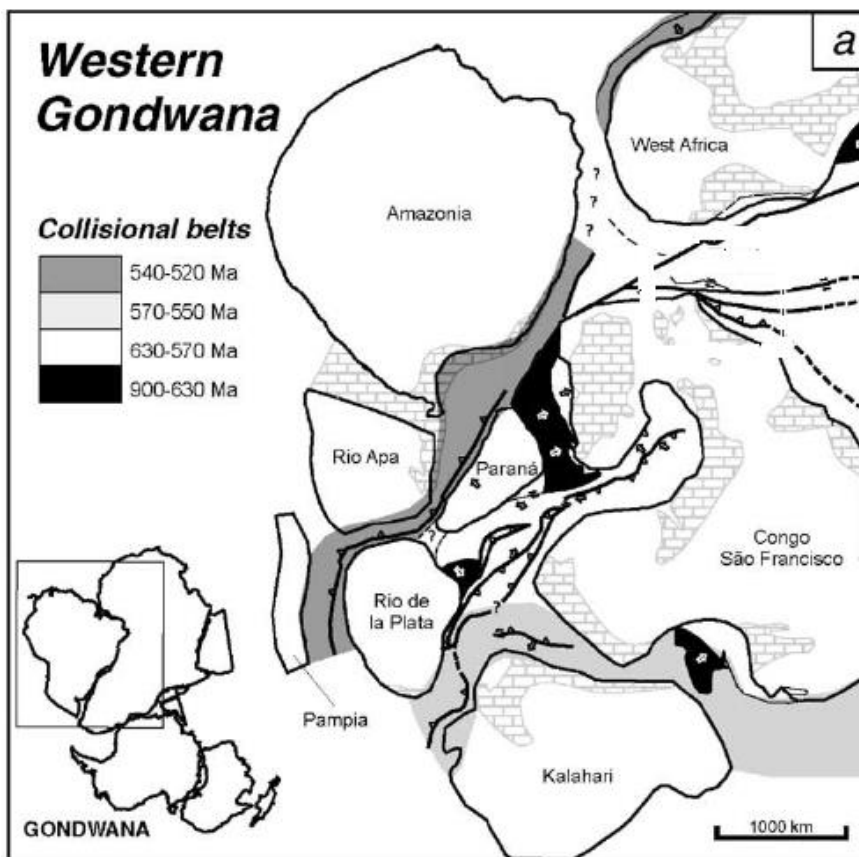


**Figura 2.4** – Modelo tectônico proposto para o Gondwana Ocidental no fim do Neoproterozoico a partir de dados paleomagnéticos (extraído de Trindade *et al.*, 2006).

A evolução tardia do Gondwana Ocidental foi sugerida também a partir de dados de proveniência sedimentar na zona externa/plataformal da Faixa Paraguai (Grupo Alto Paraguai). Os dados indicam fonte majoritariamente neoproterozoica ou mesmo da própria Faixa Paraguai, cuja idade máxima de sedimentação é registrada no Cambriano devido ao consumo do Oceano Clymene (McGee *et al.*, 2015). No trabalho de Oriolo *et al.* (2017), dados isotópicos de Hf indicam que crescimento crustal proveniente de adição de crosta continental juvenil ao longo de margens convergentes foi dominante desde o Toniano tardio em muitas regiões do Gondwana Oriental. Portanto, segundo Oriolo *et al.*, (2017), muitos oceanos tonianos-

criogenianos entre os blocos já estavam fechados durante a aglutinação, o que pode ser explicado como o resultado de isolamento de muitos crátons durante a amálgama de Rondínia. O tema da existência ou não de uma evolução entre o Neoproterozoico tardio e o Cambriano é amplo e passível de discussão, visto que os modelos são escassos, locais e pouco robustos.

### 2.3.O Lineamento Transbrasiliano-Kandi e a Tectônica strike-slip

O processo de acomodação dos esforços colisionais na fase final de aglutinação do Gondwana promoveu a geração de longo corredor alinhado ao longo de megazonas de cisalhamento na África e na América do Sul. Trata-se de um dos maiores exemplos mundiais de *intracontinental strike slip deformational system* (Fuck *et al.*, 2013), chamado de Lineamento Transbrasiliano-Kandi, que, juntamente com seu prolongamento na África, totaliza mais de 9.000 km de extensão (Fairhead e Maus, 2003; Cordani *et al.*, 2013; Fuck *et al.*, 2013). O Lineamento Transbrasiliano-Kandi transecta pelo menos as províncias Tocantins (cinturões Brasília, Araguaia e Paraguai) e Borborema, e os cinturões Dahomey e Hogar, os dois últimos na África Ocidental, e representa um ambiente de subducção de longa duração (Fairhead e Maus, 2003). O Lineamento Transbrasiliano (LTB) é a parte que transecta a Plataforma Sul-Americana, separando as unidades tectônicas relacionadas aos crátons Amazônico e São Francisco (Cordani *et al.*, 2009), e mais a sul, separa o cráton Rio de La Plata do terreno Pampia (Figura 2.5; Ramos *et al.*, 2010).

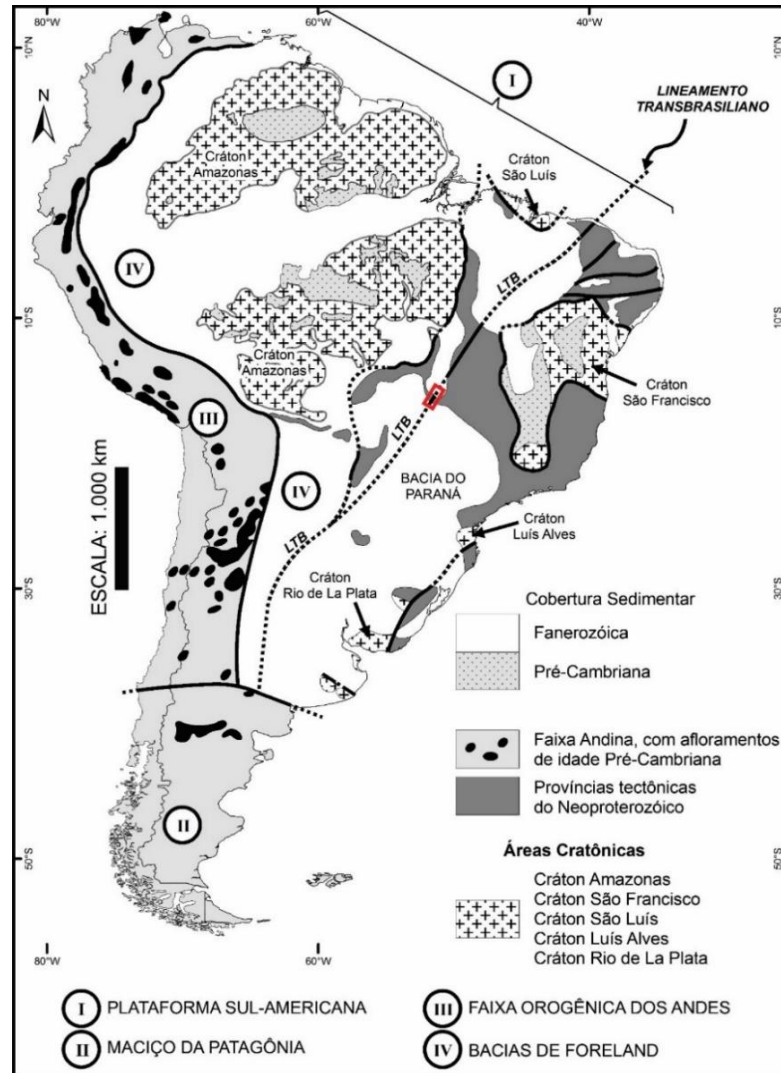


**Figura 2.5** - Localização do Lineamento Transbrasiliiano (LTB) no contexto das grandes unidades geológicas da América do Sul. O retângulo vermelho representa a área de estudo (Modificado de Fairhead e Maus, 2003; Ramos *et al.*, 2010).

Os corredores de cisalhamento podem registrar deslocamentos quilométricos e deformação intracratônica em processos orogênicos finais de um orógeno, associados a escape tectônico lateral e a estruturas de transcorrência (Dantas *et al.*, 2017). O arranjo final da geometria observada nas zonas de cisalhamento do LTB é diretamente influenciado pelo tipo de acomodação da deformação e pelo deslocamento relativo de cada bloco envolvido (Fuck *et al.*, 2013; Dantas *et al.*, 2017). A região de descontinuidade crustal que caracteriza o LTB é

reconhecida no Brasil com direção predominante N20°-30°E, sendo composta por diversas zonas de cisalhamento dúcteis-rúpteis de dimensões variáveis e histórias evolutivas diferentes (Dantas *et al.*, 2017). Ao longo da trajetória, os traçados dos cisalhamentos podem se unir em feixes menores e/ou se interconectar em feições secundárias, não podendo ser apresentadas com um traçado único (Dantas *et al.*, 2017), como foi primeiramente exposto (Marini *et al.*, 1984). A deformação predominante se dá em condições de facies xisto verde baixo, zona da clorita e biotita (Dantas *et al.*, 2007).

A maioria dos sistemas tipo *strike-slip* em escala intracontinental se estende direcionalmente por centenas ou milhares de quilômetros e dezenas de quilômetros de extensão lateral. Os sistemas de cisalhamento dúcteis, paralelos e conectados indicam que eram antigas zonas de falhas geradas em situação intraplaca, caracterizadas por deformações das antigas margens dos crátons, sugerindo que o corredor começou a se formar posteriormente às colisões das placas litosféricas (Fuck *et al.*, 2013). As tensões ao longo do sistema transcorrente de falhas são raramente resultantes de deslocamento puramente lateral, podendo desenvolver-se em curvas ao longo de sua extensão, gerando compressões ou extensões locais, como no caso típico dos cinturões orogênicos de Tianshan e Altai, no noroeste da China (Pirajno, 2010). Sistema semelhante ocorre no continente Asiático, onde é descrito grande sistema de falhas transcorrentes, resultante do fechamento dos oceanos Paleo e Neotethys (Windley *et al.*, 2007; Xiao e Kusky, 2009).

Na Província Tocantins o LTB é bem caracterizado por foliações, lineações de estiramento e eixos de alongamento maior de *boudins* dispostos no plano da foliação milonítica (Dantas *et al.*, 2007). O sistema na Província Tocantins apresenta-se subparalelo a mais de 10 faixas miloníticas entrelaçadas com largura que varia de 250 a 50 km e *trend* unidirecional N45-60E (Dantas *et al.*, 2017). Curto *et al.* (2015) observaram que as falhas de transcorrência do LTB em níveis rasos são associadas a zonas de cisalhamento em profundidade que atingem

níveis da crosta até aproximadamente 20 km. As extensas zonas de fraquezas crustais podem facilitar a ascensão e alojamento de granitos pós-orogênicos no embasamento (Curto *et al.*, 2014, 2015).

Muitos autores consideram a instalação de uma zona de cisalhamento *strike-slip* e granitogênese associada como resultado de processos pós-colisionais (Vaughan & Sacrow, 2003; Seifert, 2008; Pirajno, 2010). Ganade de Araujo *et al.* (2014) relacionam evento de formação de zonas de cisalhamento e acentuada granitogênese, entre 580 e 550 Ma, ao desenvolvimento do LTB. A partir da análise de leucossoma sin-transcorrente na Serra Azul, Fuck *et al.* (2013) sugeriram que Sistema *Strike-Slip* Transbrasiliiano-Kandi possui história dúctil em torno de 540 Ma e que, portanto, esteve ativo durante o Cambriano. Na região de Campo Grande, Mato Grosso do Sul, o LTB exerce forte controle na intrusão de granitos pós-colisionais (Coxim, Sonora e Taboco), relacionados ao magmatismo neoproterozoico da Faixa Paraguai (Godoy *et al.*, 2007, 2010). Esses corpos ocorrem bordejando o bloco crustal do Rio Apa e formam uma calha orientada ao longo do LTB (Dantas *et al.*, 2017).

### 3. MATERIAIS E MÉTODOS

Os métodos utilizados para execução desta pesquisa são compostos basicamente por: atividades pré-campo, amostragem, preparação de amostras, análises de amostras, tratamento dos dados, apresentação e interpretação dos dados.

#### 3.1. Etapa Pré-Campo

Durante esta etapa foi feito o levantamento, compilação e interpretação de dados disponíveis que auxiliaram na definição dos alvos amostrais e técnicas a serem utilizadas, facilitando e direcionando a aquisição de dados e amostras que fornecessem respostas aos objetivos do projeto.

#### 3.2. Etapa de amostragem: trabalhos de campo

Durante a etapa de campo foram coletadas amostras litológicas e dados de campo em 43 pontos de exposições rochosas tidas como pertencentes ao Grupo Cuiabá e à granito gêse relacionada à Zona Interna da Faixa Paraguai. Nos pontos, sempre que possível, foram coletadas amostras para petrografia, geoquímica e geocronologia, além do registro fotográfico e de localização utilizando o Datum: SIRGAS2000 zona 22S. Os trabalhos de campo foram realizados em duas etapas: 23/10 a 29/10/2018 e 04/02 a 11/02/2019, todas partindo de Cuiabá-MT.



### 3.3. Etapa de preparação de amostras

Durante a etapa de preparação as amostras foram fotografadas e separadas em grupos litológicos com base em sua descrição macroscópica e localização. Amostras representativas das principais unidades litológicas e setores estruturais da Faixa Paraguai foram selecionadas. Destas, 25 foram britadas e moídas no Laboratório de Preparação de Amostras do Instituto de Geociências da Universidade de Brasília e após este processo, foram separadas alíquotas para envio para a análise litoquímica e isotópica, e para concentração de grãos de zircão.

As frações corretas foram encaminhadas para concentração e catação de minerais pesados em bateia, separador isodinâmico Frantz e lupas binoculares, instalados no Laboratório de Geoquímica Isotópica e Geocronologia da Universidade de Brasília, onde foram confeccionados 8 *mounts* para análises U-Pb. As amostras destinadas a análises isotópicas pelo método Sm-Nd foram retiradas da mesma porção daquelas destinadas às análises geoquímicas, totalizando 14 amostras.

### 3.4. Análises Petrográficas

As análises petrográficas consistiram inicialmente em estudos macroscópicos, que fundamentaram a seleção de amostras para confecção de lâminas delgadas. Foram feitas 20 seções delgadas de todos os litotipos encontrados na área, descritas opticamente considerando os principais aspectos como texturas, composição mineralógica, processos de alteração, dentre outros. As seções delgadas foram produzidas no Laboratório de Laminação do Instituto de Geociências da Universidade de Brasília. As fotomicrografias das seções delgadas foram obtidas com polarizadores paralelos e cruzados, com objetivas de aumento 2,5, 4 e 10x, usando uma câmera ZEISS acoplada ao microscópio óptico binocular *Olympus*, modelo BX50.

### 3.5. Análises Litoquímicas

Para o estudo litoquímico 20 amostras mais representativas do magmatismo da área foram selecionadas e moídas em moinho de panela do Laboratório de Preparação de amostras do Instituto de Geociências da UnB e posteriormente encaminhadas para o Laboratório *ALS Minerals* (Goiânia – GO – Brasil). As análises dos elementos maiores e menores foram feitas com o emprego da técnica Fluorescência de Raio-X (XRF) depois das amostras serem diluídas em um fluxo de metaborato/tetraborato de lítio. Os elementos traços, incluindo terras raras, foram analisados com a técnica espectrometria de emissão óptica com plasma acoplado induzido (ICP-OES - *Inductively Coupled Plasma for Optical Emission Spectroscopy*). As amostras foram enviadas para ALS Brasil Ltda, Goiânia, para análise na ALS em Vancouver, Canadá. Cerca de 0,1 g das amostras foram diluídas em um fluxo de metaborato/tetraborato de lítio. O pó depois foi dissolvido em 100 mL de ácido nítrico a 4%/ácido clorídrico a 2% e aquecido em 1000°C por hora. A descrição completa dos métodos analíticos está disponível na página da ALS Chemex: ([www.alsglobal.com](http://www.alsglobal.com)). Foi utilizado para o tratamento dos dados o *software* GCDkit (versão 2.3, *Geochemical Data Toolkit for Windows*) e Microsoft Excel.

### 3.6. Análises Geocronológicas e Geoquímica Isotópica

Considerando as amostras mais representativas, sua distribuição na área de estudo, diversidade textural e mineralógica, foram separados também exemplares para análises isotópicas e geocronológicas pelos métodos U-Pb em zircão por LA-ICP-MS e Sm-Nd em rocha total, que foram analisados no Laboratório de Estudos Geodinâmicos e Ambientais da Universidade de Brasília. A análise Ar-Ar foi realizada no Laboratório de *Gaz Rare* no *Géoscience Montpellier*, Universidade de Montpellier, França. Para informações mais

detalhadas sobre os métodos analíticos utilizados, conferir nos tópicos *Materials and Methods* dos respectivos artigos apresentados nos capítulos seguintes (4 e 5).

- **U-Pb em zircão**

A preparação das amostras foi realizada de acordo com o procedimento convencional com técnicas gravimétricas e magnéticas do Laboratório de Geoquímica Isotópica e Geocronologia da Universidade de Brasília (UnB). Após a separação, os cristais de zircão foram selecionados para a montagem dos *mounts*, em resina epóxi, desgastados e polidos para a exposição do interior dos grãos, e a limpeza feita com banho de HNO<sub>3</sub> diluído (2%). Para investigar a estrutura interna dos cristais, imagens de *Backscattered* foram confeccionadas.

As análises isotópicas U-Pb foram feitas em cristais detríticos de zircão de 10 amostras, usando o Thermo-Finnigan NEPTUNE MC-ICP-MS acoplado com o *Laser Ablation New Wave* YAG UP213, também no Laboratório de Geocronologia da UnB. As condições de operação e ajustes do NEPTUNE e Laser Ablation New Wave durante as seções do processo analítico estão descritas em Matteini *et al.*, (2010). As análises de U-Pb foram realizadas pelo método de *bracketing* (Albarède *et al.*, 2004) de amostra-padrão usando o zircão padrão GJ-1 e 91500 (Jackson *et al.*, 2004), a fim de quantificar a quantidade de fracionamento do ICP-MS. As massas sintonizadas foram 238, 207, 206, 204 e 202. O tempo de integração foi de 1 segundo e o tempo de ablação foi de 40 segundos.

As análises foram feitas utilizando feixe com diâmetro de spot de 30 µm e o ajuste do laser foi de 10 Hz e 2-3 J/cm<sup>2</sup>, posicionado preferencialmente no núcleo dos cristais, evitando locais que apresentassem características internas e/ou externas que indicassem alterações químicas que pudessem interferir na qualidade dos dados. As relações <sup>206</sup>Pb/<sup>207</sup>Pb e <sup>206</sup>Pb/<sup>238</sup>U foram corrigidas no tempo. Em cristais de zircão menores (cerca de 50 µm), o fracionamento

da razão  $^{206}\text{Pb} / ^{238}\text{U}$  induzido por laser foi corrigido usando o método de regressão linear (Košler et al., 2002). A redução de dados foi realizada utilizando o software Chronus no Laboratório de Geoquímica Isotópica e Geocronologia da UnB (Oliveira, 2015) e os índices foram corrigidos. Em gráficos que utilizam idades aparentes foram utilizadas idades  $^{206}\text{Pb}/^{238}\text{U}$  para grãos mais jovens que 1000 Ma e  $^{207}\text{Pb}/^{206}\text{Pb}$  para grãos mais antigos.

- **Sm-Nd em rocha total**

As análises isotópicas Sm-Nd foram realizadas no Laboratório de Geocronologia da Universidade de Brasília, seguindo o método descrito por Gioia e Pimentel (2000). Aproximadamente 50 mg de amostra pulverizada são misturados a uma solução de  $^{149}\text{Sm}$  e  $^{150}\text{Nd}$  e dissolvida em cápsulas Saville<sup>x</sup>® por meio de ataques ácidos em HF, HNO<sub>3</sub> e HCl. Os conteúdos de Sm e Nd são extraídos por meio de colunas de troca catiônica, confeccionadas em teflon e depositados em filamentos duplos de rênio com ácido nítrico para evaporação.

Foram realizadas leituras das medidas em espectrômetro de massa multicoletor, Finnigan MAT 262 em modo estático. As incertezas para as razões Sm/Nd e  $^{143}\text{Nd}/^{144}\text{Nd}$  são inferiores a  $\pm 0,5\%$  ( $2\sigma$ ) e  $\pm 0,005\%$  ( $2\sigma$ ), baseadas em repetidas análises dos padrões internacionais BHVO-2 e BCR-1. As razões  $^{143}\text{Nd}/^{144}\text{Nd}$  foram normalizadas em função da razão  $^{146}\text{Nd}/^{144}\text{Nd}$  de 0,7219. Os valores de idades modelo ( $T_{\text{DM}}$ ) foram calculados usando o modelo de De Paolo (1981).

- **$^{40}\text{Ar}/^{39}\text{Ar}$**

As análises de  $^{40}\text{Ar}/^{39}\text{Ar}$  foram realizadas durante estágio de doutorado no órgão de pesquisa francês CNRS (*Centre National de la Recherche Scientifique*). Todas as etapas foram realizadas com o auxílio dos pesquisadores e técnicos locais, sob supervisão do responsável pelo laboratório, Professor Patrick Monié. As análises foram conduzidas no *Laboratoire de*

*Gases Rares* juntamente com a equipe “*Dynamique de la Lithosphère*” no Géoscience Montpellier, que reúne recursos de pesquisa e ensino no campo das Ciências da Terra na Université de Montpellier 2. Os procedimentos realizados iniciaram com a seleção das melhores amostras e montagem dos *mounts*, que foram posteriormente enviados para irradiação em reator nuclear. O objetivo da irradiação é transformar uma pequena proporção de  $^{39}\text{K}$  em  $^{39}\text{Ar}$  pela interação com nêutrons rápidos. A etapa de irradiação foi realizada na Itália, em Pavia, no núcleo do reator nuclear Triga Mark II. Posteriormente, as análises foram realizadas na nova geração do espectrômetro de massa multicoletor (Thermo Scientific Argus VI MS) da Géosciences Montpellier, cuja resolução nominal de massa é de  $\sim 200$  e sensibilidade para medições de argônio é de  $3.55 \times 10^{-17}$  moles/fA at  $200 \mu\text{A}$ . O espectrômetro de massas acomoda uma fonte do tipo Nier e uma matriz fixa de cinco detectores Faraday e um detector Compact Discrete Dynode (CDD).

Para o processamento dos dados foi utilizado o software padrão do laboratório para a redução e plotagem, o ArArCalc software© v2.5.2 (Koppers, 2002). Todos os dados são corrigidos por sistemas de brancos, decaimento radioativo, interferências isotópicas e discriminação de massa. As idades platôs são definidas como incluindo mais de 50% do total de  $^{39}\text{Ar}$  liberado, distribuídas em pelo menos 3 etapas contíguas de aquecimento, com proporções de  $^{40}\text{Ar}/^{39}\text{Ar}$  de acordo com a média no nível de confiança de 95%. As idades calculadas são relatadas no nível  $2\sigma$  e incluem incertezas nos valores J, mas excluem erros associados à idade do monitor de fluxo e às constantes de decaimento.

O método geocronológico  $^{40}\text{Ar}/^{39}\text{Ar}$  tem sido comumente utilizado na compreensão do momento geológico em que terrenos metamórficos são exumados, permitindo quantificar taxas e escalas de tempo de diversos processos tectônicos e geodinâmicos. O método deriva diretamente do método convencional  $^{40}\text{K}/^{40}\text{Ar}$ , cujo objetivo é estimar a acumulação do elemento filho, o  $^{40}\text{Ar}$  radiogênico, a partir da desintegração natural do elemento pai, no caso o

$^{40}\text{K}$ , seguindo os conceitos fundamentais dos demais métodos geocronológicos radiogênicos. O método  $^{40}\text{Ar}/^{39}\text{Ar}$  apresenta algumas diferenças em relação ao método pioneiro  $^{40}\text{K}/^{40}\text{Ar}$ , pois é baseado na formação não-espontânea de  $^{39}\text{Ar}$ , utilizando irradiação em reator nuclear. Em suma, a premissa do método baseia-se na substituição do  $^{40}\text{K}$  por  $^{39}\text{Ar}$  do método K-Ar convencional. A irradiação tem com objetivo a ativação por fluxo de nêutrons suficientemente elevados, que induz a desintegração/decaimento do  $^{39}\text{K}$  e formação do  $^{39}\text{Ar}$ .

O processo de análise se inicia com a *incremental heating technique*, na qual a extração do gás Ar é feita em etapas sucessivas de aquecimento por um laser  $\text{CO}_2$  em situ no material analisado. Cada etapa de aquecimento fornece uma idade independente. Sabendo-se que a razão  $^{40}\text{K}/^{39}\text{K}$  representa uma proporção natural constante, a medida do  $^{39}\text{Ar}$  vai substituir a do  $^{40}\text{K}$  do método K-Ar convencional. A equação radiométrica final para o cálculo da idade baseia-se na razão  $^{40}\text{Ar}/^{39}\text{Ar}$  da amostra analisada e de um padrão com idade K-Ar conhecida (Monié 1984).

#### 4. ARTIGO 1

**Appinitic and high Ba–Sr magmatism in central Brazil: Insights into the late accretion stage of West Gondwana. 2021. *Lithos*, 10633, 398-399.**

Artigo científico aceito para publicação no dia 28 de junho de 2021, com o seguinte DOI:

[10.1016/j.lithos.2021.106333](https://doi.org/10.1016/j.lithos.2021.106333)



Amanda Figueiredo Granja Dorilêo Leite<sup>1\*</sup> (amandafgdleite@gmail.com), Reinhardt A. Fuck<sup>1</sup>(reinhardt@unb.br), Elton L. Dantas<sup>1</sup>(elton@unb.br), Amarildo S. Ruiz<sup>2</sup> (asruiz@gmail.com)

<sup>1</sup>Instituto de Geociências, Universidade de Brasília (UnB), Brasília (DF), Brazil.

<sup>2</sup>Faculdade de Geociências, Universidade Federal de Mato Grosso (UFMT), Cuiabá (MT), Brazil.

\*Corresponding author

## ABSTRACT

Large amounts of high Ba-Sr magmatism can be produced as the result of late accretion or decompression in the final stages of continental arc evolution in orogenic systems and leads to continental crustal growth. This type of magmatism often occurs associated with mega-shear zones and displays geochemical signatures that indicate magmas deriving from the melting of enriched lithospheric mantle. Such enrichment may be an indication of slab-derived fluid and/or melt interaction, released from subducted material. The high Ba-Sr granitoids of the Brasília no Paraguay Belt, Tocantins Province, central Brazil, comprise two suites that crystallized approximately 40 My apart from each other. Both suites are composed of metaluminous to slightly peraluminous rocks ( $ASI = 0.64\text{--}1.01$ ) with magnesian character, and present high Ba (~1430 ppm), Sr (~800 ppm),  $K_2O$  (~4 wt.%), LREE and LILE contents. The negative  $\epsilon_{Nd}(T)$  values (-6.32 and -6.65) associated with high contents of incompatible elements indicate an evolution from partial melting of mantle-derived magma previously metasomatized by subducted slab fluids. Crystallization ages of  $557\pm 5.7$  Ma and  $554\pm 2.9$  Ma have been obtained for the older, high Mg-K calc-alkaline suite. It evolved from high Cr and Ni mantle-derived appinitic magma to coeval granodiorites by crystal fractionation accompanied by minor crustal contamination. The younger,  $515\pm 3.6$  Ma-old suite displays an elevated concentration in some HFSEs, show alkali-calcic affinity and is represented by high-K monzogranites. A model proposed for the two hybrid suites is based on a slab break-off and a subsequent lithospheric delamination after 40 My, where the heat flux generated by mantle upwelling led to a partial melting of the enriched subcontinental lithospheric mantle beneath the continental crust. The older calc-alkaline suite represents the end process of magmatic arc accretion in the central



Tocantins Province after ca. 600 Ma. The younger one is compatible with a transitional shoshonitic to A-type affinity, associated to post-collisional collapse stage of the orogen at Cambrian times. The petrogenesis of the investigated rocks requires an ocean closure phase at ca. 590 Ma, which could be linked to the consumption of the Clymene Ocean toward Amazonian Craton, recording a new collisional event in the central West Gondwana.

**Keywords:** West Gondwana; Tocantins Province; High Ba-Sr magmatism; Petrogenesis; Post-collisional setting; Geochronology.

#### 4.1.INTRODUCTION

Post-collisional, high Ba-Sr magmatism provides important insights into modifications of the crust and mantle characteristics, such as those caused by reworking, metasomatism, and melting of sub-continental lithospheric mantle above a subducting lithosphere slab (e.g., Fowler *et al.*, 2008). Ba- and Sr-rich granitoids, besides Ba+Sr contents >1000 ppm, present relatively weak negative Eu anomalies, high mg#, Cr, V and Ni contents, LREE and LILE enrichment, and relatively low HFSE contents (Tarney and Jones, 1994). These high Ba-Sr granites are generated in extensional or non-compressional tectonic settings, usually related to lithospheric extension by gravitational collapse or post-orogenic subduction associated with later episodes of crustal thickening (Fowler and Henney, 1996; Fowler *et al.*, 2001; Moyen *et al.*, 2017).

High Ba-Sr granites present a dual, mantle-crust chemical signature. Deep asthenospheric-sourced magmas can accumulate in the upper mantle as a consequence of partial melting of the metasomatized enriched lithospheric mantle (e.g., Tarney and Jones, 1994). These magmas subsequently differentiate at shallow depths, generating granitic liquids containing juvenile components (Fowler *et al.*, 2001, 2008; Fowler and Rollinson, 2012).

Fowler and Henney (1996) and Fowler *et al.* (2001, 2008) enhance that high Ba-Sr granites display evidence of mingling, and are most likely products of AFC involving mantle components, such as the appinitic magmas (Murphy, 2013).

Appinitic suites range in age from Late Archean to Recent (Murphy, 2013) and are commonly found as mafic stocks, sheets and dykes that mainly occur as small satellite bodies in relation to large granodiorite batholiths (Fowler *et al.*, 2001, 2008). The appinites emplacement can be related to deep crustal faults associated with post subduction slab break-off and/or delamination during the late stages of an orogeny (Ye *et al.*, 2008; Heilimo *et al.*, 2010; Murphy, 2013).

The production of high Ba-Sr melts starts in the Late Archean and persists in the Phanerozoic (Tarney and Jones, 1994). Ediacaran high Ba-Sr granites associated with precursor appinitic magmas are well represented by examples in the British Caledonian Province (Fowler *et al.*, 2008) and in the Tibetan Plateau (Ye *et al.*, 2008), where the recurrence of late subduction along shear zones after the main tectonic event is notable. Moreover, asthenosphere upwelling, and partial melting of enriched lithospheric mantle represent the main processes involved in high Ba-Sr magma genesis (Fowler *et al.*, 2008; Ye *et al.*, 2008).

The analogous tectonomagmatic circumstances in which high Ba-Sr granites and Archean sanukitoids are generated have been the focus of many debates, since both rock types highlight the importance of crust-mantle mixing to explain juvenile additions to crust formation (Heilimo *et al.*, 2010; Fowler and Rollinson, 2012). Archean sanukitoids are formed at the Archean-Proterozoic boundary and record the transition to deep subduction such that melting conditions migrated through the slab, yielding the beginning of subcontinental lithospheric mantle melting in the modern plate-tectonic regime (Martin *et al.*, 2009; Heilimo *et al.*, 2010; Laurent *et al.*, 2014a).

During the lithospheric convergence in the modern Earth, the lithospheric mantle is recycled through foundering in primitive mantle domains, that can effectively contribute to crustal growth. Late- to post-orogenic settings can be pointed out as dominated by hybrid environment, with different proportions of interacting mantle and crustal melts (Liégeois *et al.*, 1998; Bonin, 2004; Moyen *et al.*, 2017). Orogenic terrains contain a large variety of magmatic activity characterized by bimodal potassic to ultrapotassic rocks, associated to heat sources linked to large movement along mega-shear zones and/or preceding subduction stages (Tarney and Jones, 1994; Brito Neves and Fuck, 2013).

The Brasiliano-Pan-African orogeny yielded a global network of Neoproterozoic orogenic belts, which record important tectonic events during the agglutination of terranes. A large-scale example of an intracontinental strike-slip fault system, the Transbrasiliano Lineament, separates large continental masses of West Gondwana and represents significant influence in Ediacaran/Cambrian late magmatism throughout the Tocantins Province (Brito Neves and Fuck, 2013; Cordani *et al.*, 2013; Fuck *et al.*, 2013; Curto *et al.*, 2014).

The generation of Late Neoproterozoic-Early Phanerozoic high Ba-Sr granitoids, the nature of their source, and their global significance are the focus of this paper. These rocks intruded metasedimentary rocks of the Eastern Paraguay Belt, at the boundary with the Neoproterozoic Arenópolis Magmatic Arc, Brasília Belt, in central Brazil (Seer, 1985; Pimentel and Fuck, 1987). The integration and interpretation of new geochemical and geochronological (Sm-Nd and U-Pb) data allowed a better understanding of the geodynamic context of the final phase of the Tocantins Province evolution, as well as of West Gondwana stabilization.

## 4.2.GEOLOGICAL SETTING

The Brasiliano-Pan-African Orogeny (Figure 1A; Almeida, 1984) took place in response to the fragmentation of the Rodinia Supercontinent and the assembly of Gondwana between 900 and 600 Ma (Brito Neves, 2013). The Tocantins Province represents a group of orogens comprising the Araguaia, Paraguay and Brasília belts (Figure 1B), which developed due to the amalgamation of the Amazonian, São Francisco/Congo, West African/São Luís, Parnaíba and Paranapanema cratons, resulting in the West Gondwana assembly (Almeida, 1984; Pimentel, 2016 and references therein).

The Paraguay Belt is affected by Ediacaran-early Cambrian deformation and metamorphism (Geraldes *et al.*, 2008), and is divided into northern and southern sectors by the Pantanal and Paraná basins (Figure 4.1C). The stratigraphic units of the Paraguay Belt progressively pass from sedimentary sequences overlying the Amazonian Craton to folded and metamorphosed metasedimentary sequences, trending to turbiditic environments away from the craton (Alvarenga and Trompette, 1993).

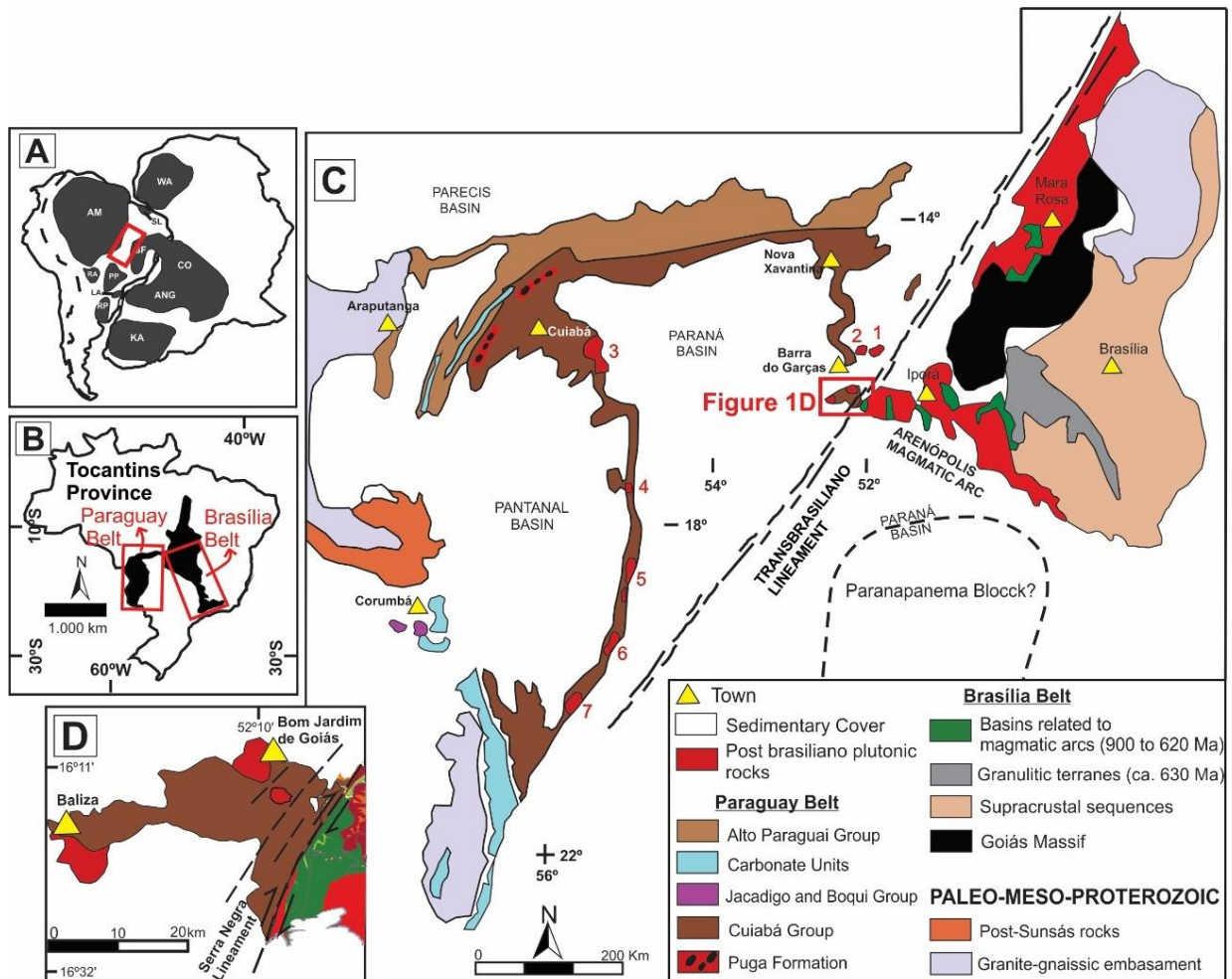


**Figure 4.1**– Geological and geotectonic context of the study area: (A) geotectonic context of the formation of the Tocantins Province during the Brasiliano Orogeny. Cratons are shown in dark gray. AM: Amazonian, WA: West Africa; CO: Congo; SF: São Francisco; KA: Kalahari; RP: Rio de la Plata; PP: Paranapanema; RA: Rio Apa. The red rectangle refers to the investigated region in the context of the Brasiliano Pan-African Orogeny (modified from Vaughan and Pankhurst, 2008); (B) location of the Tocantins Province in the Brazilian territory. The red rectangle comprises the Paraguay Belt shown in (C) Simplified geological map of the Paraguay Belt and Brasília Belt (modified after Ruiz *et al.*, 2010; Pimentel *et al.*, 2000). Red numbers related to the respective granitic intrusions in the Paraguay Belt: 1- Araguaiana; 2- Lajinha; 3- São Vicente; 4- Sonora; 5- Coxim; 6- Rio Negro; 7- Taboco; (D) simplified geological map of the study area.

The Paraguay Belt collisional event is mainly recorded in well exposed rocks of the internal zone, which is represented by the metasedimentary Cuiabá Group (Almeida, 1984).

Provenance studies based on detrital zircon U-Pb ages suggested that the main sources of the Cuiabá Group were in the Amazonian Craton (Babinski *et al.*, 2018) and that the Cuiabá sediments were deposited in a passive margin setting (Dantas *et al.*, 2009). The maximum sedimentation age is Late Ediacaran (652±5 Ma), implying the existence of a post-Sturtian basin in the internal zone (Babinski *et al.*, 2018).

The final phase and last metamorphic event in the Paraguay Belt are marked by Ar-Ar analyses of micas from the Nova Xavantina Metavolcano-Sedimentary Sequence, suggesting the interval from 541 to 531 Ma (Geraldes *et al.*, 2008). The Neoproterozoic magmatism is also related to the final phase and comprises distinct granitic intrusions (Godoy *et al.*, 2010). The granitoids located in the southern portion of the belt yield crystallization ages around 540 Ma, while those of the northern portion are dated around 509 Ma ago (Table 4.1; Godoy *et al.*, 2010; Ferreira, 2009; McGee *et al.*, 2012).

**Table 4.1** – Summary of U-Pb, Sm-Nd and tectonic environment data available in the literature on Neoproterozoic magmatism of the Paraguay Belt.

| Granite   | U-Pb (Ma)    | $\epsilon_{Nd}(0)$ | $\epsilon(0,54Ga)$ | $T_{DM}$ (Ga) | Tectonic setting       |
|-----------|--------------|--------------------|--------------------|---------------|------------------------|
| Taboco    | 546 ± 4 *    | -11,52*            | -7,72*             | 1,97 */**     | syn-colisional         |
|           | 540 ± 4.7 ** | -11,5**            | -7,4**             |               |                        |
| Rio Negro | 549 ± 5 *    | -13,37*            | -7,86*             | 1,59*/**      | pre- to syn-colisional |
|           | 547 ± 4.9 ** | -13,4**            | -7,4**             |               |                        |
| South     |              |                    |                    |               |                        |
| Coxim     | 542 ± 4 *    | -                  | -6,24*             | 1,74*/**      | pre- to syn-colisional |
|           | 540 ± 3.6 ** | 10,3*/**           | -5,9**             |               |                        |
| Sonora    | 549 ± 5 *    | -8,86*             | -                  | -             | syn-colisional         |

|       |             |                |         |         |        |                          |
|-------|-------------|----------------|---------|---------|--------|--------------------------|
|       |             | 548 ± 5.9 **   | -       | -7,0**  |        |                          |
|       | São Vicente | 521 ± 8*       | -12,93* | -6,26*  | 1,33*  | syn- to post-orogenic    |
|       |             | 504 ± 8.9**    | -9,07** | -2,26** | 1,16** |                          |
|       |             | 518 ± 4★       |         |         | 1,07△  |                          |
| North | Lajinha     | 512 ± 7 *      | -13,4*  | -8,18*  | 1,66*  | intraplate               |
|       |             | 509,4 ± 4.1 ** | -11,3** | -5,87** | 1,50** |                          |
|       | Araguaiana  | 534 ± 3*       | -9,82*  | -4,0*   | 1,27*  | late- to post-colisional |
|       |             | 505,4 ± 4.2**  | -11,7** | -5,47** | 1,37** |                          |

\*Ferreira (2009)    \*\* Godoy *et al.* (2010)    △ Pinho (2001)    ★ McGee *et al.* (2012)

The igneous bodies of the easternmost part of the Paraguay Belt (Figure 4.1D) are located near the Serra Negra discontinuity, which is a transcurrent shear zone that marks the tectonic contact between two different terranes (Seer, 1985; Curto *et al.*, 2014). The western block comprises the Paraguay Belt that overlies the Amazonian Craton (Azevedo *et al.*, 2015), and the eastern terrane includes the Arenópolis Magmatic Arc, which is the southern segment of the Goiás Magmatic Arc system, Brasília Belt (Pimentel and Fuck, 1987; Pimentel *et al.*, 1999; Pimentel, 2016).

The Serra Negra fault is a prominent magnetic anomaly of the Transbrasiliano Lineament (Curto *et al.*, 2014), which formed and evolved to accommodate the stresses from the collision of large continental masses in West Gondwana (Fuck *et al.* 2008; Brito Neves and Fuck, 2013). The sigmoidal structures in the Bom Jardim de Goiás region are interpreted from magnetic anomaly maps and are associated with intrusive bodies. The strike-slip faults are generally related to shear zones that can reach up to 20 km of depth, causing dextral ductile-plastic deformations in the country rocks (Curto *et al.*, 2014).

The Goiás Magmatic Arc comprises a Neoproterozoic complex multiple intraoceanic island arc developed between ca. 900 and 620 Ma, during the Brasiliano Orogeny (Pimentel and Fuck, 1987, Pimentel, 2016). The southern segment, the Arenópolis Magmatic Arc, consists of a mosaic of dioritic-tonalitic-granitic orthogneisses with calcic to calc-alkaline composition, exposed between bands of volcano-sedimentary sequences (Figure 4.1C; Pimentel and Fuck, 1987; Pimentel, 2016; Marques *et al.*, 2019).

The neighboring Bom Jardim metavolcanic-sedimentary sequence is usually compared to modern volcanic arcs (Seer, 1985), and displays a U-Pb age of  $749\pm 6$  Ma (Guimarães *et al.*, 2012). The last major metamorphic/deformation event recorded in the Arenópolis Magmatic Arc is represented by granite-gneisses that intruded the metavolcanic-sedimentary sequences around 630 Ma, which is compatible with the last regional metamorphic evidence in the Brasília Belt (Pimentel and Fuck, 1987; Della Giustina *et al.*, 2011; Pimentel, 2016 and references therein).

Seer (1985) described granitic intrusions in the metasedimentary rocks of the Cuiabá Group in the easternmost portion of the Paraguay Belt (Figure 4.1D), e.g., the SW Serra Verde Granite (an isotropic, porphyritic, medium- to coarse-grained pink granite; Balieiro and Cunha, 1974 *in* Seer, 1985), and a small quartz-diorite body. The third intrusive body in the area corresponds to the voluminous Bom Jardim Granite, that was firstly classified by Coimbra (2015) as an I-type post-collisional calc-alkaline pluton, with occurrences of xenoliths and enclaves, yielding a zircon U-Pb age of  $550\pm 12$  Ma.



### 4.3. MATERIALS AND METHODS

Thirty-two outcrops were sampled for this study. The sampling strategy was based to cover the fresher outcrops distributed in the study area, focusing on the observed composition ranges. Thin sections were described considering the main features of the rock, such as texture and mineral composition. The petrographic classification was made considering the QAP classification diagram of Streckeisen (1974), using modal estimates, later checked with CIPW normative minerals obtained via the GCDkit software (version 2.3; Janousek *et al.*, 2006). Mineral abbreviations of Whitney and Evans (2010) were adopted in Figures 4.3, 4.5 and 4.6.

Twenty-six representative samples were selected for geochemical analyses. The samples were crushed in the UnB Sample Preparation Laboratory. Grinding, quartering and milling to 200 mesh were performed at the ALS Global Laboratory in Goiânia (Brazil), and analyzed in the ALS Global facilities in Vancouver (Canada). Loss on ignition (LOI) was estimated using a 1.0-g sample heated in an oven to 1000 °C for 1 h, then cooled and weighed. Analyses of major and minor elements were obtained by X-ray fluorescence (XRF) after melting the samples with lithium tetraborate. Trace elements were determined from melting 0.2-g samples with lithium metaborate/tetraborate, followed by digestion in nitric acid and analysis by Inductively Coupled Plasma for Optical Emission Spectroscopy (ICP-OES). Precious metals and base metals were determined after digestion of 0.5-g sample with Aqua Regia using the Inductively Coupled Plasma-Mass Spectrometry (ICP-MS) technique. Full descriptions of the analytical methods are available on the ALS Global site ([www.alsglobal.com](http://www.alsglobal.com)). Microsoft Excel and GCDkit (Janousek *et al.*, 2006; version 2.3) programs were used to process the data for geochemical interpretations.

Zircon crystals from representative samples were separated by density and magnetic separator before concentration by hand picking to assemble the grain mounts. The polished

zircon surfaces were imaged using cathodoluminescence (CL) and back-scattered electron microscopy (BSE), with a FEI QUANTA 450 scanning electron microscope (SEM) at the UnB Laboratory of Geochronology. The U-Pb isotopic analyses were performed on zircon grains at the UnB Laboratory of Geochronology (Supplementary Table 1), using a Thermo-Fisher Neptune HR-MC-ICP-MS instrument, coupled to a Nd:YAG UP213 New Wave laser ablation system. The standard sample bracketing method of Albarède *et al.* (2004) was applied in the U-Pb analyses using the GJ-1 zircon standard (Jackson *et al.*, 2004) in order to measure the ICP-MS fractionation. During the analytical sessions, reference zircon 91500 (Wiedenbeck *et al.*, 2004) was also analyzed as an external standard to evaluate the quality and reproducibility of the analyses (AL08:  $1064 \pm 5.4$  Ma; AL01:  $1064 \pm 12$  Ma; AL27:  $1064 \pm 5.6$  Ma). The 91500 results are available in the Supplementary Table 2. Tuned masses were 238, 207, 206, 204 and 202. Integration time was one second, and ablation time was 40 seconds. The analyses were performed using a 30  $\mu\text{m}$ -diameter laser spot and the laser was adjusted to 10 Hz and 2-3 J/cm<sup>2</sup>. In addition, the  $^{206}\text{Pb}/^{207}\text{Pb}$  and  $^{206}\text{Pb}/^{238}\text{U}$  ratios were time-corrected.

Common  $^{204}\text{Pb}$  was monitored using the masses of  $^{202}\text{Hg}$  and ( $^{204}\text{Hg}+^{204}\text{Pb}$ ). Common Pb corrections were not made, as the signals were exceptionally low (<30 cps) for  $^{204}\text{Pb}$  and high for  $^{206}\text{Pb}/^{204}\text{Pb}$  ratios. Reported errors were propagated by the quadratic addition ( $2\text{SD}^2 + 2\text{SE}^2$ )<sup>1/2</sup> (SD = standard deviation; SE = standard error) for external reproducibility and performance accuracy. External reproducibility was represented by the standard deviation obtained from repeated analyses (n=20, ~1.1% for  $^{207}\text{Pb}/^{206}\text{Pb}$  and up to ~2% for  $^{206}\text{Pb}/^{238}\text{U}$ ) of the GJ-1 zircon standard during the analytical sessions and execution accuracy is the standard error calculated for each analysis. More details about the applied methods can be found in Böhn *et al.* (2009). The raw data were processed off-line and reduced using an Excel worksheet (Böhn *et al.*, 2009). Concordia diagrams, probability density plots, and weighted average ages were calculated using the Isoplot-3/Ex software (Ludwig, 2012).

Whole-rock Sm-Nd isotopic analyses were performed using the same samples analyzed by the U-Pb method, following the procedures described by Gioia and Pimentel (2000), also carried out at the UnB Laboratory of Geochronology. Approximately 50 mg of each representative sample powders were mixed with  $^{149}\text{Sm}/^{150}\text{Nd}$  spike solution and dissolved in Savillex capsules. Sm and Nd contents were extracted via conventional cation exchange chromatography technique, with Teflon columns containing LN-Spec resin (HDEHP – diethylhexyl phosphoric acid supported on PTFE powder). Sm and Nd fractions were loaded on Re evaporation filaments of double filament assemblies, and the measurements were performed on a multicollector TRITON thermal ionization mass spectrometer (TIMS) in static mode. The uncertainties of Sm/Nd and  $^{143}\text{Nd}/^{144}\text{Nd}$  ratios were better than  $\pm 0.1\%$  ( $2\sigma$  standard error) and  $\pm 0.0015\%$  ( $1\sigma$ ), respectively, according to repeated analyses of the international rock standard BHVO-1. The  $^{143}\text{Nd}/^{144}\text{Nd}$  ratios were normalized to  $^{146}\text{Nd}/^{144}\text{Nd} = 0.7219$ , and the decay constant used was ( $\lambda$ )  $6.54 \times 10^{-12}$ . The  $T_{\text{DM}}$  values were calculated using the model proposed by DePaolo (1981).

## 4.4.RESULTS

### 4.4.1. *Geology and Petrography*

The investigated igneous bodies crop out as stocks and plutons in an area of 1,400 km<sup>2</sup> (Figure 2). Host rocks are schists and phyllites related to the Cuiabá Group, and are exposed in the internal zone of the Paraguay Belt. Small band of thermal metamorphism produced albite-epidote hornfels (distal) and hornblende hornfels (proximal to the intrusions) paragenesis in the host rocks. The primary N30°E orientation of the Transbrasiliiano Lineament can be well recognized in the Cuiabá Group metasedimentary rocks.

The investigated granitic rocks were divided into two groups, on the basis of lithological and petrographic parameters. The first group corresponds to a large granodiorite pluton and a small quartz monzodiorite stock that occur in the NE of the study area. The second group includes mostly monzogranite outcrops that constitute a pluton in the SW of the study area (Figure 4.2).

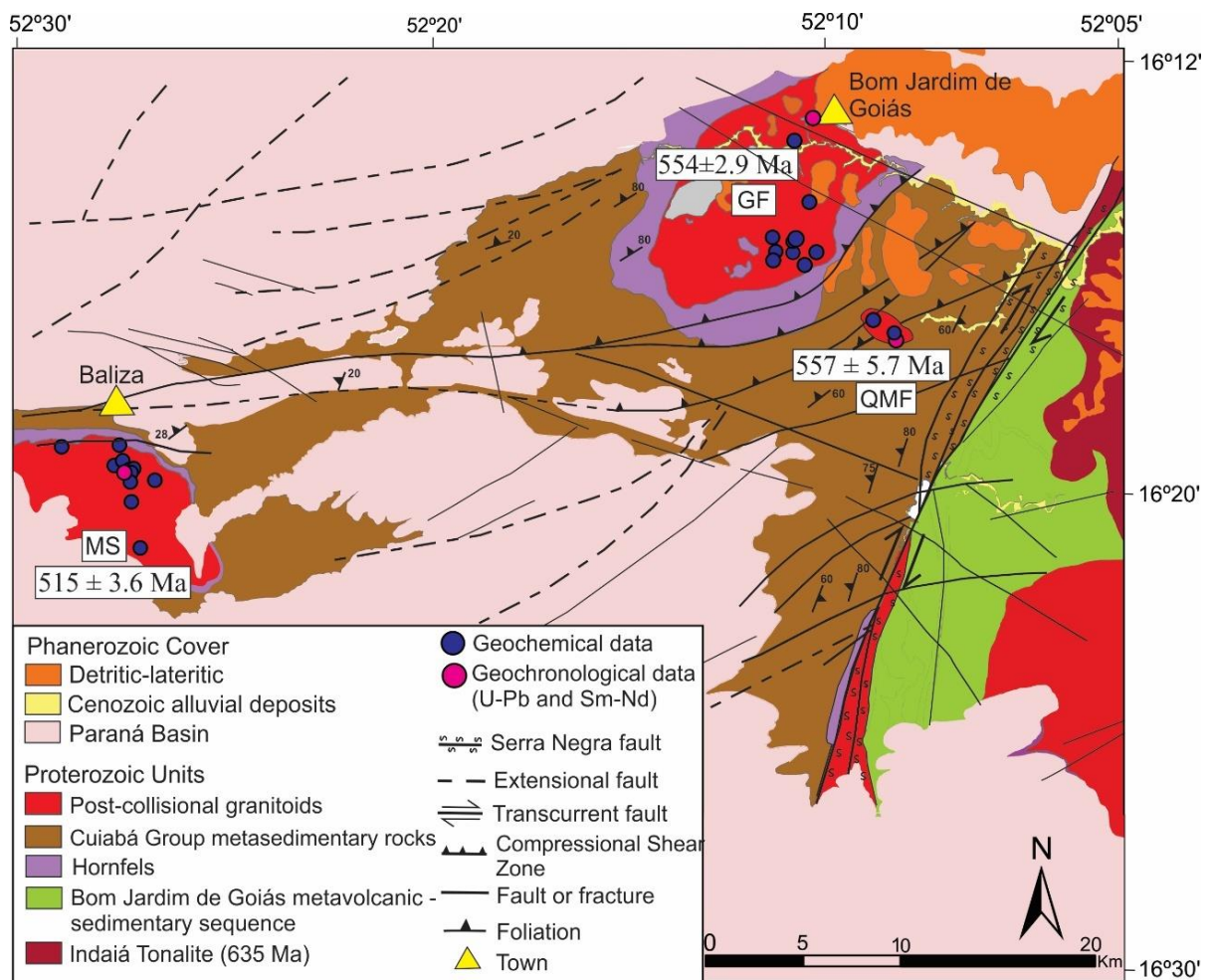


**Figure 4.2** – Geological map of the study area (modified from CPRM, 2017). MS – monzogranite suite; QMF – qz-monzodiorite facies; GF - granodiorite facies.

The first group, here named qz-monzodiorite/granodiorite suite, is dominantly correlated with the calc-alkaline granodioritic trend of the Lameyre and Bowden (1982) evolutionary magmatic series (Figure 4.3A). The second group is the monzogranite suite – the

samples plot in the field between calc-alkaline and monzonitic/shoshonitic trends of Lameyre and Bowden (1982; Figure 4.3A).

#### *4.4.1.1. The qz-monzodiorite/granodiorite suite*

First described by Seer (1985) as quartz diorite, the stock of approximately 30 km<sup>2</sup> in area corresponds to the least evolved igneous body of the Paraguay Belt. The stock is a small satellite body (Figure 2) essentially composed of plagioclase (oligoclase to andesine, An<sub>14-36</sub>, 44-42%), hornblende (17-14%), quartz (12-10%), biotite (11-9%), augite (7-6%), and microcline (5-6%). The rock is greenish-gray (Figure 3B), from fine- to very-fine grained (0.1 to 1 mm), and displays porphyritic to glomeroporphyritic texture. Hornblende is the main mafic mineral and occurs both as phenocrysts (0.5 to 1 mm) and in the matrix (up to 0.3 mm in size). The glomeroporphyritic texture is represented by clustered amphibole, plagioclase and pyroxene (Figure 3C). The accessory minerals (<5%) include titanite, apatite, zircon and monazite, and alteration products are sericite, epidote and opaque minerals. Uralitization by late magmatic fluids is intense and is evidenced by augite enveloped by hornblende.

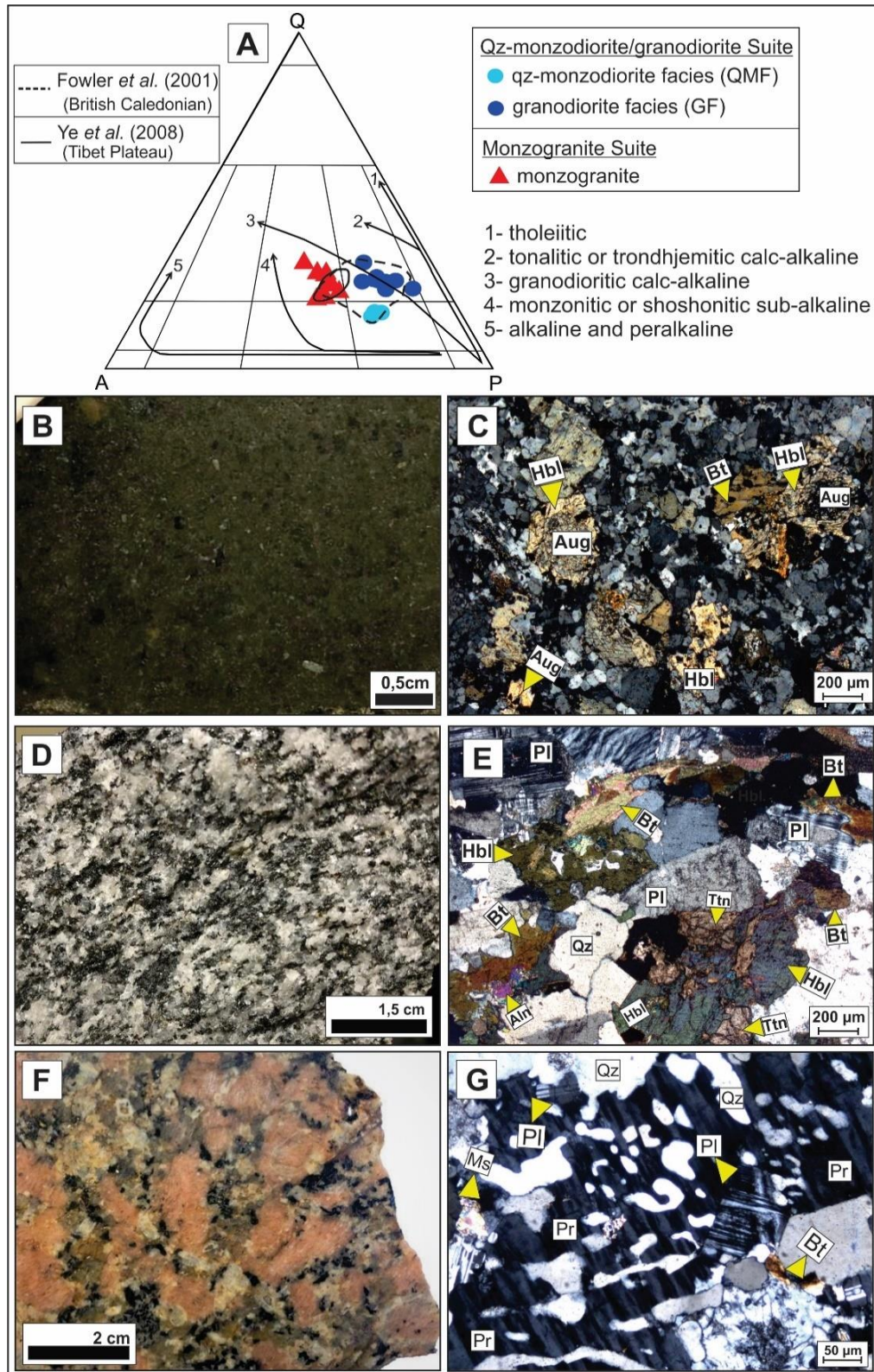


**Figure 4.3-** Petrographic aspects of the investigated rocks: (A) QAP classification diagram of Streckeisen (1974) showing CIPW normative compositions for the studied rocks. Evolutionary trend for magmatic series of Lameyre and Bowden (1982); (B) hand specimen of quartz monzodiorite showing porphyritic texture and very fine- to fine-grained, dark greenish-grey matrix; (C) photomicrograph of quartz monzodiorite showing porphyritic to

glomeroporphyritic texture and very fine-grained matrix mainly formed of plagioclase. Augite is enveloped by hornblende rims; (D) granodiorite sample showing weak foliation resulting from the orientation of mafic minerals; (E) photomicrograph of granodiorite showing discrete orientation, formed of plagioclase, hornblende, biotite, titanite and opaque minerals; (F) hand specimen of monzogranite showing porphyritic texture, in which pinkish K-feldspar phenocrysts stand out from a dark-grey matrix of plagioclase, quartz and biotite; (G) photomicrograph of monzogranite showing inequigranular, xenomorphic texture and graphic intergrowth. Photomicrographs taken under crossed polarizers. Mineral abbreviations are after Whitney and Evans (2010).

The granodiorite facies was firstly described by Coimbra (2015) and is characteristic of a larger pluton located SW of Bom Jardim de Goiás (Figure 4.2). It is essentially composed of plagioclase (44-40%), quartz (22-17%), hornblende (16-14%), biotite (13-8%) and microcline (10-8%). Plagioclase varies from oligoclase to andesine ( $An_{19-32}$ ). Accessory minerals are apatite, titanite, allanite, zircon and opaque minerals; alteration minerals are clinozoisite/zoisite and clay minerals. The rocks exhibit equigranular (~0.8 mm) to inequigranular (1 to 2.5 mm) textures, formed of subhedral feldspar and amphibole phenocrysts in hypidiomorphic to xenomorphic matrix. Incipient foliation resembling schistosity is defined by the orientation of biotite and hornblende aggregates, following the regional trend characteristic of the Transbrasiliano Lineament (Figure 4.3D). Hornblende can be partially to totally replaced by biotite, and is usually associated with titanite, allanite and opaque minerals (Figure 4.3E).

#### *4.4.1.2. The monzogranite suite*

Pinkish to gray, isotropic granite crops out south of Baliza, Mato Grosso (Figure 4.2). The rock is fine- to coarse-grained, varying from equigranular (~1 mm) to inequigranular (0.12 to 8 mm), and displays porphyritic texture with a matrix of up to 0.4 mm in grain size (Figure 4.3F). The rock-forming minerals are plagioclase (41-36%), classified as oligoclase ( $An_{21-29}$ ),

K-feldspar (29-24%), quartz (28-18%), and euhedral to subhedral biotite (7-5%), which characterizes the monzogranitic composition. Accessory minerals are titanite, zircon and apatite. Alteration phases are chlorite, muscovite and opaque minerals. Plagioclase (0.1 to 5 mm) can either compose the matrix or form twinned phenocrysts containing biotite inclusions. Graphic intergrowth of vermicular quartz is commonly found in K-feldspar grains (Figure 4.3G). Perthitic intergrowth is also common, with the sodic phase arranged as films and grains. Quartz can be vermicular, cuneiform or lobate in perthitic orthoclase, characterizing the micrographic intergrowth.

#### 4.4.2. *Lithochemical Data*

Twelve representative samples of the qz-monzodiorite/granodiorite suite were analyzed, among which three of the qz-monzodiorite facies ( $\text{SiO}_2$  ~56 wt.%) and nine of the granodiorite facies (58.8-65.3 wt.%  $\text{SiO}_2$ ). Ten samples of the monzogranite suite ( $\text{SiO}_2$  65.6-71.2 wt.%) were analyzed. High MgO contents were obtained for the qz-monzodiorite/granodiorite suite, resulting in high mg# values (56.09 to 39.58; Table 4.2), which decrease in the monzogranite suite (36.37 > mg# > 27.16). Geochemical data (major elements) published by Manzano (2009) for other granitic bodies intruded into the Cuiabá Group, Paraguay Belt, are presented for comparison. Major, minor and trace element data of this study are listed in Table 4.2.

**Table 4.2** – Results of the whole rock geochemical analyses of the investigated rocks.

| Elements                       | Granodiorite |       |       |        |      |       |       |      |       | Quartz Monzodiorite |        |       |
|--------------------------------|--------------|-------|-------|--------|------|-------|-------|------|-------|---------------------|--------|-------|
|                                | AL01         | AL02  | AL03  | AL04-A | AL21 | AL22  | AL23  | AL24 | AL25  | AL05-A              | AL05-B | AL08  |
| SiO <sub>2</sub>               | 58.8         | 62.5  | 63.9  | 65.3   | 61.3 | 59.1  | 62.6  | 63.4 | 63.4  | 56.9                | 56.8   | 56.8  |
| Al <sub>2</sub> O <sub>3</sub> | 15.15        | 15.45 | 15.25 | 15.05  | 15.3 | 15.15 | 16.05 | 15.5 | 15.55 | 14                  | 14     | 13.95 |



|                                    |        |        |        |        |       |        |       |        |        |        |        |       |
|------------------------------------|--------|--------|--------|--------|-------|--------|-------|--------|--------|--------|--------|-------|
| <b>Fe<sub>2</sub>O<sub>3</sub></b> | 7.98   | 6.23   | 5.59   | 5.62   | 6.15  | 6.96   | 5.91  | 6.33   | 5.96   | 7.59   | 7.73   | 7.57  |
| <b>FeO</b>                         | 7.18   | 5.61   | 5.03   | 5.06   | 5.54  | 6.26   | 5.32  | 5.70   | 5.36   | 6.83   | 6.96   | 6.81  |
| <b>MnO</b>                         | 0.1    | 0.07   | 0.07   | 0.08   | 0.08  | 0.1    | 0.06  | 0.11   | 0.1    | 0.12   | 0.12   | 0.14  |
| <b>MgO</b>                         | 5.17   | 2.68   | 2.31   | 2.27   | 2.96  | 4.6    | 2.89  | 2.14   | 2.19   | 5.44   | 5.47   | 5.28  |
| <b>CaO</b>                         | 6.24   | 4.78   | 4.1    | 3.72   | 4.65  | 5.88   | 4.75  | 4.1    | 4.34   | 6.63   | 6.73   | 6.56  |
| <b>Na<sub>2</sub>O</b>             | 3.4    | 3.96   | 3.69   | 3.6    | 3.62  | 3.59   | 3.94  | 3.76   | 3.75   | 3.29   | 3.29   | 3.27  |
| <b>K<sub>2</sub>O</b>              | 2.23   | 2.61   | 3.17   | 3.2    | 3.08  | 3.1    | 3.2   | 3.31   | 3.17   | 3.71   | 3.7    | 3.71  |
| <b>TiO<sub>2</sub></b>             | 0.94   | 0.78   | 0.72   | 0.65   | 0.86  | 0.88   | 0.8   | 0.77   | 0.77   | 1.04   | 1.05   | 1.04  |
| <b>P<sub>2</sub>O<sub>5</sub></b>  | 0.34   | 0.23   | 0.2    | 0.19   | 0.25  | 0.3    | 0.28  | 0.24   | 0.24   | 0.51   | 0.52   | 0.52  |
| <b>LOI</b>                         | 1.33   | 0.97   | 0.87   | 1.09   | 0.88  | 1.41   | 0.71  | 1.07   | 0.65   | 0.58   | 0.65   | 0.53  |
| <b>Total</b>                       | 101.97 | 100.47 | 100.06 | 100.94 | 99.35 | 101.35 | 101.5 | 100.92 | 100.31 | 100.41 | 100.69 | 99.99 |
| <b>Ba</b>                          | 1210   | 893    | 885    | 835    | 1095  | 1230   | 1515  | 885    | 888    | 3190   | 3290   | 3210  |
| <b>Ga</b>                          | 21.1   | 22.1   | 21.4   | 21     | 20.5  | 20.5   | 21.2  | 21.2   | 21.2   | 21.2   | 21.8   | 20.1  |
| <b>Hf</b>                          | 5.9    | 5.9    | 5.6    | 6.1    | 5.7   | 5.6    | 5.3   | 5.4    | 5.8    | 7      | 7.1    | 7.3   |
| <b>Nb</b>                          | 14.1   | 18     | 15.2   | 15.2   | 17.2  | 17.1   | 21.3  | 13.9   | 16.2   | 21.2   | 21.1   | 20    |
| <b>Rb</b>                          | 68.5   | 86.6   | 111    | 116    | 103   | 107    | 90.4  | 123    | 119    | 126.5  | 121.5  | 118   |
| <b>Sr</b>                          | 979    | 803    | 657    | 586    | 721   | 990    | 1035  | 697    | 725    | 1845   | 1830   | 1755  |
| <b>Ta</b>                          | 1.1    | 2      | 1.4    | 1.7    | 1.7   | 1.7    | 2     | 1.6    | 1.6    | 1.6    | 1.7    | 1.6   |
| <b>Th</b>                          | 22.7   | 16.8   | 18.35  | 18.75  | 19.1  | 27.6   | 19.35 | 15.6   | 15.65  | 52.3   | 53.3   | 53.6  |
| <b>Y</b>                           | 26.6   | 20.1   | 27.7   | 20     | 23.8  | 24.5   | 23.9  | 22     | 23.3   | 31.1   | 31.6   | 32.3  |
| <b>Zr</b>                          | 239    | 217    | 211    | 209    | 204   | 216    | 207   | 210    | 206    | 273    | 273    | 267   |
| <b>La</b>                          | 70.6   | 58.7   | 45.3   | 46.6   | 59.9  | 81.5   | 77.2  | 52.7   | 53.9   | 159.5  | 158    | 156.5 |
| <b>Ce</b>                          | 147.5  | 120.5  | 91.6   | 93.6   | 124.5 | 163    | 148.5 | 107.5  | 109    | 309    | 311    | 305   |
| <b>Pr</b>                          | 17.75  | 13.95  | 10.7   | 10.35  | 14.1  | 18.45  | 16.7  | 12.15  | 12     | 34.2   | 33.8   | 34    |
| <b>Nd</b>                          | 71.3   | 52.8   | 39.7   | 39.9   | 52.6  | 69.7   | 62.2  | 46.6   | 48     | 126.5  | 128.5  | 128   |

|                            |       |       |       |       |       |       |       |       |       |       |       |       |
|----------------------------|-------|-------|-------|-------|-------|-------|-------|-------|-------|-------|-------|-------|
| <b>Sm</b>                  | 12.95 | 10.05 | 7.86  | 7.47  | 9.96  | 11.45 | 10.7  | 8.61  | 8.97  | 21.2  | 21    | 20.9  |
| <b>Eu</b>                  | 2.69  | 2.18  | 1.68  | 1.66  | 2.22  | 2.65  | 2.46  | 2.03  | 2.1   | 4.31  | 4.33  | 4.46  |
| <b>Gd</b>                  | 8.14  | 6.72  | 5.96  | 5.06  | 6.77  | 7.84  | 6.72  | 5.76  | 5.83  | 12.05 | 12.35 | 11.9  |
| <b>Tb</b>                  | 1.07  | 0.93  | 0.91  | 0.75  | 0.9   | 0.98  | 0.89  | 0.8   | 0.81  | 1.41  | 1.47  | 1.39  |
| <b>Dy</b>                  | 5.55  | 4.73  | 5.08  | 4     | 5.07  | 5.25  | 4.97  | 4.71  | 7.73  | 6.91  | 7.28  | 7.35  |
| <b>Ho</b>                  | 0.88  | 0.76  | 0.88  | 0.74  | 0.88  | 0.86  | 0.74  | 0.83  | 0.87  | 1.08  | 1.11  | 1.16  |
| <b>Er</b>                  | 2.63  | 1.99  | 2.8   | 2.19  | 2.47  | 2.33  | 2.4   | 2.22  | 2.66  | 2.84  | 2.96  | 2.73  |
| <b>Tm</b>                  | 0.35  | 0.32  | 0.36  | 0.29  | 0.33  | 0.37  | 0.33  | 0.36  | 0.37  | 0.36  | 0.4   | 0.41  |
| <b>Yb</b>                  | 2.2   | 1.75  | 2.47  | 1.73  | 2.07  | 1.99  | 2.06  | 2.06  | 2.06  | 2.27  | 2.17  | 2.5   |
| <b>Lu</b>                  | 0.36  | 0.24  | 0.35  | 0.28  | 0.3   | 0.32  | 0.34  | 0.33  | 0.32  | 0.33  | 0.37  | 0.35  |
| <b>Eu/Eu*</b>              | 0.75  | 0.77  | 0.72  | 0.78  | 0.78  | 0.81  | 0.83  | 0.83  | 0.84  | 0.76  | 0.76  | 0.79  |
| <b>mg#</b>                 | 53.59 | 43.40 | 42.42 | 41.86 | 46.18 | 54.09 | 46.57 | 37.60 | 39.58 | 56.09 | 55.78 | 55.42 |
| <b>(La/Yb)<sub>N</sub></b> | 22.9  | 23.9  | 13.1  | 19.2  | 20.6  | 29.2  | 26.7  | 18.2  | 18.7  | 50.1  | 51.9  | 44.6  |
| <b>(Gd/Yb)<sub>N</sub></b> | 3.0   | 3.1   | 2.0   | 2.4   | 2.7   | 3.2   | 2.7   | 2.3   | 2.3   | 4.3   | 4.6   | 3.9   |
| <b>(Nb/Ta)<sub>N</sub></b> | 0.72  | 0.51  | 0.61  | 0.50  | 0.57  | 0.57  | 0.60  | 0.49  | 0.57  | 0.75  | 0.70  | 0.70  |
| <b>(Zr/Hf)<sub>N</sub></b> | 1.12  | 1.02  | 1.04  | 0.95  | 0.99  | 1.07  | 1.08  | 1.08  | 0.98  | 1.08  | 1.06  | 1.01  |
| <b>A/CNK</b>               | 0.78  | 0.86  | 0.90  | 0.93  | 0.86  | 0.76  | 0.86  | 0.90  | 0.89  | 0.65  | 0.65  | 0.65  |

|                                    | <b>Monzogranite</b> |             |             |               |              |              |              |              |              |              |
|------------------------------------|---------------------|-------------|-------------|---------------|--------------|--------------|--------------|--------------|--------------|--------------|
| <b>Elements</b>                    | <b>AL26</b>         | <b>AL27</b> | <b>AL28</b> | <b>AL28-B</b> | <b>SE-05</b> | <b>SE-27</b> | <b>SE-25</b> | <b>SE-38</b> | <b>SE-48</b> | <b>AL-30</b> |
| <b>SiO<sub>2</sub></b>             | 65.6                | 67.3        | 71          | 71.2          | 64.4         | 64.4         | 69           | 68           | 69.3         | 65.8         |
| <b>Al<sub>2</sub>O<sub>3</sub></b> | 15.5                | 14.9        | 13.6        | 13.7          | 14.85        | 14.9         | 14.1         | 14.05        | 14.1         | 14.7         |
| <b>Fe<sub>2</sub>O<sub>3</sub></b> | 4.67                | 3.75        | 3.03        | 3.06          | 4.44         | 4.49         | 3.69         | 4.13         | 3.6          | 3.97         |
| <b>FeO</b>                         | 4.20                | 3.38        | 2.73        | 2.75          | 4.00         | 4.04         | 3.32         | 3.72         | 3.24         | 3.57         |
| <b>MnO</b>                         | 0.08                | 0.07        | 0.05        | 0.05          | 0.08         | 0.09         | 0.07         | 0.08         | 0.07         | 0.07         |

|                                   |        |       |       |       |       |       |       |       |       |       |
|-----------------------------------|--------|-------|-------|-------|-------|-------|-------|-------|-------|-------|
| <b>MgO</b>                        | 1.36   | 1.06  | 0.65  | 0.64  | 1.32  | 1.44  | 1.1   | 1.28  | 1.05  | 1.12  |
| <b>CaO</b>                        | 2.49   | 2.13  | 1.61  | 1.65  | 2.39  | 2.5   | 1.49  | 2.15  | 1.85  | 2.53  |
| <b>Na<sub>2</sub>O</b>            | 3.71   | 3.75  | 3.36  | 3.42  | 3.57  | 3.62  | 3.66  | 3.72  | 3.69  | 4.1   |
| <b>K<sub>2</sub>O</b>             | 5.06   | 4.68  | 4.91  | 4.85  | 5.28  | 5     | 4.79  | 4.41  | 4.54  | 4.2   |
| <b>TiO<sub>2</sub></b>            | 0.75   | 0.61  | 0.48  | 0.47  | 0.73  | 0.74  | 0.54  | 0.66  | 0.54  | 0.66  |
| <b>P<sub>2</sub>O<sub>5</sub></b> | 0.31   | 0.23  | 0.13  | 0.15  | 0.3   | 0.27  | 0.21  | 0.26  | 0.22  | 0.25  |
| <b>LOI</b>                        | 0.93   | 0.72  | 0.69  | 0.75  | 0.96  | 0.99  | 0.7   | 0.62  | 0.78  | 0.93  |
| <b>Total</b>                      | 100.69 | 99.41 | 99.67 | 100.1 | 98.57 | 98.67 | 99.5  | 99.54 | 99.9  | 98.5  |
| <b>Ba</b>                         | 1480   | 1315  | 980   | 1030  | 1695  | 1440  | 1085  | 1095  | 987   | 1080  |
| <b>Ga</b>                         | 19.1   | 17.8  | 16.4  | 17.1  | 18.3  | 19.8  | 20.5  | 21    | 20.6  | 22.8  |
| <b>Hf</b>                         | 10.3   | 7.4   | 6.6   | 6.4   | 9.9   | 11    | 8.5   | 9.5   | 7.2   | 8.8   |
| <b>Nb</b>                         | 53.6   | 48.8  | 49.9  | 51.6  | 54    | 57    | 57.9  | 56.7  | 51.5  | 56.9  |
| <b>Rb</b>                         | 158    | 162   | 136.5 | 154   | 158.5 | 172.5 | 174   | 162.5 | 165   | 150   |
| <b>Sr</b>                         | 582    | 508   | 384   | 419   | 568   | 572   | 346   | 471   | 360   | 497   |
| <b>Ta</b>                         | 3.8    | 3.5   | 5.3   | 5.7   | 3.5   | 3.7   | 4.7   | 3.9   | 4.2   | 4.2   |
| <b>Th</b>                         | 32.5   | 25.9  | 22    | 22.9  | 27.4  | 31.2  | 32.8  | 1.15  | 1.08  | 1.05  |
| <b>Y</b>                          | 29.8   | 23.6  | 36.2  | 40.9  | 31.9  | 28.7  | 64.6  | 35.1  | 33    | 31.4  |
| <b>Zr</b>                         | 400    | 308   | 245   | 274   | 441   | 448   | 356   | 385   | 315   | 365   |
| <b>La</b>                         | 90.4   | 65.9  | 80.4  | 88.8  | 88.6  | 123.5 | 105   | 101.5 | 90.3  | 86.5  |
| <b>Ce</b>                         | 177.5  | 141.5 | 161.5 | 177   | 180.5 | 206   | 172.5 | 188   | 160.5 | 176   |
| <b>Pr</b>                         | 19.15  | 15.2  | 18.25 | 19.2  | 19.35 | 19.75 | 19.4  | 19.3  | 16.2  | 17.7  |
| <b>Nd</b>                         | 64.6   | 52.6  | 66.3  | 73.3  | 70.9  | 67.6  | 67.7  | 69.4  | 56.7  | 64.6  |
| <b>Sm</b>                         | 10.65  | 8.35  | 12    | 13.75 | 11.5  | 10.15 | 11.6  | 11.15 | 9.2   | 10.25 |
| <b>Eu</b>                         | 2.05   | 1.63  | 1.88  | 1.85  | 1.93  | 1.69  | 1.72  | 1.63  | 1.47  | 1.78  |
| <b>Gd</b>                         | 7.45   | 5.56  | 9.57  | 9.01  | 7.74  | 6.8   | 9.4   | 7.71  | 6.91  | 6.78  |

|                            |       |       |       |       |       |       |       |       |       |       |
|----------------------------|-------|-------|-------|-------|-------|-------|-------|-------|-------|-------|
| <b>Tb</b>                  | 1.06  | 0.82  | 1.41  | 1.35  | 1.22  | 1     | 1.54  | 1.15  | 1.08  | 1.05  |
| <b>Dy</b>                  | 6.2   | 4.54  | 8.32  | 8.38  | 6.11  | 5.66  | 9.27  | 6.23  | 6.36  | 6.01  |
| <b>Ho</b>                  | 0.98  | 0.83  | 1.42  | 1.46  | 1.15  | 0.96  | 1.86  | 1.18  | 1.11  | 1.06  |
| <b>Er</b>                  | 3.32  | 2.68  | 4.11  | 3.81  | 3.2   | 2.94  | 5.51  | 3.25  | 3.52  | 3.05  |
| <b>Tm</b>                  | 0.45  | 0.4   | 0.56  | 0.6   | 0.52  | 0.45  | 0.74  | 0.54  | 0.48  | 0.44  |
| <b>Yb</b>                  | 3     | 2.81  | 3.3   | 3.25  | 2.83  | 2.7   | 4.55  | 3.24  | 3.19  | 2.89  |
| <b>Lu</b>                  | 0.46  | 0.38  | 0.46  | 0.44  | 0.45  | 0.5   | 0.67  | 0.5   | 0.48  | 0.42  |
| <b>Eu/Eu*</b>              | 0.67  | 0.69  | 0.52  | 0.48  | 0.59  | 0.59  | 0.49  | 0.51  | 0.54  | 0.62  |
| <b>mg#</b>                 | 34.17 | 33.50 | 27.66 | 27.16 | 34.64 | 36.37 | 34.70 | 35.59 | 34.21 | 33.46 |
| <b>(La/Yb)<sub>N</sub></b> | 11.7  | 10.9  | 18.1  | 12.8  | 21.5  | 16.7  | 17.4  | 19.5  | 22.3  | 32.6  |
| <b>(Gd/Yb)<sub>N</sub></b> | 2.0   | 1.6   | 2.4   | 2.3   | 2.2   | 2.1   | 1.7   | 1.9   | 1.8   | 1.9   |
| <b>(Nb/Ta)<sub>N</sub></b> | 0.79  | 0.79  | 0.53  | 0.51  | 0.87  | 0.87  | 0.69  | 0.82  | 0.69  | 0.76  |
| <b>(Zr/Hf)<sub>N</sub></b> | 1.07  | 1.15  | 1.03  | 1.18  | 1.23  | 1.13  | 1.16  | 1.12  | 1.21  | 1.15  |
| <b>A/CNK</b>               | 0.96  | 0.99  | 0.99  | 0.99  | 0.93  | 0.94  | 1.01  | 0.95  | 0.98  | 0.93  |

In the  $\text{Na}_2\text{O}+\text{K}_2\text{O}-\text{CaO}$  vs.  $\text{SiO}_2$  diagram of Frost *et al.* (2001), the qz-monzodiorite/granodiorite suite samples plot exclusively within the calc-alkaline field, while the monzogranite suite samples plot mainly in the alkali-calcic domain (Figure 4.4A). The magmatism that originated both suites is classified as non-tholeiitic in the AFM diagram of Irvine and Baragar (1971), modified by Nardi (2016; Figure 4.4B). The  $\text{FeO}_{\text{tot}}/(\text{FeO}_{\text{tot}}+\text{MgO})$  vs.  $\text{SiO}_2$  diagram of Frost *et al.* (2001) shows that both suites display an exclusively magnesian signature (Figure 4.4C).

The A/CNK vs. A/NK diagram proposed by Maniar and Piccoli (1989; Figure 4.4D), indicates the metaluminous to slightly peraluminous ( $\text{A/CNK} = 0.64-1.01$ ) nature of both suites.

The  $K_2O$  vs.  $SiO_2$  diagram of Peccerillo and Taylor (1976; Figure 4.4E) indicates shoshonitic affinity for the qz-monzodiorite facies and high-K calc-alkaline affinity for the granodiorite facies of the qz-monzodiorite/granodiorite suite. The monzogranite suite also displays mainly ultrapotassic affinity.

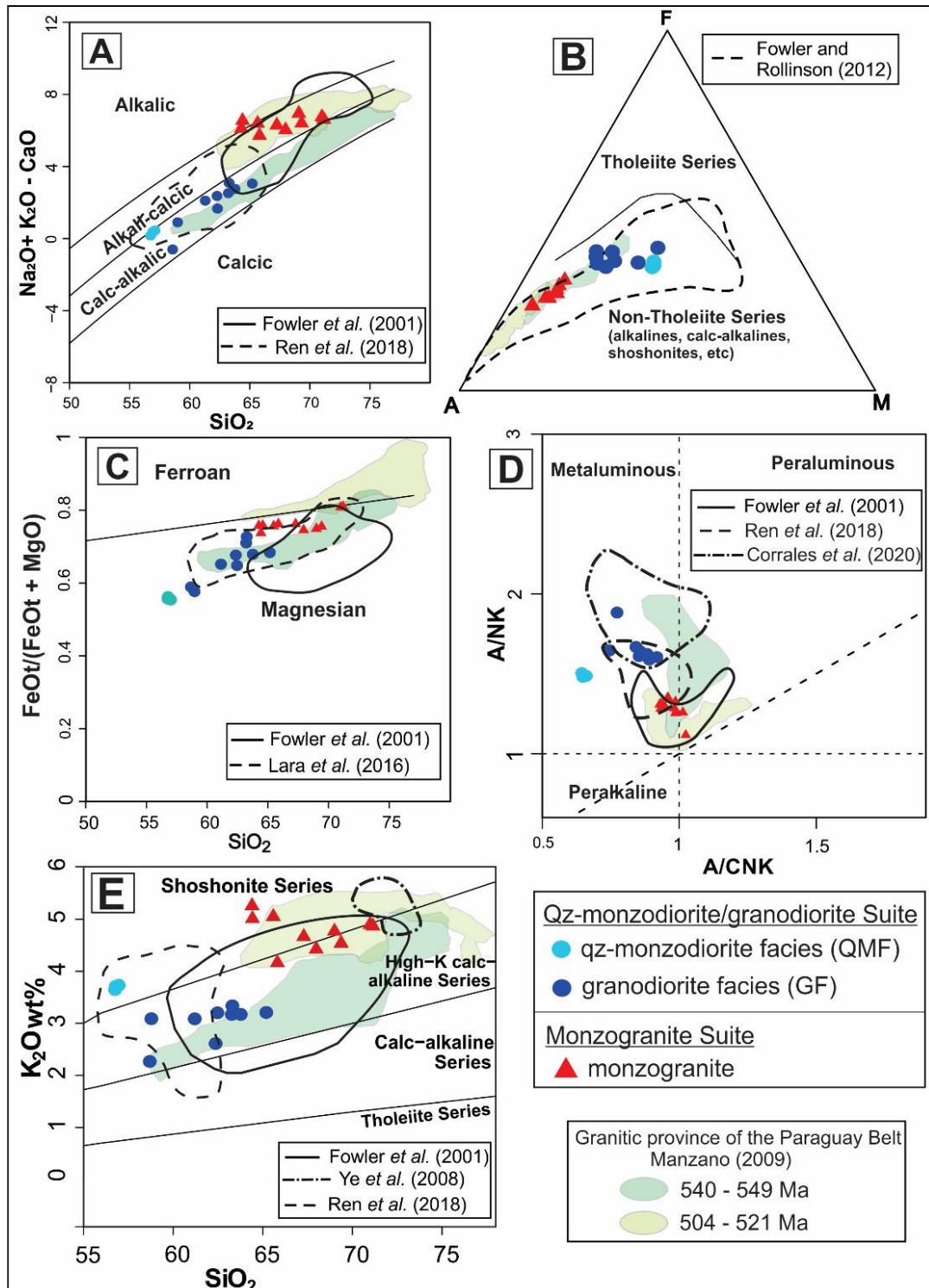


**Figure 4.4** - The continuous and dotted lines correspond to studies related to high Ba-Sr magmatism used for comparison. Distribution of representative analytical points of the investigated magmatism in the diagrams: (A)  $\text{Na}_2\text{O}+\text{K}_2\text{O}-\text{CaO}$  versus  $\text{SiO}_2$  proposed by Frost et al. (2001); (B) AFM diagram of Irvine and Baragar (1971); (C)  $\text{FeO}_{\text{tot}}/(\text{FeO}_{\text{tot}}+\text{MgO})$  versus  $\text{SiO}_2$  proposed by Frost et al. (2001); (D) A/CNK versus A/NK by Maniar and Piccolli (1989); (E)  $\text{K}_2\text{O}$  versus  $\text{SiO}_2$  of Peccerillo and Taylor (1976).

Harker diagrams (Figure 4.5) show that  $\text{SiO}_2$  in both suites correlates negatively with  $\text{MgO}$ ,  $\text{CaO}$ ,  $\text{P}_2\text{O}_5$ ,  $\text{TiO}_2$  and  $\text{FeO}_{\text{tot}}$ , whereas  $\text{K}_2\text{O}$  is rather scattered in most of the analyzed samples. Convex downward patterns are notable for  $\text{Al}_2\text{O}_3$  and  $\text{Na}_2\text{O}$  with increasing  $\text{SiO}_2$  in the qz-monzodiorite/graniodiorite suite samples. Trace element distribution indicates negative correlations between  $\text{SiO}_2$  and Ba, Sr, Cr and Ni contents. Cr and Ni contents show an almost constant trend for the monzogranitic samples (Figure 4.6A). Bivariant plots between trace elements in logarithmic diagrams (Ba-Sr, Cr-Ni-V and Ce-Zr) can be used to provide information about the crystal fractionation arrays by comparing the studied mineral trend retention with the model mineral fractionation vector based on the Rayleigh fractionation equation used by Fowler *et al.* (2001, 2008). From these diagrams, separation of plagioclase, biotite, amphibole, and some accessory minerals (mainly titanite and zircon) are well observed (Figure 4.6B).

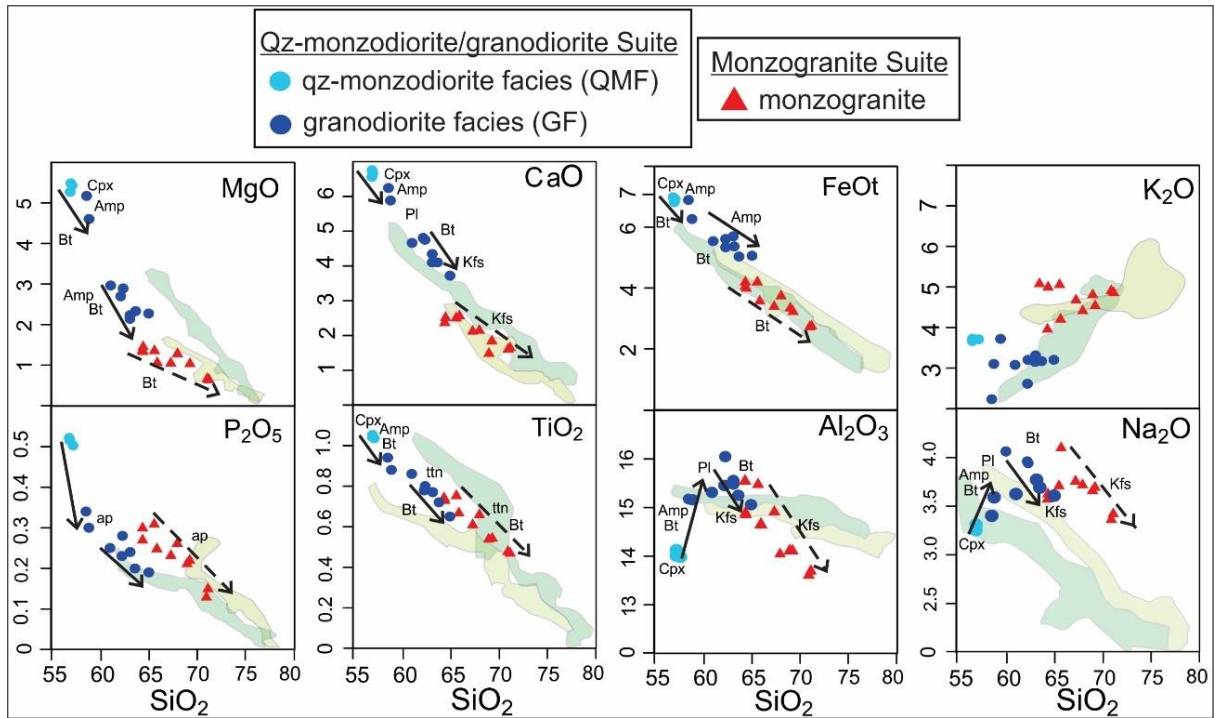


**Figure 4.5**– Harker diagrams with the distribution of major elements (in ppm) data. Each rock mineralogical composition allows qualitative assessment of possible crystal fractionation and the major elements distribution set up pathways which is represented by vectors from parental appinitic to granodiorite. Mineral abbreviations are after Whitney and Evans (2010).

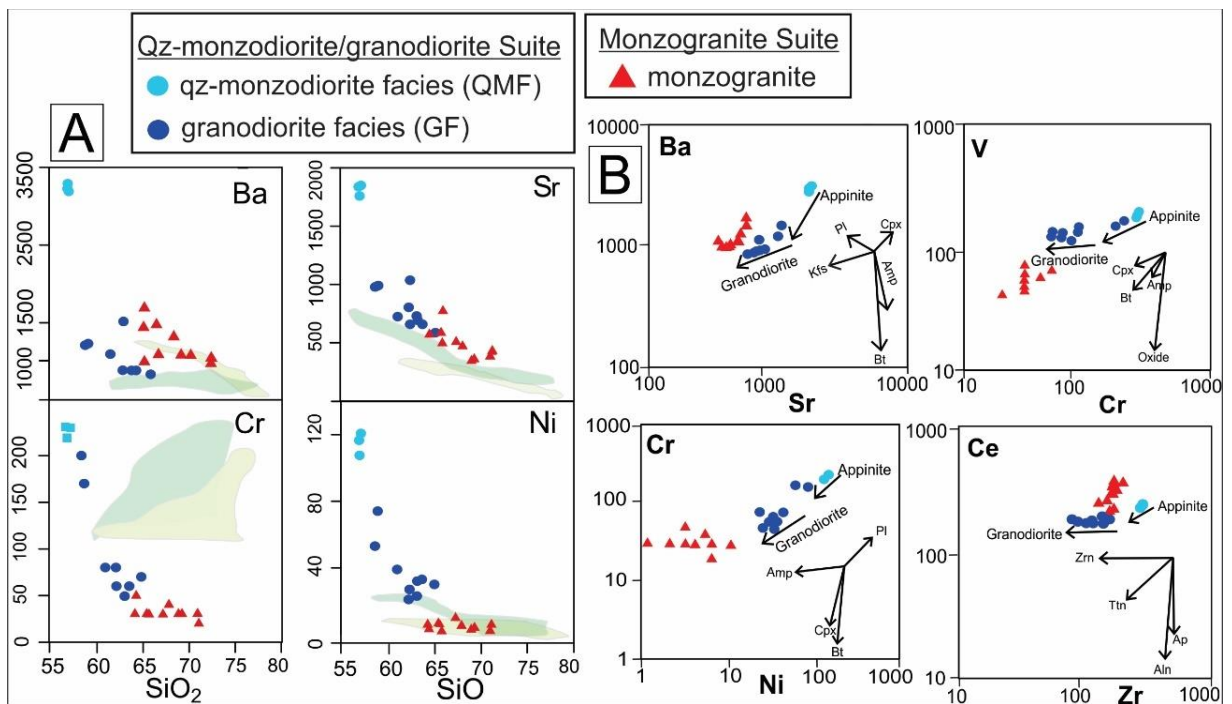


**Figure 4.6** – (A) harker diagrams with the distribution of some trace elements (in ppm) data; (B) selected bivariant trace element diagrams for studied suites. Mineral abbreviations are after Whitney and Evans (2010).

Chondrite-normalized REE data (Evensen 1978; Figure 4.7) indicate depletion of HREE in relation to LREE, as HREE concentrations average around 10x chondrite values. The qz-monzodiorite/granodiorite suite presents the highest LREE values, with  $[La/Yb]_N = 44-51$  in the qz-monzodiorite facies, and  $[La/Yb]_N = 18-29$  in the granodiorite facies (Figure 7A).  $[La/Yb]_N$  varies from 11 to 22 in the monzogranite suite (Figure 4.7B). The qz-monzodiorite/granodiorite suite exhibits slightly negative Eu anomalies, with  $(Eu/Eu^*)$  ranging between 0.75 and 0.89. The most pronounced negative Eu anomalies occur in the monzogranite suite, with  $(Eu/Eu^*)$  ranging between 0.51 and 0.74. The monzogranite suite displays a less depleted HREE pattern, with  $(Gd/Yb)_N$  of  $\sim 2$  (Figure 7B).

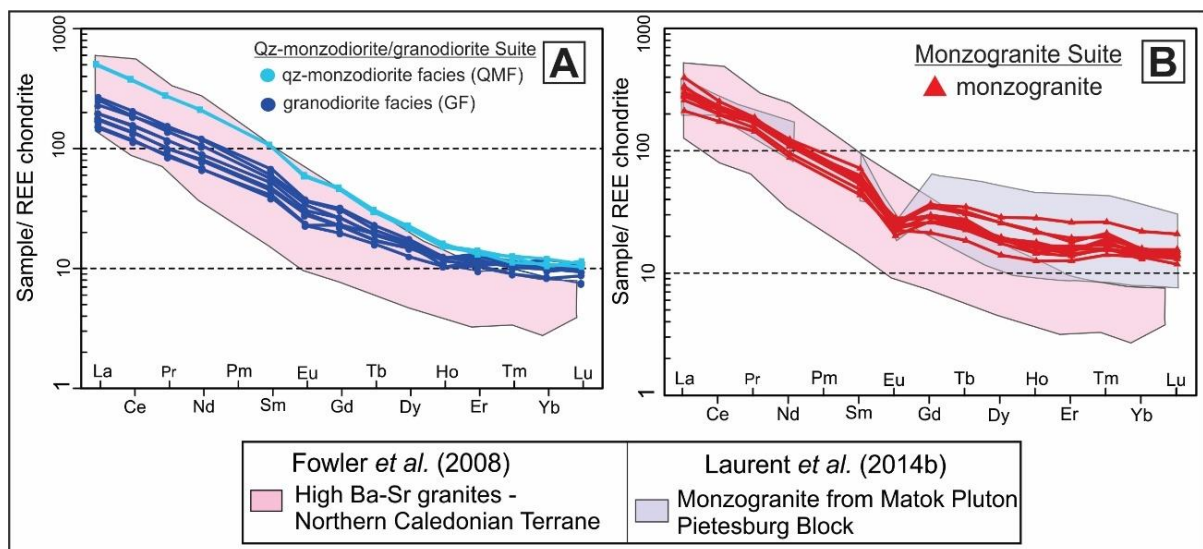


**Figure 4.7** - Rare earth elements patterns of the investigated rocks, normalized to the chondritic values of Evensen (1978), compared to high Ba-Sr granites (Fowler *et al.*, 2008) and to monzogranite values of Matok Pluton (Laurent *et al.*, 2014b).



The multielement diagrams show notable depletions in Nb, Ta, P and Ti in both suites (Figure 4.8). The qz-monzodiorite/granodiorite suite shows more pronounced positive Ba (~3230 ppm) and Th (~53 ppm) anomalies (Figure 4.8A). The monzogranite suite shows considerably less depletion in HSFE (Yb, Y, Nb, Ta, Zr and Hf), with relatively high Zr/Hf (~41) and Nb/Ta (~13) ratios (Figure 4.8B). Besides, subparallel patterns with weak depletion of Nb–Ta [(Nb/Ta)<sub>N</sub> = 0.51–0.87] and Zr–Hf [(Zr/Hf)<sub>N</sub> = 1.07–1.23] are observed in the monzogranite suite.

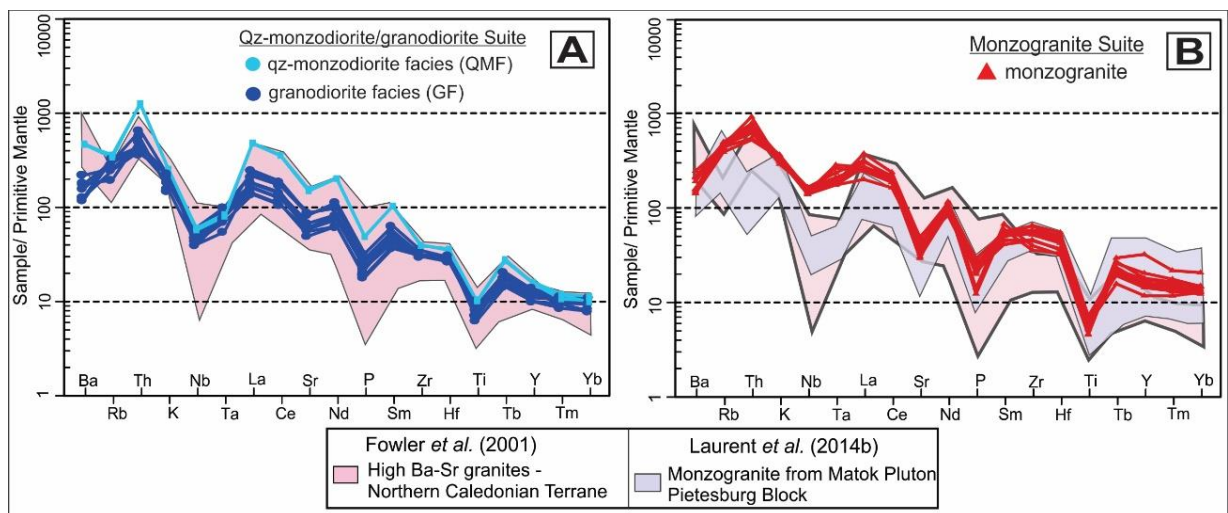


**Figure 4.8** – Multi-element distribution patterns of analyzed samples normalized to primitive mantle values (Thompson, 1982), compared to high Ba-Sr granites (Fowler *et al.*, 2001) and to monzogranite values of Matok Pluton (Laurent *et al.*, 2014b).

#### 4.4.3. Zircon U-Pb Geochronology

Representative samples of both suites were analyzed by means of the zircon U-Pb method. The location of the samples in the study area is shown on the map of Figure 4.2. The few Meso- and Paleoproterozoic ages obtained from some zircon grains were excluded from the U-Pb calculations, for not presenting acceptable analytical errors and concordance (Table 4.3).

**Table 4.3** - Data of U-Pb analyses performed through LA-ICP-MS on zircon from the investigated magmatism.

| SAMPLE   | AL08 (quartz monzodiorite facies) |          |   |   |           |  |           |  |           |      |   |        |  |       |  |        |              |
|----------|-----------------------------------|----------|---|---|-----------|--|-----------|--|-----------|------|---|--------|--|-------|--|--------|--------------|
|          |                                   |          |   |   |           |  |           |  |           |      | Apparent ages                           |        |  |       |  |        |              |
| GRAIN    | <i>f</i>                          | err      |   |   |           | err                                    |           | err                                    |           | Rho  | 2σ                                      |        | 2σ                                     |       | 2σ                                     |        | conc.<br>(%) |
|          | <sup>206</sup> Pb/<br>(%)         | Th/<br>U | <sup>206</sup> Pb/<br><sup>204</sup> Pb | <sup>207</sup> Pb/<br><sup>206</sup> Pb | (%)1<br>σ | <sup>207</sup> Pb/<br><sup>235</sup> U | (%)1<br>σ | <sup>206</sup> Pb/<br><sup>238</sup> U | (% 1<br>σ |      | <sup>207</sup> Pb/<br><sup>206</sup> Pb | 2σ     | <sup>207</sup> Pb/<br><sup>235</sup> U | 2σ    | <sup>206</sup> Pb/<br><sup>238</sup> U | 2σ     |              |
| 003-ZR1  | 0.23                              | 2.18     | 6740                                    | 0.06                                    | 0.74      | 0.76                                   | 1.18      | 0.09                                   | 0.84      | 0.71 | 599.99                                  | 31.82  | 564.18                                 | 9.03  | 571.38                                 | 10.25  | 98.74        |
| 009-ZR37 | 0.05                              | 2.75     | 28433                                   | 0.06                                    | 2.35      | 0.74                                   | 3.23      | 0.09                                   | 2.19      | 0.68 | 570.51                                  | 100.55 | 559.00                                 | 23.47 | 561.31                                 | 27.71  | 99.59        |
| 031-ZR25 | 0.09                              | 1.23     | 17294                                   | 0.06                                    | 0.50      | 0.72                                   | 1.75      | 0.09                                   | 1.64      | 0.94 | 566.96                                  | 21.49  | 549.45                                 | 17.22 | 552.90                                 | 14.85  | 99.38        |
| 024-ZR20 | 0.00                              | 1.14     | 478980                                  | 0.06                                    | 0.61      | 0.71                                   | 1.18      | 0.09                                   | 0.94      | 0.80 | 543.46                                  | 26.40  | 547.62                                 | 9.90  | 546.85                                 | 9.96   | 100.14       |
| 006-ZR4  | 0.03                              | 0.51     | 49418                                   | 0.06                                    | 0.77      | 0.85                                   | 1.26      | 0.10                                   | 0.93      | 0.74 | 666.55                                  | 32.93  | 613.72                                 | 10.88 | 625.14                                 | 625.14 | 98.17        |
| 007-ZR5  | 0.75                              | 2.27     | 2084                                    | 0.06                                    | 2.75      | 0.77                                   | 3.08      | 0.09                                   | 1.33      | 0.43 | 643.02                                  | 116.21 | 563.15                                 | 14.31 | 579.31                                 | 27.01  | 97.21        |
| 012-ZR10 | 0.03                              | 0.82     | 52608                                   | 0.06                                    | 0.90      | 0.96                                   | 1.47      | 0.11                                   | 1.11      | 0.75 | 704.56                                  | 38.03  | 676.44                                 | 14.19 | 683.01                                 | 14.59  | 99.04        |
| 020-ZR16 | 0.02                              | 0.79     | 84172                                   | 0.06                                    | 0.45      | 0.88                                   | 0.82      | 0.10                                   | 0.58      | 0.70 | 679.32                                  | 19.33  | 631.11                                 | 6.96  | 641.77                                 | 7.82   | 98.34        |
| 021-ZR17 | 0.03                              | 0.48     | 59457                                   | 0.06                                    | 1.09      | 0.90                                   | 1.36      | 0.11                                   | 0.71      | 0.53 | 674.97                                  | 46.28  | 645.32                                 | 8.78  | 651.99                                 | 13.00  | 98.98        |
| 023-ZR19 | 1.13                              | 0.09     | 1379                                    | 0.06                                    | 2.87      | 0.74                                   | 3.06      | 0.09                                   | 1.00      | 0.33 | 552.20                                  | 123.00 | 562.83                                 | 10.78 | 560.76                                 | 26.24  | 100.37       |
| 027-ZR21 | 0.02                              | 0.60     | 74612                                   | 0.06                                    | 0.94      | 0.83                                   | 1.39      | 0.10                                   | 0.95      | 0.69 | 643.55                                  | 40.14  | 602.95                                 | 10.98 | 611.59                                 | 12.73  | 98.59        |
| 006-ZR34 | 0.03                              | 2.19     | 56288                                   | 0.06                                    | 1.50      | 0.75                                   | 2.26      | 0.09                                   | 1.65      | 0.73 | 615.22                                  | 64.32  | 554.93                                 | 17.53 | 566.94                                 | 19.57  | 97.88        |
| 007-ZR35 | 0.03                              | 2.59     | 45611                                   | 0.06                                    | 2.01      | 0.68                                   | 2.45      | 0.09                                   | 1.35      | 0.55 | 505.62                                  | 87.37  | 531.93                                 | 13.73 | 527.02                                 | 20.04  | 100.93       |
| 016-ZR12 | 0.01                              | 0.34     | 206622                                  | 0.06                                    | 0.49      | 1.02                                   | 0.99      | 0.12                                   | 0.79      | 0.79 | 731.14                                  | 20.49  | 710.80                                 | 10.56 | 715.75                                 | 10.19  | 99.31        |
| 018-ZR14 | 0.01                              | 0.44     | 140522                                  | 0.07                                    | 0.92      | 1.09                                   | 1.50      | 0.12                                   | 1.13      | 0.75 | 829.02                                  | 38.03  | 723.49                                 | 15.50 | 749.81                                 | 15.89  | 96.49        |

|                 |       |      |        |      |      |      |      |      |      |      |         |        |         |       |         |        |        |
|-----------------|-------|------|--------|------|------|------|------|------|------|------|---------|--------|---------|-------|---------|--------|--------|
| <b>022-ZR18</b> | 0.00  | 0.36 | 399685 | 0.07 | 1.94 | 1.28 | 2.92 | 0.13 | 2.15 | 0.74 | 921.64  | 78.59  | 804.55  | 32.51 | 836.35  | 32.99  | 96.20  |
| <b>017-ZR43</b> | 0.23  | 0.32 | 6646   | 0.07 | 0.94 | 1.15 | 2.21 | 0.12 | 1.96 | 0.89 | 885.91  | 38.82  | 737.64  | 27.27 | 775.49  | 23.78  | 95.12  |
| <b>017-ZR13</b> | 0.01  | 0.45 | 199908 | 0.06 | 0.97 | 0.83 | 1.27 | 0.10 | 0.73 | 0.57 | 564.79  | 42.09  | 625.06  | 8.68  | 612.21  | 11.65  | 102.10 |
| 005-ZR33        | 0.03  | 2.36 | 60919  | 0.06 | 1.63 | 0.70 | 2.09 | 0.09 | 1.26 | 0.60 | 453.79  | 71.34  | 555.90  | 13.42 | 536.33  | 17.34  | 103.65 |
| 008-ZR6         | 0.00  | 0.20 | 585513 | 0.08 | 0.44 | 2.19 | 0.89 | 0.20 | 0.68 | 0.76 | 1180.60 | 17.40  | 1177.30 | 14.68 | 1178.51 | 12.42  | 99.90  |
| 033-ZR27        | 0.00  | 0.05 | 686217 | 0.08 | 0.48 | 2.24 | 1.01 | 0.20 | 0.80 | 0.80 | 1269.53 | 18.76  | 1154.39 | 16.99 | 1195.17 | 14.12  | 96.59  |
| 035-ZR29        | 0.00  | 0.24 | 730690 | 0.13 | 0.45 | 7.18 | 0.82 | 0.40 | 0.58 | 0.70 | 2101.02 | 15.89  | 2167.09 | 21.20 | 2133.42 | 14.59  | 101.58 |
| 036-ZR30        | 0.47  | 0.39 | 3225   | 0.13 | 0.59 | 6.68 | 1.02 | 0.37 | 0.75 | 0.73 | 2125.12 | 20.76  | 2015.58 | 25.84 | 2070.32 | 18.02  | 97.36  |
| 004-ZR2         | 0.02  | 1.36 | 101802 | 0.06 | 0.96 | 0.71 | 2.91 | 0.08 | 2.72 | 0.94 | 673.69  | 40.66  | 517.42  | 27.05 | 547.33  | 24.48  | 94.54  |
| 028-ZR22        | 0.04  | 1.85 | 35695  | 0.05 | 3.53 | 0.65 | 3.68 | 0.09 | 0.99 | 0.27 | 287.70  | 157.31 | 560.95  | 10.67 | 510.04  | 29.31  | 109.98 |
| 032-ZR26        | 0.02  | 0.66 | 86699  | 0.05 | 4.05 | 0.59 | 4.17 | 0.09 | 0.91 | 0.22 | 196.29  | 183.07 | 532.35  | 9.30  | 473.33  | 31.31  | 112.47 |
| 034-ZR28        | 0.02  | 2.08 | 81747  | 0.05 | 2.19 | 0.68 | 2.33 | 0.09 | 0.70 | 0.30 | 378.19  | 97.12  | 559.19  | 7.48  | 524.89  | 19.01  | 106.53 |
| 008-ZR36        | 0.03  | 2.09 | 46722  | 0.07 | 2.15 | 0.86 | 2.77 | 0.08 | 1.71 | 0.62 | 1049.27 | 85.55  | 522.50  | 17.13 | 632.76  | 25.94  | 82.57  |
| 012-ZR40        | 0.73  | 2.77 | 2141   | 0.07 | 2.27 | 0.83 | 2.72 | 0.09 | 1.45 | 0.53 | 887.54  | 92.39  | 542.61  | 15.10 | 614.17  | 24.91  | 88.35  |
| 015-ZR41        | 0.80  | 2.88 | 1945   | 0.07 | 3.03 | 0.84 | 3.52 | 0.08 | 1.76 | 0.50 | 969.06  | 121.17 | 525.44  | 17.73 | 617.03  | 32.30  | 85.16  |
| 029-ZR23        | 0.33  | 1.51 | 4740   | 0.07 | 1.26 | 0.87 | 1.96 | 0.09 | 1.46 | 0.74 | 928.19  | 51.42  | 557.13  | 15.56 | 636.24  | 18.49  | 87.57  |
| 008-ZR6         | 0.00  | 0.20 | 585513 | 0.08 | 0.44 | 2.19 | 0.89 | 0.20 | 0.68 | 0.76 | 1180.60 | 17.40  | 1177.30 | 14.68 | 1178.51 | 12.42  | 99.90  |
| 003-ZR31        | 0.35  | 1.60 | 4429   | 0.07 | 5.81 | 0.80 | 5.89 | 0.09 | 0.91 | 0.15 | 827.12  | 233.59 | 539.21  | 9.37  | 597.90  | 52.59  | 90.18  |
| 004-ZR32        | 7.93  | 1.70 | 196    | 0.21 | 4.53 | 3.79 | 4.78 | 0.13 | 1.48 | 0.31 | 2881.96 | 143.36 | 802.88  | 22.37 | 1589.62 | 75.34  | 50.51  |
| 005-ZR3         | 5.20  | 0.44 | 300    | 0.10 | 4.51 | 1.24 | 4.89 | 0.09 | 1.84 | 0.38 | 1644.53 | 162.94 | 550.81  | 19.36 | 820.52  | 54.27  | 67.13  |
| 009-ZR7         | 12.43 | 2.26 | 125    | 0.19 | 1.26 | 3.11 | 1.66 | 0.12 | 1.01 | 0.61 | 2749.45 | 41.28  | 719.19  | 13.73 | 1434.15 | 25.35  | 50.15  |
| 010-ZR38        | 4.46  | 0.53 | 349    | 0.09 | 8.89 | 1.38 | 9.58 | 0.11 | 3.54 | 0.37 | 1428.31 | 321.72 | 677.22  | 45.48 | 879.02  | 109.66 | 77.04  |
| 010-ZR8         | 1.67  | 2.51 | 933    | 0.06 | 1.25 | 0.81 | 1.81 | 0.09 | 1.26 | 0.70 | 745.76  | 52.26  | 566.49  | 13.68 | 603.68  | 16.42  | 93.84  |
| 011-ZR39        | 12.85 | 1.90 | 121    | 0.25 | 6.32 | 3.79 | 7.11 | 0.11 | 3.25 | 0.46 | 3186.06 | 193.21 | 672.22  | 41.44 | 1591.04 | 111.23 | 42.25  |

|          |       |      |     |      |      |       |      |      |      |      |         |        |         |       |         |        |       |
|----------|-------|------|-----|------|------|-------|------|------|------|------|---------|--------|---------|-------|---------|--------|-------|
| 011-ZR9  | 6.61  | 0.29 | 236 | 0.11 | 1.98 | 1.48  | 2.28 | 0.10 | 1.06 | 0.46 | 1770.81 | 71.56  | 610.49  | 12.34 | 923.54  | 27.46  | 66.10 |
| 015-ZR11 | 6.15  | 2.07 | 252 | 0.45 | 4.52 | 10.11 | 5.42 | 0.16 | 2.97 | 0.55 | 4098.87 | 131.28 | 964.94  | 53.11 | 2445.05 | 97.85  | 39.46 |
| 016-ZR42 | 1.60  | 0.97 | 973 | 0.11 | 6.45 | 1.83  | 7.64 | 0.12 | 4.08 | 0.53 | 1808.52 | 225.80 | 729.91  | 56.13 | 1055.41 | 97.91  | 69.16 |
| 019-ZR15 | 3.01  | 2.25 | 518 | 0.08 | 2.61 | 1.04  | 2.71 | 0.09 | 0.64 | 0.24 | 1251.53 | 100.52 | 563.45  | 6.95  | 721.90  | 27.86  | 78.05 |
| 030-ZR24 | 23.23 | 2.42 | 67  | 0.48 | 6.68 | 12.87 | 7.33 | 0.19 | 3.00 | 0.41 | 4185.61 | 190.64 | 1142.19 | 62.69 | 2670.26 | 133.63 | 42.77 |

| SAMPLE   | AL01 (granodiorite facies) |          |                 |                 |           |                |           |                |                   |      |                 |       |                |       |                |       |        |
|----------|----------------------------|----------|-----------------|-----------------|-----------|----------------|-----------|----------------|-------------------|------|-----------------|-------|----------------|-------|----------------|-------|--------|
|          |                            |          |                 |                 |           |                |           |                |                   |      | Apparent ages   |       |                |       |                |       |        |
| GRAIN    | <i>f</i>                   |          |                 |                 | err       |                |           | err            |                   |      |                 |       |                |       |                |       | conc.  |
|          | 206<br>(%)                 | Th/<br>U | 206Pb/<br>204Pb | 207Pb/<br>206Pb | (%)1<br>σ | 207Pb/<br>235U | (%)1<br>σ | 206Pb/<br>238U | err<br>(%)<br>1 σ | Rho  | 207Pb/<br>206Pb | 2 σ   | 207Pb/<br>235U | 2 σ   | 206Pb/<br>238U | 2 σ   | (%)    |
| 031-ZR24 | 0.01                       | 0.83     | 148663          | 0.06            | 0.85      | 0.71           | 1.33      | 0.09           | 0.96              | 0.72 | 529.88          | 36.85 | 546.61         | 10.06 | 543.41         | 11.18 | 100.59 |
| 015-ZR11 | 0.12                       | 1.06     | 13495           | 0.06            | 0.94      | 0.74           | 1.39      | 0.09           | 0.95              | 0.69 | 557.43          | 40.65 | 565.36         | 10.31 | 563.82         | 11.97 | 100.27 |
| 024-ZR20 | 0.01                       | 2.26     | 172151          | 0.06            | 0.41      | 0.71           | 0.85      | 0.09           | 0.64              | 0.76 | 535.64          | 18.01 | 548.12         | 6.75  | 545.74         | 7.15  | 100.44 |
| 023-ZR19 | 0.02                       | 2.63     | 75083           | 0.06            | 0.51      | 0.72           | 0.84      | 0.09           | 0.56              | 0.66 | 549.25          | 22.13 | 551.29         | 5.87  | 550.92         | 7.13  | 100.07 |
| 021-ZR17 | 0.03                       | 0.54     | 49858           | 0.06            | 0.57      | 0.73           | 0.93      | 0.09           | 0.64              | 0.68 | 557.14          | 24.90 | 555.53         | 6.79  | 555.88         | 7.98  | 99.94  |
| 056-ZR45 | 0.00                       | 1.10     | 331040          | 0.06            | 0.28      | 0.74           | 0.78      | 0.09           | 0.63              | 0.80 | 562.04          | 12.00 | 560.73         | 6.73  | 561.02         | 6.70  | 99.95  |
| 047-ZR38 | 0.00                       | 0.69     | 331751          | 0.06            | 0.42      | 0.73           | 0.77      | 0.09           | 0.53              | 0.69 | 542.75          | 18.19 | 560.10         | 5.64  | 556.72         | 6.56  | 100.61 |

|           |             |             |               |             |             |             |             |             |             |             |               |              |               |             |               |             |               |
|-----------|-------------|-------------|---------------|-------------|-------------|-------------|-------------|-------------|-------------|-------------|---------------|--------------|---------------|-------------|---------------|-------------|---------------|
| 053-ZR42  | 0.01        | 2.58        | 277694        | 0.06        | 0.61        | 0.73        | 0.88        | 0.09        | 0.52        | 0.59        | 536.89        | 26.45        | 562.18        | 5.57        | 557.22        | 7.53        | 100.89        |
| 054-ZR43  | 0.01        | 0.61        | 147350        | 0.06        | 0.40        | 0.71        | 0.85        | 0.09        | 0.66        | 0.77        | 521.48        | 17.30        | 550.24        | 6.97        | 544.71        | 7.19        | 101.01        |
| 008-ZR6   | 0.25        | 2.25        | 6357          | 0.06        | 1.20        | 0.72        | 1.41        | 0.09        | 0.64        | 0.45        | 549.80        | 51.86        | 548.41        | 6.72        | 548.71        | 11.89       | 99.95         |
| 058-ZR47  | 0.02        | 1.27        | 87875         | 0.07        | 0.30        | 1.17        | 0.67        | 0.13        | 0.47        | 0.70        | 776.42        | 12.69        | 792.27        | 7.04        | 788.17        | 7.35        | 100.52        |
| 010-ZR8   | 0.01        | 1.09        | 199701        | 0.06        | 0.40        | 0.72        | 1.05        | 0.09        | 0.90        | 0.86        | 533.71        | 17.45        | 555.89        | 9.59        | 551.59        | 8.94        | 100.78        |
| 055-ZR44  | <b>0.00</b> | <b>0.23</b> | <b>518606</b> | <b>0.06</b> | <b>0.27</b> | <b>0.71</b> | <b>0.71</b> | <b>0.09</b> | <b>0.54</b> | <b>0.76</b> | <b>531.90</b> | <b>11.92</b> | <b>548.02</b> | <b>5.63</b> | <b>544.94</b> | <b>5.95</b> | <b>100.57</b> |
| 034-ZR27  | 0.00        | 0.23        | 527233        | 0.06        | 0.28        | 0.75        | 0.67        | 0.09        | 0.47        | 0.71        | 534.71        | 12.45        | 573.27        | 5.21        | 565.60        | 5.77        | 101.36        |
| 040-ZR31  | 0.01        | 0.48        | 151840        | 0.06        | 0.84        | 0.75        | 1.11        | 0.09        | 0.63        | 0.56        | 540.09        | 36.58        | 571.99        | 6.89        | 565.65        | 9.64        | 101.12        |
| 059-ZR48  | 0.01        | 2.37        | 207549        | 0.06        | 0.49        | 0.69        | 1.03        | 0.09        | 0.83        | 0.80        | 539.50        | 21.48        | 534.21        | 8.48        | 535.25        | 8.57        | 99.81         |
| 061-ZR50  | 0.01        | 0.63        | 123313        | 0.06        | 0.50        | 0.83        | 0.86        | 0.10        | 0.59        | 0.69        | 605.00        | 21.52        | 613.70        | 6.91        | 611.88        | 7.86        | 100.30        |
| 036-ZR29  | 0.01        | 0.26        | 166007        | 0.06        | 0.69        | 0.774       | 1.33        | 0.10        | 1.07        | 0.81        | 530.75        | 30.02        | 594.90        | 12.17       | 581.79        | 11.71       | 102.25        |
| 003-ZR1   | 0.01        | 1.49        | 225844        | 0.06        | 0.77        | 0.75        | 1.19        | 0.09        | 0.83        | 0.70        | 524.82        | 33.46        | 580.67        | 9.19        | 569.47        | 10.33       | 101.97        |
| 011-ZR9   | 0.07        | 0.14        | 21283         | 0.13        | 0.27        | 7.06        | 1.09        | 0.39        | 0.99        | 0.91        | 2103.18       | 9.59         | 2135.07       | 35.84       | 2118.93       | 19.29       | 100.76        |
| 022-ZR18  | 0.13        | 2.57        | 12257         | 0.06        | 0.64        | 0.76        | 0.91        | 0.09        | 0.53        | 0.59        | 607.26        | 27.36        | 566.52        | 5.76        | 574.75        | 7.95        | 98.57         |
| 060-ZR49  | 0.00        | 0.77        | 475923        | 0.06        | 0.42        | 0.73        | 0.74        | 0.09        | 0.49        | 0.66        | 526.47        | 18.48        | 561.14        | 5.24        | 554.36        | 6.35        | 101.22        |
| 009-ZR7   | 0.39        | 2.25        | 3967          | 0.06        | 0.83        | 0.761       | 1.05        | 0.09        | 0.53        | 0.50        | 677.82        | 35.28        | 548.77        | 5.59        | 574.57        | 9.22        | 95.51         |
| 017-ZR13  | 0.65        | 1.01        | 2408          | 0.06        | 1.12        | 0.823       | 1.58        | 0.09        | 1.05        | 0.66        | 711.81        | 47.45        | 582.52        | 11.70       | 609.69        | 14.46       | 95.54         |
| 027-ZR21B | 0.46        | 1.82        | 3415          | 0.06        | 1.66        | 0.790       | 1.81        | 0.09        | 0.62        | 0.34        | 697.34        | 69.75        | 564.16        | 6.68        | 591.43        | 16.12       | 95.39         |
| 028-ZR21N | 1.13        | 2.06        | 1374          | 0.07        | 2.85        | 0.805       | 3.07        | 0.08        | 1.06        | 0.34        | 932.45        | 114.99       | 515.69        | 10.48       | 599.92        | 27.59       | 85.96         |
| 032-ZR25  | 0.04        | 0.38        | 40736         | 0.07        | 0.85        | 0.863       | 1.26        | 0.09        | 0.85        | 0.67        | 928.74        | 34.76        | 552.06        | 8.94        | 631.87        | 11.78       | 87.37         |
| 035-ZR28  | 2.31        | 0.30        | 676           | 0.07        | 2.43        | 0.870       | 2.97        | 0.09        | 1.67        | 0.56        | 918.81        | 98.33        | 558.77        | 17.81       | 635.53        | 27.85       | 87.92         |
| 039-ZR30  | 0.39        | 1.36        | 4007          | 0.06        | 0.88        | 0.752       | 1.37        | 0.09        | 0.99        | 0.72        | 646.49        | 37.53        | 550.03        | 10.43       | 569.22        | 11.94       | 96.63         |

|          |      |      |        |      |        |       |        |      |      |      |          |          |         |        |         |        |        |
|----------|------|------|--------|------|--------|-------|--------|------|------|------|----------|----------|---------|--------|---------|--------|--------|
| 041-ZR32 | 0.74 | 2.22 | 2103   | 0.08 | 2.00   | 0.968 | 2.09   | 0.09 | 0.50 | 0.24 | 1074.79  | 79.20    | 575.15  | 5.45   | 687.50  | 20.78  | 83.66  |
| 042-ZR33 | 0.20 | 1.94 | 7858   | 0.06 | 0.88   | 0.761 | 1.28   | 0.09 | 0.85 | 0.67 | 696.23   | 37.22    | 544.09  | 8.87   | 574.43  | 11.18  | 94.72  |
| 043-ZR34 | 0.02 | 1.75 | 78195  | 0.05 | 1.63   | 0.664 | 1.78   | 0.09 | 0.59 | 0.33 | 359.12   | 72.96    | 553.63  | 6.26   | 517.19  | 14.35  | 107.05 |
| 044-ZR35 | 1.01 | 1.25 | 1543   | 0.07 | 1.38   | 0.861 | 1.62   | 0.09 | 0.76 | 0.47 | 807.50   | 57.37    | 582.45  | 8.48   | 630.69  | 15.18  | 92.35  |
| 046-ZR37 | 0.01 | 2.67 | 166762 | 0.06 | 2.36   | 0.698 | 2.47   | 0.09 | 0.65 | 0.26 | 414.36   | 103.67   | 566.84  | 7.02   | 537.43  | 20.53  | 105.47 |
| 016-ZR12 | 0.00 | 2.24 | 438962 | 0.06 | 1.76   | 0.734 | 1.93   | 0.09 | 0.69 | 0.36 | 512.13   | 76.64    | 570.14  | 7.49   | 558.69  | 16.51  | 102.05 |
| 005-ZR3  | 0.92 | 1.56 | 1696   | 0.07 | 4.20   | 0.893 | 4.25   | 0.09 | 0.55 | 0.13 | 970.27   | 166.65   | 559.57  | 5.85   | 648.20  | 40.30  | 86.33  |
| 020-ZR16 | 0.02 | 2.09 | 100448 | 0.05 | 9.04   | 0.646 | 9.09   | 0.09 | 0.86 | 0.09 | 265.17   | 390.28   | 560.90  | 9.18   | 506.08  | 71.16  | 110.83 |
| 029-ZR22 | 0.01 | 2.35 | 143179 | 0.04 | 34.77  | 0.425 | 34.83  | 0.09 | 1.93 | 0.06 | -679.04  | 1524.57  | 539.12  | 20.00  | 359.97  | 200.84 | 149.77 |
| 030-ZR23 | 0.00 | 2.99 | 438419 | 0.06 | 1.63   | 0.730 | 1.75   | 0.09 | 0.50 | 0.29 | 495.22   | 71.09    | 571.65  | 5.51   | 556.58  | 14.91  | 102.71 |
| 033-ZR26 | 1.67 | 1.82 | 935    | 0.07 | 4.57   | 0.854 | 4.79   | 0.09 | 1.40 | 0.29 | 907.83   | 182.76   | 551.70  | 14.76  | 626.77  | 44.33  | 88.02  |
| 045-ZR36 | 0.01 | 2.08 | 274189 | 0.04 | 15.41  | 0.565 | 15.48  | 0.09 | 1.42 | 0.09 | -67.68   | 677.99   | 564.49  | 15.39  | 454.82  | 110.47 | 124.11 |
| 048-ZR39 | 0.01 | 2.73 | 161751 | 0.04 | 15.89  | 0.543 | 15.91  | 0.09 | 0.65 | 0.04 | -211.15  | 715.38   | 574.32  | 7.18   | 440.37  | 110.62 | 130.42 |
| 051-ZR40 | 0.14 | 2.55 | 10833  | 0.09 | 5.44   | 1.194 | 5.53   | 0.10 | 0.95 | 0.17 | 1383.11  | 202.05   | 605.02  | 10.97  | 797.99  | 60.26  | 75.82  |
| 052-ZR41 | 0.00 | 2.71 | 324362 | 0.01 | 134.93 | 0.116 | 134.97 | 0.08 | 2.95 | 0.02 | -8349.10 | 12717.82 | 521.12  | 29.52  | 111.37  | 266.46 | 467.91 |
| 057-ZR46 | 1.28 | 1.12 | 1217   | 0.05 | 4.92   | 0.615 | 5.23   | 0.08 | 1.72 | 0.33 | 346.79   | 215.36   | 516.76  | 17.05  | 486.60  | 40.03  | 106.20 |
| 007-ZR5  | 4.39 | 0.36 | 355    | 0.12 | 0.53   | 1.094 | 1.15   | 0.07 | 0.95 | 0.83 | 1904.42  | 18.96    | 424.46  | 7.81   | 750.48  | 12.16  | 56.56  |
| 018-ZR14 | 2.92 | 1.33 | 532    | 0.30 | 2.58   | 5.448 | 2.84   | 0.13 | 1.13 | 0.40 | 3483.00  | 78.74    | 791.33  | 16.87  | 1892.37 | 48.20  | 41.82  |
| 019-ZR15 | 5.11 | 1.84 | 305    | 0.11 | 7.43   | 1.619 | 7.45   | 0.11 | 0.42 | 0.06 | 1811.98  | 258.26   | 649.48  | 5.21   | 977.59  | 91.41  | 66.44  |
| 012-ZR10 | 0.02 | 0.20 | 61663  | 0.13 | 1.05   | 8.433 | 3.08   | 0.46 | 2.87 | 0.93 | 2143.79  | 36.36    | 2432.00 | 115.84 | 2278.72 | 55.14  | 106.73 |
| 004-ZR2  | 0.14 | 0.25 | 11491  | 0.05 | 3.17   | 0.658 | 3.26   | 0.09 | 0.67 | 0.20 | 351.54   | 140.27   | 550.40  | 7.05   | 513.37  | 26.13  | 107.21 |

|         |      |      |       |      |      |       |      |      |      |      |        |        |        |      |        |       |        |
|---------|------|------|-------|------|------|-------|------|------|------|------|--------|--------|--------|------|--------|-------|--------|
| 006-ZR4 | 0.02 | 2.33 | 79704 | 0.05 | 3.43 | 0.620 | 3.55 | 0.09 | 0.84 | 0.24 | 244.94 | 154.28 | 543.73 | 8.81 | 489.84 | 27.42 | 111.00 |
|---------|------|------|-------|------|------|-------|------|------|------|------|--------|--------|--------|------|--------|-------|--------|

| SAMPLE   | AL27 (monzogranite) |      |             |             |      |            |       |            |       |      |               |        |            |       |            |       |           |
|----------|---------------------|------|-------------|-------------|------|------------|-------|------------|-------|------|---------------|--------|------------|-------|------------|-------|-----------|
|          |                     |      |             |             |      |            |       |            |       |      | Apparent ages |        |            |       |            |       |           |
| GRAIN    | <i>f</i>            | err  |             |             |      | err        |       | err        |       | Rho  | 207Pb/206Pb   |        | 207Pb/235U |       | 206Pb/238U |       | conc. (%) |
|          | 206 (%)             | Th/U | 206Pb/204Pb | 207Pb/206Pb | (%)1 | 207Pb/235U | (%)1  | 206Pb/238U | (% 1) |      | 207Pb/206Pb   | 2 σ    | 207Pb/235U | 2 σ   | 206Pb/238U | 2 σ   |           |
| 047-ZR37 | 0.02                | 1.31 | 67904       | 0.06        | 0.64 | 0.65       | 1.09  | 0.08       | 0.80  | 0.73 | 524.40        | 28.15  | 507.72     | 7.76  | 510.79     | 8.72  | 99.40     |
| 024-ZR19 | 0.02                | 0.51 | 103381      | 0.06        | 0.52 | 0.67       | 1.09  | 0.08       | 0.88  | 0.81 | 523.43        | 22.71  | 519.66     | 8.81  | 520.39     | 8.85  | 99.86     |
| 048-ZR38 | 0.03                | 0.53 | 58649       | 0.06        | 1.06 | 0.67       | 1.55  | 0.08       | 1.07  | 0.69 | 488.32        | 46.45  | 525.85     | 10.76 | 518.91     | 12.54 | 101.34    |
| 032-ZR24 | 0.03                | 1.49 | 49986       | 0.06        | 1.09 | 0.64       | 1.50  | 0.08       | 0.96  | 0.64 | 499.47        | 47.84  | 505.91     | 9.30  | 504.77     | 11.90 | 100.22    |
| 007-ZR5  | 0.06                | 0.64 | 24180       | 0.06        | 1.92 | 0.67       | 2.13  | 0.08       | 0.84  | 0.39 | 494.05        | 83.74  | 523.05     | 8.44  | 517.71     | 17.22 | 101.03    |
| 008-ZR6N | 0.01                | 0.83 | 117520      | 0.06        | 2.03 | 0.67       | 2.30  | 0.08       | 1.01  | 0.44 | 534.09        | 87.79  | 514.10     | 10.01 | 517.82     | 18.58 | 99.28     |
| 020-ZR15 | 0.03                | 0.59 | 52362       | 0.06        | 0.43 | 0.69       | 1.08  | 0.09       | 0.92  | 0.85 | 545.12        | 18.73  | 529.63     | 9.38  | 532.59     | 8.96  | 99.44     |
| 044-ZR34 | 0.05                | 0.87 | 33468       | 0.06        | 0.87 | 0.71       | 1.40  | 0.09       | 1.04  | 0.74 | 545.86        | 37.78  | 544.71     | 10.84 | 544.96     | 11.81 | 99.95     |
| 045-ZR35 | 0.03                | 1.09 | 55020       | 0.06        | 0.81 | 0.66       | 1.36  | 0.08       | 1.03  | 0.76 | 579.88        | 34.96  | 502.57     | 10.00 | 516.77     | 11.03 | 97.25     |
| 043-ZR33 | 0.36                | 0.91 | 4281        | 0.06        | 1.38 | 0.73       | 1.60  | 0.09       | 0.71  | 0.45 | 502.31        | 60.18  | 566.63     | 7.72  | 554.01     | 13.59 | 102.28    |
| 035-ZR27 | 0.02                | 1.20 | 67684       | 0.06        | 0.64 | 0.71       | 1.07  | 0.09       | 0.78  | 0.73 | 593.62        | 27.42  | 534.17     | 7.99  | 545.63     | 9.03  | 97.90     |
| 046-ZR36 | 0.02                | 0.88 | 87706       | 0.06        | 1.75 | 0.61       | 1.94  | 0.08       | 0.76  | 0.39 | 448.73        | 76.79  | 494.24     | 7.27  | 486.27     | 14.97 | 101.64    |
| 018-ZR13 | 0.18                | 0.77 | 8558        | 0.06        | 5.94 | 0.69       | 6.03  | 0.09       | 0.98  | 0.16 | 526.38        | 250.13 | 535.60     | 10.07 | 533.88     | 49.44 | 100.32    |
| 003-ZR1  | 0.61                | 0.89 | 2566        | 0.10        | 1.38 | 0.17       | 12.59 | 0.01       | 12.51 | 0.99 | 1707.14       | 50.20  | 75.62      | 18.79 | 159.56     | 36.83 | 47.39     |

|           |       |      |       |      |       |      |       |      |      |      |         |         |         |       |         |        |        |
|-----------|-------|------|-------|------|-------|------|-------|------|------|------|---------|---------|---------|-------|---------|--------|--------|
| 004-ZR2   | 0.36  | 1.48 | 4314  | 0.08 | 6.11  | 1.01 | 6.28  | 0.09 | 1.44 | 0.23 | 1237.01 | 230.51  | 554.07  | 15.29 | 709.09  | 63.15  | 78.14  |
| 009-ZR6B  | 0.04  | 0.66 | 35867 | 0.05 | 5.26  | 0.55 | 5.47  | 0.08 | 1.44 | 0.26 | 209.19  | 235.35  | 491.20  | 13.63 | 444.49  | 39.01  | 110.51 |
| 011-ZR8   | 0.54  | 0.76 | 2912  | 0.06 | 4.35  | 0.72 | 4.47  | 0.08 | 0.96 | 0.22 | 669.36  | 180.77  | 519.01  | 9.57  | 547.82  | 37.47  | 94.74  |
| 018-ZR13  | 0.18  | 0.77 | 8558  | 0.06 | 5.94  | 0.69 | 6.03  | 0.09 | 0.98 | 0.16 | 526.38  | 250.13  | 535.60  | 10.07 | 533.88  | 49.44  | 100.32 |
| 023-ZR18  | 0.05  | 0.46 | 30499 | 0.04 | 24.24 | 0.46 | 24.27 | 0.09 | 1.10 | 0.05 | -591.82 | 1112.55 | 562.39  | 11.80 | 383.60  | 149.43 | 146.61 |
| 028-ZR21  | 0.23  | 1.30 | 6634  | 0.07 | 4.75  | 0.78 | 4.82  | 0.08 | 0.74 | 0.15 | 920.23  | 189.49  | 500.19  | 7.10  | 583.03  | 42.34  | 85.79  |
| 030-ZR23N | 0.08  | 1.42 | 19339 | 0.06 | 6.62  | 0.62 | 6.69  | 0.07 | 0.94 | 0.14 | 671.86  | 271.14  | 452.90  | 8.22  | 490.84  | 51.45  | 92.27  |
| 031-ZR23B | 0.02  | 0.71 | 80498 | 0.05 | 8.99  | 0.49 | 9.07  | 0.08 | 1.18 | 0.13 | -18.11  | 408.28  | 480.94  | 10.92 | 403.64  | 59.53  | 119.15 |
| 015-ZR10  | 3.54  | 0.83 | 440   | 0.22 | 6.75  | 1.61 | 6.94  | 0.05 | 1.59 | 0.23 | 3013.41 | 208.72  | 326.98  | 10.13 | 974.44  | 85.15  | 33.56  |
| 016-ZR11  | 2.47  | 0.72 | 631   | 0.15 | 4.68  | 2.08 | 4.98  | 0.10 | 1.66 | 0.33 | 2363.72 | 155.59  | 612.99  | 19.43 | 1143.86 | 67.26  | 53.59  |
| 019-ZR14  | 18.27 | 0.34 | 85    | 0.24 | 4.08  | 1.14 | 4.46  | 0.03 | 1.77 | 0.40 | 3113.18 | 126.89  | 218.67  | 7.59  | 771.07  | 47.59  | 28.36  |
| 034-ZR26  | 1.51  | 0.89 | 1035  | 0.03 | 32.17 | 0.38 | 32.21 | 0.08 | 1.48 | 0.05 | -884.29 | 1488.67 | 512.98  | 14.58 | 323.89  | 171.22 | 158.38 |
| 041-ZR31  | 5.63  | 0.83 | 275   | 0.34 | 7.64  | 8.96 | 7.91  | 0.19 | 2.01 | 0.25 | 3679.77 | 224.00  | 1116.18 | 41.04 | 2334.14 | 139.62 | 47.82  |
| 042-ZR32  | 3.49  | 0.50 | 447   | 0.04 | 4.74  | 0.49 | 4.79  | 0.08 | 0.59 | 0.12 | -206.96 | 229.97  | 524.27  | 5.91  | 407.99  | 31.96  | 128.50 |
| 005-ZR3   | 0.60  | 0.78 | 2565  | 0.11 | 1.35  | 2.68 | 1.83  | 0.18 | 1.17 | 0.64 | 1799.77 | 48.82   | 1048.43 | 22.62 | 1322.77 | 26.83  | 79.26  |
| 036-ZR28  | 0.33  | 0.55 | 4718  | 0.07 | 1.66  | 0.70 | 2.08  | 0.08 | 1.19 | 0.57 | 813.56  | 68.71   | 479.17  | 11.00 | 541.57  | 17.37  | 88.48  |
| 040-ZR30  | 0.49  | 1.04 | 3169  | 0.07 | 1.43  | 0.82 | 1.67  | 0.08 | 0.78 | 0.47 | 949.37  | 57.99   | 523.00  | 7.88  | 610.36  | 15.29  | 85.69  |
| 039-ZR29  | 0.03  | 0.98 | 57237 | 0.06 | 1.21  | 0.63 | 1.84  | 0.08 | 1.34 | 0.73 | 641.89  | 51.71   | 468.50  | 12.06 | 499.11  | 14.47  | 93.87  |
| 006-ZR4   | 0.02  | 1.53 | 66887 | 0.06 | 1.00  | 0.63 | 1.52  | 0.08 | 1.08 | 0.71 | 415.76  | 44.50   | 515.11  | 10.65 | 497.27  | 11.89  | 103.59 |
| 010-ZR7   | 0.02  | 1.44 | 81312 | 0.05 | 2.82  | 0.66 | 3.00  | 0.09 | 0.97 | 0.32 | 373.67  | 124.42  | 543.56  | 10.12 | 512.07  | 24.01  | 106.15 |
| 012-ZR9   | 0.07  | 0.88 | 23072 | 0.06 | 2.25  | 0.67 | 2.54  | 0.08 | 1.11 | 0.44 | 624.27  | 95.73   | 498.96  | 10.63 | 522.06  | 20.62  | 95.58  |
| 017-ZR12  | 0.25  | 0.82 | 6260  | 0.07 | 1.82  | 0.80 | 2.18  | 0.09 | 1.15 | 0.53 | 818.21  | 75.07   | 537.98  | 11.87 | 594.89  | 19.57  | 90.43  |
| 021-ZR16  | 0.24  | 1.31 | 6587  | 0.07 | 1.18  | 0.81 | 1.43  | 0.09 | 0.72 | 0.51 | 813.74  | 48.94   | 549.08  | 7.62  | 603.57  | 13.00  | 90.97  |
| 022-ZR17  | 0.09  | 0.70 | 17437 | 0.06 | 0.76  | 0.66 | 1.25  | 0.08 | 0.93 | 0.74 | 590.31  | 32.62   | 498.33  | 8.88  | 515.15  | 10.09  | 96.74  |



|          |      |      |        |      |      |      |      |      |      |      |        |       |        |       |        |       |        |
|----------|------|------|--------|------|------|------|------|------|------|------|--------|-------|--------|-------|--------|-------|--------|
| 027-ZR20 | 0.02 | 1.25 | 64281  | 0.06 | 0.83 | 0.69 | 1.26 | 0.08 | 0.87 | 0.69 | 621.88 | 35.72 | 515.63 | 8.66  | 535.68 | 10.49 | 96.26  |
| 029-ZR22 | 0.59 | 1.10 | 2636   | 0.07 | 1.83 | 0.74 | 2.03 | 0.08 | 0.78 | 0.38 | 859.72 | 75.20 | 494.34 | 7.40  | 564.82 | 17.48 | 87.52  |
| 033-ZR25 | 0.01 | 0.49 | 188757 | 0.06 | 2.26 | 0.68 | 2.95 | 0.09 | 1.85 | 0.63 | 420.92 | 99.36 | 555.05 | 19.68 | 529.54 | 24.16 | 104.82 |

#### 4.4.3.1. *The qz-monzodiorite/granodiorite suite*

##### **The qz-monzodiorite facies**

Sample AL08 zircon crystals are generally subhedral, translucent to brownish yellow, and range in size from 60 to 140  $\mu\text{m}$ . Most of the crystals display short bipyramidal prismatic habits and are less commonly elongated, showing length/width ratios around 2:1. The crystals are generally fractured, and inclusions are rare. Out of a total of 44 analyzed grains (Figure 4.9A), 18 grains yielded concordance between 95.12 and 100.93 % and a lower intercept age of  $560 \pm 34$  Ma ( $2\sigma$  error ellipses; Figure 4.9B). The lower intercept ages were obtained on zircon cores showing typical magmatic characteristics, such as regular concentric zonation and high Th/U ratios ranging from 1.1 to 2.7 (always more than 1). The older concordant grains show Th/U values between 0.3 and 0.8. Zircon crystal ZR12 ( $711 \pm 11$  Ma) is the largest crystal analyzed (130  $\mu\text{m}$ ) and displays a darker core.

The analyses of rims of core-free zircon grains displaying faint to moderate oscillatory zoning clustered around 560 Ma. A concordia age of  $557 \pm 5.7$  Ma (MSWD of 1.3), considered to be the quartz monzodiorite crystallization age, was calculated using four grains with concordance between 99.4 and 100.1% (Figure 4.9C). Analyses with concordance around 96-98 % and 101-102 % were not considered due to extremely high MSWD.

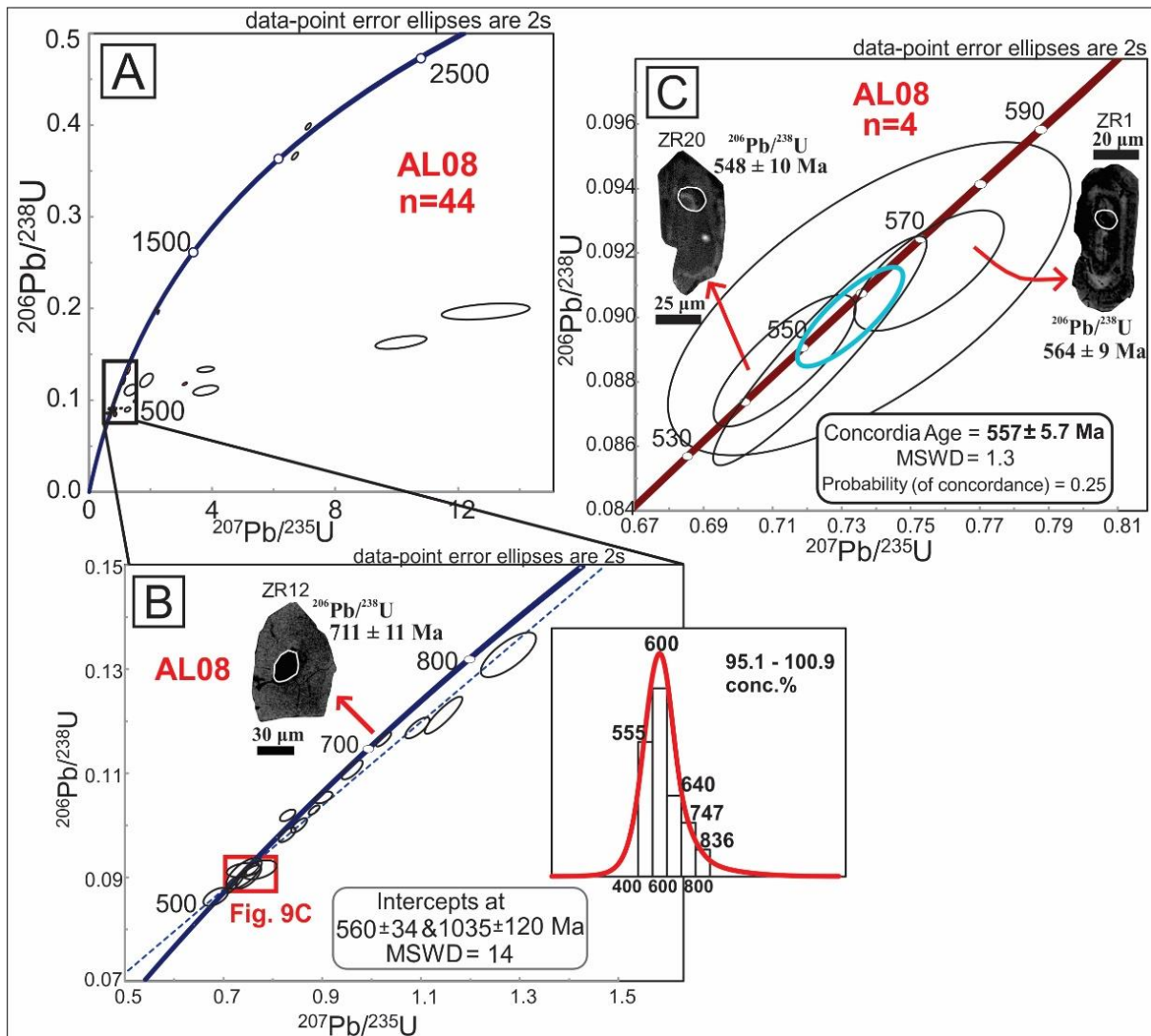


**Figure 4.9-** U-Pb geochronological diagrams for the qz-monzodiorite facies, sample AL08. The spots of 30  $\mu\text{m}$  are represented as white circles. (A) Distribution of all the 44 U–Pb data in the Wetherill Concordia Diagram; (B) U-Pb concordant isotope analyses of sample AL08 from the qz-monzodiorite facies with BSE images of zircon grain ZR12 showing upper intercept of 1035  $\pm$  120 Ma; (C) concordia diagram (557 $\pm$ 5.7 Ma) for the U-Pb analysis and CL image of representative zircon ZR20 and ZR1.

### The granodiorite facies

Sample AL01 zircon grains are colorless to dark- to light-yellow, and range in size from 50 to 130  $\mu\text{m}$ , with a few grains reaching up to 150  $\mu\text{m}$ . The most abundant are subhedral and show prismatic and sometimes rounded habits. The oscillatory zoning develops as alternating

CL intensities with variable banded shapes, mainly corresponding to the concordant analyses that clustered around 550 Ma.

Out of 51 analyzed zircon crystals (Figure 4.10A), 17 grains with the  $^{206}\text{Pb}/^{238}\text{U}$  age spectrum indicating concordance between 99.81 and 101.36% yielded an upper intercept of  $719\pm 80$  Ma and a lower intercept of  $594\pm 33$  Ma, with MSWD of 5.8 (Figure 4.10B). Some analyses with concordance of 98.6% and around 100.8-102.7% were discarded, as they did not yield acceptable MSWD. The oldest concordant age ( $792\pm 7$  Ma – ZR47) was obtained on a small (90  $\mu\text{m}$ ) zircon grain of low core-luminosity (Figure 4.10B).

Six different crystals showing 99.9-100.4 % concordance yielded a concordia age ( $2\sigma$  error ellipses) of  $554\pm 2.9$  Ma, with MSWD of 0.34 (Figure 4.10C), considered as the granodiorite crystallization age. This zircon population yielded high Th/U ratios of 0.5 to 2.6.

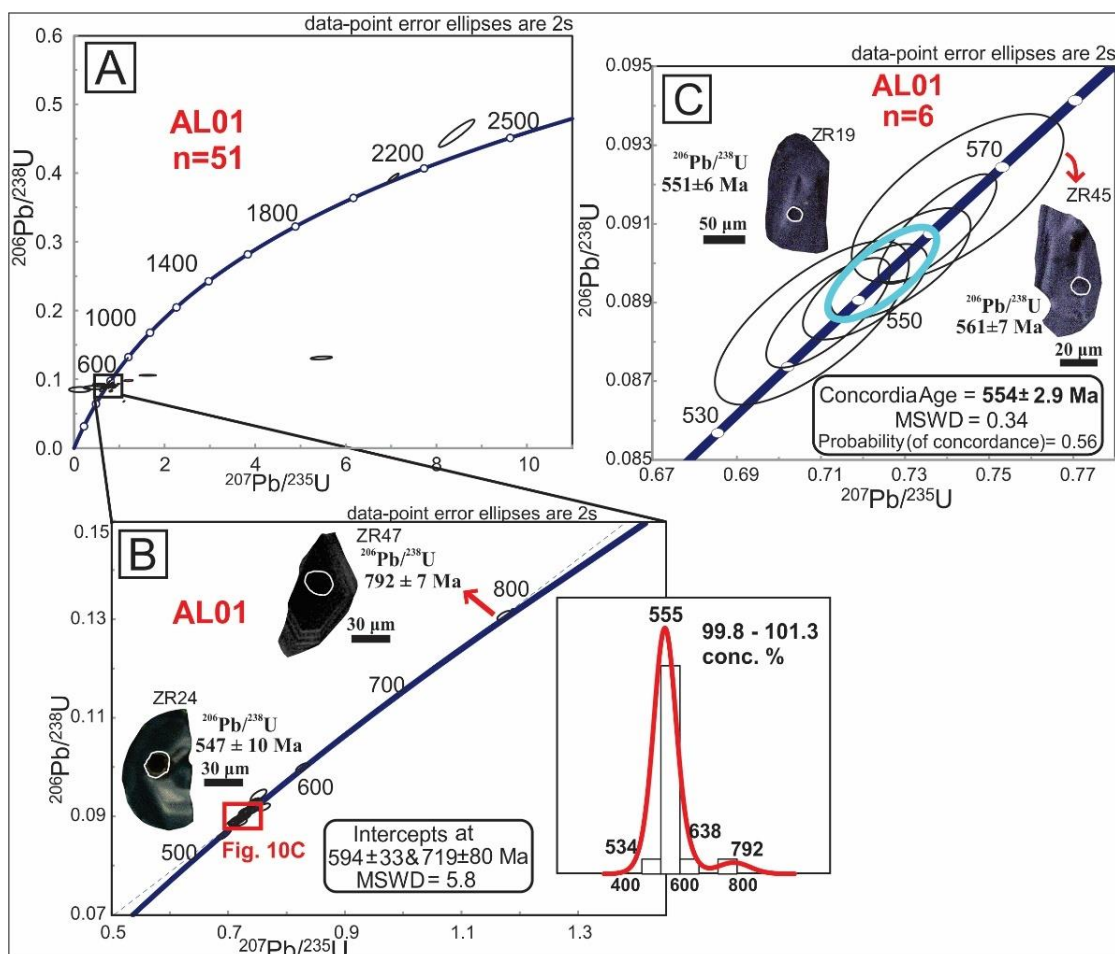


**Figure 4.10** – U-Pb geochronological diagrams for the granodiorite facies, sample AL01. The spots of 30  $\mu\text{m}$  are represented as white circles. (A) Distribution of all 51 U-Pb data in the Wetherill Concordia Diagram; (B) U-Pb isotope analysis of sample AL01 from the granodiorite facies with upper intercept age of  $719 \pm 80$  Ma; (C) concordia diagram ( $554 \pm 2.9$  Ma) for the U-Pb analysis and CL images of representative ZR19 and ZR45 zircon grains.

#### 4.4.3.2. *The monzogranite suite*

Sample AL27 zircon crystals range in size from 120 to 260  $\mu\text{m}$ , are semitransparent to light yellow, and are usually euhedral with prismatic habit and well-defined pyramidal terminations. The crystals are elongated, with length/width ratios of 3:1. The zircon population preserves regular parallel bands of alternating light CL patches, and many grains contain well outlined cores. Out of 41 analyzed crystals (Figure 4.11A), 13 yielded concordance between 99 and 101% and an upper intercept of  $527 \pm 86$  Ma, with MSWD of 2.8 (Figure 4.11B). Zircon grain ZR33 yielded the oldest concordant age of  $567 \pm 8$  Ma (concordance of 102.3%), and shows a darker, low-intensity core in the CL image (Figure 4.11B) with a Th/U ratio of 0.9.

Six zircon grains yielded concordance between 99.2 and 101.3% and a concordia age of  $515 \pm 3.6$  Ma (Figure 4.11C; MSWD = 0.0018), considered as the monzogranite crystallization age. High Th/U ratios predominate in these zircon grains, ranging from 0.5 to 1.4. Some analyses with concordance around 97 to 101% were discarded during concordia age calculations, because of unacceptable errors.

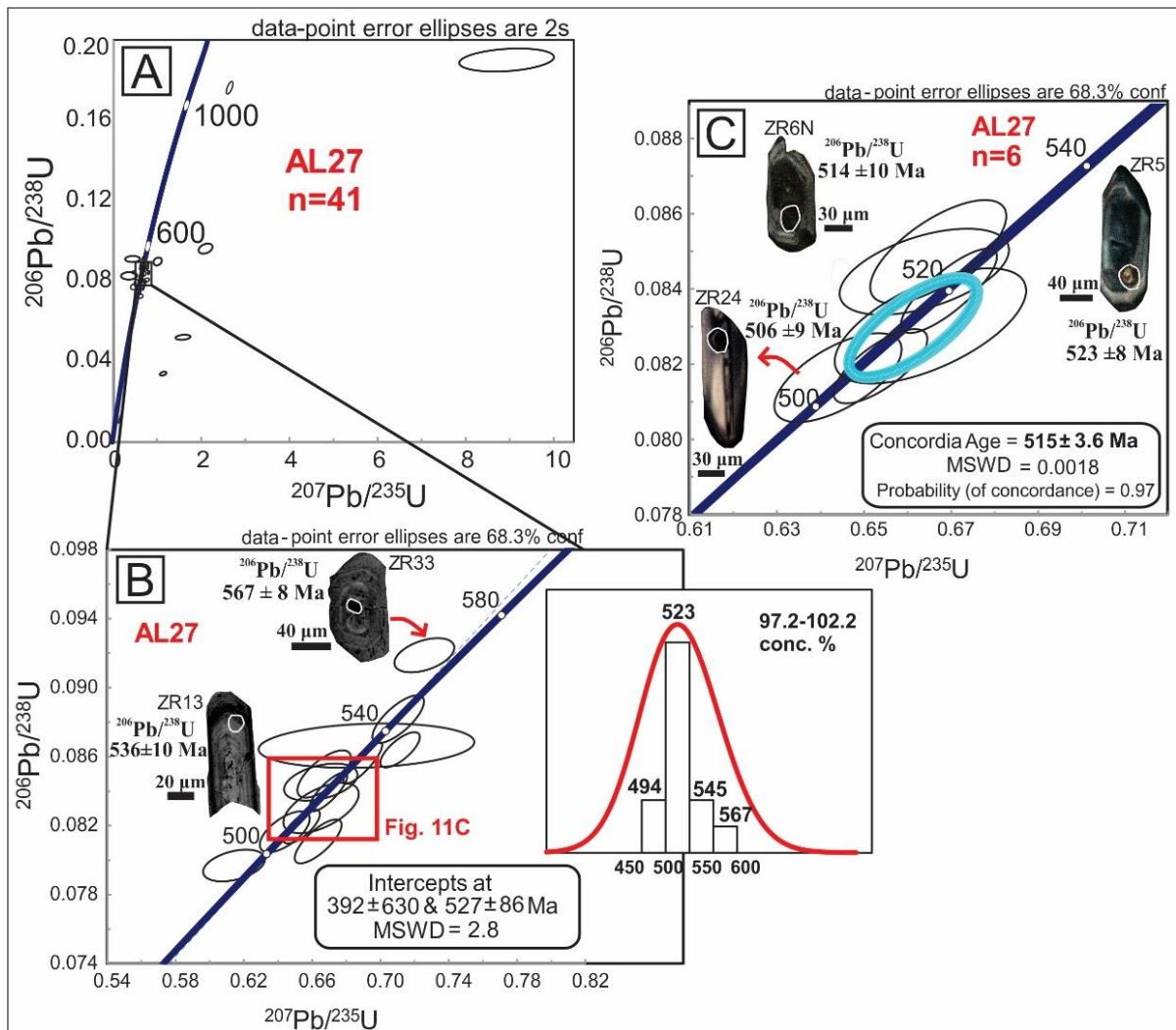


**Figure 4.11-** U-Pb geochronological diagrams for the monzogranite, sample AL27. The spots of 30  $\mu\text{m}$  are represented as white circles. (A) Distribution of all 47 U–Pb data in the Wetherill Concordia Diagram; (B) U-Pb concordant isotope analyses of monzogranite sample AL27; CL images of zircon grains showing upper intercept ages older than 527 ± 86 Ma; (C) concordia diagram (515 ± 3.6 Ma) for the U-Pb analyses and CL images of representative zircon grains ZR06N, ZR24 and ZR5.

#### 4.4.4. *Sm-Nd isotope data of whole-rock samples*

The Sm-Nd isotope analysis of the qz-monzodiorite sample AL08 yielded a negative  $\epsilon_{\text{Nd}}$  value of -6.65, when recalculated with the crystallization age of 557 Ma, and Mesoproterozoic  $T_{\text{DM}}$  model age of 1.53 Ga. Granodiorite sample AL01 produced a negative

$\epsilon_{Nd}$  (-6.62) and a  $T_{DM}$  model age of 1.47 Ga. Monzogranite sample AL27 yielded a negative  $\epsilon_{Nd}$  value of -6.32 and a Mesoproterozoic  $T_{DM}$  model age of 1.34 Ga (Table 4.4; Figure 4.12).

The  $T_{DM}$  model ages of the granitic province of the Paraguay Belt (Godoy *et al.*, 2007; 2010) vary from 1.97 to 1.07 Ga (Ferreira, 2009; Pinho, 2001), and the  $\epsilon_{Nd}(T)$  values are also negative (Figure 4.12).

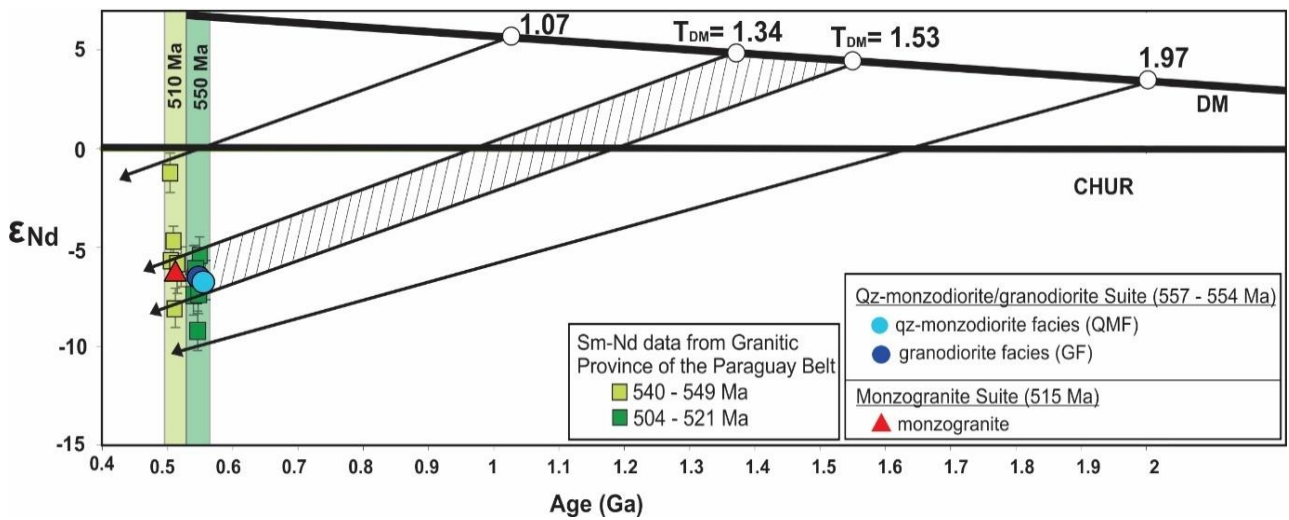


**Figure 4.12** – Age (Ga) vs.  $\epsilon_{Nd}$  diagram for samples from the studied high Ba-Sr intrusions. For comparison, values from the Neoproterozoic granitic province of the Paraguay Belt are also plotted. Data from Ferreira (2009), Godoy *et al.*, (2010) and Pinho (2001).

**Table 4.4** - Sm-Nd isotope results.

| Sample   | Sm (ppm) | Nd (ppm) | $^{147}\text{Sm}/^{144}\text{Nd}$ | $^{143}\text{Nd}/^{144}\text{Nd}$ | $\epsilon_{Nd}(T)$ min | SiO <sub>2</sub> | $\epsilon_{Nd}(T)$ máx | $T_{DM}$ (Ga) | U-Pb (Ma) |
|----------|----------|----------|-----------------------------------|-----------------------------------|------------------------|------------------|------------------------|---------------|-----------|
| MS AL27  | 9.464    | 63.040   | 0.0908                            | 0.511957+/-13                     | -13.28                 | 64%              | -6.32                  | 1.34          | 515       |
| GF AL01  | 19.934   | 117.543  | 0.1025                            | 0.511959+/-4                      | -13.25                 | 59%              | -6.62                  | 1.47          | 554       |
| QMF AL08 | 19.123   | 105.596  | 0.1095                            | 0.511979+/-9                      | -12.86                 | 56%              | -6.65                  | 1.53          | 558       |

## 4.5.DISCUSSION

### 4.5.1. *Interpretation of U-Pb data*

Crystallization ages obtained for the qz-monzodiorite/granodiorite suite are  $557\pm 5.7$  Ma (qz-monzodiorite facies) and  $554\pm 2.9$  Ma (granodiorite facies), and for the monzogranite suite,  $515\pm 3.6$  Ma. There is a distinct temporal gap of ca. 40 My between the two suites, which raises the doubt of a petrogenetic link between them.

For both suites, the pattern of concordant analytical ages is associated with clear oscillatory zoning in zircon grains, which may have developed due to the kinematics of large-scale magma mixing, which causes periods of Zr sub-saturation in the liquid (Corfu *et al.*, 2003).

Regarding the qz-monzodiorite/granodiorite suite, from the association of ages with zircon internal structures, we found out that older crystals that did not plot within the cluster of ~550 Ma ages (mostly defined by granodiorite sample AL01) seldom display luminescent cores and more likely represent inherited crystals. In turn, the zircon grains that yielded the oldest concordant ages of  $711\pm 11$  Ma (e.g., ZR12 – Figure 9B) and  $792\pm 7$  Ma (e.g., ZR47 – Figure 10B) can be taken as evidence of involvement of older units as zircon sources. The nearby Bom Jardim volcano-sedimentary sequence, which yields U-Pb ages of  $749\pm 6$  Ma (Guimarães *et al.*, 2012), is here pointed out as a possible source of these inherited crystals. Other possibility sources are the orthogneisses of the Arenópolis Magmatic Arc emplaced from ca. 899 to 636 Ma; Pimentel *et al.*, 1999), which was already accreted for a certain time when the qz-monzodiorite/granodiorite suite was emplaced.



We may also assume that the host Cuiabá Group could have participated in the incorporation of components inherited from the root of the continental crust during the final phase of magmatic evolution of the older studied suite, since the distribution of ages of sedimentary provenance determined by Leite *et al.* (in prep.) includes 68% of Cryogenian/Ediacaran zircon crystals for the Cuiabá Group in this portion of the Paraguay Belt. The monzogranite suite sample zircons crystals did not yield concordant ages older than 567 Ma (Figure 11B), indicating lesser inherited components, differently from those zircon grains observed in the qz-monzodiorite/granodiorite suite samples.

Although the geochemical data of the Paraguay Belt magmatic province (Manzano, 2009; Godoy *et al.*, 2010) and of the suites investigated here point to distinct petrological evolutions, the crystallization ages allow to make correlations regarding the post-collisional phase of the Brasiliano-Pan-African Orogeny in the Tocantins Province. The geochronological data obtained for the qz-monzodiorite/granodiorite suite are comparable with the less evolved intrusions dated between 540 and 549 Ma (Manzano, 2009). The age obtained for the monzogranite suite sample correlates well with a younger group of intrusions of the Paraguay Belt magmatic province, typically dated between 504 and 521 Ma (Manzano, 2009; Godoy *et al.*, 2010).

#### *4.5.1.1. Magma temperatures*

U and Th concentrations in magmatic zircon change with increasing temperature, increasing Th contents relative to U contents in the magma (Xiang *et al.*, 2011). The high Th/U ratios (up to 2.7) obtained for both suites suggest that liquid disequilibrium and temperatures were elevated during zircon crystallization (Kirkland *et al.*, 2015).

Zircon saturation thermometry ( $T_{Zr}$ ) can contribute with the estimating of magma temperatures, using the associations between zircon solubility, temperature and major element composition of the melt (Watson and Harrison, 1983). The calculated zircon saturation temperature (Watson and Harrison, 1983; Supplementary Table 4.3) from the qz-monzodiorite/granodiorite suite ranges from 729 °C to 790 °C, while the monzogranite suite rocks display zircon saturation temperature always higher than 800 °C (ranging from 806 to 870 °C).

According to Miller *et al.* (2003),  $T_{Zr}$  higher than 800 °C indicates that hot magma can dissolve zircon crystals into a hydrated melt, leading to Zr-rich (>200 ppm) and inherited zircon-poor granitic liquids. Thus, the high magma temperature can well explain why it was not possible to find inherited zircon grains in the investigated monzogranite sample (AL27). It suggests convective heat transfer from the mantle for the monzogranite suite generation, which triggered a temperature increase in the lithosphere.

#### 4.5.2. Type of Magmatism

The suites investigated in this study are represented by two distinct trends, according to the evolutionary magmatic series of Lameyre and Bowden (1982): the qz-monzodiorite/granodiorite suite follows the granodioritic calc-alkaline trend, and the monzogranite suite displays a shoshonitic sub-alkaline trend (Figure 3A). Whole-rock analyses indicate high K contents, magnesian and metaluminous to slightly peraluminous signatures (A/CNK index < 1.1), and LILE and LREE enrichment (between 100 and 1000x chondrite values). Regarding Sr and Ba content, the samples of both suites plot within the high Ba-Sr

discriminant field in the Sr-Rb-Ba ternary diagram of Tarney and Jones (1994; Figure 4.13A), similarly to the Scottish Caledonian high Ba-Sr granitoids (Tarney and Jones, 1994).

The high Ba-Sr content is suggestive of magma generation from partial melting of subducted oceanic crust in island arc setting, melting of lower crust triggered by underplated mafic magma, and mainly by partial melting of enriched lithospheric mantle followed by fractional crystallization and minor interaction with crustal material (Tarney and Jones, 1994; Fowler *et al.*, 2001; Atherton and Ghani, 2002; Ren *et al.*, 2018). Fowler *et al.* (2008) proposed that the high Ba-Sr signature of Northern Highlands granitoids occurred intimately related to partial melting of an early appinitic underplate with involvement of enriched mantle-derived magma and/or lower crustal material. Appinitic rocks preserve evidence of mantle processes that produce voluminous late- to post-collisional granitoid batholiths by fractionation mechanisms (Fowler and Henney, 1996; Murphy, 2013, 2019). Late Neoproterozoic and Early Cambrian high Ba-Sr granitoids associated with appinitic rocks are detailed in several studies of post-collisional settings along orogenic belts worldwide (see Table 4.5).

**Table 4.5** – Worldwide documented appinitic rocks associated to high Ba-Sr magmatism generated at the end of the Proterozoic and beginning of the Phanerozoic.

| Reference                 | Name of Magmatism/Region  | Age (Ma)/ Geochronologic method | Characteristics   |
|---------------------------|---|---------------------------------|---|
| Ghani and Atherton (2006) | Late Caledonian Donegal Granites and Appinites/Late Caledonian, Ireland | 407–402/U-Pb in zircon          | monzogranites and granodiorites and minor quartz monzodiorites. |

|                               |  |                                     |   |
|-------------------------------|--|-------------------------------------|---|
| Fowler <i>et al.</i> (2008)   | Appinite-granite suite/British Caledonian Province, Scotland | 425±4/Rb-Sr whole rock              | granite, granodiorite, diorite and ultramafic rock.   |
| Ye <i>et al.</i> (2008)       | High Ba-Sr appinite-granites/NW of Tibet Plateau             | 430 Ma/ SHRIMP U-Pb in zircon       | alkaline feldspar granites with coeval appinite enclaves.                                       |
| Zhang <i>et al.</i> (2014)    | Appinitic intrusions/Northern China craton                   | 320–317 Ma – LA – ICPMS zircon U-Pb | hornblende diorites, diorites and monzodiorites   |
| Lara <i>et al.</i> (2017)     | Uruguayan HiBaSr granitoids/Dom Feliciano Belt - Brazil      | 634–597 Ma/ LA-ICPMS zircon U-Pb    | quartz monzonite, granodiorite and monzogranite   |
| Ren <i>et al.</i> (2018)      | Intrusions in the North Qinling terrane/China                | 439-429/LA-ICPMS zircon U-Pb        | diorite and quartz diorite.   |
| Corrales <i>et al.</i> (2020) | Marceleza and Leopoldina stocks/Ribeira Belt - Brazil        | 650-600/ LA-ICPMS zircon U-Pb       | gabbros, dioritic gabbros, tonalites and granodiorites, besides rocks of the monzonitic series. |

---

Low Sr/Y ratios (Figure 4.13B) preclude any relation to adakite-like granitoids, as the rocks of this study display higher Y and Yb contents. In the Th/Yb vs. Nb/Yb diagram of Pearce and Peate (1995; Figure 4.13C), both suites plot within the continental arc field, which can have developed from the accretion of an oceanic arc to a continental margin (Condie and Kröner, 2013). Granitoids with a continental arc-like signature can also be generated when an accreted

ocean arc becomes thicker and starts to melt from its roots in response to delamination processes, leading to a delayed interaction of the subcontinental mantle wedge and deeper material. High Th/Yb values suggest involvement of crustal material at the metasomatized source (Figure 4.13D). The post-collisional nature of both suites is supported by the Rb vs. (Y + Nb) discriminant diagram of Pearce *et al.* (1984, 1996; Figure 4.13E) and the high (Zr + Nb + Ce + Y) contents of the analyzed monzogranite suite samples point to the within-plate character of this suite (Whalen *et al.*, 1987; Figure 4.13F).

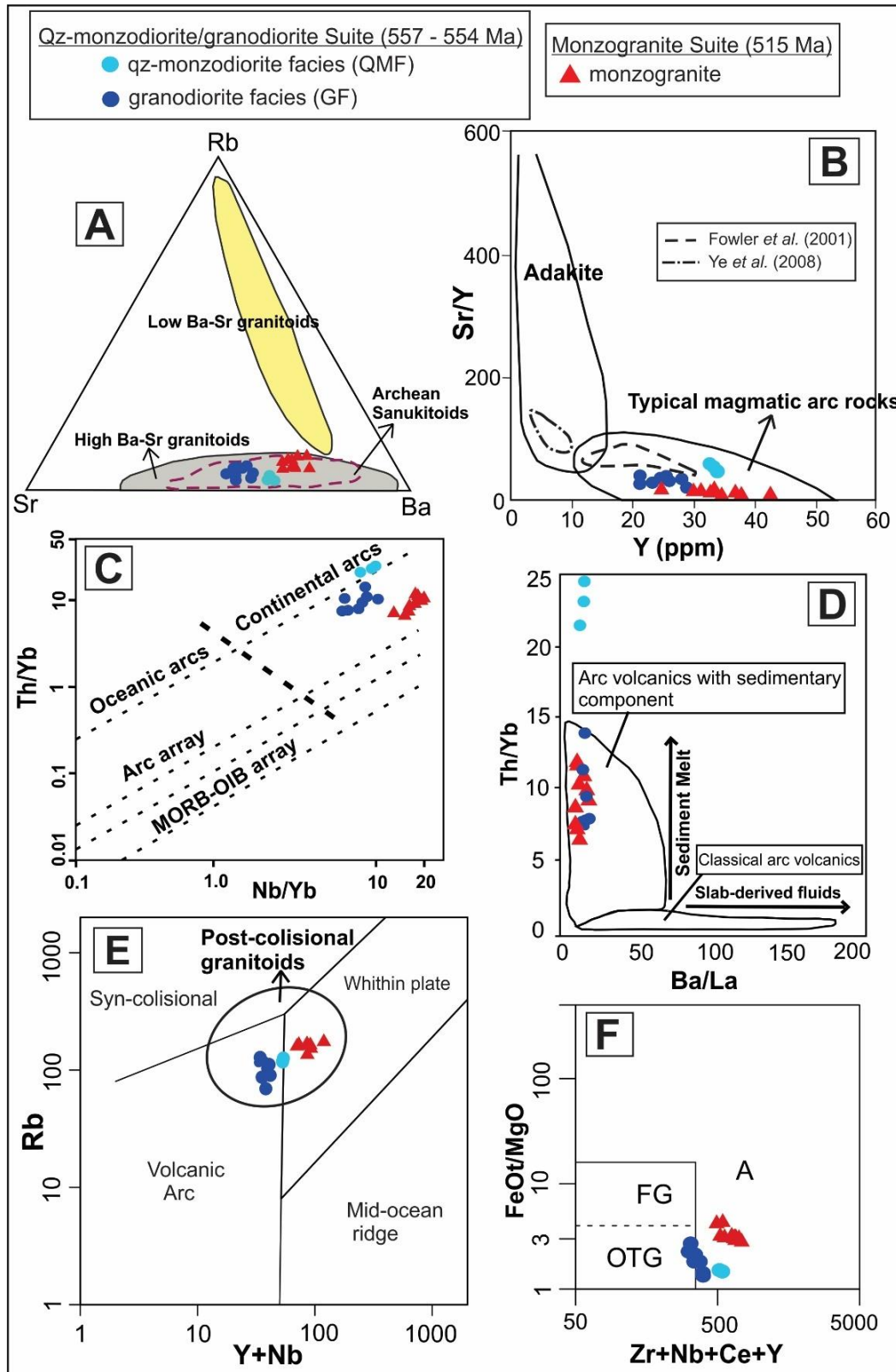


**Figure 4.13** - (A) Discrimination diagram for high Ba-Sr intrusions (Tamey and Jones, 1994); (B) Sr/Y versus Y proposed by Fowler *et al.* (2008); (C) Th/Yb vs. Nb/Yb diagram proposed by Pearce and Peate (1995), with the boundary between felsic igneous rocks from oceanic and continental arcs adapted from Condie and Kröner (2013);

(D) Ba/La vs. Th/Yb proposed by Woodhead *et al.* (2001); (E) Rb versus Ta+Yb of Pearce *et al.* (1984), modified by Pearce *et al.* (1996); (F) FeOt/MgO versus Zr + Nb + Ce + Y proposed by Whalen *et al.* (1987).

The negative  $\varepsilon_{\text{Nd}}(\text{T})$  values between -6.32 and -6.65 for the respective U-Pb crystallization ages indicate significant contribution of older crustal components in the magma genesis. The  $\varepsilon_{\text{Nd}}(\text{T})$  values suggest that both suites are unlikely to have solely resulted from mantle-derived melt or from crustal materials, supporting the idea of an enriched mantle source. The narrow range of  $T_{\text{DM}}$  from 1.34 to 1.53 Ga reflects reworking of Mesoproterozoic material that contributed significantly to the investigated rocks petrogenesis. The  $\varepsilon_{\text{Nd}}(\text{T})$  and the model ages patterns indicates that their protoliths could have been affected by an old metasomatic event during Mesoproterozoic times, or by young metasomatism controlled by older crustal materials.

#### 4.5.3. *Petrogenesis of the qz-monzodiorite/granodiorite suite*

The qz-monzodiorite/granodiorite suite includes a hypabyssal satellite stock (qz-monzodiorite facies) and a voluminous pluton (granodiorite facies).

The presence of dark microgranular enclaves hosted in granitic plutons commonly indicate interaction of a mantle-derived mafic magma with a felsic magma (Roberts and Clemens, 1993). Fowler *et al.* (2008) report this type of evidence of mixing and mingling in the Caledonian high Ba-Sr granites and argue that they can be an indicator for high Ba-Sr magmatism. Although such enclaves were not observed in the studied outcrops during field work, Coimbra (2015) described mafic enclaves and xenoliths in the investigated granodiorite facies. Further geochemical studies focusing on these enclaves may contribute to our hypothesis.

#### 4.5.3.1. *The qz-monzodiorite facies: evidence of appinitic affinity*

The qz-monzodiorite facies is characterized by ~56 wt.% SiO<sub>2</sub>, high mg# (~56), and relatively high Ni (~115 ppm), V (~163 ppm), and Cr (~225 ppm) contents, sufficiently high to point to a mantle-derived signature for their parental source. The higher amount of Ba+Sr (~5000 ppm), K<sub>2</sub>O (~3.7%) and Th (~53 ppm) and significantly negative anomalies of Nb and Ta relative to La of the qz-monzodiorite facies (Nb/La ~0.13; Figure 4.8) strongly reinforce the model of lithospheric mantle enrichment by interaction with dehydration-derived fluids from the subducted slab, allowing for large input of volatile content in the magmatic system. Such features, associated with the peripheric character and small volume of the facies, as well as the occurrence of hornblende phenocrysts, strongly direct us to the Caledonian appinites of Scotland, which are intimately related to coeval voluminous high Ba-Sr granites (Fowler and Henney, 1996; Fowler et al., 2008).

Appinitic rocks occur mainly in the earliest magmatic stages and correspond to a group of dark-colored plutonic and/or hypabyssal rocks, in which hornblende occurs as large prismatic phenocrysts in a finer-grained matrix (Murphy, 2013). The dominance of hornblende as mafic mineral is evidence of an anomalous water-rich magma. Magmas with increased water content reach the hornblende stability field, which expands relatively to the olivine and pyroxene fields. The viscosity of the melt is diminished, enhancing rapid hornblende growth (Mysen, 1990).

#### 4.5.3.2. *Cogeneticity of qz-monzodioritic and granodioritic rocks*

The granodioritic samples display higher SiO<sub>2</sub> (~62%), Na<sub>2</sub>O and Al<sub>2</sub>O<sub>3</sub> contents, and medium Mg# (37–50), Cr (~90 ppm) and Ni (~37 ppm) amounts. The major elements occupy slightly distinct fields on Harker diagrams (Figure 5), in which the two main evolutionary trends



could be linked by fractional crystallization processes. The first and less evolved trend is essentially related to the decreasing of major MgO, FeO, TiO<sub>2</sub> and CaO towards higher Si<sub>2</sub>O content, which is consistent with progressive removal of observed mafic minerals (clinopyroxene, amphibole and biotite) from the appinitic mantle-derived parental magma (Figure 5 and 6). The transition for the second evolutionary pattern is well demonstrated in the convex-upward distribution of Al<sub>2</sub>O<sub>3</sub> and Na<sub>2</sub>O, with a broad inflection at ca. 60 wt% Si<sub>2</sub>O, suggesting an important shift in the liquid-mineralogy from biotite- and amphibole-dominated to feldspar-dominated crystallization. The former trend is related to the qz-monzodioritic mineral fractionation and the latter to the granodiorite mineral phase separation (Figure 5 and 6).

Through trace elements bivariate relations, the plots of Ba-Sr fractionation vectors favor mainly the control of feldspar and biotite separation, while Cr-Ni indicate retention of clinopyroxene, biotite and amphibole during melt evolution (Figure 4.6B). Accessory minerals such as titanite, zircon, apatite and allanite are shown broadly fractionated in the Zr-Ce correlation (Figure 4.6B). Such data strongly indicate that the appinitic magma could have had a significant role as a mantle-derived component in the granodiorite rock formation, providing evidence of both temporal and genetic relationship. The further coherent and parallel array of REE patterns also confirm the cogenetic nature of the suite components and provide further evidence for crystal fractionation, since the highest [La/Yb]<sub>N</sub> ratios (44 to 52) are concentrated in the qz-monzodiorite facies samples and systematically decrease toward the more evolved granodioritic samples.

The strike-slip faults associated to the large Transbrasiliano Lineament system played an important role in the older suite development, which would facilitate the emplacement to higher structural levels working as a conduit. We suggest that this suite was originated at deeper depth from hydrous mafic magma, which was trapped by deep-seated faults and underwent

stages of crystal fractionation in agreement with different phases of removing elements and crustal levels. The parental magma tends to be much more voluminous at depth than its surface representation would suggest, since the felsic magma rises along faults to shallower levels and forms a kind of rheological barrier to the subsequent ascent of mafic magma (Murphy *et al.*, 2019). Such a system explains the peripheric position of the appinitic rocks in relation to the granodiorite pluton, which may be related to the possibility of preventing or reducing early mafic intrusions in the study area.

The radiogenic isotopes signature is clearly linked to a long-term incompatible element enrichment of the parental source, compatible with subduction-derived fluids interaction coupled with minor assimilation–contamination processes within the overlying lower crust. Such magma type suggests potential calc-alkaline lamprophyres (or phlogopite-bearing metasomatized magma) as a mafic parental source at depth, that became enriched in LILEs by water-rich magma (Rock, 1991; Roberts and Clemens, 1993; Fowler and Henney, 1996). This process can cause a replacement of olivine and pyroxene by hornblende and biotite (phlogopite) as the magma ascends to higher levels (Pitcher *et al.*, 1997; Atherton and Ghani, 2002; Murphy, 2013, 2019). Since no pyroxene has been observed in thin sections of the granodioritic rocks, fractionation of hornblende, rather than pyroxene, was likely dominant in the magmatic evolution.

#### 4.5.4. *Petrogenesis of the monzogranite suite*

Some of the geochemical features of the monzogranite suite dated at  $515 \pm 3.6$  Ma are similar to those of the qz-monzodiorite/granodiorite suite, such as high LILE, LREE enrichment and Nd isotopic compositions, although the suites are set apart by ca. 40 My. The correlations observed in the Harker diagrams reflect a significant role of fractional crystallization processes

(mainly biotite and feldspar) during the magmatic evolution, since the overall plotted elements display negative correlation with the  $\text{Si}_2\text{O}$  index, with the exception of an absence of pattern for  $\text{K}_2\text{O}$  distribution (Figure 4.5). Such pattern can be explained by the input of enriched fluid or melt during crystallization. The monzogranite suite can be related to a higher degree of fractionation, marked also by the more pronounced negative Eu, Sr, Zr, P, and Ti anomalies, indicating the dominance of retention of feldspar and accessory phases such as apatite, zircon and titanite (Figures 4.5, 4.6). Its lower Ni and Cr contents could be related to the advanced degree of crystal fractionation or to a major crustal contamination rate.

The petrogenetic differences between the two investigated suites are marked by a lower mg# (27–36) and Ba+Sr of the younger one, as well as by larger negative Eu anomaly pattern, which requires melting of source rock within or above the stability field of the plagioclase phase. The alkali-calcic character, higher zirconium saturation temperature and relatively larger retention of some HFSE (Zr + Nb + Ce + Y) also highlights the contrast with the older suite, pointing to an increase of the within-plate component towards the monzogranitic suite (Pearce *et al.*, 1984; Whalen *et al.*, 1987; Figure 4.13E and 4.13F).

The higher  $\text{FeOt}/(\text{FeOt}+\text{MgO})$  and lower  $[\text{La}/\text{Yb}]_N$  data, associated to the features pointed out above, lead to propose a transitional shoshonitic to A-type affinity to the monzogranite suite (Whalen *et al.*, 1987; Laurent *et al.*, 2014b; Figure 4.13F). A similar transitional scenario is described by Laurent *et al.* (2014b) to explain the contrast between Mg-K and Fe-K potassic suites. Following this idea, we suggest the interaction of two magmatic components: metasomatized subcontinental lithospheric mantle-derived magma and another that would include some component of a hot rising magma derived from asthenospheric mantle. The geochemistry signature led us to consider a widespread and ubiquitous passive OIB-affinity component or an alkaline-type enrichment of the thermal boundary layer between the lowest

lithosphere and upper asthenosphere, leading to a net veined subcontinental lithospheric mantle (Black and Liégeois, 1993; Bonin, 2004).

The magmatic evolution scenario implies an elevation of temperature to provide enough heat and generate partial melting of a hybridized lithospheric mantle, which subsequently underwent high degree of fractional crystallization to remove mineral phases (mainly biotite and feldspar as primary association) during the ascent, generating water-bearing magmas as end members (Bonin, 2004). Such a process could be accompanied also by lower crust material interaction during wall-rock reactions.

#### 4.5.5. *Tectonic interpretations*

The U-Pb ages (~555 and 515 Ma) determined for the investigated suites indicate that their generation does not relate to the last regional closure stages of the Goiás Magmatic Arc at ca. 630 Ma (Della Giustina *et al.*, 2011). The main point for the establishment of the tectonic setting is that the generation of the older suite needs the former existence of an important subduction phase to produce its enriched source (Tarney and Jones, 1994; Fowler *et al.*, 2001, 2008; Murphy *et al.*, 2013). Such subduction event mainly takes place ca. 40 My before this magma type generation (Atherton and Ghani, 2002), leading us to suggest a new subduction event at ca. 590 Ma (Figure 4.14A).

Considering the tectonic context of the time period around 590 and 540 Ma in Brasiliano-Pan-African orogeny, the magmatic arcs occurred mainly interconnected to transform zones systems that evolved to accretion stages, triggering the emplacement of post-collisional high-K calc-alkaline to alkaline granitoids (Boullier *et al.*, 1986; Black and Liégeois, 1993; Dantas and Fuck, 2017). As a result of this process in West Gondwana, the late collision

of the Amazonian Craton and eastern cratons or terranes/blocks led to the closure of the Clymene Ocean (Tohver *et al.*, 2010, 2012; Dantas and Fuck, 2017 and references therein). The subduction stage proposed at ca. 590 Ma in this work appears to corroborate the existence of an oceanic crust between the Amazonian Craton (beneath the Paraguay Belt) and the western boundary of Goiás Magmatic Arc, that started to be consumed only after 600 Ma.

#### 4.5.5.1. *The qz-monzodiorite/granodiorite suite*

Appinitic magmatism typically takes place after a collisional process, such as cessation of subduction and consume of oceanic crust (Murphy, 2013, 2019). We suggest a late- to post-collisional magmatic event at ca. 557 Ma (Figure 9A), when the subducted oceanic slab possibly underwent slab break-off, inducing the upwelling of the asthenosphere by isostasy. Such a tectonic setting could have supplied enough energy to initiate melting of the overlying subcontinental lithospheric mantle, that was previously metasomatized by subducted slab fluids, generating the appinitic signature at ca. 557 Ma (Figure 4.14B).

Slab break-off mechanism is related to a buoyancy-driven detachment of the subducted oceanic lithosphere from the light continental lithosphere at the end of a collision event (Davies and von Blanckenburg, 1995). The continued deep return flow can cause slow heat and partial melting of the enriched underplated basic material, as well as the subsequent crystal fractionation, yielding the bimodal signature magmatism (Black and Liégeois, 1993; Atherton and Ghani, 2002). The subsequent fractionation process during the magma ascends triggered mafic (hornblende), accessory minerals (e.g., titanite, apatite and allanite) and subsequent feldspar crystallization (Figure 4.6) and led to the generation of a voluminous granodioritic pluton at ca. 554 Ma (Figure 4.14B).

The appinitic rocks mainly occur where a subduction zone was replaced by an active transform fault system, which would facilitate the emplacement of water-rich enigmatic magmas in higher structural levels in the post-collisional setting (Murphy, 2013, 2019). The final closure of the central Tocantins Province between the Amazonian and eastern paleocontinents occurred with the development of extensive N–NE trending shear zones related to the Transbrasiliano Lineament (Cordani *et al.*, 2013; Curto *et al.*, 2014). We propose that in the study area, the Transbrasiliano Lineament faults system worked as a weakness zone to accommodate the subduction effort, which would also contribute to the complex array of mantle material, as well as with the metasomatic and hybrid character of the older suite.

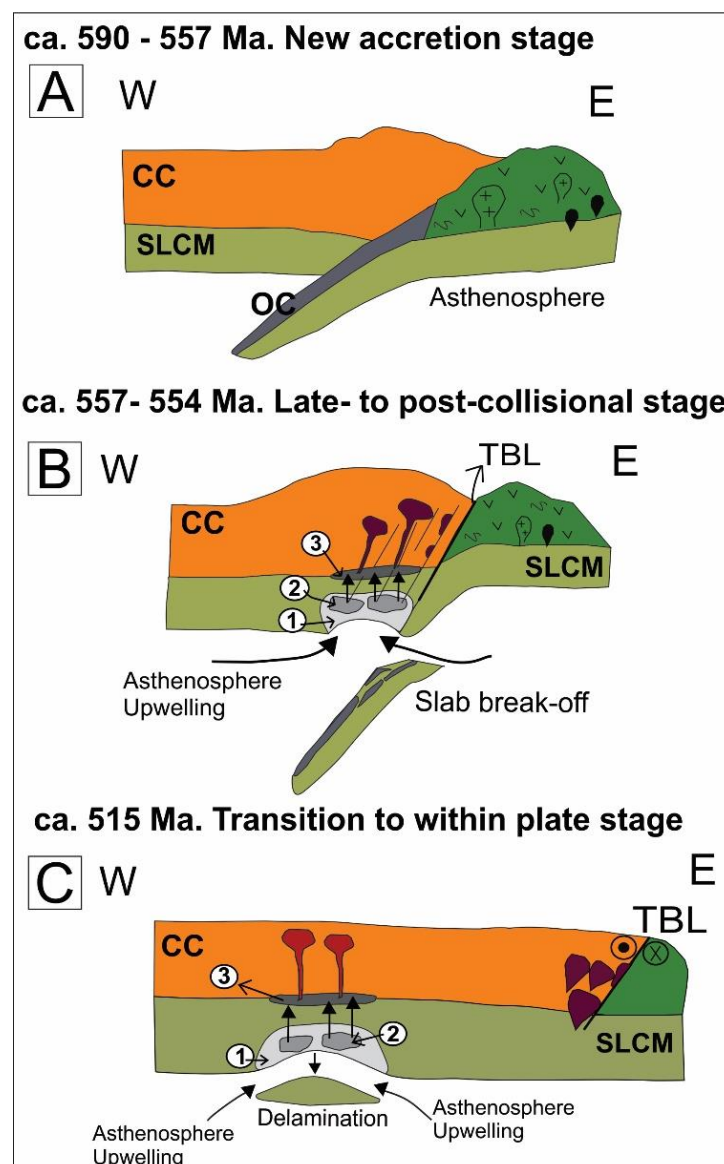


**Figure 4.14** - Schematic model for the evolution of the investigated high Ba–Sr intrusions and the generation of two contrasting groups at post-collisional scenario. See text for discussions. (A) new accretion stage with onset at ca. 590 Ma; (B) late- to post-collisional stage with the petrogenetic model for the older suite: 1) lithospheric mantle enriched by subducted slab-derived fluid and/or melt; 2) mafic magma rich in LREE and LILE derived from partial melting of the enriched lithospheric mantle; 3) magma mixing between the mafic magma from the enriched lithospheric mantle and the silicic magma from partial melting of the overlying lower crust, that has been passing through degrees of crystal fractionation to generate the older suite; (C) transitional to within-plate stage which generated the younger suite: 1) metasomatized lithospheric mantle; 2) magma rich in LREE, LILE and some HFSE derived from partial melting of enriched lithospheric mantle and asthenospheric OIB-affinity component; 3) hybridized magma and differentiation at the mechanical boundary level to form the hybridized granitic signature. CC – Continental crust; OC – Oceanic crust; SCLM – Subcontinental lithospheric mantle; TBL – Transbrasiliano Lineament.

#### 4.5.5.2. *The monzogranite suite*

The subducted slab derived fluid can continue to much greater depth and over a lateral extent, providing variable degrees of melting that could permeate large areas of the lithospheric mantle (Tarney and Jones, 1994). The precedent late-to post-collisional high Mg-K calc-alkaline magmatism at ca. 555 Ma indicates a tectonic setting related to a slab break-off mechanism, that played an important role in providing the favorable lithospheric mantle enrichment conditions beneath the upper plate, leading to a long duration of post-collisional setting. Thus, the younger magma formation occurred related to the preceding collisional event, justifying the use of the expression “post-collisional” for both investigated suites.

The geochemical features of the studied younger suite indicate an intermediate rock composition between sanukitoids and ferroan, likely “A-type” granites affinities, showing an increase of the within-plate components. Therefore, we suggest an emplacement position more distant from the oceanic trench for this suite at ca. 515 Ma (Figure 4.14C). The generation of

the monzogranite suite can be related to the mobility of an alkaline-type enrichment component at the base of recently enriched subcontinental lithospheric mantle, that could be explained by a “lithospheric reworking” process (Liégeois *et al.*, 1998; Laurent *et al.*, 2014b). The interaction between these magmas in the thermal boundary layer would particularly takes place at the very end of a collisional stage, when deep lithospheric weaknesses induce local lithospheric mantle delamination, allowing the upper asthenospheric component to rise (Black and Liégeois, 1993; Liégeois *et al.*, 1998; Gao *et al.*, 2004; Bonin, 2004).

In consequence of lithospheric delamination, the thermal anomaly and decompression stage generated the partial melting of both recently enriched lithospheric mantle and the uprising alkaline asthenosphere component, as well as can triggered some degree of hybridization with the overlying continental crust. The generation of a magma with temperature higher than 800°C requires heating influx of the asthenosphere source component (Miller *et al.*, 2003) to melt the most fusible part of lithospheric mantle and to support the crustal mix at lower levels, contributing to the generation of high K alkali-calcic magmas in the extensional collapse stage (Bonin, 2004).

#### 4.5.6. *Sanukitoids and high Ba-Sr connections*

The persistence of high Ba-Sr magmas worldwide in the Phanerozoic characterizes large juvenile contributions to granitoid genesis, giving rise to the recognition and discussions about continental growth mechanisms in the modern Earth. The distinctive geochemistry of the investigated high Ba-Sr suites provides similarities with Archean sanukitoids, since both groups of rocks present links with the intermediate chemistry found between Archean TTG and modern arc granites (Fowler and Henney, 1996; Stem *et al.*, 1989; Martin *et al.*, 2009). The transition



to sanukitoid magmatism has been interpreted to reflect stabilization of cratons and the increase of crustal thickness, allowing subduction driven tectonics to take place (Martin and Moyen, 2005; Sizova *et al.*, 2010). The sanukitoids commonly range from diorite/monzodiorite to granodiorite/granite by AFC mechanism and display high Ba, Sr and other LILEs, fractionated REE patterns and negative Nb anomalies (Martin and Moyen, 2005; Martin *et al.*, 2009). The hybrid source of the sanukitoids results from the moment in the ancient Earth when heat flow is so low that the direct slab melting is precluded, recording interactions at mantle wedge levels between upwelling mafic magmas and a component rich in incompatible elements, either a melt or a fluid from metabasalts or metasedimentary rocks, derived from subduction events (Martin *et al.*, 2009; Heilimo *et al.*, 2010; Fowler and Rollinson, 2012). Thus, there is a consensus on a sediment-metasomatized mantle source for the emergence of sanukitoids, which become a kind of chronological marker of the onset of crustal material recycling into the mantle (Martin and Moyen, 2005; Martin *et al.*, 2009; Heilimo *et al.*, 2010; Laurent *et al.*, 2014a).

The formation of Archean sanukitoids and high Ba-Sr granites can be well explained by the recurrence of tectonomagmatic processes, linked to similar mechanisms and thermal context of generation (Heilimo *et al.*, 2010; Fowler and Rollinson, 2012; Laurent *et al.*, 2014a). The similar signature is marked essentially by two metasomatic events, the first of which is linked to enrichment of lithosphere mantle by subduction-related fluids and the second one to the fluids/melts deriving from upwelling asthenospheric mantle at the end of an orogenic event (Heilimo *et al.*, 2010). The slab break-off and lithosphere delamination mechanisms have been responsible for the thermal flux that causes asthenospheric mantle uprising and partial melting in the mantle wedge, generating the parental magmas of sanukitoids and high Ba-Sr granites (Liégeois *et al.*, 1998; Gao *et al.*, 2004; Bonin, 2004; Fowler *et al.*, 2001, 2008; Heilimo *et al.*, 2010).

The diagrams proposed by Laurent *et al.* (2014a) confirm the affinities of the investigated appinitic qz-monzodiorite/granodiorite suite with Archean sanukitoids (Figure 4.14), suggesting a close petrogenesis association with this rock type. The younger monzogranite suite plotted in the same diagrams (Figure 15) show a similar trend to the hybridized granites field and partially overlaps the sanukitoids domain, which can have resulted from interaction of a K-rich mafic magma with higher amount of crustal material (Laurent *et al.*, 2014a). The younger investigated suite is compositionally close, but not analogous to the sanukitoid series, differing in the higher K and FeOt/(FeOt+MgO) contents and lower Mg, Ni and Cr values. The generation of this signature could be seen as a transition feature between high K calc-alkaline (including sanukitoids) to alkaline and A-type granites affinity, which has been well recorded in Archean (e.g. Laurent *et al.*, 2014b), Proterozoic (e.g. Bersan *et al.*, 2021) and Mesozoic-Paleozoic terrains (e.g. Boullier *et al.*, 1986). This context is related to the decrease of the orogen thickness at very end of orogeny, recording magmatic episodes during which the continental lithosphere becomes more and more depleted and dehydrated by repetitive generation of water-bearing magmas.

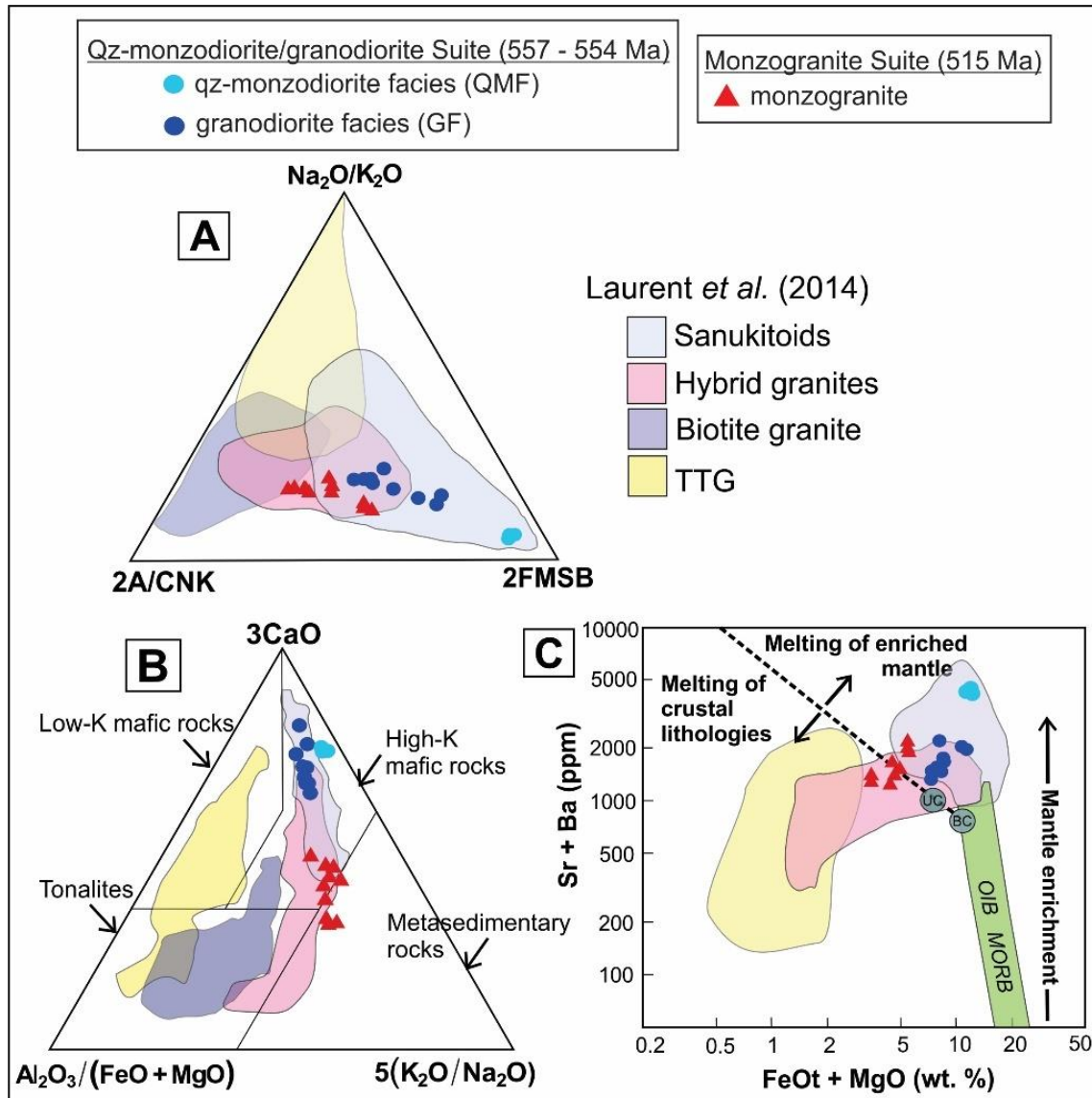


**Figure 4.15** - Distribution of representative analytical points of the studied rocks in the diagrams proposed by Laurent *et al.* (2014a): (A) ternary diagram  $((\text{Na}_2\text{O}/\text{K}_2\text{O}) - 2 \cdot \text{A/CNK} - 2 \cdot [(\text{FeOt} + \text{MgO}) \text{ wt.} \% \cdot (\text{Sr} + \text{Ba}) \text{ wt.} \%]) = \text{FMSB}$  of sanukitoids and high-K anatectic granites; (B) ternary diagram  $\text{Al}_2\text{O}_3/(\text{FeOt} + \text{MgO}) - 3 \cdot \text{CaO} - 5 \cdot (\text{K}_2\text{O}/\text{Na}_2\text{O})$ ; (C) Plots of incompatible element contents (Sr+Ba) plotted as a function of FeOt+MgO (wt.%) concentrations.

The geodynamic model presented in Figure 4.14 for the investigated suites indicates that the asthenospheric upwelling would first trigger heat flux and partial melting of the sub-continental enriched mantle lithosphere, generating the high Mg-K older suite (sanukitoids affinity). The subsequent ca. 40 Ma later evolution yielded the mixing of two different mantle

sources (lithospheric and asthenospheric) and their melting product trigger the Fe-K younger suite. Emerging of these rock types with such geochemical signatures is a useful indicator of crustal recycling into the mantle during distinct stages of the subduction process, also recoding different melting and crustal anatexis conditions in a common syn-to post-collisional setting.

#### 4.6. CONCLUSION

The qz-monzodiorite/granodiorite and monzogranite suites intrude metasedimentary units of the Brasiliano Paraguay Belt, central Brazil, during a late-to post-collisional stage, separated in time by ca. 40 My. The extremely LREE and LILE enrichment relative to HFSE depletion supports the petrogenetic association with magma derived from melting of an enriched lithospheric mantle. A regional-scale strike-slip fault linked to the Transbrasiliano Lineament system could have facilitated the petrological evolution. Some of the main conclusions of this work are:

- (1) The older high K-Mg older suite is associated to coeval appinitic rocks, considered as compositionally viable mantle-derived components for the evolved granodiorite, with crystallization ages constrained between 557 and 554 Ma by zircon U-Pb dating. Petrogenesis is similar to what has been found in Archean sanukitoids.
- (2) The Nd negative isotopic signature identified in both suites confirm an important contribution of ancient crustal material in the process of mantle metasomatism.
- (3) The younger high K younger suite crystallized at ca. 515 Ma shows a transitional shoshonitic/A-type signature, with enrichment in LILE and LREE and some HFSE, formed by hybridization of enriched lithospheric mantle and asthenosphere upwelling component.

- (4) The tectonic scenario allows the process of slab break-off in the end of the subduction phase and subsequent lithospheric delamination ca. 40 My later in a collapse transitional stage of the orogen.
- (5) A new magmatic arc period occurred in the central Tocantins Province related to the consumption of the Clymene Ocean toward the Amazonian Craton (beneath the Paraguay Belt), recording the last magmatic episode associated to a final tectonic configuration within West Gondwana after 600 Ma.

### **Acknowledgments**

This study was financed in part by the *Coordenação de Aperfeiçoamento de Pessoal de Nível Superior* (CAPES) – Finance Code 001. The authors wish to thank the *Instituto Nacional de Ciência e Tecnologia – Estudos Tectônicos* (INCT-ET, CNPq grant 46.5613/2014-4, FAPDF grant 193.001.263/2017) for financial support, and once again CAPES (grant 88887.137872/2017-00) for the Ph.D. scholarship granted to the first author. The first author also acknowledge the support of the Laboratório de Geocronologia (Universidade de Brasília). RAF, ELD and ASR are grateful to CNPq for the research fellowships. The authors would like to thank Prof. M. Fowler and the anonymous reviewer for their helpful corrections and suggestions on the former version of this manuscript, and to M. Roden for the editorial handling.

### **REFERENCES**

- Albarède, F., Telouk P., Blichert-Toft, J., Boyet, M., Agranier, A., Nelson, B., 2004. Precise and accurate isotopic measurements using multiple collector ICPMS. *Geochimica et Cosmochimica Acta* 68, 2725-2744.
- Almeida, F.F.M., 1984. Província Tocantins, setor sudoeste. In: Almeida, F.F.M. de, Hasui, Y., 1984. *O Pré-Cambriano do Brasil*. São Paulo, Edgard Blücher 265-281.

- Alvarega, C.J.S., Trompette R., 1993. Evolução Tectônica Brasileira da Faixa Paraguai: a estruturação da região de Cuiabá. *Revista Brasileira de Geociências* 23, 18-30.
- Atherton, M.P., Ghani, A.A., 2002. Slab breakoff: a model for Caledonian, Late Granite syn-collisional magmatism in the orthotectonic (metamorphic) zone of Scotland and Donegal, Ireland. *Lithos* 62, 65–85.
- Azevedo, P. A. de, Rocha, M. P., Soares, J. E.P., Fuck., R.A., 2015. Thin lithosphere between the Amazonian and São Francisco Cratons, in Central Brazil, revealed by seismic P-wave tomography. *Geophysical Journal International* 201, 61–69.
- Babinski, M., McGee, B. Tokashiki, C.C., Tassinari, C.C.G., Saes, G.S., Pinho, F.E.C., 2018. Comparing Two Arms of an Orogenic Belt during Gondwana Amalgamation: Age and Provenance of the Cuiabá Group, Northern Paraguay Belt, Brazil. *Journal of South American Earth Sciences* 85, 6–42.
- Bersan, S.M., Dandefér, A., Storey, C., Bruno, H., Moreira, H., Abreu, F., Lana, C., Gonçalves, L., Nahas, I., 2021. A perspective on potassic and ultrapotassic rocks: Constraints on the Paleoproterozoic late to post-collisional event in the São Francisco paleocontinent. *Geoscience Frontiers*, <https://doi.org/10.1016/j.gsf.2021.101179>.
- Black, R., Liégeois, J.-P., 1993. Cratons, mobile belts, alkaline rocks and continental lithospheric mantle: the Pan-African testimony. *Journal of the Geological Society of London* 150, 89–98.
- Brito Neves, B.B., Fuck, R.A., 2013. Neoproterozoic evolution of the basement of the South-American platform. *Journal of South American Earth Sciences* 47, 72-89.
- Bonin, B., 2004. Do coeval mafic and felsic magmas in post-collisional to within-plate regimes necessarily imply two contrasting, mantle and crustal, sources? A review. *Lithos* 78 (1), 1–24.

- Boullier, A.M., Liégeois, J.P., Black, R., Fabre, J., Sauvage, M., Bertrand, J.M., 1986. Late Pan-African tectonics marking the transition from subduction-related calc-alkaline magmatism to within-plate alkaline granitoids (Adrar des Iforas Mali). *Tectonophysics* 132, 233–246.
- Bühn, B., Pimentel, M.M., Matteini, M., Dantas, E.L., 2009. High spatial resolution analysis of Pb and U isotopes for geochronology by laser ablation multi-collector inductively coupled plasma mass spectrometry (LA-MC-ICP-MS). *Annals of the Brazilian Academy of Sciences* 81, 99-114.
- Coimbra, K.T.O., 2015. Petrologia do Plutão Bom Jardim de Goiás (PBJG): implicação na evolução neoproterozoica da Província Tocantins. MSc dissertation, Universidade Federal do Rio Grande do Norte, Natal-RN.
- Condie, K.C., Kröner, A., 2013. The building blocks of continental crust: Evidence for a major change in the tectonic setting of continental growth at the end of the Archean. *Gondwana Research* 23, 394–402.
- Cordani, U.G., [Pimentel, M.M.](#), Araújo, C.E.G., Fuck R.A., 2013. The significance of the Transbrasiliano-Kandi tectonic corridor for the amalgamation of Western Gondwana. *Brazilian Journal of Geology* 43, 583-597.
- Corrales, F.F.P., Dussin, I.A., Heilbron, M., Bruno, H., Bersan, S., Valeriano, C.M., Pedrosa-Soares, A.C., Tedeschi, M., 2020. Coeval high Ba-Sr arc-related and OIB Neoproterozoic rocks linking precollisional magmatism of the Ribeira and Araçuaí orogenic belts, SE-Brazil. *Precambrian Research* 337, 105476.
- CPRM., 2017. Carta Geológica-Geofísica - Folha SE.22-V-B-I Bom Jardim de Goiás. Programa gestão estratégica da geologia, da mineração e da transformação mineral carta Geológica - Geofísica escala 1:100.000.

- Corfu, F., Hanchar, J.M., Hoskin, P.W.O., Kinny, P., 2003. Atlas of zircon textures. *Reviews in Mineralogy and Geochemistry* 53, 469–500.
- Curto, J.B., Vidotti R.M., Fuck, R.A., Blakel, R.J. 2014., The tectonic evolution of the Transbrasiliano Lineament in northern Paraná Basin, Brazil, as inferred from aeromagnetic data. *Journal of Geophysical Research* 119, 1544–1562.
- Dantas, E. L., Alvarenga, C.J.S., Santos, R.V.and Pimentel, M.M., 2009. Using Nd Isotopes to Understand the Provenance of Sedimentary Rocks from a Continental Margin to a Foreland Basin in the Neoproterozoic Paraguay Belt, Central Brazil. *Precambrian Research* 170, 1–12.
- Dantas, E.L., Fuck, R.F., 2017. Peri-gondwana terranes in central Brasil. *Willian Smith Meeting, Plate Tectonic at 50*, 128.
- Davies, J.H., von Blanckenburg, F., 1995. Slab breakoff: a model of lithosphere detachment and its test in the magmatism and deformation of collisional orogens. *Earth and Planetary Science Letters* 129, 85–102.
- Della Giustina, M.E.S., Pimentel, M.M., Ferreira Filho, C.F., Holanda, M.H.B.H., 2011. Dating coeval mafic magmatism and ultrahigh temperature metamorphism in the Anápolis Itaucú Complex, central Brazil. *Lithos*, 124, 82-201.
- DePaolo, D.J., 1981. A neodymium and strontium isotopic study of the Mesozoic calc-alkaline granitic batholiths of the Sierra Nevada and Peninsular Ranges, California. *Journal Geophysical Research*, 86, 10470-10488.
- Evensen, N.M, Hamilton, P.J., O’Nions, R.K, et al., 1978. Rare-earth abundances in chondritic meteorites. *Geochimica et Cosmochimica Acta* 42, 1199–1212.
- Ferreira, C.O., 2009. A Extensão do Arco Magmático de Goiás ao longo do Lineamento Transbrasiliano: estudo baseado na aplicação dos métodos U-Pb e Lu-Hf por LA-MC-ICP-MS, MSc Dissertation, Universidade de Brasília. 76 p.



- Fowler, M.B., Henney, P.J., 1996. Mixed Caledonian appinite magmas: implications for lamprophyre fractionation and high Ba–Sr granite genesis. *Contributions to Mineralogy and Petrology* 126, 199–215.
- Fowler, M. B., Henney, P. J., Darbyshire, D. P.F. and Greenwood. P. B., 2001. Petrogenesis of High Ba-Sr Granites: The Rogart Pluton, Sutherland. *Journal of the Geological Society, London* 158, 521–534.
- Fowler, M. B., Kocks, H., Darbyshire, D. P.F. and Greenwood, P. B., 2008. Petrogenesis of High Ba-Sr Plutons from the Northern Highlands Terrane of the British Caledonian Province. *Lithos* 105, 129–148.
- Fowler, M., Rollinson, H., 2012. Phanerozoic Sanukitoids from Caledonian Scotland: Implications for Archean Subduction. *Geology* 40, 1079–82.
- Frost, B. R., Arculus R. J., Barnes C. G., Collins W. J., Ellis D. J., Frost C. D., 2001. A geochemical classification of granitic rocks. *Journal of Petrology* 42, 2033–2048.
- Fuck R. A., Brito Neves B.B., Schobbenhaus C., 2008. Rodinia descendants in South America. *Precambrian Research* 160, 108–126.
- Fuck R. A., Dantas E. L., Vidotti R. M., Roig H. L., Almeida T., 2013. Deformação intracontinental em sistemas transcorrentes: o caso do Lineamento Transbrasiliano: geometria, idade e significado. *Anais do XIV Simpósio Nacional de Estudos Tectônicos – SNET. Mato Grosso.*
- Gao, S., Rudnick, R.L., Yuan, H.L., Liu, X.M., Liu, Y.S., Xu, W.L., Ling, W.L., Ayers, J., Wang, X.C., Wang, Q.H., 2004. Recycling lower continental crust in the North China craton. *Nature* 432, 892–897.
- Geraldes, M. C., Tassinari, C. C.G., Babinski, M., Martinelli, C. D., Iyer, S. S., Barboza, E. S., Pinho, F. E.C., Onoe, A. T., 2008. Isotopic Evidence for the Late Brasiliano (500–550

- Ma) Ore-Forming Mineralization of the Araés Gold Deposit, Brazil. *International Geology Review* 50, 177–90.
- Ghani, A.A., Atherthon, M.P., et al., 2006. The chemical character of the Late Caledonian Donegal Granites, Ireland, with comments on their genesis. *Transactions of the Royal Society of Edinburgh: Earth Sciences* 97, 437–454.
- Gioia, S.M.C.L., Pimentel, M.M., 2000. The Sm–Nd isotopic method in the Geochronology Laboratory of the University of Brasília. *Anais Academia Brasileira de Ciências* 72, 219–245.
- Godoy, A. M., Pinho, F. E. C., Manzano, J. C., de Araújo, L. M. B., da Silva, J. A., Figueiredo, M., 2010. Estudos isotópicos das rochas granitóides neoproterozoicas da Faixa de Dobramento Paraguai. *Revista Brasileira de Geociências* 40, 380–391.
- Guimarães, S. B., Moura, M. A., Dantas, E. L., 2012. Petrology and geochronology of the Bom Jardim de Goiás copper deposit (GO). *Revista Brasileira de Geologia* 42, 841-862.
- Heilimo, E., Halla, J., and Hölttä, P., 2010, Discrimination and origin of the sanukitoid series: Geochemical constraints from the Neoproterozoic western Karelian Province (Finland). *Lithos* 115, 27–39.
- Irvine, T.N., Baragar, W.R.A., 1971. A guide to the chemical classification of the common volcanic rocks. *Canadian Journal of Earth Sciences* 8, 523-547.
- Jackson, S.E., Pearson, N.J., Griffin, W.L., Belousova, E.A., 2004. The application of laser ablation-inductively coupled plasma-mass spectrometry to in situ U-Pb zircon geochronology. *Chemical Geology* 211, 47-69.
- Janousek, V., Farrow, C.M., Erban, V., 2006. Interpretation of Whole-rock Geochemical Data in Igneous Geochemistry: Introducing Geochemical Data Toolkit (GCDkit). *Journal of Petrology* 47, 1255-1259.

- Kirkland, C., Smithies, R.H., Taylor, R.J.M., 2015. Zircon Th-U ratios in magmatic environs. *Lithos* 212-215, 397-414.
- Lameyre, J. & Bowden, P., 1982. Plutonic rock type series: discriminations of various granitoid series and related rocks. *Journal of Volcanology and Geothermal Research* 14, 169-186.
- Lara, P., Oyhantçabal, P., Dadd, K., 2017. Post-collisional, late Neoproterozoic, high-Ba- Sr granitic magmatism from the Dom Feliciano Belt and its cratonic foreland, Uruguay: Petrography, geochemistry, geochronology, and tectonic implications. *Lithos* 277, 178–198.
- Laurent, O., Martin, H., Moyen, J. F., and Doucelance, R., 2014a. The Diversity and Evolution of Late-Archean Granitoids: Evidence for the Onset of ‘Modern-Style’ Plate Tectonics between 3.0 and 2.5 Ga. *Lithos* 205, 208–35.
- Laurent, O., Rapopo, M., Stevens, G., Moyen, J.F., Martin, H., Doucelance, R., Bosq, C., 2014b. Contrasting petrogenesis of Mg–K and Fe–K granitoids and implications for postcollisional magmatism: case study from the Late-Archean Matok pluton (Pietersburg block, South Africa). *Lithos* 196-197, 131–149.
- Liégeois, J.P., Navez, J., Hertogen, J. and Black, R., 1998. Contrasting Origin of Post-Collisional High-K Calc-Alkaline and Shoshonitic versus Alkaline and Peralkaline Granitoids. The Use of Sliding Normalization. *Lithos* 45 (1–4), 1–28.
- Ludwig, K.R., 2012. Isoplot 3.75 - A geochronological Toolkit for Microsoft Excel, vol. 4. Special Publication, Berkeley Geochronology Center, p. 75.
- Maniar, P. D. & Piccoli, P. M., 1989. Tectonic discrimination of granitoids. *Geological Society of America Bulletin* 101, 635-643.
- Manzano J.C., 2009. Caracterização dos Granitóides Brasileiros da Faixa de Dobramento Paraguai, MT e MS. MSc dissertation. Instituto de Geociências e Ciências Exatas, Universidade Estadual Paulista, p. 99.

- Marques, G.C., Oliveira, C.G., Espada, E., [Dantas, E.L., 2019](#). The Fazenda Nova gold deposit, Goiás Magmatic Arc: Late Neoproterozoic intrusion-related auriferous mineralization controlled by intracontinental strike-slip faulting. *Ore Geology* 107, 546-572.
- Martin, H., Moyen, J. F., 2005. The Archaean-Proterozoic transition: sanukitoid and Closepet type magmatism. *Mineralogical Society of Poland - Special Papers* 26, 57–68.
- Martin, H., Moyen, J.F., Rapp, R., 2009. The sanukitoid series: magmatism at the Archaean-Proterozoic transition. *Earth and Environmental Science Transactions of the Royal Society of Edinburgh* 100, 15–33.
- McGee B., Collins A. S., and Trindade R. I. F., 2012. G'day Gondwana, the final accretion of a supercontinent: U/Pb ages for the post-orogenic São Vicente Granite, northern Paraguay Belt, Brazil. *Gondwana Research* 21, 316–322.
- Miller, C.F., McDowell, S.M., Mapes, R.W., 2003. Hot and cold granites? Implications of zircon saturation temperatures and preservation of inheritance. *Geological Society of America* 31 (6), 529–532.
- Moyen, J.F., Laurent, O., Chelle-Michou, C., Couzinié, S., Vanderhaeghe, O., Zeh, A., Villaros, A. & Gardien, V., 2017. Collision vs. subduction-related magmatism: two contrasting ways of granite formation and implications for crustal growth. *Lithos* 277, 154-177.
- Murphy, J.B., 2013. Appinite suites: A record of the role of water in the genesis, transport, emplacement and crystallization of magma. *Earth-Science Reviews* 119, 35–59.
- Murphy, J.B., 2019. Appinites suites and their genetic relationship with coeval voluminous granitoid batholiths. *International Geology Review*, 65, 683-713.
- Mysen, B.O., 1988. Relationship between silicate melt structure and petrologic processes. *Earth-Sciences Reviews* 27 (4), 281-365.
- Pankhurst, R.J., Vaughan, A.P.M., 2008. Tectonic overview of the West Gondwana margin. *Gondwana Research* 13:2, 150–162.

- Pearce, J.A., Harris, N.B.W., Tindle, A.G., 1984. Trace Element Discrimination Diagrams for the Tectonic Interpretation of Granitic Rocks. *Journal of Petrology* 25 (4), 956-983.
- Pearce, J.A., Peate, D.W., 1995. Tectonic implications of the composition of volcanic arc magmas. *Annual Review of Earth and Planetary Sciences* 23, 251–285.
- Peccerillo, A. & Taylor, S. R., 1976. Geochemistry of the Eocene calc-alkaline volcanic rocks from the Kastamonu area, northern Turkey. *Contributions to Mineralogy and Petrology* 58, 63–81.
- Pimentel, M.M., Fuck, R.A., 1987. Origem e evolução das rochas metavulcânicas e metaplutônicas da região de Arenópolis (GO), *Revista Brasileira de Geociências* 17, 2-14.
- Pimentel, M.M., Fuck, R.A., Botelho, N.F., 1999. Granites and the geodynamic history of the neoproterozoic Brasília belt, Central Brazil: a review. *Lithos* 46, 463-483.
- Pimentel, M.M., 2016. The tectonic evolution of the Neoproterozoic Brasília Belt, central Brazil: a geochronological and isotopic approach. *Brazilian Journal of Geology* 46, 67-82.
- Pinho, M. A. S. B., 2001. Petrografia geoquímica e geocronologia do Magmatismo Bimodal paleoproterozóico ocorrente no Norte do Estado de Mato Grosso. Tese (Doutorado em Geociências) – Instituto de Geociências, Universidade Federal do Rio Grande Do Sul. Porto Alegre. p. 162.
- Pitcher, W.S., 1997. *The Nature and Origin of Granite*, 2nd edition. Chapman and Hall, London 395.
- Ren, L., Liang, H., Bao, Z., Zhang, J., Li, K., Huang, W., 2018. The petrogenesis of early Paleozoic high Ba-Sr intrusions in the North Qiling terrane, China, and tectonic implications. *Lithos* 314-315, 534-550.

- Roberts M.P., Clemens J.D., 1993. Origin of high-potassium, calc-alkaline, I-type granitoids. *Geology* 21, 825-828.
- Rodrigues, J.B., Gioia, S.M.C., Pimentel, M.M., 1999. Geocronologia e geoquímica de ortognaisses da região entre Iporá e Firminópolis: Implicações para a evolução do Arco Magmático de Goiás. *Revista Brasileira de Geociências* 29(2): 207-216.
- Ruiz, A.S., Matos, J.B, Sousa, M.Z.A., Lima, G.A., Batata, M.E.F., et al., 2010. Mapeamento Geológico e Levantamento de Recursos Minerais da Folha Santa Bárbara (SD.21-Y-C-V). Convênio CPRM-UFMT. Programa Geologia do Brasil, Relatório Etapa de Mobilização 1–35.
- Seer H.J., 1985. Geologia, deformação e mineralização de cobre no complexo vulcano-sedimentar de Bom Jardim de Golás. MSc Dissertation, UnB, Brasília, 190 p.
- Sizova, E., Gerya, T., Brown, M., Perchuk, L.L., 2010. Subduction styles in the Precambrian: insight from numerical experiments. *Lithos* 116, 209–229.
- Streckeisen, A., 1974. Classification and Nomenclature of Plutonic Rocks. *Geologische Rundschau* 63, 773–786.
- Tarney, J., Jones, C.E., 1994. Trace Element Geochemistry of Orogenic Igneous Rocks and Crustal Growth Models. *Journal of the Geological Society, London* 151, 855–868.
- Tohver, E., Trindade, R. I. F., Solum, J. G., Hall, C. M., Riccomini, C., and Nogueira, A. C., 2010. Closing the Clymene Ocean and Bending a Brasiliano belt: Evidence for the Cambrian formation of Gondwana from southeast Amazon Craton. *Geology*, 38, 267–270.
- Tohver, E., Cawood, P. A., Rossello, E. A., and Jourdan, F., 2012. Closure of the Clymene Ocean and formation of West Gondwana in the Cambrian: Evidence from the Sierras Australes of the southernmost Rio de la Plata Craton, Argentina. *Gondwana Research* 21, 394–405.

- Thompson, R.N., 1982. Magmatism of the British tertiary volcanic province. *Scot. J. Geol.* 18, 49–107.
- Watson, E.B., Harrison, T.M., 1983. Zircon saturation revisited: temperature and composition effects in a variety of crustal magma types. *Earth and Planetary Science Letters* 64, 295–304.
- Whalen, J.B., Currie, K.L., Chappell, B.W., 1987. A-type granites: geochemical characteristics, discrimination and petrogenesis. *Contribution to Mineralogy and Petrology* 95, 407–419.
- Wiedenbeck, M., Hanchar, J.M., Peck, W.H., Sylvester, P., Valley, J., Whitehouse, M., Kronz, A., Morishita, Y., Nasdala, L., Fiebig, J., Franchi, I., Girard, J.P., Greenwood, R.C., Hinton, R., Kita, N., Mason, P.R.D., Norman, M., Ogasawara, M., Piccoli, P.M., Rhede, D., Satoh, H., Schulz-Dobrick, B., Skår, O., Spicuzza, M.J., Terada, K., Tindle, A., Togashi, S., Vennemann, T., Xie, Q., Zheng, Y.F., 2004. Further characterisation of the 91500 zircon crystal. *Geostandards and Geoanalytical Research* 28, 9–39.
- Woodhead, J.D., Hergt, J.M., Davidson, J.P., Eggins, S.M., et al., 2001. Hafnium Isotope Evidence for ‘conservative’ Element Mobility during Subduction Zone Processes. *Earth and Planetary Science Letters.* 192, 331–346.
- Ye, H.M., Li, X.H., Li, Z.X., Zhang, C.L., 2008. Age and origin of high Ba–Sr appinite–granites at the northwestern margin of the Tibet Plateau: Implications for early Paleozoic tectonic evolution of the Western Kunlun orogenic belt. *Gondwana Research* 13, 126–138.
- Xiang, W., Griffin, W.L., Jie, C., Pinyun, H., Xiang, L., 2011. U and Th contents and Th/U ratios of zircon in felsic and mafic magmatic rocks: improved zircon-melt distribution coefficients. *Acta Geologica Sinica* 85 (1), 164–174.

Zhang, X., Gao, Y., Wang, Z., Liu, H., Ma, Y., et al., 2012. Carboniferous appinitic intrusions from the northern North China craton: geochemistry, petrogenesis and tectonic implications. *Journal of the Geological Society, London* 169, 337–351.

## ANEXOS ARTIGO 1

**Supplementary Table 4.1** – U-Pb general conditions at Laboratory of Geochronology and Isotope Geochemistry of the Universidade de Brasília - UnB.

| <b>Laboratory and Sample Preparation</b> |  |
|--|--|
| Laboratory name                          | Laboratory of Geochronology and Isotope Geochemistry of the Brasilia University-UnB.                 |
| Sample type/mineral                      | Zircon   |
| Sample preparation                       | Conventional mineral separation, 0.5 cm resin mount, 1 µm polish to finish                           |
| Imaging                                  | BSE, FEI Quanta 450, 10 nA, 20kV, 13.8 mm working distance   |
| <b>Laser ablation system</b>             |  |
| Make, Model and type                     | ESI/New Wave Research, UP-213, Nd:YAG  |
| Ablation cell and volume                 | Low volume cell, ca. 4 cm <sup>3</sup>   |
| Laser wavelength (nm)                    | 213 nm   |
| Pulse width (ns)                         | 3 ns   |
| Fluence (J cm <sup>-2</sup> )            | 3.0 - 3.5 J cm <sup>-2</sup>   |
| Repetition rate (Hz)                     | 10 Hz (U-Pb) and 7 Hz (Lu-Hf)  |
| Spot size                                | 25 µm (U-Pb), 40 µm (Lu-Hf)  |
| Sampling mode / pattern                  | single spot analyses   |
| Carrier gas                              | 100% He, Ar make-up gas combined using a Y-piece along the sample transport line close to the torch. |



|  |   |
|--|---|
| Pre-ablation laser warm-up<br>(background collection)  | 10 s  |
| Ablation duration (s)  | 40 s  |
| Wash-out delay   | 20 s  |
| Ablation pit depth / ablation<br>rate  | ~10 µm pit depth  |
| Cell carrier gas flow (l min <sup>-1</sup> )   | 0.40 l min <sup>-1</sup> He   |
| <b>ICP-MS Instrument</b>   |   |
| Make, Model and type   | Thermo-Fischer, Neptune, MC-ICP-MS  |
| Sample introduction  | Ablation aerosol  |
| RF power (W)   | 1050 W  |
| Make-up gas flow (l min <sup>-1</sup> )  | 0.7 l min <sup>-1</sup>   |
| Detection system   | mixed Faraday cups and multiple ion counting<br>(MIC) array   |
| Masses measured for U-Pb   | Faraday <sup>232</sup> Th, <sup>238</sup> U and <sup>206</sup> Pb; MIC <sup>202</sup> Hg, <sup>204</sup> Pb,<br><sup>207</sup> Pb and <sup>208</sup> Pb |
| Masses measured for Lu-hf<br>methodology   | Faraday 171, 173, 175, 176, 177, 178, 179, 180  |
| Integration time per<br>peak/dwell times (ms);<br>quadrupole settling time<br>between mass jumps | #N.A.   |
| Total integration time per<br>output data point (s)  | 1.049 s   |
| Dead time (ns)   | #N.A.   |
| <b>Data Processing</b>   |   |
| Gas blank  | 20 s  |
| Calibration strategy   | GJ1 used as primary reference material,<br>TEMORA used as secondary/validation  |

|  |   |
|--|---|
| Reference Material info                            | GJ1 (Jackson <i>et al.</i> 2004, Horstwood <i>et al.</i> 2016)<br>Wiedenbeck <i>et al.</i> , 1995, 2004   |
| Data processing package used / Correction for LIEF | Inhouse U-Pb table (Buhn <i>et al.</i> , 2009) and Lu-Hf table (Matteini <i>et al.</i> , 2010)  |
| Mass discrimination                                | Standard-sample bracketing with $^{207}\text{Pb}/^{206}\text{Pb}$ and $^{206}\text{Pb}/^{238}\text{U}$ ratios normalized to reference material GJ1                |
| Common-Pb correction, composition and uncertainty  | none  |
| Uncertainty level and propagation                  | Ages are quoted at 2s absolute, propagation is by quadratic addition. Excess variance and age uncertainty of reference material are propagated where appropriate. |
| Quality control / Validation                       | o<br>Systematic uncertainty for propagation is 1% (2s).   |

**Supplementary Table 4.2** - Data of U-Pb analyses performed through LA-ICP-MS on zircon from 91500.

| SAMPLE                    | 91500         |       |             |             |       |            |       |            |       |      |             |     |            |     |            |     |          |
|---------------------------|---------------|-------|-------------|-------------|-------|------------|-------|------------|-------|------|-------------|-----|------------|-----|------------|-----|----------|
|                           | Apparent ages |       |             |             |       |            |       |            |       |      |             |     |            |     |            |     |          |
| GRAIN                     | <i>f</i>      | err 1 |             |             |       | err 1      |       | err 1      |       | Rho  | 2 σ         |     | 2 σ        |     | 2 σ        |     | conc (%) |
|                           | 206 (%)       | Th/U  | 206Pb/204Pb | 207Pb/206Pb | 6 (%) | 207Pb/235U | 6 (%) | 206Pb/238U | 6 (%) |      | 207Pb/206Pb | 2 σ | 206Pb/238U | 2 σ | 207Pb/235U | 2 σ |          |
| <b>Sample AL08 -91500</b> |               |       |             |             |       |            |       |            |       |      |             |     |            |     |            |     |          |
| 003-91500                 | 0.0127        | 0.240 | 122581      | 0.07503     | 0.42  | 1.724      | 0.87  | 0.1667     | 0.67  | 0.76 | 1069        | 17  | 994        | 12  | 1018       | 11  | 97.7     |
| 005-91500                 | 0.0151        | 0.241 | 103085      | 0.07502     | 0.53  | 1.691      | 0.97  | 0.1634     | 0.73  | 0.75 | 1069        | 21  | 976        | 13  | 1005       | 12  | 97.1     |
| 006-91500                 | 0.0052        | 0.242 | 300079      | 0.07459     | 0.46  | 1.754      | 0.84  | 0.1705     | 0.60  | 0.71 | 1057        | 18  | 1015       | 11  | 1028       | 11  | 98.7     |
| 007-91500                 | 0.0153        | 0.240 | 101233      | 0.07532     | 0.38  | 1.759      | 0.84  | 0.1694     | 0.66  | 0.78 | 1077        | 15  | 1009       | 12  | 1031       | 11  | 97.9     |
| 008-91500                 | 0.0136        | 0.239 | 114232      | 0.07490     | 0.50  | 1.699      | 0.89  | 0.1645     | 0.63  | 0.71 | 1066        | 20  | 982        | 11  | 1008       | 11  | 97.4     |
| 009-91500                 | 0.0149        | 0.245 | 104077      | 0.07498     | 0.51  | 1.741      | 0.90  | 0.1684     | 0.65  | 0.71 | 1068        | 21  | 1003       | 12  | 1024       | 12  | 98.0     |
| 010-91500                 | 0.0215        | 0.242 | 72045       | 0.07450     | 0.46  | 1.772      | 0.87  | 0.1725     | 0.64  | 0.73 | 1055        | 19  | 1026       | 12  | 1035       | 11  | 99.1     |
| 011-91500                 | 0.0182        | 0.244 | 85056       | 0.07521     | 0.38  | 1.756      | 0.81  | 0.1693     | 0.61  | 0.75 | 1074        | 15  | 1008       | 11  | 1029       | 10  | 98.0     |
| 012-91500                 | 0.0068        | 0.241 | 227540      | 0.07471     | 0.51  | 1.720      | 0.92  | 0.1670     | 0.67  | 0.73 | 1061        | 21  | 995        | 12  | 1016       | 12  | 98.0     |
| 017-91500                 | 0.0147        | 0.224 | 105306      | 0.07461     | 0.48  | 1.826      | 0.96  | 0.1775     | 0.74  | 0.77 | 1058        | 19  | 1053       | 14  | 1055       | 13  | 99.8     |
| 018-91500                 | 0.0137        | 0.226 | 113166      | 0.07423     | 0.48  | 1.812      | 0.90  | 0.1770     | 0.67  | 0.75 | 1048        | 19  | 1051       | 13  | 1050       | 12  | 100.1    |
| 019-91500                 | 0.0102        | 0.225 | 151987      | 0.07520     | 0.46  | 1.802      | 0.89  | 0.1738     | 0.66  | 0.74 | 1074        | 19  | 1033       | 13  | 1046       | 12  | 98.7     |
| 020-91500                 | 0.0143        | 0.224 | 108158      | 0.07448     | 0.47  | 1.769      | 0.84  | 0.1722     | 0.59  | 0.70 | 1054        | 19  | 1024       | 11  | 1034       | 11  | 99.1     |
| 021-91500                 | 0.0147        | 0.224 | 105751      | 0.07480     | 0.54  | 1.794      | 0.91  | 0.1739     | 0.62  | 0.69 | 1063        | 22  | 1034       | 12  | 1043       | 12  | 99.1     |

|           |        |       |        |         |      |       |      |        |      |      |      |    |      |    |      |    |       |
|-----------|--------|-------|--------|---------|------|-------|------|--------|------|------|------|----|------|----|------|----|-------|
| 022-91500 | 0.0127 | 0.223 | 121819 | 0.07477 | 0.40 | 1.770 | 0.81 | 0.1717 | 0.59 | 0.73 | 1062 | 16 | 1022 | 11 | 1035 | 10 | 98.7  |
| 023-91500 | 0.0120 | 0.219 | 129780 | 0.07503 | 0.34 | 1.725 | 0.75 | 0.1668 | 0.56 | 0.74 | 1069 | 14 | 994  | 10 | 1018 | 10 | 97.7  |
| 024-91500 | 0.0159 | 0.225 | 97552  | 0.07465 | 0.52 | 1.786 | 0.90 | 0.1735 | 0.63 | 0.70 | 1059 | 21 | 1031 | 12 | 1040 | 12 | 99.1  |
| 025-91500 | 0.0200 | 0.225 | 77708  | 0.07474 | 0.44 | 1.776 | 0.78 | 0.1723 | 0.53 | 0.67 | 1062 | 18 | 1025 | 10 | 1037 | 10 | 98.9  |
| 026-91500 | 0.0164 | 0.224 | 94377  | 0.07518 | 0.69 | 1.772 | 1.01 | 0.1709 | 0.64 | 0.63 | 1073 | 28 | 1017 | 12 | 1035 | 13 | 98.3  |
| 032-91500 | 0.0094 | 0.243 | 164143 | 0.07514 | 0.31 | 1.895 | 0.69 | 0.1829 | 0.49 | 0.71 | 1072 | 12 | 1083 | 10 | 1079 | 9  | 100.3 |
| 033-91500 | 0.0105 | 0.245 | 147579 | 0.07528 | 0.32 | 1.911 | 0.73 | 0.1841 | 0.54 | 0.74 | 1076 | 13 | 1089 | 11 | 1085 | 10 | 100.4 |
| 034-91500 | 0.0109 | 0.244 | 142008 | 0.07483 | 0.30 | 1.892 | 0.67 | 0.1833 | 0.48 | 0.71 | 1064 | 12 | 1085 | 10 | 1078 | 9  | 100.7 |
| 035-91500 | 0.0070 | 0.242 | 221600 | 0.07487 | 0.38 | 1.858 | 0.76 | 0.1800 | 0.55 | 0.72 | 1065 | 15 | 1067 | 11 | 1066 | 10 | 100.0 |
| 036-91500 | 0.0135 | 0.242 | 114468 | 0.07486 | 0.29 | 1.860 | 0.69 | 0.1802 | 0.50 | 0.73 | 1065 | 12 | 1068 | 10 | 1067 | 9  | 100.1 |
| 037-91500 | 0.0098 | 0.242 | 158887 | 0.07503 | 0.31 | 1.836 | 0.76 | 0.1775 | 0.59 | 0.77 | 1069 | 13 | 1053 | 11 | 1059 | 10 | 99.5  |
| 038-91500 | 0.0070 | 0.242 | 221435 | 0.07432 | 0.32 | 1.842 | 0.76 | 0.1798 | 0.58 | 0.77 | 1050 | 13 | 1066 | 11 | 1061 | 10 | 100.5 |
| 039-91500 | 0.0109 | 0.242 | 141615 | 0.07486 | 0.33 | 1.847 | 0.77 | 0.1790 | 0.59 | 0.77 | 1065 | 13 | 1061 | 12 | 1062 | 10 | 99.9  |
| 040-91500 | 0.0127 | 0.240 | 121590 | 0.07516 | 0.35 | 1.825 | 0.74 | 0.1761 | 0.53 | 0.72 | 1073 | 14 | 1045 | 10 | 1054 | 10 | 99.2  |

**Sample AL01 -91500**

|           |        |       |        |         |      |       |      |        |      |      |      |    |      |    |      |    |      |
|-----------|--------|-------|--------|---------|------|-------|------|--------|------|------|------|----|------|----|------|----|------|
| 004-91500 | 0.0054 | 0.231 | 285937 | 0.07498 | 0.30 | 1.830 | 0.66 | 0.1770 | 0.46 | 0.70 | 1068 | 12 | 1050 | 9  | 1056 | 9  | 99.4 |
| 005-91500 | 0.0060 | 0.234 | 258132 | 0.07469 | 0.35 | 1.807 | 0.78 | 0.1755 | 0.59 | 0.75 | 1060 | 14 | 1042 | 11 | 1048 | 10 | 99.4 |
| 006-91500 | 0.0061 | 0.234 | 252746 | 0.07502 | 0.39 | 1.823 | 0.75 | 0.1762 | 0.52 | 0.70 | 1069 | 15 | 1046 | 10 | 1054 | 10 | 99.3 |
| 007-91500 | 0.0058 | 0.237 | 267191 | 0.07492 | 0.41 | 1.800 | 0.72 | 0.1743 | 0.47 | 0.65 | 1066 | 16 | 1036 | 9  | 1046 | 9  | 99.0 |
| 008-91500 | 0.0073 | 0.236 | 213102 | 0.07511 | 0.48 | 1.807 | 0.79 | 0.1745 | 0.50 | 0.63 | 1071 | 19 | 1037 | 10 | 1048 | 10 | 98.9 |
| 009-91500 | 0.0079 | 0.207 | 197178 | 0.07485 | 0.46 | 1.809 | 0.81 | 0.1753 | 0.56 | 0.69 | 1065 | 18 | 1041 | 11 | 1049 | 11 | 99.3 |
| 010-91500 | 0.0079 | 0.229 | 197414 | 0.07507 | 0.43 | 1.786 | 0.79 | 0.1725 | 0.55 | 0.69 | 1070 | 17 | 1026 | 10 | 1040 | 10 | 98.6 |
| 011-91500 | 0.0061 | 0.244 | 254683 | 0.07493 | 0.52 | 1.782 | 0.88 | 0.1725 | 0.62 | 0.70 | 1067 | 21 | 1026 | 12 | 1039 | 11 | 98.7 |
| 012-91500 | 0.0059 | 0.244 | 262961 | 0.07503 | 0.39 | 1.764 | 0.84 | 0.1705 | 0.64 | 0.77 | 1069 | 16 | 1015 | 12 | 1032 | 11 | 98.3 |

|           |        |       |        |         |      |       |      |        |      |      |      |    |      |    |      |    |      |
|-----------|--------|-------|--------|---------|------|-------|------|--------|------|------|------|----|------|----|------|----|------|
| 017-91500 | 0.0141 | 0.233 | 110158 | 0.07498 | 0.30 | 1.784 | 0.70 | 0.1726 | 0.52 | 0.74 | 1068 | 12 | 1026 | 10 | 1040 | 9  | 98.7 |
| 018-91500 | 0.0138 | 0.234 | 112417 | 0.07489 | 0.34 | 1.778 | 0.74 | 0.1722 | 0.54 | 0.73 | 1066 | 14 | 1024 | 10 | 1038 | 10 | 98.7 |
| 019-91500 | 0.0136 | 0.231 | 114290 | 0.07548 | 0.36 | 1.760 | 0.74 | 0.1691 | 0.53 | 0.72 | 1081 | 14 | 1007 | 10 | 1031 | 10 | 97.7 |
| 020-91500 | 0.0121 | 0.232 | 127751 | 0.07531 | 0.37 | 1.779 | 0.72 | 0.1713 | 0.50 | 0.69 | 1077 | 15 | 1019 | 9  | 1038 | 9  | 98.2 |
| 021-91500 | 0.0145 | 0.230 | 106746 | 0.07492 | 0.39 | 1.761 | 0.72 | 0.1704 | 0.49 | 0.67 | 1066 | 16 | 1014 | 9  | 1031 | 9  | 98.4 |
| 022-91500 | 0.0217 | 0.238 | 71419  | 0.07488 | 0.49 | 1.745 | 0.83 | 0.1690 | 0.56 | 0.67 | 1065 | 20 | 1006 | 10 | 1025 | 11 | 98.2 |
| 023-91500 | 0.0136 | 0.236 | 113632 | 0.07505 | 0.33 | 1.733 | 0.72 | 0.1675 | 0.52 | 0.72 | 1070 | 13 | 998  | 10 | 1021 | 9  | 97.8 |
| 024-91500 | 0.0151 | 0.236 | 102479 | 0.07532 | 0.45 | 1.769 | 0.78 | 0.1703 | 0.52 | 0.67 | 1077 | 18 | 1014 | 10 | 1034 | 10 | 98.0 |
| 025-91500 | 0.0144 | 0.236 | 107537 | 0.07489 | 0.40 | 1.758 | 0.73 | 0.1703 | 0.48 | 0.66 | 1065 | 16 | 1014 | 9  | 1030 | 9  | 98.4 |
| 026-91500 | 0.0155 | 0.236 | 99905  | 0.07464 | 0.47 | 1.759 | 0.79 | 0.1709 | 0.53 | 0.66 | 1059 | 19 | 1017 | 10 | 1031 | 10 | 98.7 |

**Sample AL27 -91500**

|           |        |       |        |         |      |       |      |        |      |      |      |    |      |    |      |    |       |
|-----------|--------|-------|--------|---------|------|-------|------|--------|------|------|------|----|------|----|------|----|-------|
| 004-91500 | 0.0114 | 0.247 | 136201 | 0.07530 | 0.39 | 1.824 | 0.82 | 0.1756 | 0.62 | 0.75 | 1077 | 16 | 1043 | 12 | 1054 | 11 | 99.0  |
| 005-91500 | 0.0096 | 0.248 | 161572 | 0.07483 | 0.34 | 1.832 | 0.71 | 0.1775 | 0.50 | 0.70 | 1064 | 14 | 1053 | 10 | 1057 | 9  | 99.7  |
| 006-91500 | 0.0183 | 0.251 | 84761  | 0.07496 | 0.27 | 1.879 | 0.72 | 0.1817 | 0.55 | 0.77 | 1067 | 11 | 1076 | 11 | 1074 | 9  | 100.3 |
| 008-91500 | 0.0176 | 0.254 | 88252  | 0.07504 | 0.36 | 1.871 | 0.74 | 0.1808 | 0.53 | 0.72 | 1070 | 15 | 1071 | 10 | 1071 | 10 | 100.1 |
| 009-91500 | 0.0189 | 0.256 | 81995  | 0.07474 | 0.43 | 1.842 | 0.77 | 0.1787 | 0.52 | 0.68 | 1062 | 17 | 1060 | 10 | 1061 | 10 | 100.0 |
| 010-91500 | 0.0114 | 0.255 | 136415 | 0.07463 | 0.28 | 1.816 | 0.68 | 0.1765 | 0.50 | 0.73 | 1059 | 11 | 1048 | 10 | 1051 | 9  | 99.7  |
| 011-91500 | 0.0129 | 0.256 | 120416 | 0.07431 | 0.41 | 1.824 | 0.79 | 0.1780 | 0.57 | 0.72 | 1050 | 16 | 1056 | 11 | 1054 | 10 | 100.2 |
| 012-91500 | 0.0149 | 0.255 | 103816 | 0.07501 | 0.44 | 1.864 | 0.76 | 0.1803 | 0.50 | 0.65 | 1069 | 18 | 1068 | 10 | 1069 | 10 | 100.0 |
| 017-91500 | 0.0126 | 0.260 | 123213 | 0.07456 | 0.54 | 1.803 | 1.02 | 0.1754 | 0.78 | 0.76 | 1057 | 22 | 1042 | 15 | 1047 | 13 | 99.5  |
| 018-91500 | 0.0186 | 0.263 | 83167  | 0.07479 | 0.50 | 1.803 | 0.82 | 0.1748 | 0.53 | 0.65 | 1063 | 20 | 1039 | 10 | 1047 | 11 | 99.2  |
| 019-91500 | 0.0079 | 0.265 | 196975 | 0.07515 | 0.35 | 1.808 | 0.73 | 0.1745 | 0.52 | 0.72 | 1073 | 14 | 1037 | 10 | 1048 | 10 | 98.9  |
| 020-91500 | 0.0164 | 0.264 | 94570  | 0.07514 | 0.42 | 1.807 | 0.79 | 0.1744 | 0.56 | 0.71 | 1072 | 17 | 1036 | 11 | 1048 | 10 | 98.9  |
| 021-91500 | 0.0139 | 0.250 | 111332 | 0.07480 | 0.36 | 1.807 | 0.73 | 0.1752 | 0.51 | 0.71 | 1063 | 14 | 1041 | 10 | 1048 | 10 | 99.3  |

|           |        |       |         |         |      |       |      |        |      |      |      |    |      |    |      |    |       |
|-----------|--------|-------|---------|---------|------|-------|------|--------|------|------|------|----|------|----|------|----|-------|
| 023-91500 | 0.0158 | 0.262 | 97860   | 0.07491 | 0.43 | 1.777 | 0.78 | 0.1720 | 0.53 | 0.68 | 1066 | 17 | 1023 | 10 | 1037 | 10 | 98.7  |
| 024-91500 | 0.0130 | 0.266 | 118941  | 0.07489 | 0.36 | 1.837 | 0.73 | 0.1779 | 0.51 | 0.71 | 1065 | 14 | 1056 | 10 | 1059 | 10 | 99.7  |
| 025-91500 | 0.0157 | 0.263 | 98512   | 0.07495 | 0.46 | 1.816 | 0.84 | 0.1757 | 0.60 | 0.71 | 1067 | 18 | 1044 | 11 | 1051 | 11 | 99.3  |
| 026-91500 | 0.0150 | 0.264 | 103167  | 0.07464 | 0.44 | 1.823 | 0.77 | 0.1771 | 0.52 | 0.67 | 1059 | 18 | 1051 | 10 | 1054 | 10 | 99.8  |
| 032-91500 | 0.0103 | 0.273 | 150461  | 0.07493 | 0.34 | 1.791 | 0.81 | 0.1734 | 0.63 | 0.78 | 1067 | 14 | 1031 | 12 | 1042 | 10 | 98.9  |
| 033-91500 | 0.0113 | 0.272 | 137110  | 0.07501 | 0.34 | 1.801 | 0.76 | 0.1741 | 0.57 | 0.75 | 1069 | 14 | 1035 | 11 | 1046 | 10 | 98.9  |
| 034-91500 | 0.0115 | 0.271 | 134741  | 0.07503 | 0.37 | 1.798 | 0.77 | 0.1737 | 0.57 | 0.74 | 1069 | 15 | 1033 | 11 | 1045 | 10 | 98.9  |
| 036-91500 | 0.0156 | 0.259 | 99568   | 0.07487 | 0.43 | 1.844 | 0.83 | 0.1786 | 0.60 | 0.73 | 1065 | 17 | 1059 | 12 | 1061 | 11 | 99.8  |
| 037-91500 | 0.0130 | 0.270 | 119170  | 0.07450 | 0.50 | 1.840 | 0.88 | 0.1791 | 0.63 | 0.71 | 1055 | 20 | 1062 | 12 | 1060 | 12 | 100.2 |
| 038-91500 | 0.0014 | 0.273 | 1082114 | 0.07503 | 0.37 | 1.830 | 0.86 | 0.1769 | 0.68 | 0.79 | 1069 | 15 | 1050 | 13 | 1056 | 11 | 99.4  |
| 039-91500 | 0.0090 | 0.271 | 173075  | 0.07444 | 0.40 | 1.842 | 0.79 | 0.1795 | 0.57 | 0.72 | 1053 | 16 | 1064 | 11 | 1061 | 10 | 100.3 |
| 040-91500 | 0.0085 | 0.270 | 182361  | 0.07524 | 0.35 | 1.859 | 0.84 | 0.1792 | 0.66 | 0.79 | 1075 | 14 | 1062 | 13 | 1067 | 11 | 99.6  |

**Supplementary Table 4.3** - Calculation of zircon saturation temperatures ( $T_{Zr.sat.C}$ ) of the Zr concentrations for both suites.

|     | Samples | M        | Zr.obs | Zr.sat | $T_{Zr.sat.C}$ |
|-----|---------|----------|--------|--------|----------------|
|     | AL02    | 2.467356 | 217    | 259    | <b>735.8</b>   |
|     | AL03    | 2.073568 | 211    | 185.3  | <b>760.6</b>   |
|     | AL04-A  | 1.915619 | 209    | 162    | <b>771.1</b>   |
| QMF | AL21    | 1.818216 | 204    | 149.2  | <b>776.1</b>   |
|     | AL22    | 2.07834  | 216    | 186.1  | <b>762.3</b>   |
|     | AL23    | 2.507025 | 207    | 267.9  | <b>729.5</b>   |
|     | AL24    | 2.079105 | 210    | 186.2  | <b>759.9</b>   |
|     | AL25    | 1.948298 | 206    | 166.6  | <b>767.5</b>   |
|     | AL05-A  | 1.965681 | 273    | 169.1  | <b>790.4</b>   |
| GF  | AL05-B  | 3.032926 | 273    | 418.8  | <b>716.4</b>   |
|     | AL08    | 3.069688 | 267    | 432.1  | <b>712.4</b>   |
|     | AL26    | 3.012537 | 400    | 411.7  | <b>747.7</b>   |
|     | AL27    | 1.744673 | 308    | 140.1  | <b>818.2</b>   |
|     | AL28    | 1.631925 | 245    | 127.3  | <b>806</b>     |
|     | AL28-B  | 1.534001 | 274    | 117.1  | <b>823.9</b>   |
| MS  | SE-05   | 1.536531 | 441    | 117.4  | <b>870</b>     |
|     | SE-27   | 1.793394 | 448    | 146    | <b>849.8</b>   |
|     | SE-25   | 1.787714 | 356    | 145.3  | <b>828.3</b>   |
|     | SE-38   | 1.548344 | 385    | 118.6  | <b>855.4</b>   |
|     | SE-48   | 1.682702 | 315    | 132.9  | <b>825.2</b>   |
|     | AL30    | 1.592928 | 365    | 123.2  | <b>846.5</b>   |

## 5. ARTIGO 2

### **Tectonic significance of the early-Cambrian syn-orogenic basin in the easternmost portion of the Paraguay Belt, Tocantins Province, central Brazil.**

Artigo submetido no dia 28 de outubro de 2021 na revista *Gondwana Research*. *Status atual: Under review.*

Amanda Figueiredo Granja Dorilêo Leite<sup>1\*</sup> ([amandafgdlite@gmail.com](mailto:amandafgdlite@gmail.com)), Reinhardt A. Fuck<sup>1</sup>([reinhardt@unb.br](mailto:reinhardt@unb.br)), Elton L. Dantas<sup>1</sup>([elton@unb.br](mailto:elton@unb.br)), Amarildo S. Ruiz<sup>2</sup> ([asruiz@gmail.com](mailto:asruiz@gmail.com)), Patrick Monié<sup>3</sup>([patrick.monie@umontpellier.fr](mailto:patrick.monie@umontpellier.fr)), Arthur Iemmolo<sup>3</sup> ([arthur.iemmolo@umontpellier.fr](mailto:arthur.iemmolo@umontpellier.fr))

<sup>1</sup>Instituto de Geociências, Universidade de Brasília (UnB), Asa Norte, Brasília, DF, 70910, Brazil.

<sup>2</sup>Faculdade de Geociências, Universidade Federal de Mato Grosso (UFMT), Avenida Fernando Correa da Costa, 2367, Boa Esperança, Cuiabá, MT, 78060-900, Brazil.

<sup>3</sup>Géosciences Montpellier, Université de Montpellier, CNRS, Université des Antilles, UMR5243, F-34095 Montpellier, France.

\*Corresponding author



**ABSTRACT**

Sedimentary provenance studies using detrital zircon U-Pb ages represent an important tool to investigate evolution of orogenic basins and to suggest tectonic setting reconstructions. Syn-orogenic basins worldwide are characterized by a large proportion of zircon with ages close to the maximum depositional period, reflecting the proximity of recently formed magmatic rocks. In this work, we combine field observations, U-Pb detrital zircon ages, Sm-Nd whole rock and Ar-Ar in mica isotopic analyses to constrain the final tectonic evolution of a restricted basin located in a poorly studied region at the easternmost limit to the Paraguay Belt, Tocantins Province, central Brazil. The investigated area corresponds to the boundary sector with the Brasília Belt, which is also transected by the strike-slip fault system associated to the large Transbrasiliano Lineament. We provide 465 new detrital zircon U-Pb data with ages distributed from early Cambrian to Archean, of which approximately 60% of analyzed grains are derived from Ediacaran-Cryogenian sources. The maximum depositional age of the basin is defined at ca. 594 Ma, constrained by the youngest age peak. The syn-orogenic character of the basin is inferred based on the main peak of the detrital zircon population ages around 620 Ma, which is very close to the maximum depositional period and points to a short time between erosion, deposition, and burial processes. The  $^{40}\text{Ar}/^{39}\text{Ar}$  muscovite age of 536-546 Ma obtained for the muscovite-schist metamorphosed under greenschist facies conditions indicates that the regional thermal regime was maintained up to the early-Cambrian in the area. The minimum fast cooling rate of 25°C/Myr defined in the investigated area is constrained by the  $^{40}\text{Ar}/^{39}\text{Ar}$  biotite analysis ( $549.2 \pm 3.9$  Ma) from a syn-to late-kinematic granodiorite intrusion. The very rapid magma emplacement occurred into relatively shallow crustal levels through the associated strike-slip faults. The Transbrasiliano Lineament would have facilitated the rapid unroofing of the study area and thus, the syn-orogenic deposition in a foreland domain at the final phase of West Gondwana amalgamation. The data provide evidence of a late convergent basin that was formed

coevally to the growth of a contemporaneous magmatic arc and active margin between the Amazonian Craton and the eastern blocks/cratons (São Francisco-Congo and Rio de la Plata cratons and Paranapanema Block) to Cambrian times. Our results support the existence of the younger Clymene Ocean and subsequent Cambrian final assembly of West Gondwana.

**Keywords:** West Gondwana; Sedimentary provenance; Syn-orogenic basin; Thermal conditions; Tocantins Province; Paraguay Belt; Clymene Ocean.

## 5.1.INTRODUCTION

Collisional orogens result from a complex geological and dynamic process, which is essential to understand in the frame of the plate tectonic theory (Wilson, 1966). The rocks caught between colliding blocks record remarkable features during and after the convergent phase, which are often related to uplift, erosion, deposition, magmatism, and metamorphism. During tectonically active periods, the large debris accumulation from the same terrain is often linked to the uplift event of such source area (Ring *et al.*, 1999; Cawood *et al.*, 2012). The syn-orogenic basins are examples of the sedimentation that occurs coevally with an accretionary event, deposited frequently in the foreland domain of the orogen (Ingersoll *et al.*, 1995, 2013). Among the different tools used to investigate the syn-orogenic basins, the sedimentary provenance study appears to combine a large spectrum of geological data, so that the age spectra of detrital zircon from sedimentary packages can reflect the tectonic setting of the basin in which they were deposited (Hawkesworth *et al.*, 2009).

The relationships between source rocks and detrital zircon age populations are central to unravel the sedimentary recycling pathways and paleogeography through orogenic terrains and constrain basin depositional processes (Hawkesworth *et al.*, 2009; Cawood *et al.*, 2012).

High nearby uplifted mountain ranges and rapid weathering processes are the main mechanisms that control the sedimentation of a basin that displays more than 50% of a single population of zircon ages (Cawood *et al.*, 2012). Thus, recently formed magmatic arcs in a convergent boundary are more likely to undergo fast erosion, loading a syn-magmatic/orogenic sedimentary basin (Stern, 1994; Cawood *et al.*, 2012). The worldwide depositional systems that well represent this depositional system type are the Himalaya-Bengal, Appalachian-Ouachita and Caledonides areas (Dewey and Kidd, 1974; Graham *et al.*, 1975; Moiola and Shanmugam, 1984; Ingersoll *et al.*, 1995, 2003; Murphy *et al.*, 2019).

The Late-Ediacaran and Early Cambrian assembly periods of Gondwana are still matter of debate, since this interval corresponds to recurring late consumption of local oceans and collision processes of small blocks and/or terrains (Meet, 2003; Pisarevsky *et al.*, 2008; Cordani *et al.*, 2013; Schmitt *et al.*, 2018). In the South American context, the traditional view of the West Gondwana final amalgamation phase is typically associated to the closure of the long-lived Goiás-Pharusian ocean at ca. 620 Ma as the result of the assembly of the Amazonian-West African, São Francisco-Congo, Rio de la Plata cratons and Paranapanema Block (Kröner and Cordani, 2003; Cordani *et al.*, 2009, 2013).

Alternatively, the last closure of West Gondwana has been also linked to the consumption of a younger ocean between the Amazonian-West Africa and proto-Gondwana, labelled as Clymene Ocean (Trindade *et al.*, 2003, 2006), which can have generated several magmatic arcs along the Araguaia-Paraguay-Pampean belts, constrained with a series of 555-500 Ma syn-to late tectonic granitoids from the Araguaia (Moura *et al.*, 1993; Gorayeb *et al.*, 2013; Alves *et al.*, 2019) and Paraguay (Godoy *et al.*, 2010; Leite *et al.*, 2021) belts and western Argentina (Rapela *et al.*, 1998, 2007). Paleomagnetic, seismic, magnetotelluric and gravimetric evidence also remark the existence of such a Clymene Ocean, that would have shaped the final stage of West Gondwana assembly along a younger orogenic corridor (D'Agrella-Filho *et al.*,

1998, 2000; Soares *et al.*, 2006; Bologna *et al.*, 2011; Perarnau *et al.*, 2012; Assumpção *et al.*, 2013; Tohver *et al.*, 2010; Wen *et al.*, 2020).

The Paraguay Belt corresponds to a sequence of folded sedimentary rocks formed on a passive margin of the Amazonian Craton, which was thought to be the most obvious source area when considering potential sediment provenance (Alvarenga & Trompette, 1992). In this new contribution, we combined U-Pb, Sm-Nd and  $^{40}\text{Ar}/^{39}\text{Ar}$  isotopic analyses to clarify several aspects of the tectonic evolution of the easternmost portion of the Paraguay Belt, located close to the boundary of the Goiás Magmatic Arc, Brasília Belt. The main goals of this paper are to (1) obtain further information on maximum depositional ages of the metasedimentary rocks; (2) provide insights on the source areas from which the sediments have been shed; (3) give constraints on the thermal history on this portion of the Paraguay Belt, and finally, (4) discuss the existence of the Clymene Ocean at the onset of Cambrian times in the Tocantins Province, central Brazil.

## 5.2.GEOLOGICAL SETTING

The Paraguay Belt is an extensive geotectonic unit that belongs to a group of orogens formed during the Brasiliano-Pan-African Orogeny (Kennedy, 1964; Almeida, 1984), as a result of the amalgamation of Gondwana (Rogers, 1996) between 900 and 600 Ma (Brito Neves and Fuck, 2013; Figure 5.1A), after the fragmentation of the Rodinia supercontinent. Located in the central part of Western Gondwana, the Paraguay Belt, together with the Araguaia and Brasília belts, constitutes the Tocantins Province, formed in response to the assembly of the Amazonian and São Francisco cratons and the Rio Apa, Parnaíba and Paranapanema blocks (Almeida, 1984; Brito Neves and Fuck, 2013; Figure 5.1B).

The belt which is located on the outskirts of the Amazonian Craton is divided into northern and southern sectors by Cenozoic sediments of the Pantanal Basin as well as into lithotectonic domains. Structural analyses allow to characterize three structural domains in the Paraguay Belt (Figure 5.1C): internal, external and platform domains (Alvarenga and Trompette, 1993). Established stratigraphy and correlations indicate a gradual transition from a glacio-marine environment in the platform zone and glacio-marine with turbidity currents to a turbiditic environment in its innermost zone (Alvarenga, 1990; Alvarenga and Saes, 1992; Alvarenga & Trompette, 1993). Deformation and metamorphism intensity in the different units of the belt decreases toward the southern margin of the Amazonian Craton (Alvarenga, 1990; Tohver *et al.*, 2006). Different processes occur simultaneously in the northern and southern arms as results of the final stages of the belt evolution (Campanha *et al.*, 2011; Babinski *et al.*, 2018).

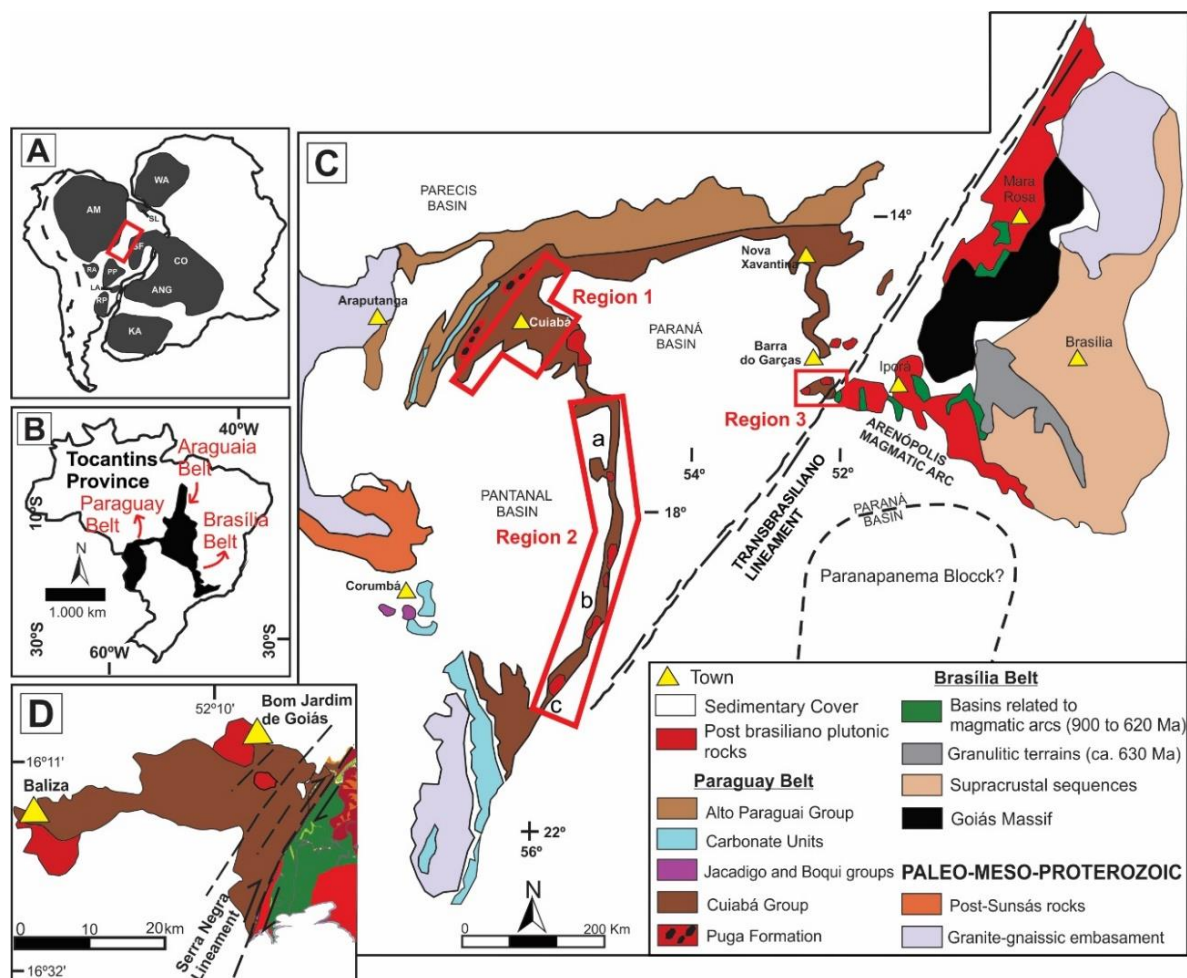


**Figure 5.1** - Geological sketch of the study area: (A) geotectonic context of the formation of the Tocantins Province during the Brasiliano Orogeny. Cratons are shown in dark gray (modified from Vaughan and Pankhurst, 2008); (B) location of the Tocantins Province in the Brazilian territory; (C) simplified geological map of the Paraguay Belt (modified from Ruiz et al., 2010). Red polygons indicate three different regions in the Paraguay Belt; (D) simplified geological map of the investigated area, which corresponds to the Region 3 in the Figure 1C.

The Nova Xavantina metavolcanic sedimentary sequence, described as basement of the Cuiabá Group, records the initial stages of sedimentation associated to the rupture of the Rodinia Supercontinent. This unit shows a W-E trend and is characterized as a basal volcano-sedimentary succession related to initial seafloor spreading or retro-arc basin (Pinho, 1990; Lacerda Filho *et al.*, 2004). The 822, 771 and 750 Ma Tonian U-Pb ages for the metavolcanic rocks of the Nova Xavantina unit can be associated to the first sedimentary deposits in the

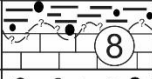


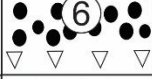
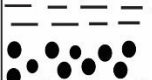
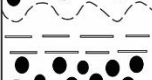



Paraguay Belt (Dantas *et al.*, 2007; Silva, 2018; Silva *et al.*, 2020). The analyzed black slate in the Planalto da Serra region was associated to strong weathering of juvenile material that provided a Re-Os age of  $784\pm 8$  Ma (Manoel *et al.*, 2020). Such data indicate a potential link with the early rifting of the Gondinia supercontinent.

The internal zone is essentially represented by the Cuiabá Group, described as the basal folded sequence, followed by the Puga Formation and by the Araras Group carbonate deposits in the proximity of the external/plataformal zone. The platform units of the external zone occur over the cratonic area and attest to the existence of a foreland basin, comprising the sedimentary rocks of the Alto Paraguay Group, which records exhumation and final sedimentation at  $541\pm 7$  Ma using the U-Pb method in detrital zircon grains (Figure 5.1C; Alvarenga & Saes, 1992; Tokashiki & Saes, 2008; Bandeira *et al.*, 2012). The late stages of the belt evolution are associated with a series of granitic intrusions into the Cuiabá Group, dated between 558 and 509 Ma and showing syn- to late-collisional signatures (Godoy *et al.*, 2010; McGee *et al.*, 2012; Leite, *et al.*, 2021). Ages of metamorphism within the core of the Paraguay Belt range from ca. 540 to 490 Ma (Geraldés *et al.*, 2008; Tohver *et al.*, 2010).

### **The Cuiabá Group**

The Cuiabá Group (Figure 5.2) comprises a sedimentary succession that records the development of a passive margin on the southeastern Amazonian Craton, and a greenschist facies metamorphism related to the main collisional event (Almeida, 1984; Lacerda Filho *et al.*, 2004). The Cuiabá Group is stratigraphically divided into three formations: Campina de Pedra Formation, Acorizal Formation and the upper Coxipó Formation (Tokashiki & Saes, 2008). The rocks at base of the Cuiabá Group are typically described in the Region 1 of the belt (Figure 5.1C) and display detrital zircon ages varying from ca. 900 Ma to 1860 Ma of the Campina de

Pedra and Acorizal formations, dominantly derived from Mesoproterozoic sources (1200 to 1250 Ma; Babinski *et al.*, 2018).

|                             |                |   |  |   |   |                        |
|-----------------------------|----------------|---|--|---|---|------------------------|
| CUIABÁ GROUP                | PASSIVE MARGIN | Coxipó Fm.  | Guia Member  |  | Limestones, arenites and pelites                | Age (Ma)               |
|                             |                |   | Margazão Member  |  | Diamictites, arenites and pelites               | 652±5(a)               |
|                             |                |   |  |  |   | 923(b)                 |
|                             |                | Pai Joaquim Member  |   | Conglomerates, arenites and pelites   | 951(b)  |                        |
|                             |                | Acorizal Fm.  | Engenho/Cangas Member  |  | Massive Diamictite                              | 711±11(a)              |
|                             |                |   |  |  |   | 934(b)                 |
|                             |                |   | Transition Layer   |  | Diamictite, conglomerates, arenites and pelites | 844±14(a)<br>810±11(a) |
|                             |                | Pindaival Member  |  | Conglomerates and litharenites  | 923(b)  |                        |
| Campina de Pedras Formation | SYNT           |  | Pelites, arenite and carbonaceous pelites  | 905±5(a)  |   |                        |
|                             |                |   |  | 927(b)  |   |                        |
| Nova Xavantina Unit         |                |   |  |   |   |                        |

**Figure 5.2** - Schematic model illustrating the stratigraphic column of the northern segment of the Cuiabá Group (modified after Manoel *et al.* 2020 and Tokashiki and Saes, 2008). The unit numbers correspond to the subunits of Luz *et al.* (1980). The syn-rift formations are composed of the units 1 and 2: intercalated pelites and carbon-rich pelites, marbles and metagraywackes; The passive margin formations comprise the units 3 to 8. Unit 3 and 5: metaconglomerates, metarenites and graded phyllites, meta-arkoses and quartzites; Unit 4: metadiamicrites (Engenho Facies) and psammitic to pelitic metarhythmites with dropstones (Cangas Facies); Units 6, 7 and 8: phyllites, metadiamicrites, quartzites (Mata-Mata Facies) and marbles (Guia Facies). The ages (Ma) represent U-



Pb detrital zircon ages of each unit, the youngest concordant age of which is interpreted as maximum depositional age: (a) Babinski *et al.*, (2018); (b) Batalha (2017).

The Coxipó Formation, defined as the upper Cuiabá Group, records the maximum depositional age with the younger detrital zircon analyses at 923 Ma (Batalha, 2016). Babinski *et al.* (2018) reported U-Pb zircon ages from the same formation and dated the youngest sediment input throughout the Cuiabá Group at  $652\pm 5$  Ma, interpreted as a post-Sturtian deposition. Samples of the Cuiabá Group exposed in the center-south of the Paraguay Belt (south of the São Vicente Granite and vicinity of the Paraná Basin; Region 2; Figure 5.1C) have a maximum depositional age of  $602\pm 13$  Ma (Pelosi, 2017) and  $523\pm 5$  Ma (Vasconcelos, 2018), and display ca. 60-70% of the zircon grains derived from Neoproterozoic sources.

The data presented in this work correspond to the poorly investigated metasedimentary rocks in the easternmost part of the Paraguay Belt (Figure 5.1D). The Cuiabá Group in the vicinity of Bom Jardim de Goiás (Region 3) comprises fine-grained metasedimentary rocks, such as phyllites and schists associated with fine-grained quartzite lenses (Seer, 1985; Pimentel and Fuck, 1987). The Transbrasiliiano Transcontinental Lineament (TBL) has behaved as a major zone of weakness to accommodate the Neoproterozoic collisional stress at the end of the Brasiliano Orogeny (Fuck *et al.* 2008; Brito Neves and Fuck, 2013; Curto *et al.*, 2014, 2015). The strike-slip fault system related to TBL in the studied area corresponds to the contact between the southwestern segment of the Goiás Magmatic Arc, Brasília Belt and the Paraguay Belt (Seer, 1985; Guimarães *et al.*, 2012; Curto *et al.*, 2014, 2015; Leite *et al.*, 2021). In the Tocantins Province, the large TBL affects part of the three mobile belts, the Paraguay, Araguaia, and Brasília belts, reworking different protoliths along large dextral mylonitic shear zones and their ramifications (Dantas *et al.*, 2007; Fuck *et al.* 2008; Cordani *et al.*, 2013).

Seer (1985) described the occurrence of different granitic bodies intruding the metasedimentary host rocks of the Cuiabá Group in the study region and recently, Leite *et al.* (2021) associated their evolution to the activity of the Transbrasiliano Lineament fault system and last compressional constraints. The present study seeks to present the source-to-sink relationship in the Region 3 (Figure 5.1C) through the determination of detrital zircon populations U-Pb ages, as well as to define the probable depositional setting. The investigated area is a key portion of the Paraguay orogen, where the low-grade metamorphic rocks contain micas suitable for  $^{40}\text{Ar}/^{39}\text{Ar}$  dating, by contrast with the Cuiabá Group formations elsewhere that are mostly mica free. The combination of U-Pb and Ar-Ar isotopic methods is an effective tool to constrain the orogenic evolution of the study area, providing substantial clues to terranes sources, thermal history, and tectonic evolution in the central Tocantins Province.

### 5.3.MATERIALS AND METHODS

The four collected samples for U-Pb LA-ICP-MS isotopic analyses are located in different portions of the investigated area (see Figure 5.3). The samples were mechanically crushed and subsequently sieved. The fraction smaller than 500  $\mu\text{m}$  was panned in order to obtain a heavy mineral separate, which was submitted to a Franz magnetic separator. Under binocular lenses a concentrate of zircon was prepared and subsequently mounted in epoxy. These mounts were polished to expose the interior of the grains and carefully cleaned with diluted  $\text{HNO}_3$ . The polished zircon surfaces were imaged using backscattered electron microscopy (BSE; Figure 6), with a FEI QUANTA 450 scanning electron microscope (SEM) at the same laboratory. The U-Pb isotopic analyses were performed on zircon grains at the UnB Laboratory of Geochronology (Supplementary Table 5.1), using a Thermo-Fisher Neptune HR-MC-ICP-MS coupled with an Nd:YAG UP213 New Wave laser ablation system. The zircon

isotopic analyses were carried out by the standard-sample bracketing method (Albarède *et al.*, 2004), using the GJ-1 standard zircon (Jackson *et al.*, 2004) in order to quantify the amount of ICP-MS fractionation. During the analytical sessions, the zircon standard 91500 (Wiedenbeck *et al.*, 2004) was also analyzed as an external standard. The tuned masses were 238, 207, 206, 204 and 202, and the integration time was one second and the ablation time was 40 seconds. 30  $\mu\text{m}$  spot size was used and the laser setting was 10 Hz and 2-3  $\text{J}/\text{cm}^2$ . The  $^{206}\text{Pb}/^{207}\text{Pb}$  and  $^{206}\text{Pb}/^{238}\text{U}$  ratios were time-corrected. Helium mixed with argon was used to flow the gas inside the equipment. Corrections of common Pb were not necessary due to low signals of  $^{204}\text{Pb}$  (<30 cps) and high  $^{206}\text{Pb}/^{204}\text{Pb}$  ratios, but their values were taken into account to select only results with discordance of less than 10% for U-Pb plots. For plots of apparent ages,  $^{206}\text{Pb}/^{238}\text{U}$  ages from grains younger than 1000 Ma were used, and  $^{207}\text{Pb}/^{206}\text{Pb}$  ages from grains older than 1000 Ma. The raw data were processed using the Chronus version 2.0 (Oliveira *et al.*, 2015) and the concordia diagrams ( $2\sigma$  error ellipses), probability density plots, and weighted average ages were calculated using the Isoplot-3/Ex software (Ludwig, 2008).

Eight samples were analyzed by the Sm-Nd method, and of these samples, four correspond to those analyzed by the U-Pb method (see Figure 3). The whole rock Sm-Nd isotopic analyses were carried out at the Laboratory of Geochronology at Universidade de Brasília, following the procedures described by Gioia and Pimentel (2000). Approximately 50 Mg of powder sample were mixed with  $^{149}\text{Sm}$ - $^{150}\text{Nd}$  spike solution and dissolved in Saville x capsules by means of acid attacks with HF,  $\text{HNO}_3$  and HCl. Sm and Nd extraction of whole rock samples followed conventional cation exchange techniques by using Teflon columns containing LN-Spec resin (HDEHP-diethylhexyl phosphoric acid supported on PTFE powder). The samples were loaded with nitric acid on Re double evaporation filaments assemblies and the isotopic measurements were carried out on a multi-collector Finnigan MAT 262 mass spectrometer in static mode. The uncertainties for Sm-Nd and  $^{143}\text{Nd}/^{144}\text{Nd}$  ratios were lower

than  $\pm 0.5\%$  ( $2\sigma$ ) and  $\pm 0.005\%$  ( $2\sigma$ ), respectively, based on repeated analyses of international BHVO-1 and BCR-1 rock standards. The  $^{143}\text{Nd}/^{144}\text{Nd}$  ratios were normalized to  $^{146}\text{Nd}/^{144}\text{Nd}$  ratio of 0.7219, and the decay constant used was  $6.54 \times 10^{-12} \text{a}^{-1}$ . The  $T_{\text{DM}}$  values were calculated using the model proposed by De Paolo (1981) and the procedure blanks for Nd were higher than 100 pg.

For  $^{40}\text{Ar}/^{39}\text{Ar}$  analyses, the samples preparation was performed without chemical treatment to avoid any impact on the structure of the minerals. Biotite and muscovite grains were carefully handpicked under a stereo microscope in the 80-130  $\mu\text{m}$  fractions and conditioned in aluminium pockets. Samples were irradiated for 20 h in the core of the TRIGA Mark-II reactor of Pavia University (Italy), with several aliquots of the Taylor Creek sanidine standard ( $28.61 \pm 0.32 \text{ Ma}$ ; Renne, 2011) as flux monitor. Argon isotopic interferences on K and Ca were obtained by irradiation of KF and  $\text{CaF}_2$  (correction factors:  $(^{40}\text{Ar}/^{39}\text{Ar})_{\text{K}} = 0.00969 \pm 0.00038$ ,  $(^{38}\text{Ar}/^{39}\text{Ar})_{\text{K}} = 0.01297 \pm 0.00045$ ,  $(^{39}\text{Ar}/^{37}\text{Ar})_{\text{Ca}} = 0.0007474 \pm 0.000021$  and  $(^{36}\text{Ar}/^{37}\text{Ar})_{\text{Ca}} = 0.000288 \pm 0.000016$ ). The  $^{40}\text{Ar}/^{39}\text{Ar}$  dating was performed at Géosciences Montpellier, Université de Montpellier, France. Mass discrimination was calculated using a value of  $^{40}\text{Ar}/^{36}\text{Ar}$  ratio of 298.6. The analytical procedure consists of an i) IR- $\text{CO}_2$  laser of 100 kHz used at 5-15% for 60 seconds of heating at variable power; (ii) a lens system for beam focusing; (iii) a steel chamber, maintained at  $10^{-8}$ - $10^{-9}$  mbar, with a drilled copper plate; (iv) an inlet line for purification of gases including two Zr-Al getters and a nitrogen cold finger and (v) a multi-collector mass spectrometer (Argus VI from Thermo-Fisher). The collector system is composed of 5  $10^{12}$  ohm Faraday cups (for  $^{39}\text{Ar}$  to  $^{37}\text{Ar}$ ) and one CDD (Compact Discrete Dynode) detector for accurate measurement of  $^{36}\text{Ar}$ . One blank analysis was performed every three samples to measure the argon background within the system. A custom-made software (Labview) was used to control the laser intensity, the timing of extraction/purification and the data acquisition. The Logiciel ArArCalc software© v2.5.2

(Koppers, 2002) was used for data reduction and plotting. The plateau criteria involved at least 50% of the  $^{39}\text{Ar}$  released in three or more contiguous steps, with ages that agree within two sigma errors and include the error on the irradiation factor J. A complete set of isotopic results is given in the Supplementary Table 2.

## 5.4.RESULTS

### 5.4.1. *Field observations and Petrography*

The investigated detrital rocks crop out in the vicinity of Bom Jardim de Goiás and occur sometimes covered by sandstones of the Devonian Furnas Formation of the Paraná Basin (Figure 5.3). A sequence of very fine- to fine-grained foliated layers of meta-pelites intercalated with pure or micaceous meta-psammities were observed. The alternating greenish and gray centimeter-thick folded layers generate a laminated structure (Figure 5.4A), corresponding to compositional variation of mudstone and sandstone in well-marked bedding planes. The most abundant lithofacies are labeled as muscovite-chlorite phyllite (Figure 5.4B) and muscovite-biotite schist (Figure 5.4C). Subordinately, fine-grained quartzites are mainly composed of angular to sub-rounded grains of polycrystalline quartz in addition to very fine-grained muscovite (Figure 5.4D).

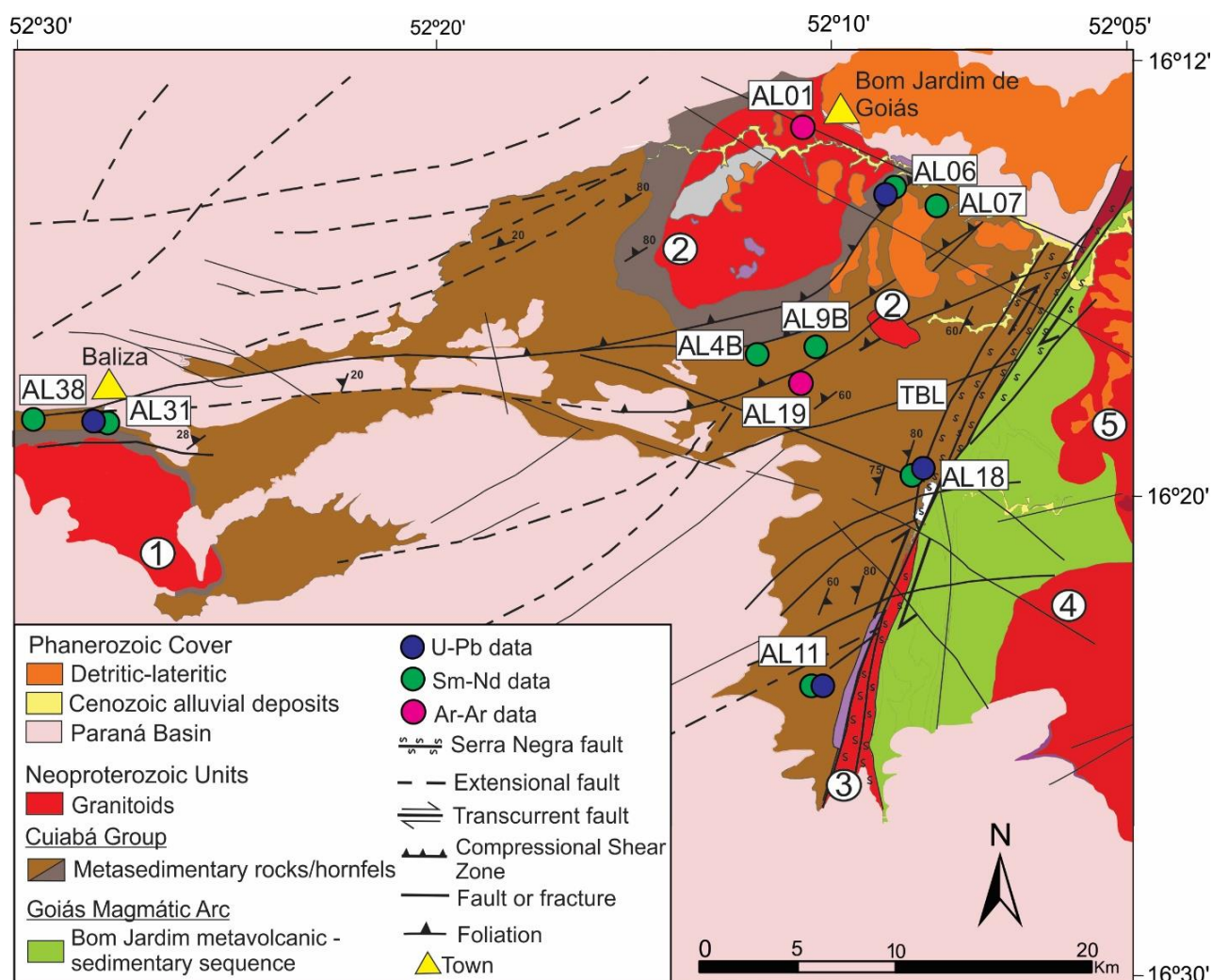


**Figure 5.3** - Geological map of the study area (modified from CPRM, 2017). Colored dots indicate the samples localities. Circled numbers refer to granitoids: 1 – monzogranite (Leite *et al.*, 2021); 2- granodiorite and quartz-monzodiorite (Leite *et al.*, 2021); 3- Macacos syenogranite (Seer, 1987); 4- Serra Negra syenogranite (Guimarães, 2012); 5- Indaiá tonalite (CPRM, 2017). See text for details.

The mineralogical composition of the studied rocks is basically quartz, mica (muscovite, biotite), chlorite and feldspar (microcline and plagioclase), while tourmaline, apatite, sericite and zircon are accessory minerals. The quartz grains are subhedral, up to 0.5 mm in size, while the phyllosilicates are not larger than 0.3 mm. The mineral paragenesis testifies essentially to greenschist metamorphic conditions in the area, varying from the chlorite up to the biotite zone. The local occurrence of coarser-grained sillimanite-cordierite schist correspond to the presence of a hornfels aureole surrounding the granodiorite plutons (Figure 5.4E-F).

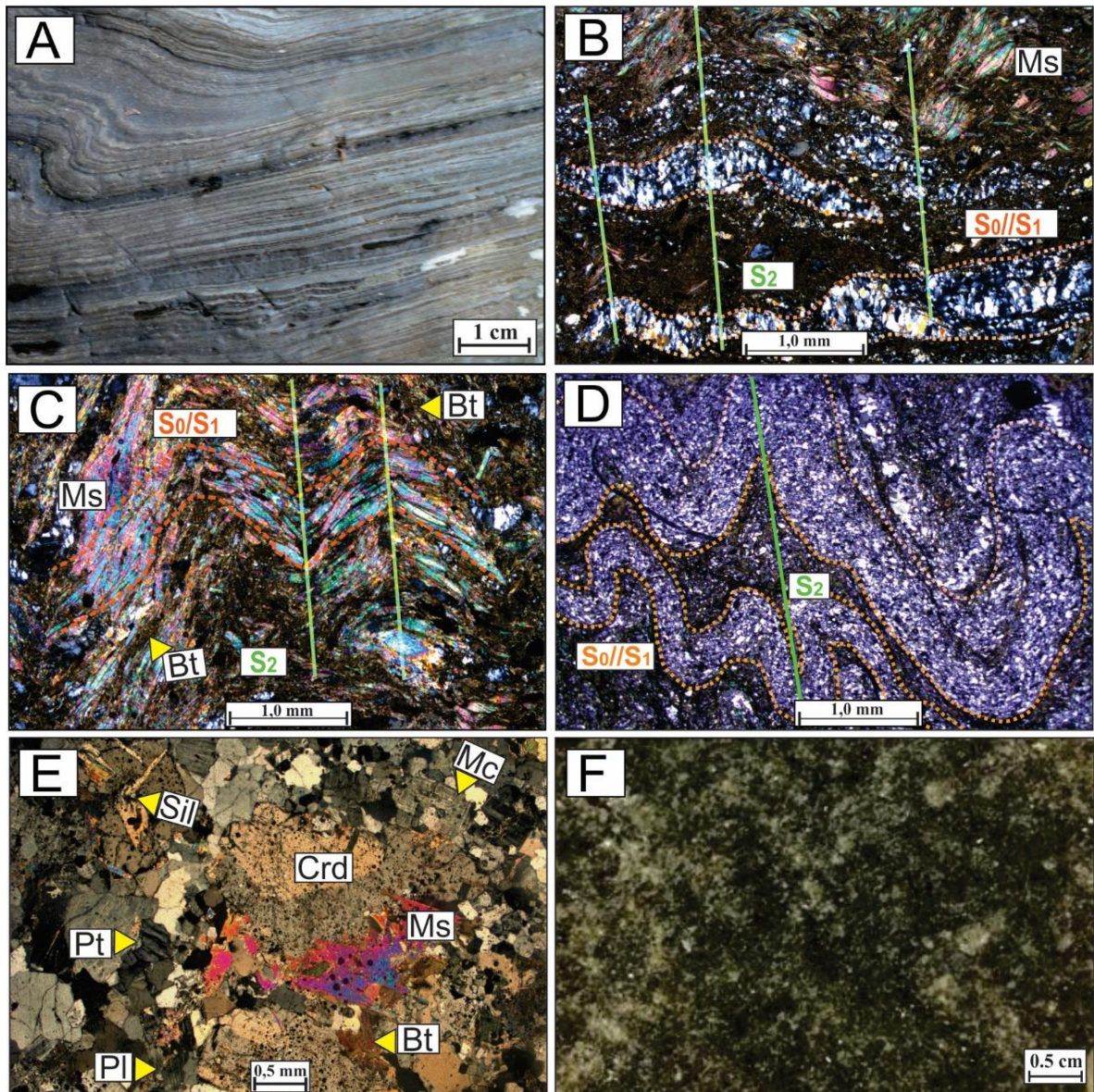


**Figure 5.4** – (A) macroscopic field aspect of the laminated structure, that corresponds to bedding planes and compositional variation and rhythmic alternation between quartzite and phyllite; (B) photomicrography of muscovite-chlorite phyllite with foliations highlighted and layers of polycrystalline quartz intercalated with mica; (C) photomicrography of muscovite-biotite schist. Oriented and metamorphic mica reach up to the biotite zone – sample AL019; (D) photomicrography of the quartzite portion of polycrystalline quartz and well-marked open folds; (E) photomicrography of schist with cordierite and sillimanite – sample AL06; (F) hand specimen of dark-colored fine to medium-grained schist – sample AL06. Mineral abbreviations are after Whitney and Evans (2010). Pt= perthite.

The first  $F_1$  deformational phase generated the regional foliation  $S_1$  (parallel to  $S_0$ ) and is associated with west verging tectonic structures of crenulation cleavage. The second  $F_2$  phase yielded soft and open folds (D2), the axial-planes of which are orthogonal to  $S_0/S_1$  and parallel to  $S_2$  (Figure 5.4C-D, 5.5A). The easternmost portion of the area records the ductile-brittle influence of the TBL and is taken as the  $F_3$  deformational phase (Table 5.1). The strike-slip dextral deformation along the TBL overprinted the older structures, transposing axial planes of D2 (Figure 5.5B). The mylonitic foliation is characterized by rotated sigmoidal quartz and feldspar porphyroclasts (Figure 5.5C). Following the mylonite classification of Sibson (1977), we recognized criteria of chlorite-muscovite mylonite and chlorite-muscovite ultramylonite (Figure 5.5D; sample AL18).

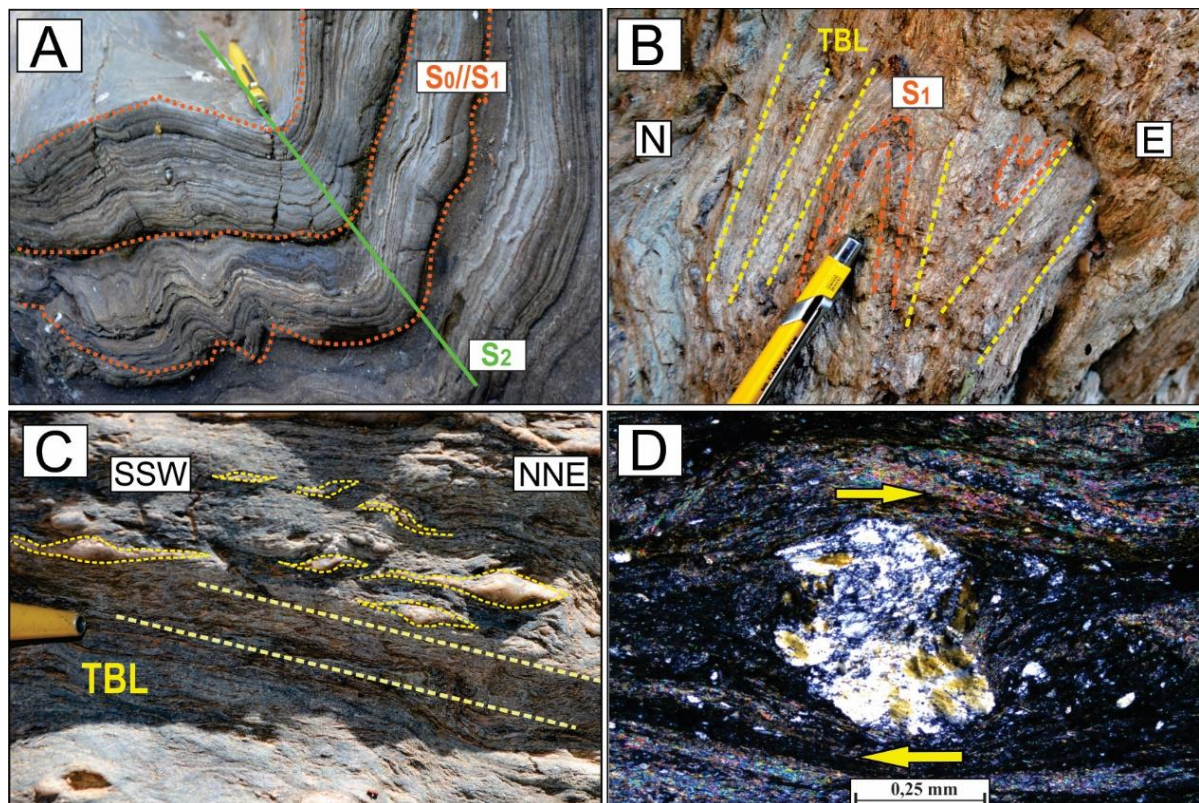


**Figure 5.5** – (A) photograph of open fold with deformation phases highlighted; (B) photograph of the preserved axial planes of the D2, resulting in relict axial planes  $S_1$  foliation overprinted by TBL; (C) outcrop photograph representing the TBL trend in the rocks and the rotated porphyroclasts with sigmoidal structures; (D) photomicrography showing mylonitic foliation with rotated quartz phenoclast – sample AL18.



**Table 5.1** – Summary of the deformation phases and general structural characteristics in the investigated area.

|  | Foliation type      | Preferential orientation | Deformational characteristics                                     | Associated fold                                   |
|--|---------------------|--------------------------|---|---|
| F <sub>1</sub> - S <sub>0</sub> //S <sub>1</sub> | crenulation         | N42E/82NW                | recrystallization and flattening of                               | -   |
|  | cleavage            | N50E/60NW                | quartz grains and formation of                                    |   |
|  |                     | N42E/78NW                | granoblastic and lepidoblastic texture. Biotite metamorphic zone. |   |
| F <sub>2</sub> – S <sub>2</sub>                  | slate               | N45W/75NE                | intracrystalline deformation in quartz                            | Open folds (D2) with axial plane orthogonal to S1 |
|  | cleavage            | N33W/60NE                | grains and orientation of   |   |
|  |                     | N21W/71NE                | phyllosilicates   |   |
| F <sub>3</sub> - TBL                             | slate               | N28E/21SW                | granolepidoblastic texture forming                                | Overprint D2, S1 and S2.                          |
|  | cleavage            | N40E/35SW                | in phyllosilicate-rich layers that                                |   |
|  | and                 | N35E/17SW                | surround mantled quartz   |   |
|  | mylonitic foliation |                          | porphyroclasts. Dextral sense.                                    |   |

#### 5.4.2. U-Pb geochronology of detrital zircon grains

The four analyzed samples with the LA-ICP-MS technique were collected from fine-grained banded phyllites and schists. Samples AL18 and AL11 are located in the easternmost portion of the area, while samples AL06 and AL31 were collected in the north and west, respectively (e. g. Figure 5.3). The results of 465 U-Pb dating spots on detrital zircon grains are presented in Table 5.2. Out of these 465 U-Pb dating analyses, 140 zircon grains were excluded from the calculation due to their high age discordance (outside of the 96-103% interval) and/or high common Pb. The analyzed detrital zircon grains are colorless or display light yellow or

brown colors and subhedral to euhedral shapes. Their grain size varies from 50 to 320  $\mu\text{m}$  in length and length/width ratios mostly of ca. 2 to 3. In general, the youngest analyzed grains (up to 700 Ma) present smaller size, while the older ones, recording Paleoproterozoic and Archean ages, are larger-sized grains (Figure 5.6).

**Table 5.2** - Data of U-Pb analyses performed through LA-ICP-MS on detrital zircon from the investigated metasedimentary rocks.

| SAMPLE    | AL18     |       |             |             |       |            |       |            |       |       |               |        |            |        |            |        |           |
|-----------|----------|-------|-------------|-------------|-------|------------|-------|------------|-------|-------|---------------|--------|------------|--------|------------|--------|-----------|
|           |          |       |             |             |       |            |       |            |       |       | Apparent ages |        |            |        |            |        |           |
| GRAIN     | <i>f</i> | err   |             |             |       | err        |       | err        |       | Rho   | 207Pb/206Pb   |        | 206Pb/238U |        | 207Pb/235U |        | conc. (%) |
|           | 206 (%)  | Th/U  | 206Pb/204Pb | 207Pb/206Pb | (%)1  | 207Pb/235U | (%)1  | 206Pb/238U | (% 1) |       | 207Pb/206Pb   | 2 σ    | 206Pb/238U | 2 σ    | 207Pb/235U | 2 σ    |           |
| 047-ZR88  | 0,015    | 0.322 | 101051      | 0,057       | 0,847 | 0,651      | 1,241 | 0,083      | 0,828 | 0,667 | 498,052       | 37,109 | 511,575    | 8,145  | 509,140    | 9,918  | 100.48    |
| 028-ZR72  | 0,038    | 0.810 | 40867       | 0,061       | 0,958 | 0,800      | 1,644 | 0,096      | 1,283 | 0,781 | 623,346       | 41,070 | 589,640    | 14,450 | 596,675    | 14,778 | 98.82     |
| 124-ZR148 | 0,008    | 0.809 | 201532      | 0,061       | 0,609 | 0,805      | 1,229 | 0,096      | 1,002 | 0,815 | 637,127       | 26,088 | 589,796    | 11,289 | 599,692    | 11,106 | 98.35     |
| 122-ZR146 | 0,013    | 0.421 | 122769      | 0,061       | 0,760 | 0,805      | 1,326 | 0,096      | 1,021 | 0,770 | 627,651       | 32,588 | 592,430    | 11,557 | 599,811    | 11,976 | 98.77     |
| 116-ZR140 | 0,013    | 0.799 | 124218      | 0,061       | 0,488 | 0,807      | 0,962 | 0,097      | 0,742 | 0,771 | 623,582       | 20,973 | 594,512    | 8,421  | 600,620    | 8,704  | 98.98     |
| 072-ZR107 | 0,030    | 0.488 | 51548       | 0,062       | 0,980 | 0,816      | 1,541 | 0,096      | 1,129 | 0,733 | 656,957       | 41,779 | 592,272    | 12,772 | 605,881    | 14,011 | 97.75     |
| 121-ZR145 | 0,018    | 0.298 | 85206       | 0,061       | 0,651 | 0,817      | 1,138 | 0,097      | 0,857 | 0,753 | 647,096       | 27,837 | 595,626    | 9,746  | 606,482    | 10,366 | 98.21     |
| 115-ZR139 | 0,006    | 0.611 | 256428      | 0,060       | 0,802 | 0,807      | 1,189 | 0,097      | 0,795 | 0,669 | 609,473       | 34,486 | 598,402    | 9,084  | 600,753    | 10,751 | 99.61     |
| 023-ZR18  | 0,027    | 0.797 | 58162       | 0,060       | 1,136 | 0,807      | 1,438 | 0,098      | 0,800 | 0,556 | 603,458       | 48,780 | 599,931    | 9,162  | 600,703    | 12,998 | 99.87     |
| 070-ZR105 | 0,021    | 0.731 | 74044       | 0,060       | 0,674 | 0,812      | 1,078 | 0,098      | 0,755 | 0,701 | 615,348       | 28,980 | 600,116    | 8,652  | 603,348    | 9,783  | 99.46     |
| 055-ZR44  | 0,084    | 0.106 | 18489       | 0,061       | 0,573 | 0,817      | 1,417 | 0,098      | 1,242 | 0,876 | 628,373       | 24,618 | 600,735    | 14,242 | 606,593    | 12,905 | 99.03     |
| 051-ZR40  | 0,007    | 0.872 | 235773      | 0,061       | 0,464 | 0,820      | 0,914 | 0,098      | 0,695 | 0,760 | 634,269       | 19,921 | 600,914    | 7,975  | 607,986    | 8,348  | 98.84     |
| 031-ZR75  | 0,052    | 0.818 | 30152       | 0,061       | 1,273 | 0,830      | 1,718 | 0,098      | 1,093 | 0,636 | 648,494       | 54,232 | 603,978    | 12,595 | 613,468    | 15,764 | 98.45     |
| 030-ZR74  | 0,023    | 0.547 | 66458       | 0,061       | 0,633 | 0,824      | 1,084 | 0,098      | 0,799 | 0,737 | 628,318       | 27,145 | 605,593    | 9,230  | 610,443    | 9,924  | 99.21     |
| 017-ZR12  | 0,036    | 0.385 | 43322       | 0,061       | 0,804 | 0,823      | 1,159 | 0,099      | 0,748 | 0,645 | 624,293       | 34,500 | 606,100    | 8,651  | 609,988    | 10,603 | 99.36     |

|                  |       |       |        |       |       |       |       |       |       |       |         |        |         |        |         |        |        |
|------------------|-------|-------|--------|-------|-------|-------|-------|-------|-------|-------|---------|--------|---------|--------|---------|--------|--------|
| 117-ZR141        | 0,026 | 0.442 | 59805  | 0,062 | 1,010 | 0,841 | 1,555 | 0,099 | 1,122 | 0,722 | 665,037 | 42,975 | 607,366 | 13,003 | 619,741 | 14,372 | 98.00  |
| 092-ZR121        | 0,037 | 1.291 | 42096  | 0,060 | 1,054 | 0,817 | 1,666 | 0,099 | 1,236 | 0,742 | 603,075 | 45,275 | 607,447 | 14,318 | 606,558 | 15,156 | 100.15 |
| 062-ZR51         | 0,012 | 0.483 | 131286 | 0,061 | 0,510 | 0,833 | 1,134 | 0,099 | 0,943 | 0,832 | 638,781 | 21,848 | 609,004 | 10,959 | 615,387 | 10,444 | 98.96  |
| 060-ZR49         | 0,017 | 0.498 | 90426  | 0,060 | 1,025 | 0,816 | 1,339 | 0,099 | 0,777 | 0,580 | 592,393 | 44,153 | 609,013 | 9,025  | 605,538 | 12,175 | 100.57 |
| 106-ZR132        | 0,016 | 0.596 | 98507  | 0,062 | 0,802 | 0,846 | 1,152 | 0,099 | 0,740 | 0,642 | 667,614 | 34,156 | 609,719 | 8,603  | 622,182 | 10,692 | 98.00  |
| <b>054-ZR92</b>  | 0,023 | 0.354 | 68330  | 0,060 | 0,834 | 0,818 | 1,231 | 0,099 | 0,826 | 0,671 | 591,577 | 35,949 | 610,944 | 9,625  | 606,881 | 11,214 | 100.67 |
| 059-ZR48         | 0,019 | 1.556 | 82939  | 0,062 | 1,201 | 0,846 | 1,568 | 0,099 | 0,937 | 0,597 | 664,400 | 51,058 | 611,210 | 10,920 | 622,674 | 14,544 | 98.16  |
| <b>030-ZR23</b>  | 0,007 | 0.338 | 213582 | 0,061 | 0,381 | 0,840 | 0,813 | 0,100 | 0,615 | 0,757 | 647,058 | 16,310 | 611,517 | 7,175  | 619,164 | 7,521  | 98.76  |
| <b>004-ZR2</b>   | 0,020 | 0.409 | 78057  | 0,061 | 0,770 | 0,843 | 1,164 | 0,100 | 0,791 | 0,679 | 645,900 | 32,908 | 613,801 | 9,255  | 620,727 | 10,783 | 98.88  |
| 043-ZR34         | 0,026 | 0.646 | 60377  | 0,061 | 0,961 | 0,841 | 1,484 | 0,100 | 1,069 | 0,720 | 638,382 | 41,073 | 614,453 | 12,522 | 619,621 | 13,721 | 99.17  |
| <b>061-ZR50</b>  | 0,013 | 0.639 | 119700 | 0,060 | 0,521 | 0,832 | 0,919 | 0,100 | 0,660 | 0,718 | 605,592 | 22,441 | 617,013 | 7,765  | 614,608 | 8,454  | 100.39 |
| <b>056-ZR94N</b> | 0,018 | 0.641 | 85255  | 0,061 | 0,627 | 0,848 | 0,986 | 0,101 | 0,665 | 0,674 | 645,900 | 26,816 | 617,594 | 7,826  | 623,732 | 9,168  | 99.02  |
| 012-ZR61         | 0,052 | 0.976 | 29806  | 0,060 | 3,888 | 0,837 | 5,388 | 0,101 | 3,711 | 0,689 | 603,709 | #####  | 621,154 | 43,876 | 617,446 | 49,247 | 100.60 |
| <b>019-ZR14</b>  | 0,003 | 0.061 | 572782 | 0,060 | 0,276 | 0,840 | 0,647 | 0,101 | 0,454 | 0,701 | 609,701 | 11,896 | 621,436 | 5,372  | 618,949 | 5,991  | 100.40 |
| <b>008-ZR6</b>   | 0,013 | 0.521 | 116535 | 0,061 | 1,014 | 0,851 | 1,225 | 0,101 | 0,579 | 0,473 | 639,376 | 43,302 | 621,531 | 6,859  | 625,426 | 11,405 | 99.38  |
| 103-ZR129        | 0,008 | 0.493 | 206449 | 0,062 | 0,641 | 0,866 | 1,018 | 0,101 | 0,699 | 0,687 | 676,088 | 27,288 | 621,572 | 8,281  | 633,489 | 9,575  | 98.12  |
| <b>017-ZR64</b>  | 0,037 | 0.738 | 42270  | 0,060 | 0,691 | 0,843 | 1,120 | 0,102 | 0,800 | 0,714 | 611,966 | 29,703 | 623,368 | 9,500  | 620,946 | 10,376 | 100.39 |
| 105-ZR131        | 0,047 | 0.657 | 33414  | 0,061 | 1,221 | 0,857 | 1,793 | 0,102 | 1,260 | 0,702 | 646,132 | 52,054 | 623,806 | 14,969 | 628,689 | 16,740 | 99.22  |
| 009-ZR7          | 0,021 | 1.009 | 72980  | 0,059 | 1,001 | 0,833 | 1,478 | 0,102 | 1,023 | 0,692 | 575,335 | 43,215 | 625,893 | 12,200 | 615,085 | 13,595 | 101.76 |
| <b>065-ZR100</b> | 0,009 | 1.424 | 183045 | 0,061 | 0,527 | 0,854 | 0,947 | 0,102 | 0,694 | 0,733 | 626,805 | 22,627 | 626,955 | 8,290  | 626,957 | 8,839  | 100.00 |
| <b>041-ZR82</b>  | 0,006 | 0.471 | 254817 | 0,061 | 0,455 | 0,857 | 0,883 | 0,102 | 0,660 | 0,747 | 630,476 | 19,549 | 627,708 | 7,896  | 628,345 | 8,261  | 99.90  |
| <b>011-ZR60</b>  | 0,028 | 2.434 | 56144  | 0,061 | 0,761 | 0,859 | 1,137 | 0,102 | 0,759 | 0,668 | 636,087 | 32,576 | 627,762 | 9,079  | 629,609 | 10,640 | 99.71  |
| 052-ZR41         | 0,004 | 0.387 | 379113 | 0,061 | 0,326 | 0,860 | 0,767 | 0,102 | 0,587 | 0,766 | 639,032 | 13,981 | 627,810 | 7,027  | 630,289 | 7,192  | 99.61  |
| 057-ZR94B        | 0,051 | 0.349 | 30567  | 0,062 | 1,054 | 0,877 | 1,283 | 0,102 | 0,632 | 0,492 | 677,705 | 44,719 | 628,682 | 7,566  | 639,491 | 12,140 | 98.31  |

|           |       |       |        |       |       |       |       |       |       |       |         |        |         |        |         |        |        |
|-----------|-------|-------|--------|-------|-------|-------|-------|-------|-------|-------|---------|--------|---------|--------|---------|--------|--------|
| 83-ZR116  | 0,074 | 0.660 | 21000  | 0,061 | 1,071 | 0,856 | 1,594 | 0,103 | 1,121 | 0,703 | 623,490 | 45,878 | 629,223 | 13,434 | 628,012 | 14,879 | 100.19 |
| 96-ZR124B | 0,039 | 0.086 | 40161  | 0,063 | 0,460 | 0,885 | 1,046 | 0,103 | 0,864 | 0,825 | 691,651 | 19,569 | 629,933 | 10,360 | 643,590 | 9,951  | 97.88  |
| 040-ZR81B | 0,017 | 0.589 | 93136  | 0,062 | 0,840 | 0,876 | 1,234 | 0,103 | 0,825 | 0,669 | 666,407 | 35,762 | 630,797 | 9,916  | 638,658 | 11,670 | 98.77  |
| 063-ZR52  | 0,007 | 0.520 | 216328 | 0,060 | 0,386 | 0,852 | 1,065 | 0,103 | 0,920 | 0,865 | 607,926 | 16,652 | 630,884 | 11,059 | 625,934 | 9,925  | 100.79 |
| 054-ZR43  | 0,005 | 0.442 | 299333 | 0,060 | 0,835 | 0,850 | 1,316 | 0,103 | 0,948 | 0,720 | 597,281 | 35,952 | 631,962 | 11,408 | 624,475 | 12,242 | 101.20 |
| 019-ZR66  | 0,019 | 1.258 | 83676  | 0,060 | 0,829 | 0,853 | 1,384 | 0,103 | 1,045 | 0,755 | 604,157 | 35,666 | 632,179 | 12,582 | 626,126 | 12,899 | 100.97 |
| 039-ZR81N | 0,042 | 0.439 | 36675  | 0,062 | 0,749 | 0,891 | 1,107 | 0,104 | 0,726 | 0,656 | 677,865 | 31,842 | 638,097 | 8,822  | 646,962 | 10,565 | 98.63  |
| 104-ZR130 | 0,045 | 0.445 | 34314  | 0,060 | 1,463 | 0,862 | 2,085 | 0,104 | 1,439 | 0,690 | 606,273 | 62,678 | 638,316 | 17,477 | 631,340 | 19,515 | 101.10 |
| 016-ZR63  | 0,019 | 0.450 | 80940  | 0,061 | 0,834 | 0,872 | 1,312 | 0,104 | 0,942 | 0,718 | 627,673 | 35,755 | 639,403 | 11,462 | 636,858 | 12,373 | 100.40 |
| 052-ZR90B | 0,002 | 0.027 | 897666 | 0,062 | 0,362 | 0,899 | 0,763 | 0,105 | 0,561 | 0,735 | 667,515 | 15,451 | 646,448 | 6,898  | 651,194 | 7,326  | 99.27  |
| 021-ZR68N | 0,032 | 1.837 | 49320  | 0,061 | 1,029 | 0,896 | 1,505 | 0,107 | 1,035 | 0,687 | 636,395 | 43,974 | 653,481 | 12,853 | 649,693 | 14,398 | 100.58 |
| 016-ZR11B | 0,051 | 0.513 | 30466  | 0,063 | 0,495 | 0,944 | 0,890 | 0,108 | 0,640 | 0,719 | 713,188 | 20,980 | 663,748 | 8,067  | 675,144 | 8,758  | 98.31  |
| 077-ZR110 | 0,016 | 0.357 | 98291  | 0,061 | 0,517 | 0,920 | 1,006 | 0,109 | 0,780 | 0,775 | 648,933 | 22,110 | 666,216 | 9,866  | 662,324 | 9,765  | 100.59 |
| 078-ZR111 | 0,038 | 0.256 | 41003  | 0,061 | 1,700 | 0,939 | 2,074 | 0,111 | 1,129 | 0,544 | 648,187 | 72,180 | 679,792 | 14,562 | 672,545 | 20,298 | 101.08 |
| 118-ZR142 | 0,032 | 0.472 | 49334  | 0,063 | 1,023 | 1,001 | 1,779 | 0,115 | 1,407 | 0,791 | 721,690 | 43,130 | 698,977 | 18,626 | 704,428 | 17,992 | 99.23  |
| 055-ZR93  | 0,051 | 0.309 | 30303  | 0,063 | 0,818 | 0,995 | 1,440 | 0,115 | 1,125 | 0,782 | 705,112 | 34,602 | 699,899 | 14,921 | 701,176 | 14,527 | 99.82  |
| 058-ZR47  | 0,028 | 0.503 | 55651  | 0,063 | 0,841 | 0,998 | 1,248 | 0,115 | 0,844 | 0,676 | 708,552 | 35,586 | 700,731 | 11,202 | 702,631 | 12,618 | 99.73  |
| 015-ZR11N | 0,009 | 0.773 | 167703 | 0,064 | 0,353 | 1,007 | 0,823 | 0,115 | 0,644 | 0,783 | 729,055 | 14,947 | 700,806 | 8,555  | 707,598 | 8,371  | 99.04  |
| 035-ZR79  | 0,031 | 0.315 | 50681  | 0,062 | 0,950 | 0,994 | 1,313 | 0,116 | 0,827 | 0,630 | 681,602 | 40,339 | 706,737 | 11,063 | 700,789 | 13,249 | 100.85 |
| 042-ZR83  | 0,038 | 0.583 | 40887  | 0,063 | 0,915 | 1,011 | 1,227 | 0,117 | 0,729 | 0,594 | 700,472 | 38,731 | 712,427 | 9,831  | 709,592 | 12,494 | 100.40 |
| 012-ZR10  | 0,008 | 0.624 | 193129 | 0,064 | 0,482 | 1,052 | 0,845 | 0,119 | 0,587 | 0,695 | 737,543 | 20,330 | 727,550 | 8,071  | 730,043 | 8,778  | 99.66  |
| 020-ZR67  | 0,054 | 0.342 | 28956  | 0,063 | 2,031 | 1,035 | 2,983 | 0,120 | 2,153 | 0,722 | 700,573 | 85,325 | 728,091 | 29,615 | 721,420 | 30,578 | 100.92 |
| 005-ZR55  | 0,019 | 0.475 | 83519  | 0,063 | 0,710 | 1,032 | 1,044 | 0,120 | 0,670 | 0,641 | 692,216 | 30,138 | 728,528 | 9,222  | 719,723 | 10,737 | 101.22 |
| 027-ZR71  | 0,007 | 0.747 | 226991 | 0,064 | 0,453 | 1,064 | 0,986 | 0,121 | 0,793 | 0,804 | 734,474 | 19,144 | 736,343 | 11,031 | 735,920 | 10,295 | 100.06 |

|           |       |       |         |       |       |       |       |       |       |       |          |        |          |        |          |        |        |
|-----------|-------|-------|---------|-------|-------|-------|-------|-------|-------|-------|----------|--------|----------|--------|----------|--------|--------|
| 006-ZR4   | 0,012 | 0.669 | 129270  | 0,064 | 0,472 | 1,086 | 1,064 | 0,122 | 0,878 | 0,825 | 756,498  | 19,871 | 743,165  | 12,319 | 746,536  | 11,213 | 99.55  |
| 006-ZR56  | 0,014 | 0.468 | 111274  | 0,065 | 0,600 | 1,104 | 1,037 | 0,124 | 0,760 | 0,733 | 758,129  | 25,203 | 754,458  | 10,822 | 755,424  | 11,020 | 99.87  |
| 95-ZR124N | 0,144 | 0.739 | 10799   | 0,067 | 0,530 | 1,173 | 0,884 | 0,127 | 0,602 | 0,682 | 832,180  | 22,024 | 772,695  | 8,770  | 788,203  | 9,667  | 98.03  |
| 097-ZR125 | 0,011 | 0.095 | 138256  | 0,066 | 0,566 | 1,171 | 0,963 | 0,128 | 0,685 | 0,712 | 812,165  | 23,567 | 778,200  | 10,043 | 787,078  | 10,517 | 98.87  |
| 073-ZR108 | 0,040 | 0.257 | 38624   | 0,065 | 0,681 | 1,160 | 1,470 | 0,129 | 1,249 | 0,850 | 779,138  | 28,502 | 782,728  | 18,405 | 781,838  | 15,972 | 100.11 |
| 023-ZR69  | 0,022 | 0.379 | 71533   | 0,066 | 0,760 | 1,180 | 1,141 | 0,130 | 0,767 | 0,672 | 796,209  | 31,707 | 789,418  | 11,386 | 791,237  | 12,506 | 99.77  |
| 079-ZR112 | 0,028 | 0.267 | 55387   | 0,066 | 0,898 | 1,200 | 1,798 | 0,131 | 1,513 | 0,841 | 813,834  | 37,339 | 795,548  | 22,629 | 800,416  | 19,819 | 99.39  |
| 071-ZR106 | 0,014 | 0.419 | 109512  | 0,067 | 0,498 | 1,213 | 1,060 | 0,131 | 0,860 | 0,811 | 835,709  | 20,685 | 795,973  | 12,865 | 806,551  | 11,767 | 98.69  |
| 046-ZR87  | 0,087 | 0.389 | 17871   | 0,067 | 1,280 | 1,225 | 1,833 | 0,132 | 1,258 | 0,686 | 852,189  | 52,764 | 797,583  | 18,867 | 812,167  | 20,394 | 98.20  |
| 004-ZR54  | 0,016 | 0.224 | 94955   | 0,065 | 0,608 | 1,195 | 1,038 | 0,134 | 0,756 | 0,728 | 769,676  | 25,487 | 808,643  | 11,485 | 798,378  | 11,448 | 101.29 |
| 074-ZR109 | 0,008 | 0.263 | 200595  | 0,065 | 0,769 | 1,242 | 1,598 | 0,139 | 1,351 | 0,845 | 773,558  | 32,186 | 836,840  | 21,185 | 819,766  | 17,895 | 102.08 |
| 008-ZR58  | 0,011 | 0.301 | 144583  | 0,069 | 0,722 | 1,323 | 1,461 | 0,139 | 1,215 | 0,832 | 893,176  | 29,670 | 841,153  | 19,156 | 855,627  | 16,830 | 98.31  |
| 060-ZR97  | 0,016 | 0.631 | 100154  | 0,069 | 1,008 | 1,408 | 1,386 | 0,147 | 0,876 | 0,632 | 909,404  | 41,231 | 885,589  | 14,492 | 892,470  | 16,391 | 99.23  |
| 007-ZR5   | 0,001 | 0.026 | 1675040 | 0,071 | 0,852 | 1,508 | 1,340 | 0,155 | 0,966 | 0,721 | 947,867  | 34,669 | 927,289  | 16,672 | 933,449  | 16,293 | 99.34  |
| 015-ZR62  | 0,013 | 0.249 | 119556  | 0,072 | 0,520 | 1,724 | 0,900 | 0,173 | 0,634 | 0,704 | 991,737  | 21,080 | 1029,303 | 12,053 | 1017,406 | 11,530 | 101.17 |
| 045-ZR36  | 0,011 | 0.221 | 137196  | 0,079 | 0,539 | 2,097 | 0,962 | 0,193 | 0,706 | 0,734 | 1164,527 | 21,273 | 1138,702 | 14,734 | 1147,677 | 13,189 | 99.22  |
| 098-ZR126 | 0,008 | 0.754 | 194708  | 0,082 | 0,557 | 2,417 | 0,910 | 0,214 | 0,617 | 0,678 | 1246,781 | 21,747 | 1248,315 | 13,987 | 1247,806 | 13,030 | 100.04 |
| 048-ZR89  | 0,006 | 0.275 | 243798  | 0,083 | 0,543 | 2,445 | 0,908 | 0,215 | 0,627 | 0,690 | 1260,896 | 21,149 | 1252,811 | 14,264 | 1255,843 | 13,048 | 99.76  |
| 110-ZR136 | 0,011 | 0.298 | 145538  | 0,084 | 0,691 | 2,477 | 1,122 | 0,213 | 0,802 | 0,715 | 1302,286 | 26,726 | 1243,536 | 18,130 | 1265,278 | 16,161 | 98.28  |
| 051-ZR90N | 0,008 | 0.598 | 197155  | 0,085 | 0,484 | 2,385 | 0,967 | 0,204 | 0,751 | 0,776 | 1315,022 | 18,701 | 1194,265 | 16,359 | 1238,080 | 13,787 | 96.46  |
| 003-ZR1   | 0,013 | 0.448 | 122467  | 0,086 | 0,747 | 2,711 | 1,304 | 0,228 | 1,003 | 0,769 | 1340,331 | 28,741 | 1325,936 | 24,010 | 1331,506 | 19,256 | 99.58  |
| 053-ZR91  | 0,006 | 0.408 | 245662  | 0,094 | 0,437 | 3,184 | 0,818 | 0,247 | 0,584 | 0,714 | 1501,302 | 16,484 | 1420,720 | 14,890 | 1453,372 | 12,608 | 97.75  |
| 094-ZR123 | 0,008 | 0.364 | 190714  | 0,095 | 0,471 | 3,590 | 0,920 | 0,275 | 0,698 | 0,759 | 1521,059 | 17,702 | 1566,461 | 19,389 | 1547,289 | 14,554 | 101.24 |
| 010-ZR59B | 0,004 | 0.450 | 433849  | 0,108 | 0,417 | 4,842 | 0,817 | 0,325 | 0,597 | 0,731 | 1768,867 | 15,186 | 1812,239 | 18,856 | 1792,222 | 13,707 | 101.12 |

|           |       |       |        |       |       |        |       |       |       |       |          |        |          |        |          |        |        |
|-----------|-------|-------|--------|-------|-------|--------|-------|-------|-------|-------|----------|--------|----------|--------|----------|--------|--------|
| 009-ZR59N | 0,010 | 0.675 | 149530 | 0,109 | 0,413 | 4,827  | 0,810 | 0,321 | 0,589 | 0,728 | 1781,488 | 15,022 | 1796,389 | 18,471 | 1789,567 | 13,572 | 100.38 |
| 112-ZR138 | 0,006 | 0.519 | 257594 | 0,112 | 0,531 | 4,567  | 0,931 | 0,296 | 0,670 | 0,719 | 1830,047 | 19,182 | 1671,651 | 19,710 | 1743,223 | 15,459 | 95.89  |
| 033-ZR77  | 0,013 | 0.634 | 117322 | 0,115 | 0,418 | 5,497  | 0,865 | 0,346 | 0,660 | 0,763 | 1882,176 | 15,034 | 1916,348 | 21,863 | 1900,058 | 14,805 | 100.86 |
| 024-ZR19  | 0,003 | 0.393 | 541517 | 0,120 | 0,483 | 5,384  | 1,214 | 0,324 | 1,050 | 0,865 | 1962,711 | 17,194 | 1810,252 | 33,101 | 1882,342 | 20,683 | 96.17  |
| 069-ZR104 | 0,016 | 1.354 | 94236  | 0,122 | 0,856 | 5,752  | 1,386 | 0,341 | 1,026 | 0,740 | 1987,950 | 30,283 | 1893,671 | 33,632 | 1939,146 | 23,845 | 97.65  |
| 059-ZR96  | 0,003 | 0.557 | 451110 | 0,125 | 0,540 | 6,070  | 0,897 | 0,351 | 0,613 | 0,683 | 2034,035 | 19,054 | 1940,095 | 20,513 | 1986,018 | 15,578 | 97.69  |
| 039-ZR30  | 0,005 | 0.214 | 325816 | 0,129 | 0,626 | 7,002  | 1,300 | 0,394 | 1,077 | 0,829 | 2084,166 | 21,934 | 2139,972 | 39,167 | 2111,712 | 22,963 | 101.34 |
| 010-ZR8   | 0,015 | 0.502 | 101943 | 0,129 | 0,678 | 6,506  | 1,137 | 0,366 | 0,835 | 0,734 | 2084,775 | 23,755 | 2008,936 | 28,784 | 2046,669 | 19,922 | 98.16  |
| 041-ZR32  | 0,008 | 0.488 | 199439 | 0,130 | 0,620 | 6,689  | 0,979 | 0,375 | 0,660 | 0,675 | 2091,285 | 21,728 | 2050,759 | 23,174 | 2071,111 | 17,218 | 99.02  |
| 080-ZR113 | 0,011 | 0.626 | 142048 | 0,131 | 0,415 | 6,844  | 0,943 | 0,379 | 0,762 | 0,807 | 2109,504 | 14,542 | 2072,936 | 26,978 | 2091,407 | 16,649 | 99.12  |
| 068-ZR103 | 0,003 | 0.418 | 446544 | 0,134 | 0,392 | 6,950  | 0,806 | 0,376 | 0,599 | 0,743 | 2153,864 | 13,659 | 2055,283 | 21,067 | 2105,023 | 14,262 | 97.64  |
| 003-ZR53  | 0,003 | 0.278 | 480954 | 0,135 | 0,469 | 7,444  | 0,816 | 0,401 | 0,555 | 0,681 | 2159,345 | 16,314 | 2173,517 | 20,474 | 2166,304 | 14,552 | 100.33 |
| 046-ZR37  | 0,009 | 0.910 | 163237 | 0,135 | 0,539 | 7,312  | 0,910 | 0,393 | 0,633 | 0,695 | 2164,334 | 18,753 | 2135,537 | 22,987 | 2150,318 | 16,199 | 99.31  |
| 082-ZR115 | 0,007 | 0.738 | 221147 | 0,159 | 0,463 | 9,570  | 0,835 | 0,436 | 0,587 | 0,703 | 2445,545 | 15,640 | 2334,271 | 22,978 | 2394,247 | 15,289 | 97.50  |
| 093-ZR122 | 0,007 | 0.394 | 219857 | 0,162 | 0,362 | 10,448 | 0,839 | 0,466 | 0,660 | 0,787 | 2481,164 | 12,168 | 2467,963 | 27,050 | 2475,279 | 15,491 | 99.70  |
| 034-ZR78  | 0,020 | 0.651 | 73743  | 0,163 | 0,548 | 10,761 | 0,995 | 0,477 | 0,743 | 0,747 | 2492,105 | 18,390 | 2515,667 | 30,920 | 2502,720 | 18,398 | 100.52 |
| 119-ZR143 | 0,005 | 0.439 | 322272 | 0,165 | 0,399 | 10,400 | 0,974 | 0,458 | 0,807 | 0,829 | 2502,606 | 13,401 | 2432,702 | 32,663 | 2471,045 | 17,956 | 98.45  |

| SAMPLE   | AL06     |      |             |             |       |            |       |            |       |       |               |        |            |        |            |        |        |
|----------|----------|------|-------------|-------------|-------|------------|-------|------------|-------|-------|---------------|--------|------------|--------|------------|--------|--------|
|          |          |      |             |             |       |            |       |            |       |       | Apparent ages |        |            |        |            |        |        |
| GRAIN    | <i>f</i> | err  |             |             |       | err        |       | err        |       | Rho   | 207Pb/206Pb   |        | 206Pb/238U |        | 207Pb/235U |        | conc.  |
|          | 206 (%)  | Th/U | 206Pb/204Pb | 207Pb/206Pb | (%)1  | 207Pb/235U | (%)1  | 206Pb/238U | (% 1) |       | 207Pb/206Pb   | 2 σ    | 206Pb/238U | 2 σ    | 207Pb/235U | 2 σ    | (%)    |
| 011-ZR7  | 0.03     | 1.00 | 59256       | 0.06        | 0,992 | 0,687      | 1,438 | 0,085      | 0,972 | 0,676 | 539,944       | 43,118 | 528,737    | 9,868  | 530,881    | 11,855 | 99.60  |
| 094-ZR72 | 0.03     | 0.39 | 54737       | 0.06        | 1,884 | 0,743      | 2,136 | 0,091      | 0,936 | 0,438 | 570,540       | 80,936 | 562,534    | 10,079 | 564,156    | 18,405 | 99.71  |
| 047-ZR36 | 0.06     | 0.76 | 27618       | 0.06        | 1,817 | 0,795      | 2,402 | 0,096      | 1,526 | 0,635 | 607,506       | 77,639 | 590,692    | 17,213 | 594,211    | 21,493 | 99.41  |
| 018-ZR12 | 0.06     | 1.09 | 25257       | 0.06        | 2,049 | 0,824      | 3,009 | 0,097      | 2,172 | 0,722 | 653,202       | 86,729 | 598,818    | 24,821 | 610,345    | 27,420 | 98.11  |
| 044-ZR33 | 0.01     | 1.05 | 116727      | 0.06        | 0,444 | 0,797      | 0,989 | 0,097      | 0,803 | 0,811 | 597,500       | 19,174 | 594,276    | 9,110  | 594,979    | 8,888  | 99.88  |
| 072-ZR54 | 0.03     | 1.03 | 46866       | 0.06        | 0,821 | 0,816      | 1,145 | 0,097      | 0,708 | 0,618 | 649,064       | 35,048 | 594,534    | 8,037  | 606,024    | 10,426 | 98.10  |
| 036-ZR27 | 0.01     | 0.84 | 143522      | 0.06        | 0,646 | 0,809      | 1,141 | 0,097      | 0,865 | 0,758 | 615,908       | 27,767 | 598,423    | 9,886  | 602,121    | 10,343 | 99.39  |
| 082-ZR62 | 0.06     | 1.82 | 25346       | 0.06        | 1,341 | 0,793      | 1,610 | 0,098      | 0,810 | 0,503 | 565,653       | 57,881 | 600,166    | 9,285  | 593,029    | 14,413 | 101.20 |
| 004-ZR1B | 0.15     | 0.04 | 10192       | 0.06        | 0,677 | 0,824      | 1,048 | 0,099      | 0,709 | 0,677 | 609,767       | 29,119 | 610,081    | 8,253  | 610,049    | 9,588  | 100.01 |
| 056-ZR43 | 0.01     | 0.94 | 131478      | 0.06        | 0,798 | 0,832      | 1,221 | 0,100      | 0,847 | 0,693 | 612,747       | 34,288 | 615,305    | 9,932  | 614,793    | 11,230 | 100.08 |
| 029-ZR20 | 0.23     | 0.43 | 6832        | 0.06        | 1,339 | 0,858      | 1,679 | 0,101      | 0,943 | 0,561 | 667,166       | 56,828 | 618,138    | 11,110 | 628,798    | 15,681 | 98.30  |
| 111-ZR86 | 0.01     | 0.64 | 305058      | 0.06        | 0,785 | 0,839      | 1,118 | 0,101      | 0,705 | 0,630 | 622,882       | 33,703 | 617,547    | 8,298  | 618,727    | 10,338 | 99.81  |
| 035-ZR26 | 0.02     | 0.78 | 73450       | 0.06        | 0,720 | 0,841      | 1,248 | 0,101      | 0,950 | 0,761 | 619,457       | 30,908 | 619,640    | 11,222 | 619,635    | 11,545 | 100.00 |
| 097-ZR75 | 0.03     | 0.91 | 61966       | 0.06        | 0,818 | 0,846      | 1,156 | 0,101      | 0,728 | 0,630 | 621,950       | 35,082 | 622,255    | 8,637  | 622,224    | 10,727 | 100.00 |
| 007-ZR3B | 0.09     | 0.01 | 18185       | 0.06        | 0,482 | 0,865      | 0,854 | 0,102      | 0,600 | 0,702 | 661,060       | 20,597 | 625,164    | 7,149  | 633,030    | 8,033  | 98.76  |
| 126-ZR99 | 0.03     | 0.63 | 50257       | 0.06        | 1,076 | 0,889      | 1,492 | 0,103      | 0,965 | 0,647 | 691,298       | 45,558 | 632,568    | 11,628 | 645,602    | 14,209 | 97.98  |
| 049-ZR38 | 0.03     | 0.34 | 59439       | 0.06        | 0,488 | 0,861      | 0,992 | 0,103      | 0,780 | 0,786 | 623,595       | 20,979 | 632,504    | 9,391  | 630,595    | 9,295  | 100.30 |



|           |      |      |        |      |       |       |       |       |       |       |         |        |         |        |         |        |        |
|-----------|------|------|--------|------|-------|-------|-------|-------|-------|-------|---------|--------|---------|--------|---------|--------|--------|
| 092-ZR70  | 0.01 | 1.26 | 110407 | 0.06 | 0,794 | 0,888 | 1,152 | 0,105 | 0,748 | 0,649 | 655,434 | 33,880 | 642,028 | 9,139  | 645,039 | 10,971 | 99.53  |
| 061-ZR47B | 0.02 | 0.00 | 63147  | 0.06 | 0,675 | 0,897 | 1,085 | 0,105 | 0,764 | 0,704 | 676,171 | 28,736 | 642,434 | 9,335  | 649,993 | 10,386 | 98.84  |
| 067-ZR49  | 0.02 | 1.16 | 97428  | 0.06 | 0,406 | 0,869 | 1,075 | 0,105 | 0,924 | 0,859 | 607,016 | 17,502 | 642,633 | 11,297 | 634,837 | 10,122 | 101.23 |
| 058-ZR45  | 0.02 | 0.55 | 100734 | 0.06 | 0,676 | 0,875 | 1,129 | 0,105 | 0,824 | 0,730 | 620,163 | 29,035 | 643,290 | 10,089 | 638,223 | 10,666 | 100.79 |
| 109-ZR84B | 0.00 | 0.00 | 713528 | 0.06 | 0,364 | 0,897 | 0,768 | 0,107 | 0,565 | 0,736 | 641,152 | 15,633 | 652,759 | 7,018  | 650,197 | 7,361  | 100.39 |
| 012-ZR8   | 0.02 | 0.53 | 94446  | 0.06 | 0,776 | 0,895 | 1,078 | 0,107 | 0,650 | 0,603 | 622,669 | 33,299 | 656,653 | 8,116  | 649,080 | 10,314 | 101.17 |
| 068-ZR50  | 0.03 | 0.77 | 50652  | 0.06 | 0,580 | 0,914 | 1,099 | 0,109 | 0,857 | 0,780 | 642,965 | 24,817 | 664,133 | 10,811 | 659,373 | 10,630 | 100.72 |
| 125-ZR98  | 0.01 | 0.33 | 255800 | 0.06 | 0,458 | 0,919 | 1,025 | 0,109 | 0,838 | 0,818 | 636,937 | 19,651 | 669,414 | 10,657 | 662,061 | 9,943  | 101.11 |
| 055-ZR42  | 0.05 | 0.37 | 31613  | 0.06 | 1,530 | 0,979 | 2,266 | 0,111 | 1,630 | 0,719 | 745,421 | 64,011 | 677,110 | 20,939 | 693,160 | 22,639 | 97.68  |
| 106-ZR82  | 0.02 | 0.42 | 74312  | 0.06 | 0,415 | 1,006 | 1,054 | 0,113 | 0,896 | 0,850 | 755,409 | 17,453 | 691,457 | 11,741 | 706,729 | 10,708 | 97.84  |
| 098-ZR76  | 0.02 | 0.39 | 90723  | 0.06 | 0,924 | 0,992 | 1,405 | 0,117 | 0,991 | 0,705 | 657,318 | 39,385 | 712,892 | 13,366 | 699,681 | 14,154 | 101.89 |
| 009-ZR5   | 0.86 | 1.13 | 1806   | 0.07 | 1,427 | 1,095 | 1,775 | 0,122 | 0,988 | 0,557 | 780,675 | 59,427 | 740,912 | 13,821 | 750,914 | 18,752 | 98.67  |
| 015-ZR9   | 0.01 | 0.72 | 271637 | 0.06 | 0,610 | 1,080 | 1,246 | 0,122 | 1,022 | 0,820 | 744,453 | 25,676 | 743,049 | 14,332 | 743,439 | 13,095 | 99.95  |
| 050-ZR39  | 0.02 | 0.46 | 69781  | 0.06 | 0,526 | 1,073 | 1,055 | 0,124 | 0,836 | 0,793 | 708,054 | 22,279 | 751,111 | 11,854 | 740,418 | 11,062 | 101.44 |
| 103-ZR79  | 0.02 | 0.58 | 80622  | 0.06 | 1,111 | 1,108 | 1,374 | 0,126 | 0,720 | 0,524 | 735,452 | 46,678 | 764,569 | 10,374 | 757,228 | 14,617 | 100.97 |
| 023-ZR16  | 0.01 | 0.30 | 172731 | 0.07 | 0,605 | 1,154 | 1,017 | 0,128 | 0,728 | 0,716 | 786,009 | 25,301 | 776,748 | 10,656 | 779,184 | 11,032 | 99.69  |
| 003-ZR1N  | 0.21 | 0.55 | 7430   | 0.07 | 0,861 | 1,174 | 1,385 | 0,128 | 1,020 | 0,736 | 819,343 | 35,759 | 777,730 | 14,942 | 788,609 | 15,138 | 98.62  |
| 005-ZR2   | 0.01 | 0.41 | 136221 | 0.07 | 0,580 | 1,171 | 1,065 | 0,130 | 0,813 | 0,763 | 777,133 | 24,295 | 790,611 | 12,087 | 787,133 | 11,630 | 100.44 |
| 031-ZR22  | 0.03 | 0.60 | 55399  | 0.07 | 0,406 | 1,192 | 0,786 | 0,131 | 0,561 | 0,714 | 811,463 | 16,954 | 791,916 | 8,364  | 797,100 | 8,661  | 99.35  |
| 075-ZR57  | 0.04 | 0.18 | 43727  | 0.06 | 1,027 | 1,162 | 1,304 | 0,131 | 0,714 | 0,547 | 750,375 | 43,074 | 794,208 | 10,665 | 782,829 | 14,185 | 101.45 |
| 008-ZR4   | 0.02 | 0.29 | 86125  | 0.06 | 0,684 | 1,191 | 1,050 | 0,133 | 0,705 | 0,671 | 771,525 | 28,671 | 805,315 | 10,668 | 796,439 | 11,557 | 101.11 |
| 096-ZR74  | 0.06 | 0.31 | 27749  | 0.07 | 0,419 | 1,274 | 0,850 | 0,137 | 0,640 | 0,753 | 855,600 | 17,343 | 826,254 | 9,929  | 834,291 | 9,650  | 99.04  |
| 010-ZR6   | 0.06 | 0.61 | 27454  | 0.07 | 0,660 | 1,390 | 1,264 | 0,144 | 1,013 | 0,801 | 922,671 | 27,011 | 869,399 | 16,463 | 884,603 | 14,877 | 98.28  |
| 027-ZR18  | 0.00 | 0.33 | 388767 | 0.07 | 0,452 | 1,395 | 0,874 | 0,149 | 0,650 | 0,743 | 861,137 | 18,717 | 897,183 | 10,883 | 886,887 | 10,315 | 101.16 |

|           |      |      |        |      |       |        |       |       |       |       |          |        |          |        |          |        |        |
|-----------|------|------|--------|------|-------|--------|-------|-------|-------|-------|----------|--------|----------|--------|----------|--------|--------|
| 030-ZR21  | 0.01 | 0.48 | 109271 | 0.07 | 0,848 | 1,567  | 1,307 | 0,158 | 0,923 | 0,706 | 987,194  | 34,321 | 943,942  | 16,205 | 957,064  | 16,140 | 98.63  |
| 118-ZR91  | 0.01 | 0.31 | 136719 | 0.07 | 0,510 | 1,730  | 0,891 | 0,171 | 0,629 | 0,707 | 1027,094 | 20,543 | 1016,155 | 11,828 | 1019,677 | 11,427 | 99.65  |
| 087-ZR67  | 0.07 | 0.35 | 21247  | 0.08 | 0,722 | 1,812  | 1,092 | 0,172 | 0,731 | 0,669 | 1100,418 | 28,735 | 1025,314 | 13,844 | 1049,625 | 14,235 | 97.68  |
| 037-ZR28  | 0.01 | 0.27 | 203458 | 0.08 | 0,862 | 1,937  | 1,412 | 0,179 | 1,055 | 0,747 | 1164,135 | 33,991 | 1059,036 | 20,585 | 1094,011 | 18,823 | 96.80  |
| 117-ZR90  | 0.01 | 0.33 | 225694 | 0.08 | 0,508 | 2,339  | 1,233 | 0,211 | 1,060 | 0,860 | 1208,244 | 19,925 | 1233,306 | 23,784 | 1224,272 | 17,461 | 100.74 |
| 016-ZR10  | 0.01 | 0.27 | 192805 | 0.09 | 0,427 | 2,645  | 0,997 | 0,221 | 0,821 | 0,824 | 1357,198 | 16,438 | 1286,471 | 19,144 | 1313,289 | 14,644 | 97.96  |
| 038-ZR29  | 0.05 | 0.52 | 31209  | 0.09 | 1,006 | 2,849  | 1,598 | 0,230 | 1,185 | 0,742 | 1419,130 | 38,221 | 1336,263 | 28,575 | 1368,534 | 23,882 | 97.64  |
| 048-ZR37  | 0.01 | 0.10 | 165770 | 0.09 | 0,532 | 3,390  | 1,173 | 0,262 | 0,977 | 0,833 | 1506,314 | 20,047 | 1498,960 | 26,103 | 1502,068 | 18,305 | 99.79  |
| 127-ZR100 | 0.00 | 0.37 | 682299 | 0.10 | 0,442 | 4,216  | 0,906 | 0,298 | 0,699 | 0,771 | 1670,625 | 16,288 | 1682,245 | 20,673 | 1677,142 | 14,814 | 100.30 |
| 017-ZR11  | 0.01 | 0.41 | 118990 | 0.11 | 0,541 | 4,702  | 0,956 | 0,313 | 0,695 | 0,727 | 1781,375 | 19,678 | 1755,967 | 21,357 | 1767,664 | 15,945 | 99.34  |
| 095-ZR73  | 0.01 | 1.12 | 294871 | 0.11 | 0,476 | 5,125  | 0,890 | 0,324 | 0,654 | 0,735 | 1875,790 | 17,101 | 1808,997 | 20,613 | 1840,319 | 15,059 | 98.30  |
| 124-ZR97  | 0.01 | 0.65 | 114816 | 0.11 | 0,765 | 5,144  | 1,333 | 0,330 | 1,027 | 0,770 | 1848,321 | 27,552 | 1838,943 | 32,819 | 1843,410 | 22,543 | 99.76  |
| 060-ZR47N | 0.01 | 0.68 | 253679 | 0.12 | 0,377 | 6,420  | 0,807 | 0,377 | 0,610 | 0,756 | 2009,586 | 13,354 | 2060,166 | 21,501 | 2035,068 | 14,137 | 101.23 |
| 123-ZR96  | 0.01 | 1.03 | 290296 | 0.12 | 0,413 | 5,881  | 1,038 | 0,356 | 0,877 | 0,845 | 1954,731 | 14,729 | 1961,808 | 29,625 | 1958,432 | 17,932 | 100.17 |
| 020-ZR14  | 0.04 | 0.86 | 34683  | 0.13 | 0,896 | 6,566  | 1,448 | 0,365 | 1,075 | 0,743 | 2106,196 | 31,278 | 2003,916 | 36,979 | 2054,841 | 25,354 | 97.52  |
| 112-ZR87  | 0.01 | 0.70 | 104628 | 0.14 | 0,647 | 7,127  | 1,057 | 0,380 | 0,749 | 0,708 | 2175,794 | 22,462 | 2077,481 | 26,572 | 2127,368 | 18,737 | 97.65  |
| 053-ZR40  | 0.01 | 0.79 | 130059 | 0.13 | 0,409 | 7,252  | 0,949 | 0,392 | 0,772 | 0,813 | 2153,379 | 14,244 | 2131,841 | 27,979 | 2142,895 | 16,859 | 99.48  |
| 045-ZR34  | 0.01 | 0.49 | 243596 | 0.14 | 0,413 | 7,613  | 0,787 | 0,399 | 0,558 | 0,709 | 2208,300 | 14,314 | 2163,024 | 20,507 | 2186,415 | 14,086 | 98.93  |
| 019-ZR13  | 0.01 | 0.85 | 128942 | 0.14 | 0,499 | 7,603  | 0,864 | 0,401 | 0,600 | 0,695 | 2194,165 | 17,286 | 2175,501 | 22,139 | 2185,189 | 15,443 | 99.56  |
| 034-ZR25  | 0.02 | 0.45 | 60291  | 0.14 | 0,649 | 7,809  | 2,176 | 0,411 | 2,044 | 0,939 | 2200,450 | 22,443 | 2218,562 | 76,500 | 2209,228 | 38,801 | 100.42 |
| 119-ZR92  | 0.00 | 0.58 | 301125 | 0.14 | 0,378 | 7,945  | 0,946 | 0,418 | 0,784 | 0,829 | 2199,470 | 13,107 | 2252,377 | 29,791 | 2224,848 | 17,000 | 101.24 |
| 059-ZR46  | 0.01 | 0.47 | 119806 | 0.20 | 0,395 | 15,092 | 1,257 | 0,540 | 1,135 | 0,903 | 2848,311 | 12,832 | 2782,865 | 51,194 | 2821,038 | 23,808 | 98.65  |

| SAMPLE   | AL11       |          |                 |                 |            |                |           |                |           |       |                 |        |                |        |                |        |              |
|----------|------------|----------|-----------------|-----------------|------------|----------------|-----------|----------------|-----------|-------|-----------------|--------|----------------|--------|----------------|--------|--------------|
|          |            |          |                 |                 |            |                |           |                |           |       | Apparent ages   |        |                |        |                |        |              |
| GRAIN    | <i>f</i>   |          |                 |                 | <i>err</i> | <i>err</i>     |           | <i>err</i>     |           |       |                 |        |                |        |                |        | <i>conc.</i> |
|          | 206<br>(%) | Th/<br>U | 206Pb/<br>204Pb | 207Pb/<br>206Pb | (%)1<br>6  | 207Pb/<br>235U | (%)1<br>6 | 206Pb/<br>238U | (% 1<br>6 | Rho   | 207Pb/<br>206Pb | 2 6    | 206Pb/<br>238U | 2 6    | 207Pb/<br>235U | 2 6    | (%)          |
| 051-ZR37 | 0.03       | 0.85     | 50112           | 0.06            | 0,650      | 0,787          | 1,185     | 0,095          | 0,918     | 0,775 | 595,145         | 28,061 | 587,735        | 10,311 | 589,295        | 10,565 | 99.74        |
| 098-ZR75 | 0.05       | 1.15     | 28583           | 0.06            | 1,202      | 0,787          | 1,858     | 0,096          | 1,367     | 0,736 | 583,522         | 51,781 | 590,673        | 15,424 | 589,232        | 16,544 | 100.24       |
| 060-ZR44 | 0.01       | 0.76     | 120811          | 0.06            | 0,724      | 0,797          | 1,230     | 0,096          | 0,923     | 0,750 | 602,180         | 31,204 | 593,261        | 10,453 | 595,147        | 11,050 | 99.68        |
| 049-ZR35 | 0.01       | 0.74     | 252302          | 0.06            | 1,756      | 0,793          | 2,003     | 0,098          | 0,890     | 0,444 | 562,369         | 75,627 | 601,192        | 10,210 | 593,155        | 17,920 | 101.35       |
| 059-ZR43 | 0.02       | 0.75     | 84369           | 0.06            | 1,130      | 0,791          | 1,480     | 0,097          | 0,881     | 0,595 | 565,301         | 48,861 | 598,789        | 10,068 | 591,876        | 13,235 | 101.17       |
| 093-ZR70 | 0.00       | 0.58     | 340417          | 0.06            | 0,557      | 0,820          | 0,954     | 0,098          | 0,681     | 0,713 | 628,050         | 23,906 | 602,813        | 7,834  | 608,177        | 8,715  | 99.12        |
| 119-ZR92 | 0.04       | 1.14     | 40031           | 0.06            | 0,904      | 0,809          | 1,484     | 0,098          | 1,117     | 0,753 | 589,190         | 38,973 | 604,941        | 12,896 | 601,668        | 13,430 | 100.54       |
| 069-ZR50 | 0.01       | 0.83     | 183560          | 0.06            | 0,370      | 0,848          | 0,875     | 0,101          | 0,701     | 0,801 | 642,515         | 15,876 | 618,261        | 8,269  | 623,526        | 8,141  | 99.16        |
| 048-ZR34 | 0.01       | 1.88     | 218821          | 0.06            | 1,042      | 0,841          | 1,496     | 0,101          | 1,007     | 0,673 | 624,224         | 44,620 | 618,104        | 11,868 | 619,453        | 13,825 | 99.78        |
| 019-ZR11 | 0.01       | 0.40     | 225939          | 0.06            | 0,394      | 0,849          | 0,924     | 0,101          | 0,750     | 0,811 | 631,439         | 16,905 | 621,688        | 8,887  | 623,829        | 8,599  | 99.66        |
| 025-ZR17 | 0.01       | 0.29     | 156515          | 0.06            | 0,619      | 0,870          | 1,233     | 0,102          | 1,000     | 0,811 | 674,803         | 26,351 | 624,231        | 11,893 | 635,318        | 11,612 | 98.25        |
| 080-ZR59 | 0.01       | 0.18     | 105807          | 0.06            | 0,894      | 0,849          | 1,378     | 0,102          | 0,981     | 0,712 | 620,695         | 38,350 | 624,945        | 11,678 | 624,061        | 12,807 | 100.14       |
| 087-ZR66 | 0.01       | 0.36     | 111821          | 0.06            | 0,498      | 0,848          | 1,067     | 0,102          | 0,869     | 0,814 | 616,345         | 21,428 | 625,223        | 10,346 | 623,339        | 9,921  | 100.30       |
| 012-ZR8  | 0.04       | 0.55     | 38795           | 0.06            | 1,143      | 0,868          | 1,667     | 0,102          | 1,156     | 0,693 | 660,764         | 48,608 | 627,406        | 13,809 | 634,736        | 15,673 | 98.85        |
| 075-ZR56 | 0.01       | 0.34     | 139737          | 0.06            | 0,579      | 0,854          | 1,040     | 0,102          | 0,780     | 0,750 | 629,199         | 24,846 | 626,141        | 9,308  | 626,839        | 9,703  | 99.89        |

|          |      |      |        |      |       |       |       |       |       |       |         |        |         |        |         |        |        |
|----------|------|------|--------|------|-------|-------|-------|-------|-------|-------|---------|--------|---------|--------|---------|--------|--------|
| 057-ZR41 | 0.01 | 0.71 | 184597 | 0.06 | 0,472 | 0,861 | 1,009 | 0,103 | 0,811 | 0,804 | 630,546 | 20,249 | 630,356 | 9,740  | 630,433 | 9,454  | 99.99  |
| 084-ZR63 | 0.02 | 1.25 | 78974  | 0.06 | 0,679 | 0,886 | 1,250 | 0,103 | 0,982 | 0,786 | 676,883 | 28,887 | 634,741 | 11,872 | 644,098 | 11,891 | 98.55  |
| 099-ZR76 | 0.02 | 1.05 | 73442  | 0.06 | 0,621 | 0,860 | 1,064 | 0,104 | 0,781 | 0,734 | 608,168 | 26,739 | 635,904 | 9,456  | 629,884 | 9,967  | 100.96 |
| 032-ZR20 | 0.01 | 0.44 | 294261 | 0.06 | 0,398 | 0,883 | 1,213 | 0,104 | 1,084 | 0,894 | 656,798 | 17,043 | 638,423 | 13,175 | 642,522 | 11,519 | 99.36  |
| 018-ZR10 | 0.01 | 0.93 | 193691 | 0.06 | 0,434 | 0,866 | 0,907 | 0,104 | 0,705 | 0,778 | 607,254 | 18,704 | 640,530 | 8,598  | 633,265 | 8,530  | 101.15 |
| 076-ZR57 | 0.03 | 0.49 | 47157  | 0.06 | 1,134 | 0,867 | 1,971 | 0,105 | 1,569 | 0,796 | 599,850 | 48,742 | 643,841 | 19,218 | 634,206 | 18,513 | 101.52 |
| 092-ZR69 | 0.01 | 0.27 | 208124 | 0.06 | 0,404 | 0,898 | 0,751 | 0,105 | 0,513 | 0,683 | 672,313 | 17,246 | 644,290 | 6,293  | 650,582 | 7,203  | 99.03  |
| 068-ZR49 | 0.02 | 0.88 | 71369  | 0.06 | 1,647 | 0,884 | 2,140 | 0,106 | 1,315 | 0,615 | 629,372 | 70,190 | 647,194 | 16,189 | 643,274 | 20,294 | 100.61 |
| 045-ZR31 | 0.05 | 0.14 | 28774  | 0.06 | 2,931 | 0,885 | 3,472 | 0,106 | 1,822 | 0,525 | 623,441 | #####  | 649,704 | 22,505 | 643,901 | 32,840 | 100.90 |
| 050-ZR36 | 0.03 | 0.30 | 56943  | 0.06 | 0,876 | 0,881 | 1,275 | 0,106 | 0,849 | 0,666 | 606,999 | 37,650 | 651,217 | 10,519 | 641,441 | 12,090 | 101.52 |
| 070-ZR51 | 0.03 | 0.33 | 55810  | 0.06 | 0,525 | 0,914 | 0,988 | 0,107 | 0,751 | 0,760 | 667,792 | 22,382 | 656,689 | 9,371  | 659,235 | 9,559  | 99.61  |
| 008-ZR5N | 0.01 | 0.67 | 109170 | 0.06 | 0,762 | 0,910 | 1,103 | 0,107 | 0,706 | 0,640 | 658,075 | 32,523 | 657,028 | 8,820  | 657,300 | 10,649 | 99.96  |
| 009-ZR5B | 0.01 | 0.41 | 106073 | 0.06 | 0,496 | 0,909 | 0,840 | 0,108 | 0,569 | 0,677 | 639,427 | 21,245 | 661,391 | 7,149  | 656,468 | 8,110  | 100.75 |
| 064-ZR47 | 0.00 | 0.07 | 550136 | 0.06 | 0,367 | 0,926 | 1,001 | 0,108 | 0,854 | 0,854 | 673,536 | 15,655 | 663,159 | 10,761 | 665,559 | 9,748  | 99.64  |
| 026-ZR18 | 0.10 | 0.40 | 15797  | 0.06 | 0,691 | 0,947 | 1,581 | 0,109 | 1,373 | 0,868 | 710,988 | 29,223 | 666,447 | 17,375 | 676,742 | 15,559 | 98.48  |
| 034-ZR22 | 0.02 | 0.34 | 91500  | 0.06 | 0,710 | 0,924 | 1,303 | 0,109 | 1,028 | 0,789 | 657,567 | 30,315 | 666,682 | 13,013 | 664,642 | 12,672 | 100.31 |
| 094-ZR71 | 0.02 | 0.34 | 73630  | 0.06 | 0,575 | 0,952 | 1,233 | 0,110 | 1,025 | 0,832 | 707,705 | 24,382 | 670,673 | 13,054 | 679,269 | 12,174 | 98.73  |
| 106-ZR81 | 0.03 | 0.42 | 61238  | 0.06 | 0,564 | 0,965 | 1,185 | 0,110 | 0,973 | 0,822 | 731,247 | 23,821 | 671,879 | 12,415 | 685,720 | 11,777 | 97.98  |
| 112-ZR87 | 0.01 | 0.18 | 104027 | 0.06 | 0,626 | 0,945 | 0,984 | 0,110 | 0,663 | 0,673 | 687,046 | 26,612 | 672,136 | 8,459  | 675,610 | 9,689  | 99.49  |
| 115-ZR88 | 0.01 | 1.06 | 282086 | 0.06 | 0,456 | 0,953 | 1,194 | 0,110 | 1,040 | 0,871 | 701,348 | 19,351 | 673,234 | 13,288 | 679,777 | 11,802 | 99.04  |
| 085-ZR64 | 0.02 | 0.38 | 103107 | 0.06 | 0,754 | 0,961 | 1,444 | 0,111 | 1,175 | 0,813 | 703,658 | 31,933 | 677,507 | 15,103 | 683,625 | 14,321 | 99.11  |
| 109-ZR84 | 0.01 | 0.66 | 145971 | 0.06 | 0,399 | 0,960 | 0,837 | 0,111 | 0,635 | 0,759 | 692,164 | 16,986 | 680,555 | 8,206  | 683,294 | 8,309  | 99.60  |
| 052-ZR38 | 0.12 | 1.34 | 13498  | 0.06 | 2,356 | 1,007 | 3,350 | 0,113 | 2,352 | 0,702 | 763,242 | 97,793 | 690,059 | 30,745 | 707,533 | 33,854 | 97.53  |
| 083-ZR62 | 0.00 | 0.05 | 554315 | 0.06 | 0,627 | 1,000 | 1,050 | 0,115 | 0,756 | 0,720 | 709,115 | 26,556 | 702,302 | 10,060 | 703,965 | 10,635 | 99.76  |

|          |      |      |        |      |       |       |       |       |       |       |          |        |          |        |          |        |        |
|----------|------|------|--------|------|-------|-------|-------|-------|-------|-------|----------|--------|----------|--------|----------|--------|--------|
| 036-ZR24 | 0.01 | 0.13 | 137739 | 0.06 | 0,247 | 0,992 | 0,707 | 0,116 | 0,549 | 0,777 | 668,537  | 10,561 | 709,469  | 7,375  | 699,759  | 7,137  | 101.39 |
| 108-ZR83 | 0.01 | 0.32 | 195884 | 0.06 | 0,688 | 1,019 | 1,074 | 0,116 | 0,738 | 0,687 | 722,923  | 29,040 | 710,210  | 9,918  | 713,311  | 10,981 | 99.57  |
| 103-ZR78 | 0.01 | 0.71 | 244432 | 0.06 | 0,574 | 1,068 | 1,077 | 0,119 | 0,832 | 0,773 | 770,263  | 24,083 | 727,154  | 11,441 | 737,841  | 11,263 | 98.55  |
| 116-ZR89 | 0.01 | 0.30 | 105492 | 0.07 | 1,215 | 1,111 | 2,120 | 0,123 | 1,697 | 0,801 | 794,432  | 50,545 | 746,545  | 23,901 | 758,675  | 22,528 | 98.40  |
| 056-ZR40 | 0.02 | 0.56 | 66648  | 0.06 | 4,742 | 1,098 | 4,931 | 0,125 | 1,300 | 0,264 | 733,050  | #####  | 759,028  | 18,608 | 752,517  | 51,746 | 100.87 |
| 082-ZR61 | 0.06 | 0.40 | 26240  | 0.06 | 2,664 | 1,096 | 3,131 | 0,125 | 1,602 | 0,512 | 723,073  | #####  | 760,905  | 22,981 | 751,407  | 32,974 | 101.26 |
| 118-ZR91 | 0.01 | 0.48 | 168221 | 0.07 | 0,461 | 1,146 | 0,990 | 0,125 | 0,793 | 0,802 | 816,391  | 19,215 | 761,381  | 11,391 | 775,547  | 10,706 | 98.17  |
| 125-ZR98 | 0.01 | 0.36 | 110443 | 0.06 | 0,672 | 1,116 | 1,233 | 0,126 | 0,965 | 0,783 | 753,689  | 28,252 | 763,475  | 13,890 | 761,028  | 13,164 | 100.32 |
| 081-ZR60 | 0.01 | 0.32 | 118454 | 0.06 | 0,541 | 1,148 | 1,038 | 0,129 | 0,805 | 0,775 | 759,285  | 22,718 | 782,096  | 11,848 | 776,242  | 11,232 | 100.75 |
| 044-ZR30 | 0.02 | 0.28 | 93803  | 0.06 | 0,704 | 1,180 | 1,355 | 0,132 | 1,097 | 0,809 | 765,978  | 29,543 | 800,556  | 16,509 | 791,516  | 14,848 | 101.14 |
| 071-ZR52 | 0.04 | 0.29 | 39903  | 0.07 | 1,206 | 1,238 | 1,663 | 0,134 | 1,083 | 0,652 | 835,565  | 49,850 | 811,202  | 16,507 | 817,781  | 18,593 | 99.20  |
| 121-ZR94 | 0.01 | 0.95 | 194160 | 0.07 | 0,506 | 1,283 | 0,899 | 0,139 | 0,643 | 0,716 | 839,513  | 21,000 | 837,868  | 10,107 | 838,361  | 10,230 | 99.94  |
| 105-ZR80 | 0.01 | 0.33 | 142457 | 0.07 | 0,539 | 1,419 | 0,961 | 0,148 | 0,704 | 0,732 | 916,072  | 22,119 | 889,305  | 11,686 | 897,063  | 11,417 | 99.14  |
| 022-ZR14 | 0.01 | 0.07 | 221074 | 0.07 | 0,348 | 1,453 | 0,706 | 0,149 | 0,489 | 0,693 | 947,675  | 14,234 | 896,109  | 8,181  | 911,166  | 8,471  | 98.35  |
| 091-ZR68 | 0.01 | 0.14 | 179328 | 0.07 | 0,469 | 1,553 | 0,893 | 0,159 | 0,663 | 0,743 | 954,012  | 19,120 | 950,684  | 11,724 | 951,735  | 11,001 | 99.89  |
| 107-ZR82 | 0.00 | 0.15 | 521829 | 0.07 | 0,351 | 1,581 | 0,785 | 0,160 | 0,596 | 0,760 | 975,663  | 14,285 | 957,061  | 10,600 | 962,765  | 9,740  | 99.41  |
| 122-ZR95 | 0.02 | 0.83 | 99884  | 0.07 | 0,481 | 1,658 | 0,962 | 0,164 | 0,746 | 0,776 | 1019,763 | 19,421 | 980,562  | 13,567 | 992,792  | 12,151 | 98.77  |
| 040-ZR28 | 0.00 | 0.51 | 321755 | 0.07 | 0,339 | 1,710 | 0,800 | 0,172 | 0,623 | 0,778 | 986,202  | 13,782 | 1024,486 | 11,795 | 1012,404 | 10,230 | 101.19 |
| 072-ZR53 | 0.01 | 0.81 | 236662 | 0.08 | 0,403 | 1,911 | 0,794 | 0,183 | 0,575 | 0,724 | 1086,561 | 16,134 | 1083,792 | 11,467 | 1084,762 | 10,559 | 99.91  |
| 033-ZR21 | 0.01 | 0.56 | 183869 | 0.07 | 0,369 | 1,842 | 1,533 | 0,183 | 1,441 | 0,940 | 1010,799 | 14,933 | 1084,656 | 28,736 | 1060,445 | 20,074 | 102.28 |
| 039-ZR27 | 0.01 | 0.63 | 138613 | 0.07 | 0,490 | 1,873 | 1,161 | 0,186 | 0,985 | 0,849 | 1015,165 | 19,773 | 1099,671 | 19,910 | 1071,732 | 15,315 | 102.61 |
| 086-ZR65 | 0.01 | 0.24 | 196450 | 0.08 | 0,663 | 2,032 | 0,966 | 0,188 | 0,598 | 0,618 | 1155,496 | 26,195 | 1111,250 | 12,193 | 1126,371 | 13,110 | 98.66  |
| 095-ZR72 | 0.06 | 0.74 | 25098  | 0.08 | 2,196 | 2,253 | 2,971 | 0,197 | 1,967 | 0,662 | 1268,907 | 84,550 | 1158,465 | 41,650 | 1197,649 | 41,368 | 96.73  |
| 043-ZR29 | 0.01 | 0.71 | 239889 | 0.08 | 0,559 | 2,372 | 1,950 | 0,206 | 1,831 | 0,939 | 1279,638 | 21,729 | 1208,185 | 40,290 | 1234,149 | 27,672 | 97.90  |

|          |      |      |          |      |       |        |       |       |       |       |          |        |          |        |          |        |        |
|----------|------|------|----------|------|-------|--------|-------|-------|-------|-------|----------|--------|----------|--------|----------|--------|--------|
| 097-ZR74 | 0.04 | 0.43 | 34753    | 0.08 | 0,511 | 2,340  | 0,954 | 0,208 | 0,716 | 0,750 | 1240,112 | 19,971 | 1215,488 | 15,850 | 1224,446 | 13,534 | 99.27  |
| 003-ZR1  | 0.01 | 0.27 | 154333   | 0.08 | 0,465 | 2,523  | 0,855 | 0,220 | 0,614 | 0,718 | 1270,629 | 18,101 | 1283,321 | 14,273 | 1278,638 | 12,390 | 100.37 |
| 124-ZR97 | 0.01 | 0.29 | 188346   | 0.09 | 0,629 | 2,781  | 1,031 | 0,234 | 0,728 | 0,706 | 1345,998 | 24,208 | 1352,982 | 17,747 | 1350,334 | 15,339 | 100.20 |
| 037-ZR25 | 0.05 | 0.40 | 34117    | 0.09 | 1,393 | 2,940  | 2,358 | 0,242 | 1,866 | 0,791 | 1381,996 | 53,050 | 1399,023 | 46,853 | 1392,349 | 35,420 | 100.48 |
| 005-ZR3N | 0.01 | 0.26 | 191609   | 0.09 | 0,365 | 3,306  | 0,799 | 0,257 | 0,606 | 0,759 | 1492,402 | 13,799 | 1475,321 | 15,971 | 1482,399 | 12,415 | 99.52  |
| 074-ZR55 | 0.02 | 0.17 | 68831    | 0.10 | 0,816 | 3,569  | 1,715 | 0,267 | 1,462 | 0,853 | 1564,903 | 30,432 | 1526,567 | 39,680 | 1542,770 | 27,019 | 98.95  |
| 120-ZR93 | 0.02 | 0.32 | 79878    | 0.10 | 0,759 | 3,574  | 1,269 | 0,268 | 0,947 | 0,746 | 1558,719 | 28,340 | 1532,852 | 25,800 | 1543,816 | 20,030 | 99.29  |
| 104-ZR79 | 0.01 | 0.72 | 144226   | 0.11 | 0,595 | 4,986  | 1,043 | 0,317 | 0,772 | 0,741 | 1863,579 | 21,389 | 1776,388 | 23,964 | 1816,917 | 17,563 | 97.77  |
| 031-ZR19 | 0.00 | 0.24 | 492289   | 0.11 | 0,389 | 5,267  | 1,017 | 0,338 | 0,864 | 0,849 | 1849,638 | 14,025 | 1875,761 | 28,094 | 1863,464 | 17,289 | 100.66 |
| 088-ZR67 | 0.04 | 1.52 | 38358    | 0.11 | 0,618 | 5,566  | 1,058 | 0,351 | 0,775 | 0,732 | 1879,680 | 22,195 | 1939,588 | 25,930 | 1910,859 | 18,136 | 101.50 |
| 100-ZR77 | 0.01 | 0.41 | 164941   | 0.11 | 0,553 | 5,030  | 0,914 | 0,319 | 0,626 | 0,685 | 1869,893 | 19,869 | 1784,568 | 19,513 | 1824,329 | 15,420 | 97.82  |
| 111-ZR86 | 0.03 | 0.16 | 54211    | 0.12 | 0,904 | 4,973  | 2,222 | 0,307 | 1,996 | 0,898 | 1917,756 | 32,259 | 1726,254 | 60,302 | 1814,733 | 37,225 | 95.12  |
| 063-ZR46 | 0.01 | 0.56 | 156536   | 0.12 | 0,411 | 6,007  | 0,760 | 0,360 | 0,521 | 0,685 | 1969,533 | 14,622 | 1983,823 | 17,774 | 1976,901 | 13,188 | 100.35 |
| 127-     |      |      |          |      |       |        |       |       |       |       |          |        |          |        |          |        |        |
| ZR100    | 0.01 | 0.53 | 144772   | 0.12 | 0,531 | 5,655  | 1,034 | 0,338 | 0,806 | 0,780 | 1978,273 | 18,864 | 1874,916 | 26,203 | 1924,533 | 17,767 | 97.42  |
| 117-ZR90 | 0.00 | 0.84 | 38872876 | 0.13 | 0,349 | 6,395  | 0,731 | 0,368 | 0,524 | 0,718 | 2042,430 | 12,305 | 2020,904 | 18,179 | 2031,640 | 12,791 | 99.47  |
| 004-ZR2  | 0.00 | 0.37 | 469997   | 0.13 | 0,356 | 6,779  | 1,318 | 0,388 | 1,214 | 0,921 | 2054,172 | 12,542 | 2112,254 | 43,640 | 2083,050 | 23,189 | 101.40 |
| 079-ZR58 | 0.00 | 0.63 | 719062   | 0.17 | 0,340 | 12,147 | 0,986 | 0,511 | 0,848 | 0,860 | 2580,761 | 11,344 | 2661,117 | 36,943 | 2615,788 | 18,424 | 101.73 |

| SAMPLE   | AL31                   |          |                 |                 |                  |                |                  |                |                  |       |                 |        |                |        |                |        |              |
|----------|------------------------|----------|-----------------|-----------------|------------------|----------------|------------------|----------------|------------------|-------|-----------------|--------|----------------|--------|----------------|--------|--------------|
|          |                        |          |                 |                 |                  |                |                  |                |                  |       | Apparent ages   |        |                |        |                |        |              |
| GRAIN    | <i>f</i><br>206<br>(%) | Th/<br>U | 206Pb/<br>204Pb | 207Pb/<br>206Pb | err<br>(%)1<br>6 | 207Pb/<br>235U | err<br>(%)1<br>6 | 206Pb/<br>238U | err<br>(% 1<br>6 | Rho   | 207Pb/<br>206Pb | 2 6    | 208Pb/<br>238U | 2 6    | 207Pb/<br>235U | 2 6    | conc.<br>(%) |
| 085-ZR67 | 0.01                   | 1.16     | 198732          | 0.06            | 0,462            | 0,780          | 1,087            | 0,093          | 0,911            | 0,839 | 634,716         | 19,820 | 572,610        | 9,982  | 585,308        | 9,646  | 97.83        |
| 090-ZR70 | 0.05                   | 0.93     | 30977           | 0.06            | 1,386            | 0,806          | 2,017            | 0,096          | 1,418            | 0,703 | 633,108         | 59,135 | 591,790        | 16,022 | 600,447        | 18,204 | 98.56        |
| 103-ZR81 | 0.04                   | 0.64     | 43489           | 0.06            | 0,483            | 0,824          | 1,108            | 0,098          | 0,926            | 0,836 | 643,327         | 20,687 | 601,524        | 10,628 | 610,402        | 10,139 | 98.55        |
| 092-ZR72 | 0.02                   | 0.56     | 74713           | 0.06            | 0,492            | 0,815          | 1,191            | 0,098          | 1,020            | 0,856 | 621,817         | 21,154 | 601,009        | 11,700 | 605,422        | 10,837 | 102.71       |
| 044-ZR36 | 0.01                   | 0.58     | 196819          | 0.06            | 0,355            | 0,807          | 0,934            | 0,097          | 0,780            | 0,836 | 615,690         | 15,286 | 596,918        | 8,893  | 600,879        | 8,452  | 99.34        |
| 033-ZR27 | 0.03                   | 0.40     | 61973           | 0.06            | 1,286            | 0,797          | 1,537            | 0,098          | 0,756            | 0,492 | 557,453         | 55,577 | 605,065        | 8,732  | 595,166        | 13,795 | 101.66       |
| 080-ZR62 | 0.02                   | 1.15     | 102512          | 0.06            | 0,749            | 0,823          | 1,192            | 0,099          | 0,851            | 0,714 | 619,042         | 32,148 | 607,195        | 9,858  | 609,739        | 10,902 | 99.58        |
| 011-ZR9  | 0.02                   | 0.61     | 66662           | 0.06            | 0,580            | 0,837          | 1,011            | 0,100          | 0,741            | 0,733 | 627,858         | 24,909 | 614,498        | 8,681  | 617,393        | 9,335  | 99.53        |
| 102-ZR80 | 0.01                   | 0.21     | 134226          | 0.06            | 0,527            | 0,847          | 1,026            | 0,101          | 0,798            | 0,778 | 637,405         | 22,615 | 619,090        | 9,413  | 623,074        | 9,529  | 102.30       |
| 096-ZR76 | 0.01                   | 0.44     | 192951          | 0.06            | 0,351            | 0,859          | 1,075            | 0,101          | 0,946            | 0,880 | 663,208         | 14,991 | 620,374        | 11,183 | 629,708        | 10,060 | 105.32       |
| 118-ZR94 | 0.09                   | 0.06     | 17000           | 0.06            | 0,912            | 0,867          | 1,393            | 0,102          | 0,985            | 0,707 | 672,750         | 38,789 | 623,255        | 11,700 | 634,091        | 13,095 | 106.10       |
| 020-ZR16 | 0.04                   | 0.56     | 35681           | 0.06            | 1,628            | 0,841          | 1,774            | 0,101          | 0,602            | 0,339 | 607,509         | 69,617 | 622,747        | 7,145  | 619,504        | 16,391 | 100.52       |
| 022-ZR18 | 0.01                   | 0.73     | 172956          | 0.06            | 0,492            | 0,848          | 0,906            | 0,102          | 0,665            | 0,734 | 609,785         | 21,180 | 627,153        | 7,946  | 623,431        | 8,426  | 100.60       |
| 107-ZR85 | 0.01                   | 0.62     | 197894          | 0.06            | 0,326            | 0,860          | 0,897            | 0,102          | 0,749            | 0,835 | 636,566         | 14,004 | 628,104        | 8,964  | 629,982        | 8,405  | 99.70        |

|          |      |      |        |      |       |       |       |       |       |       |         |        |         |        |         |        |        |
|----------|------|------|--------|------|-------|-------|-------|-------|-------|-------|---------|--------|---------|--------|---------|--------|--------|
| 052-     |      |      |        |      |       |       |       |       |       |       |         |        |         |        |         |        |        |
| ZR41B    | 0.01 | 0.40 | 211735 | 0.06 | 0,631 | 0,858 | 1,133 | 0,102 | 0,865 | 0,764 | 630,848 | 27,059 | 628,474 | 10,354 | 629,025 | 10,596 | 99.91  |
| 083-ZR65 | 0.01 | 0.50 | 183330 | 0.06 | 0,503 | 0,853 | 0,986 | 0,103 | 0,762 | 0,774 | 611,252 | 21,648 | 630,304 | 9,154  | 626,203 | 9,191  | 97.61  |
| 034-ZR28 | 0.01 | 0.83 | 160082 | 0.06 | 0,492 | 0,863 | 0,972 | 0,103 | 0,752 | 0,774 | 634,054 | 21,104 | 631,177 | 9,041  | 631,841 | 9,124  | 99.89  |
| 054-ZR42 | 0.01 | 0.66 | 132763 | 0.06 | 0,743 | 0,881 | 1,397 | 0,103 | 1,123 | 0,804 | 669,612 | 31,634 | 633,265 | 13,545 | 641,315 | 13,239 | 104.41 |
| 035-ZR29 | 0.03 | 1.66 | 55531  | 0.06 | 0,942 | 0,873 | 1,459 | 0,103 | 1,050 | 0,720 | 650,712 | 40,202 | 633,456 | 12,669 | 637,282 | 13,764 | 102.11 |
| 079-ZR61 | 0.00 | 0.37 | 517121 | 0.06 | 0,321 | 0,876 | 0,801 | 0,103 | 0,634 | 0,791 | 653,097 | 13,767 | 634,445 | 7,655  | 638,584 | 7,583  | 99.35  |
| 124-     |      |      |        |      |       |       |       |       |       |       |         |        |         |        |         |        |        |
| ZR100    | 0.01 | 0.63 | 144666 | 0.06 | 0,583 | 0,875 | 1,112 | 0,103 | 0,872 | 0,784 | 653,897 | 24,912 | 633,707 | 10,518 | 638,182 | 10,511 | 102.46 |
| 006-ZR4  | 0.01 | 1.31 | 158785 | 0.06 | 0,326 | 0,882 | 0,791 | 0,104 | 0,618 | 0,782 | 662,850 | 13,925 | 636,271 | 7,488  | 642,178 | 7,514  | 99.08  |
| 007-ZR5  | 0.16 | 0.66 | 9921   | 0.06 | 0,432 | 0,886 | 0,884 | 0,104 | 0,676 | 0,765 | 673,732 | 18,413 | 636,077 | 8,191  | 644,448 | 8,416  | 98.70  |
| 042-ZR34 | 0.00 | 0.05 | 547959 | 0.06 | 0,295 | 0,875 | 0,909 | 0,104 | 0,776 | 0,854 | 644,000 | 12,669 | 636,766 | 9,410  | 638,394 | 8,601  | 99.74  |
| 109-ZR87 | 0.01 | 0.19 | 250059 | 0.06 | 0,448 | 0,870 | 0,949 | 0,104 | 0,750 | 0,790 | 625,982 | 19,274 | 638,532 | 9,110  | 635,809 | 8,947  | 100.43 |
| 010-ZR8  | 0.01 | 0.50 | 112234 | 0.06 | 0,510 | 0,868 | 1,053 | 0,105 | 0,843 | 0,801 | 608,691 | 21,981 | 641,480 | 10,290 | 634,312 | 9,907  | 101.13 |
| 005-ZR3  | 0.04 | 0.54 | 35799  | 0.06 | 1,699 | 0,849 | 2,539 | 0,102 | 1,849 | 0,728 | 625,774 | 72,440 | 623,606 | 21,961 | 624,109 | 23,534 | 100.27 |
| 057-ZR45 | 0.26 | 0.14 | 5931   | 0.06 | 0,522 | 0,888 | 1,842 | 0,105 | 1,728 | 0,938 | 648,820 | 22,326 | 644,118 | 21,163 | 645,198 | 17,519 | 100.56 |
| 121-ZR97 | 0.02 | 0.55 | 72800  | 0.06 | 0,705 | 0,907 | 1,187 | 0,105 | 0,881 | 0,742 | 690,016 | 29,920 | 645,649 | 10,819 | 655,641 | 11,438 | 105.24 |
| 004-ZR2  | 0.00 | 0.48 | 459552 | 0.06 | 0,415 | 0,890 | 0,843 | 0,105 | 0,633 | 0,751 | 645,031 | 17,789 | 646,386 | 7,782  | 646,120 | 8,040  | 99.83  |
| 015-ZR11 | 0.04 | 1.04 | 41784  | 0.06 | 1,166 | 0,875 | 1,531 | 0,106 | 0,920 | 0,601 | 608,923 | 50,033 | 646,814 | 11,316 | 638,477 | 14,460 | 95.37  |
| 053-     |      |      |        |      |       |       |       |       |       |       |         |        |         |        |         |        |        |
| ZR41N    | 0.00 | 0.62 | 935085 | 0.06 | 0,263 | 0,898 | 0,842 | 0,107 | 0,708 | 0,842 | 644,700 | 11,288 | 652,494 | 8,788  | 650,785 | 8,071  | 99.07  |
| 056-ZR44 | 1.10 | 0.55 | 1410   | 0.06 | 1,804 | 0,893 | 2,259 | 0,108 | 1,309 | 0,579 | 608,735 | 77,048 | 659,173 | 16,394 | 647,918 | 21,528 | 93.95  |
| 119-ZR95 | 0.02 | 0.73 | 70690  | 0.06 | 0,714 | 0,928 | 1,185 | 0,108 | 0,871 | 0,735 | 681,166 | 30,347 | 662,059 | 10,954 | 666,450 | 11,552 | 102.21 |
| 063-ZR49 | 0.01 | 0.38 | 185166 | 0.06 | 0,522 | 0,915 | 0,982 | 0,108 | 0,745 | 0,758 | 646,404 | 22,364 | 663,605 | 9,387  | 659,744 | 9,507  | 97.98  |



|          |      |      |        |      |       |       |       |       |       |       |          |        |          |        |          |        |        |
|----------|------|------|--------|------|-------|-------|-------|-------|-------|-------|----------|--------|----------|--------|----------|--------|--------|
| 104-ZR82 | 0.02 | 1.49 | 70523  | 0.06 | 0,880 | 0,959 | 1,236 | 0,109 | 0,785 | 0,635 | 733,015  | 37,044 | 667,706  | 9,960  | 682,871  | 12,253 | 107.34 |
| 106-ZR84 | 0.01 | 0.95 | 143569 | 0.06 | 0,363 | 0,954 | 0,833 | 0,111 | 0,652 | 0,782 | 686,507  | 15,452 | 678,193  | 8,385  | 680,158  | 8,239  | 100.93 |
| 110-ZR88 | 0.01 | 0.73 | 222542 | 0.06 | 0,325 | 0,941 | 1,235 | 0,111 | 1,132 | 0,917 | 649,761  | 13,932 | 680,675  | 14,619 | 673,579  | 12,124 | 96.46  |
| 017-ZR13 | 0.03 | 0.39 | 47127  | 0.06 | 0,710 | 0,970 | 1,165 | 0,112 | 0,846 | 0,726 | 701,125  | 30,107 | 684,227  | 10,976 | 688,218  | 11,613 | 101.88 |
| 098-ZR78 | 0.03 | 0.67 | 56391  | 0.06 | 0,746 | 0,991 | 1,254 | 0,113 | 0,938 | 0,748 | 726,303  | 31,472 | 691,079  | 12,284 | 699,456  | 12,640 | 103.84 |
| 069-ZR55 | 0.01 | 0.47 | 242410 | 0.06 | 0,450 | 1,004 | 1,120 | 0,115 | 0,956 | 0,854 | 727,200  | 19,024 | 699,290  | 12,664 | 705,988  | 11,361 | 103.00 |
| 123-ZR99 | 0.01 | 0.44 | 267904 | 0.06 | 0,611 | 0,991 | 1,224 | 0,115 | 0,994 | 0,812 | 691,981  | 25,955 | 701,695  | 13,211 | 699,426  | 12,340 | 98.94  |
| 027-ZR21 | 0.03 | 0.18 | 44491  | 0.07 | 0,460 | 1,116 | 1,172 | 0,123 | 1,012 | 0,864 | 801,501  | 19,220 | 747,411  | 14,274 | 761,136  | 12,512 | 105.30 |
| 021-ZR17 | 0.01 | 0.30 | 178088 | 0.07 | 0,373 | 1,165 | 0,851 | 0,129 | 0,669 | 0,786 | 785,802  | 15,623 | 783,713  | 9,876  | 784,298  | 9,280  | 100.19 |
| 122-ZR98 | 0.01 | 0.70 | 263057 | 0.06 | 0,418 | 1,168 | 0,894 | 0,131 | 0,698 | 0,781 | 761,636  | 17,580 | 794,138  | 10,428 | 785,694  | 9,759  | 96.94  |
| 116-ZR92 | 0.02 | 0.31 | 94098  | 0.07 | 0,844 | 1,210 | 1,314 | 0,133 | 0,937 | 0,713 | 808,465  | 35,134 | 803,647  | 14,149 | 804,967  | 14,560 | 100.43 |
| 077-ZR59 | 0.01 | 0.38 | 163544 | 0.07 | 0,355 | 1,536 | 0,921 | 0,155 | 0,764 | 0,830 | 980,410  | 14,431 | 929,770  | 13,227 | 944,972  | 11,292 | 105.44 |
| 030-ZR24 | 0.01 | 0.11 | 223990 | 0.07 | 0,535 | 1,477 | 0,861 | 0,151 | 0,563 | 0,654 | 952,812  | 21,821 | 907,691  | 9,528  | 920,986  | 10,394 | 103.46 |
| 086-ZR68 | 0.00 | 0.34 | 386094 | 0.07 | 0,421 | 1,543 | 0,879 | 0,153 | 0,676 | 0,770 | 1015,443 | 17,005 | 918,561  | 11,575 | 947,573  | 10,795 | 108.44 |
| 089-ZR69 | 0.00 | 0.52 | 383049 | 0.07 | 0,352 | 1,589 | 0,946 | 0,158 | 0,796 | 0,842 | 1016,141 | 14,217 | 943,707  | 13,972 | 965,758  | 11,756 | 102.46 |
| 071-ZR57 | 0.00 | 0.82 | 333651 | 0.07 | 0,547 | 1,653 | 0,902 | 0,163 | 0,614 | 0,680 | 1032,812 | 22,036 | 971,727  | 11,066 | 990,702  | 11,379 | 102.71 |
| 051-ZR40 | 0.00 | 0.42 | 769122 | 0.07 | 0,402 | 1,609 | 1,274 | 0,163 | 1,151 | 0,903 | 976,606  | 16,352 | 972,612  | 20,757 | 973,885  | 15,894 | 105.39 |
| 093-ZR73 | 0.01 | 1.01 | 144701 | 0.07 | 0,606 | 1,668 | 0,975 | 0,165 | 0,668 | 0,685 | 1020,914 | 24,449 | 985,259  | 12,201 | 996,420  | 12,344 | 93.66  |
| 082-ZR64 | 0.01 | 0.48 | 231745 | 0.07 | 0,306 | 1,702 | 0,974 | 0,168 | 0,848 | 0,870 | 1031,917 | 12,338 | 998,672  | 15,677 | 1009,182 | 12,426 | 101.53 |
| 060-ZR48 | 0.01 | 1.13 | 106613 | 0.07 | 0,381 | 1,664 | 1,231 | 0,168 | 1,110 | 0,902 | 983,499  | 15,472 | 1000,132 | 20,557 | 994,983  | 15,556 | 101.70 |
| 095-ZR75 | 0.01 | 0.53 | 104008 | 0.07 | 0,563 | 1,719 | 0,939 | 0,169 | 0,654 | 0,697 | 1031,217 | 22,671 | 1008,291 | 12,205 | 1015,592 | 12,021 | 102.30 |
| 094-ZR74 | 0.02 | 0.52 | 67383  | 0.07 | 0,587 | 1,764 | 1,551 | 0,176 | 1,387 | 0,894 | 1000,715 | 23,759 | 1047,059 | 26,789 | 1032,206 | 20,008 | 105.32 |
| 117-ZR93 | 0.01 | 0.33 | 104120 | 0.08 | 1,137 | 2,149 | 2,012 | 0,201 | 1,617 | 0,804 | 1132,687 | 44,950 | 1182,072 | 34,891 | 1164,804 | 27,690 | 98.06  |
| 045-ZR37 | 0.01 | 1.12 | 111826 | 0.08 | 0,596 | 2,378 | 1,099 | 0,216 | 0,846 | 0,769 | 1195,438 | 23,438 | 1259,483 | 19,341 | 1236,110 | 15,656 | 106.10 |

|          |      |      |         |      |       |        |       |       |       |       |          |        |          |        |          |        |        |
|----------|------|------|---------|------|-------|--------|-------|-------|-------|-------|----------|--------|----------|--------|----------|--------|--------|
| 009-ZR7  | 0.00 | 0.52 | 663882  | 0.12 | 0,418 | 5,409  | 0,910 | 0,328 | 0,719 | 0,790 | 1952,807 | 14,878 | 1826,257 | 22,841 | 1886,243 | 15,538 | 100.27 |
| 029-ZR23 | 0.00 | 0.21 | 889878  | 0.12 | 0,350 | 5,927  | 0,724 | 0,353 | 0,514 | 0,710 | 1983,742 | 12,446 | 1947,593 | 17,253 | 1965,242 | 12,537 | 97.81  |
| 065-ZR51 | 0.01 | 0.88 | 147681  | 0.13 | 0,345 | 6,367  | 0,837 | 0,356 | 0,667 | 0,796 | 2094,470 | 12,110 | 1962,761 | 22,552 | 2027,771 | 14,646 | 101.05 |
| 105-ZR83 | 0.01 | 0.25 | 250370  | 0.12 | 1,217 | 6,193  | 1,944 | 0,367 | 1,469 | 0,756 | 1988,719 | 42,990 | 2017,560 | 50,799 | 2003,411 | 33,700 | 100.29 |
| 032-ZR26 | 0.00 | 0.22 | 333042  | 0.14 | 0,283 | 7,141  | 0,707 | 0,378 | 0,531 | 0,752 | 2190,244 | 9,823  | 2066,405 | 18,771 | 2129,196 | 12,552 | 97.61  |
| 019-ZR15 | 0.01 | 0.80 | 154609  | 0.13 | 0,303 | 7,060  | 0,911 | 0,390 | 0,775 | 0,851 | 2113,055 | 10,623 | 2125,058 | 28,038 | 2119,031 | 16,145 | 100.35 |
| 018-ZR14 | 0.00 | 0.33 | 1042470 | 0.17 | 0,724 | 10,089 | 1,172 | 0,439 | 0,843 | 0,720 | 2525,433 | 24,225 | 2345,100 | 33,108 | 2443,008 | 21,535 | 104.41 |

The backscattered (BSE) images reveal that the zircon grains of the four representative samples show oscillatory zoned cores, with some also marked bright rims, although some crystals display homogeneous sectors. In general, the crystals preserve parallel bands of alternating light BSE patches in the rims, some of which were not dated due to analytical limitations (Figure 5.6). The oscillatory zoning is a typical feature of primary magmatic growth (Corfu *et al.*, 2003). The Th/U ratios are majoritarian higher than 0.1, highlighting the magmatic origin of the zircon grains (Hanchar and Rudnick, 1995; Corfu *et al.*, 2003; Rubato, 2017). Few zircon crystals (~1%) record rims ages varying from 610 to 652 Ma and showing low Th/U ratios (< 0.1), which probably reflect its metamorphic origin (Figure 5.6).

The overall concordant ages vary from ca. 590 to 2848 Ma, and ca. 70% of the zircon crystals display Neoproterozoic ages, clustering mainly around the Ediacaran-Cryogenian interval. Essentially, the major peak constrained for each sample was found to be around 620 Ma. The Concordia age of each sample was found to be around 600 Ma by weighted mean of the youngest concordant population of zircon, while the subordinate nearest young population is dated around 620 Ma (Figures 5.6 and 5.7).

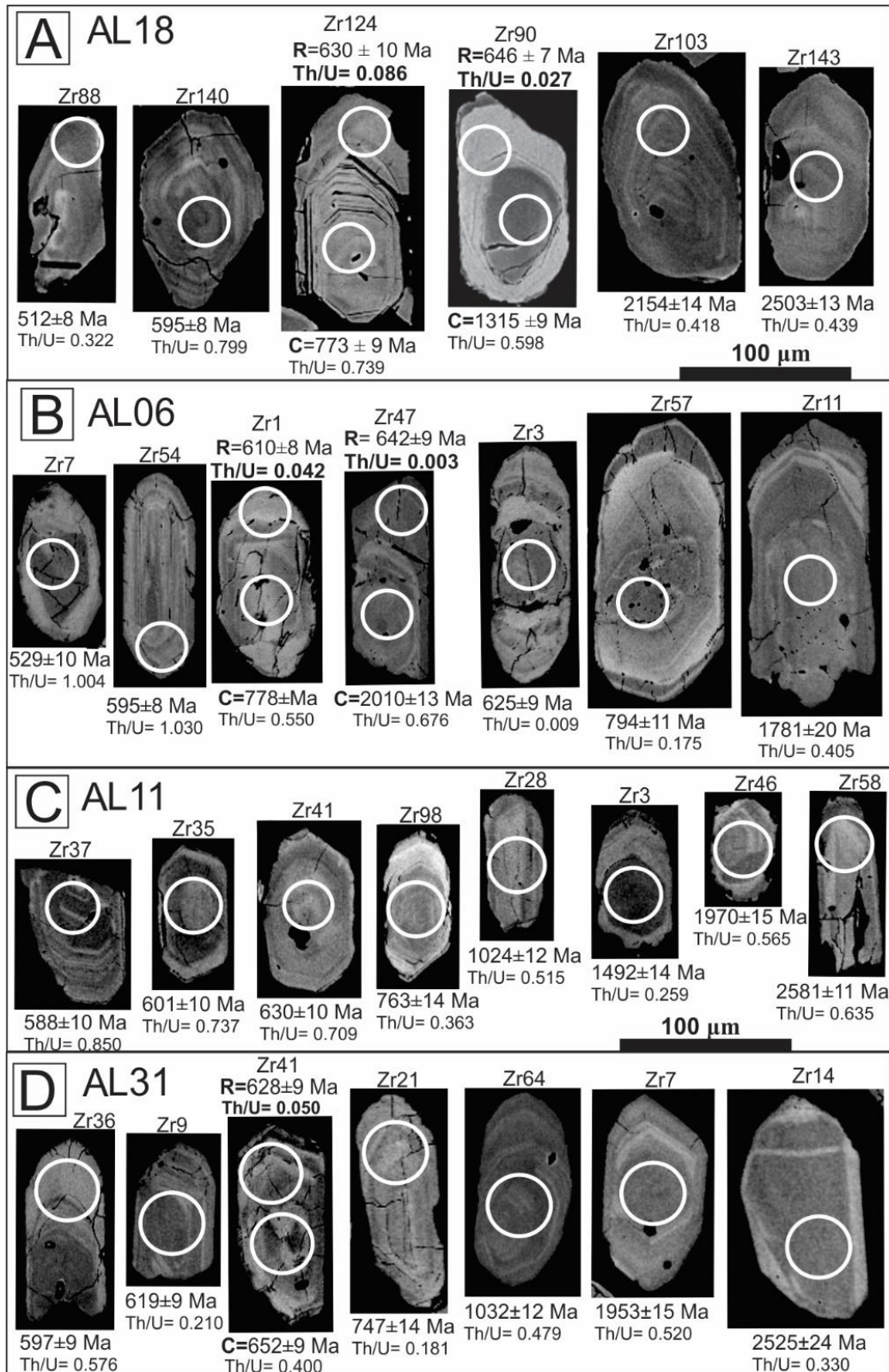


**Figure 5.6** – Backscattered images of some representative grains from the analyzed samples. U-Pb measurement spots are indicated in white circles with 30  $\mu$ m. See text for details. C= Core; R= Rim

The sample AL18 is mainly characterized by N30E mylonitic foliation, related to Transbrasiliano Lineament overprint (e.g. Figure 5.5B). Out of 165 analyzed grains, 104 detrital zircon crystals yielded concordant ages with discordance of less than 10%. The concordant ages range from 512 to 2503 Ma, of which 74% are Neoproterozoic, and of these, 61% correspond to the Ediacaran-Cryogenian interval (Figure 5.7A). The dominant clustered ages between 590 and 650 Ma generated the major peak at ca. 620 Ma, while subordinate minor peaks (< 10 zircon grains) at ca. 720 Ma, ca. 800 Ma and ca. 2127 Ma are observed (Figure 5.7B). The scattered and single youngest zircon grain is dated at  $512 \pm 8$  Ma.

The sample AL06, a schist with cordierite and sillimanite, is located near Bom Jardim de Goiás and underwent thermal metamorphism due to intrusion of the granodiorite pluton (e.g. Figure 5.4F). Of the 104 analyzed grains, 64 presented concordances between 97 and 101%, ranging from 529 to 2821 Ma in age. Most of the zircon grains display Th/U ratios between 0.3 and 1.8. It is noteworthy that low Th/U ratios (<0,1) of some grains with  $^{206}\text{Pb}/^{238}\text{U}$  between 610 and 642 Ma were only recorded on crystal rims, suggesting that these grains underwent metamorphism. Main provenance points to Neoproterozoic sources, consisting in 67% of the analyzed grains, of which 47% are of Ediacaran-Cryogenian ages (Figure 5.7C). The contribution of grains dated between 591 and 648 Ma yielded the major peak at ca. 618 Ma (Figure 5.7D). Minor prominent peaks are observed at ca. 776 Ma and 2178 Ma, while the youngest crystal is dated at  $529 \pm 10$  Ma.

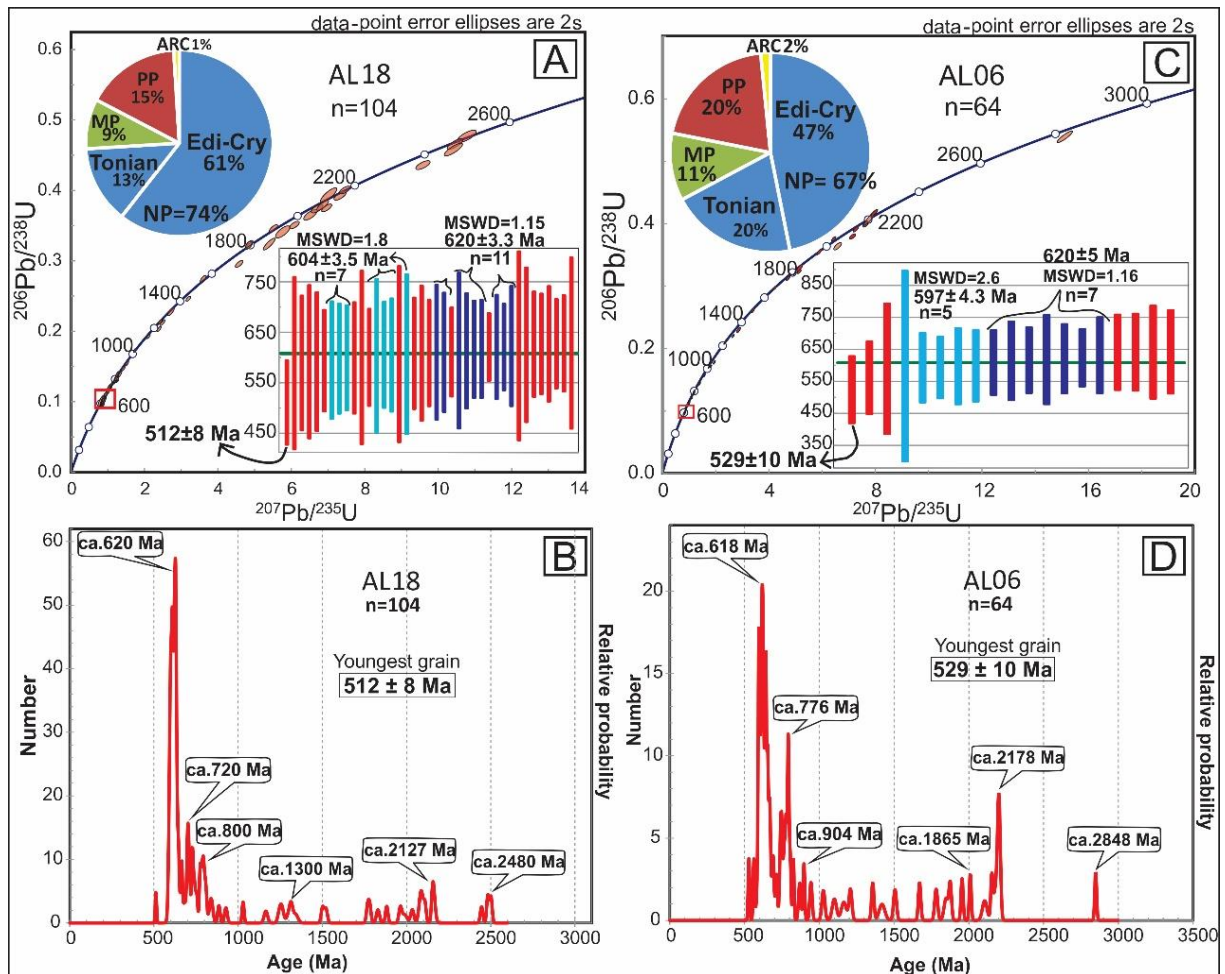


**Figure 5.7** - (A) weighted mean average plot of 104 analyzed concordant grains of sample AL18; (B) probability density diagram showing  $^{206}\text{Pb}/^{238}\text{U}$  age spectra of the concordant analyzed grains of sample AL18; (C) weighted mean average plot of 64 analyzed concordant grains of sample AL06; (D) probability density diagram showing  $^{206}\text{Pb}/^{238}\text{U}$  age spectra of the concordant analyzed grains of sample AL06.

The zircon crystals from the samples AL31 and AL11 show smaller grain size, ranging between 50 and 180  $\mu\text{m}$  (e.g. Figure 5.6), which is linked to the phylitic lithofacies. Of the 103 analyzed zircon crystals from the sample AL11, 81 yielded concordant ages with concordance between 93 and 101%. The spectrum of ages ranges from 588 to 2581 Ma, of which 69% are from Neoproterozoic sources, and of these, 53% correspond to the Ediacaran-Cryogenian age interval. Mesoproterozoic grains represent 12% of the grains and Paleoproterozoic grains 9% (Figure 5.8C). The dominant clustered  $^{206}\text{Pb}/^{238}\text{U}$  ages range between 588 Ma and 667 Ma,

yielding the major peak at ca. 628 Ma (Figure 5.8D). Subordinate peaks (< 13 zircon grains) at ca. 750 Ma and ca. 1955 Ma are observed. The sample AL31 is located in the westernmost portion of the studied area and of the 102 analyzed grains, 66 returned ages with less than 10% of discordance, with an age spectrum from 573 to 2525 Ma. Of these concordant ages, 78% are from Neoproterozoic sources, 64% being of Ediacaran/Cryogenian ages (Figure 5.8A). The large contribution of grains dated between 573 and 672 Ma yielded the major peak at ca. 623 Ma (Figure 5.8B).

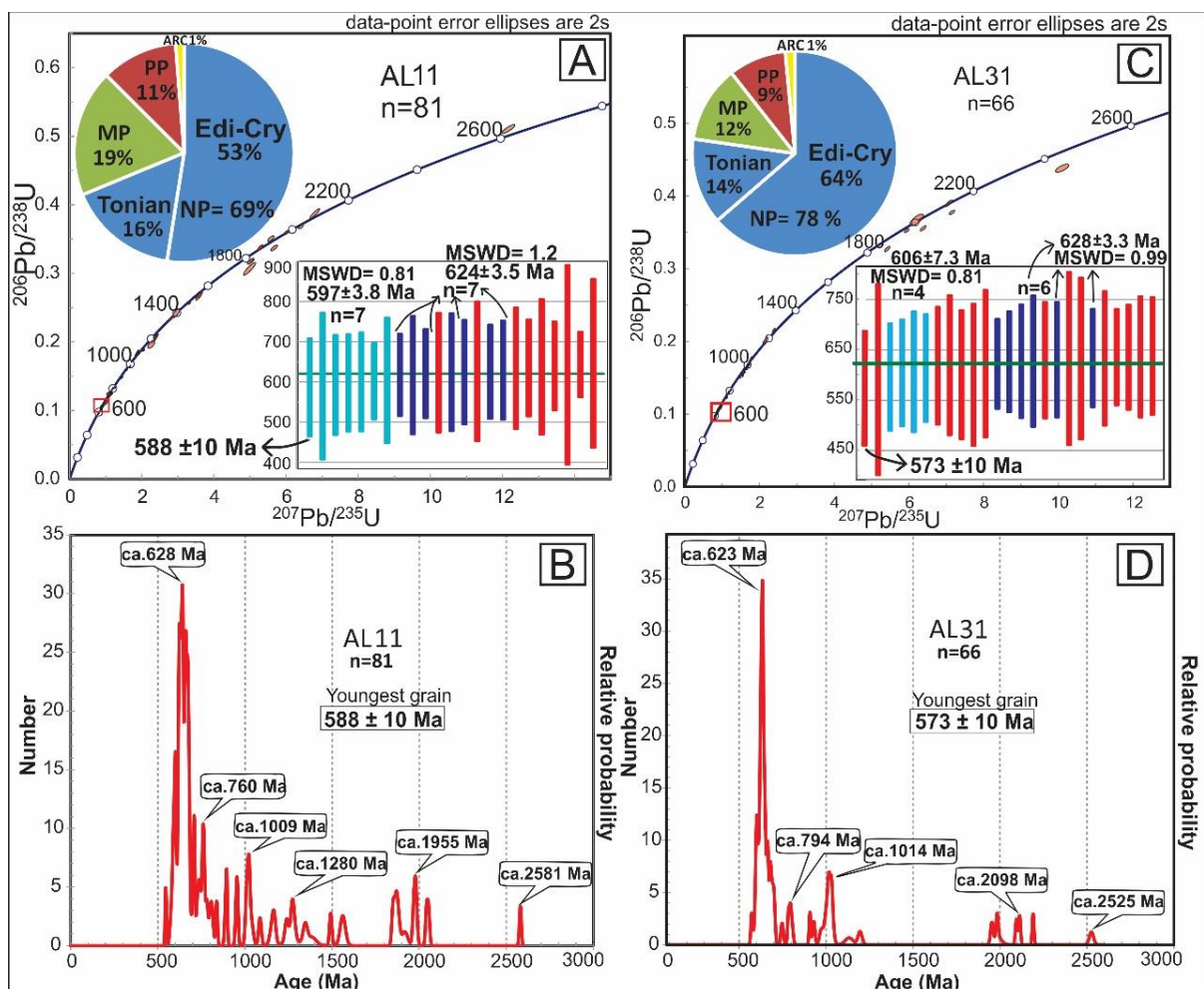


**Figure 5.8** - Distribution of probability density diagrams using weighted mean average calculation of samples AL11 and AL31. Some of the analyses were automatically rejected during the Concordia age plotting. (A) weighted mean average plot of 104 analyzed concordant grains of sample AL11; (B) probability density diagram showing  $^{206}\text{Pb}/^{238}\text{U}$  age spectra of the concordant analyzed grains of sample AL11; (C) weighted mean average

plot of 64 analyzed concordant grains of sample AL31; (D) probability density diagram showing  $^{206}\text{Pb}/^{238}\text{U}$  age spectra of the concordant analyzed grains of sample AL31.

### 5.4.3. *Sm-Nd isotope data of whole-rock samples*

The investigated metasedimentary rock samples yielded similar values of  $^{147}\text{Sm}/^{144}\text{Nd}$  ratios, which range from 0.11 to 0.12, with  $T_{\text{DM}}$  model ages between 1.37 and 1.76 (Figure 5.9). The  $\epsilon_{\text{Nd}}(590)$  values are always negative, varying between -4.02 and -8.70 (Table 5.3).

**Table 5.3** – Sm-Nd analytical data for the metasedimentary rocks.

| Sample | Sm (ppm) | Nd (ppm) | $^{147}\text{Sm}/^{144}\text{Nd}$ | $^{143}\text{Nd}/^{144}\text{Nd}$ | $\epsilon_{\text{Nd}}(0)$ | $\epsilon_{\text{Nd}}(540)$ | $T_{\text{DM}}$<br>(Ga) |
|--------|----------|----------|-----------------------------------|-----------------------------------|---------------------------|-----------------------------|-------------------------|
| AL18   | 4.732    | 23.957   | 0.1194                            | 0.512128+/-7                      | -9.95                     | -4.62                       | 1.46                    |
| AL06   | 7.332    | 38.655   | 0.1147                            | 0.511870+/-7                      | -14.98                    | -9.33                       | 1.76                    |
| AL31   | 5.664    | 27.711   | 0.1236                            | 0.512042+/-8                      | -11.63                    | -6.59                       | 1.66                    |
| AL11   | 7.072    | 37.065   | 0.1153                            | 0.512040+/-5                      | -11.67                    | -6.06                       | 1.53                    |
| AL4B   | 6.725    | 35.416   | 0.1148                            | 0.511873+/-9                      | -14.92                    | -9.28                       | 1.76                    |
| AL07   | 3.051    | 15.481   | 0.1191                            | 0.512191+/-8                      | -8.72                     | -3.37                       | 1.37                    |
| AL09B  | 2.267    | 12.587   | 0.1089                            | 0.512087+/-16                     | -10.75                    | -4.70                       | 1.38                    |
| AL38   | 11.385   | 62.499   | 0.1101                            | 0.512029+/-9                      | -11.88                    | -5.91                       | 1.48                    |



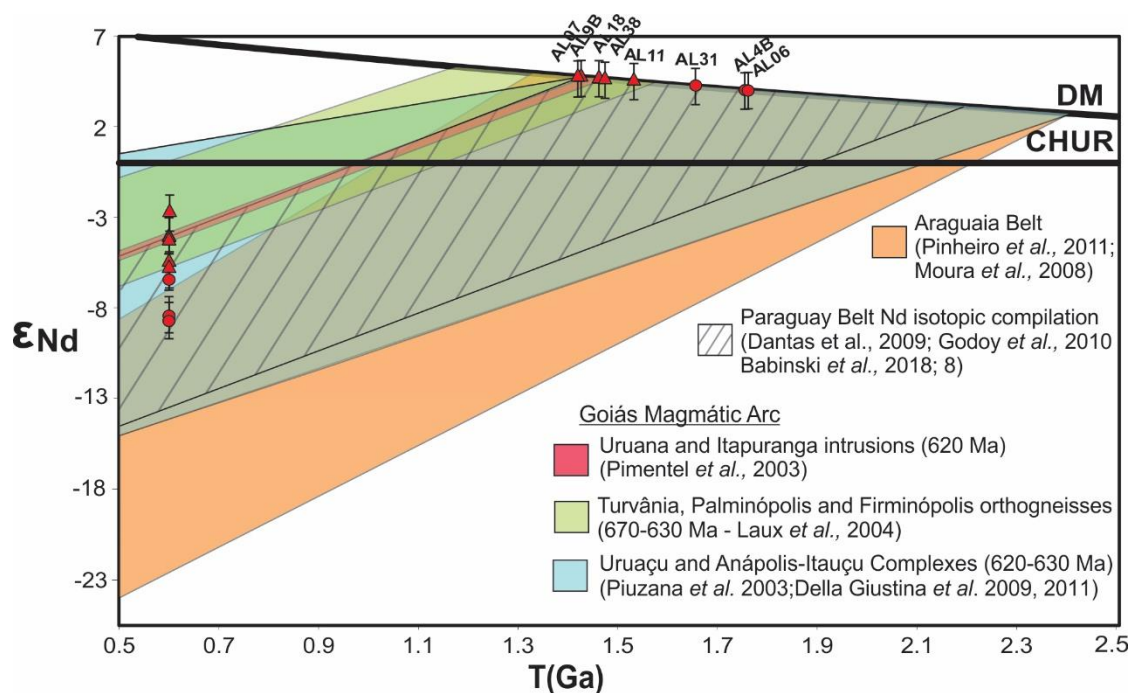


**Figure 5.9** - Sm-Nd plots for metasedimentary rocks of the studied rocks in comparison with Nd values of likely source areas of the nearby Goiás Magmatic Arc, Paraguay Belt and Brasília Belt. See text for detailed discussions.

#### 5.4.4. $^{40}\text{Ar}/^{39}\text{Ar}$ data

The results of  $^{40}\text{Ar}/^{39}\text{Ar}$  step-heating data for the representative samples AL01 and AL19 are shown in Supplementary Table 5.2. The K/Ca and Cl/K spectra for each sample are shown homogeneously distributed along all the step heating ages. Sample AL01 corresponds to a syn-to late-collisional granodiorite pluton, genetically associated to an appinitic suite (Leite *et al.*, 2021). The intrusion into the low-grade metasedimentary rocks generated a local metamorphic contact aureole. This sample AL01 is located in the northern part of the pluton and displays an incipient schistosity defined by the orientation of biotite and hornblende aggregates, following the regional characteristic trend of the Transbrasiliiano Lineament (Figure 5.10A). The analyzed biotite sample yielded a flat spectrum for nearly 57% of  $^{39}\text{Ar}$  released in the mid-temperature range, which generated a statistically valuable plateau age of  $549.2 \pm 3.9$

Ma (MSWD=2.06; Figure 5.10B). The last heating increments provide slightly younger ages while the first heating steps give evidence of argon loss, probably due to weathering effects that are significant throughout the region. For this reason, the total gas age of  $539.4 \pm 3.8$  Ma can be considered as the minimum cooling age for this biotite.

The sample AL19 is located far from the granodiorite intrusion and its contact aureole (e.g. Figure 5.3) and corresponds to a muscovite schist metamorphosed under greenschist facies conditions (Figure 5.10C). The muscovite grains from this sample released about 70% of their argon in three steps that correspond to a plateau age of  $536 \pm 4.1$  Ma, with MSDW=1.17 (Figure 5.10D), in agreement with the total gas fusion age ( $539 \pm 1.2$  Ma). The final portion of the age spectrum displays slightly older ages, possibly related to the polyphased tectonic activity in the studied area. However, these ages do not significantly influence the total gas age of this sample ( $539 \pm 1.2$  Ma) which is in agreement with the plateau age defined by the first heating steps.

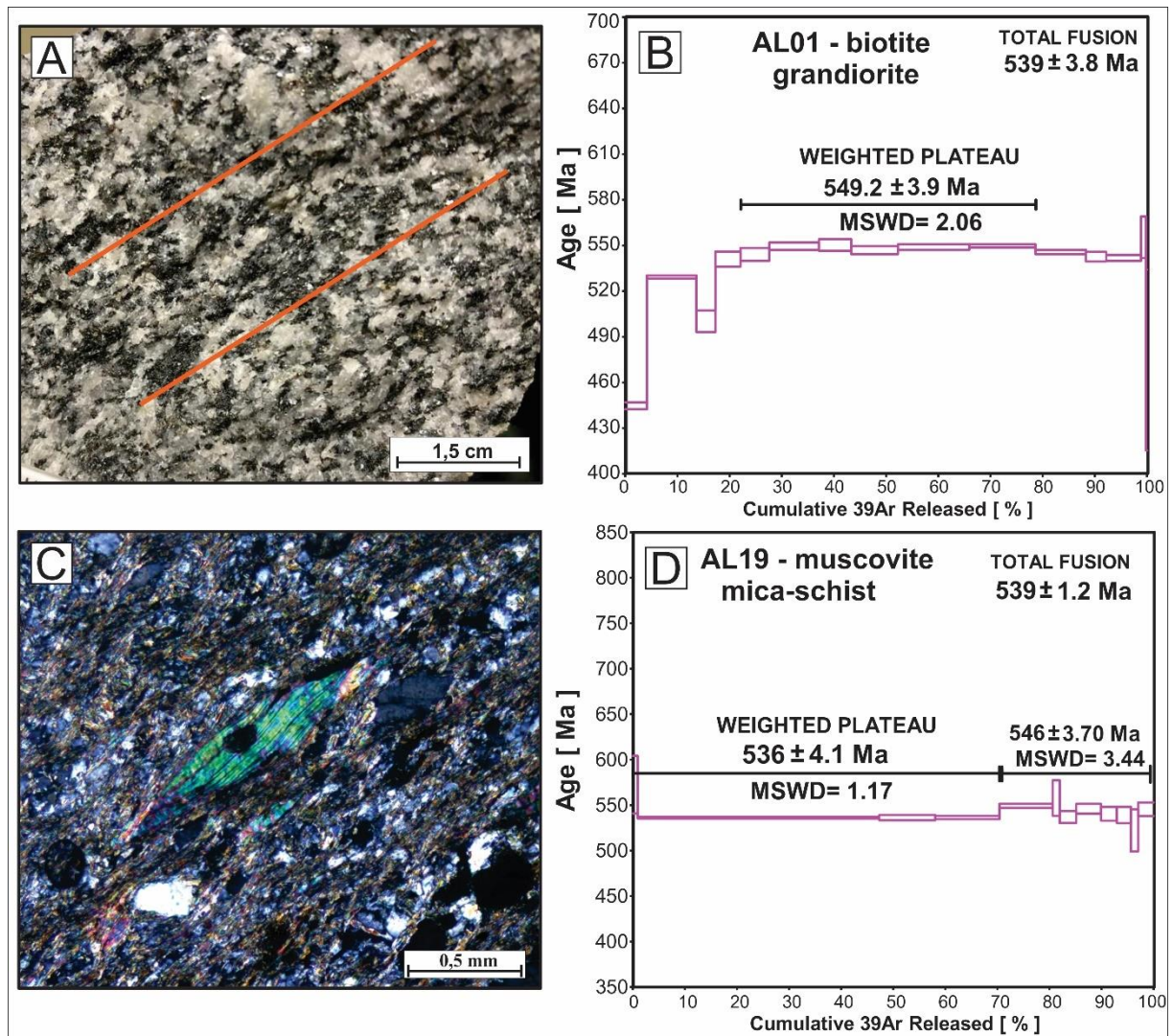


**Figure 5.10** – (A) Hand specimen of granodiorite highlighting the weak schistosity marked by oriented mafic minerals. The plutonic body was emplaced in the investigated metasedimentary rocks and the analyzed biotite grains presented orientation parallel to the Transbrasiliano Lineament trend; (B) age spectrum of biotite from this granodiorite; (C) photomicrograph of mica schist, highlighting a muscovite porphyroblast; (D) age spectrum of white micas from this mica schist.

## 5.5.DISCUSSION

### 5.5.1. Age of sedimentation and depositional setting

The overall distribution of ages of the detrital zircon ages is assumed to reflect the ages of the sources that have contributed material to the sedimentary basin, basically from recycling of older rocks (Dickinson and Gehrels, 2009). The maximum deposition age of a sedimentary rock can be constrained via the youngest statistical population of U-Pb ages of detrital zircon (Coutts *et al.*, 2019). The 25 youngest analyzed grains correspond to 7,7% of the concordant zircon grains, clustered between 600 and 512 Ma, and generate a major statistical peak at ca. 594 Ma (Figure 5.11). Of these 25 zircon grains, 21 vary from 588 to 600 Ma, while the four isolated youngest grains display a scattered age decrease pattern, ranging from 573 to 512 Ma.

We assumed that the four scattered youngest zircon ages accumulated between the late Ediacaran/early Cambrian likely reflect contaminated grains or even indicate common Pb loss. According to Andersen *et al.* (2019), concealed ancient lead loss and over-correction for common  $^{207}\text{Pb}$  may create false indications of the maximum sedimentary period. Moreover, to calculate the maximum depositional age just from one or two youngest grains should be avoided (Sharman and Malkowski, 2020). Thus, for discussions, we assume that the final sedimentary deposition period is related to the main youngest peak, constrained at ca. 594 Ma.

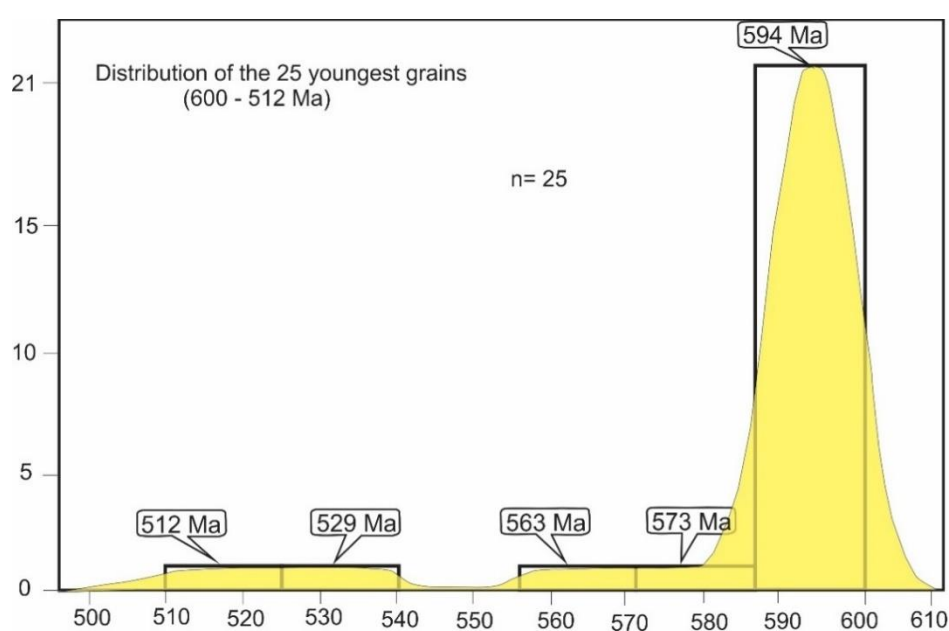


**Figure 5.11** – Distribution of the youngest dated grains, which vary between 600 and 512 Ma.

The source-to-sink relationship provides essential information to the sedimentary basin investigation, concerning the paleoenvironment at the time of deposition (Cawood *et al.*, 2012). The euhedral to subhedral morphology features, 1-3 aspect ratios, concentric oscillatory zoning and mainly high Th/U ratios of the analyzed detrital zircon grains (e.g. Figure 5.5) allow to suggest a magmatic origin and a short-distance sediment transportation (Pupin *et al.*, 1980; Hanchar and Rudnick, 1995; Corfu *et al.*, 2003). The Ediacaran-Cryogenian age population represents approximately 60% of the concordant grains and displays the smallest grain size (up to 90  $\mu\text{m}$ ), as well as does not show a wide variation in terms of morphologies and internal zonation (e.g. Figure 5.5). These features strongly support the idea that the narrow range of zircon ages indicates a restricted sedimentary provenance, probably coming from the same terrain/formation.

The major peak defined for the four analyzed samples is constrained at ca. 620 Ma, with zircon ages ranging between 590 and 650 Ma, while the maximum time of sedimentation is constrained by the youngest zircon grains at ca. 594 Ma. According to the model proposed by Cawood *et al.* (2012), an age distribution in which more than 50% of zircon grains have ages close to that of the depositional age reflects tectonic collisional and/or accretionary settings of basins located nearby contemporaneous magmatic arcs (Figure 5.12A). The adjoining magmatic arc denudation triggers a syn-collisional sedimentation, in which most of the curves in the Cawood *et al.* (2012) diagram represent clear similarities with the unimodal detrital zircon population pattern observed in foreland basins (Figure 5.12B). The investigated samples plot in the field described by Cawood *et al.* (2012) as F-land 2, associated to the Appalachian Orogen (United States) and as in the F-land 3, that is correlated to the Grenville Orogen (Canada, Scotland and United States). As a result of a foreland setting, there is an extremely rapid sedimentation to form basins within an active continental margin in the final stage of an orogenic system (Miall, 1995; Ingersoll *et al.*, 2003).

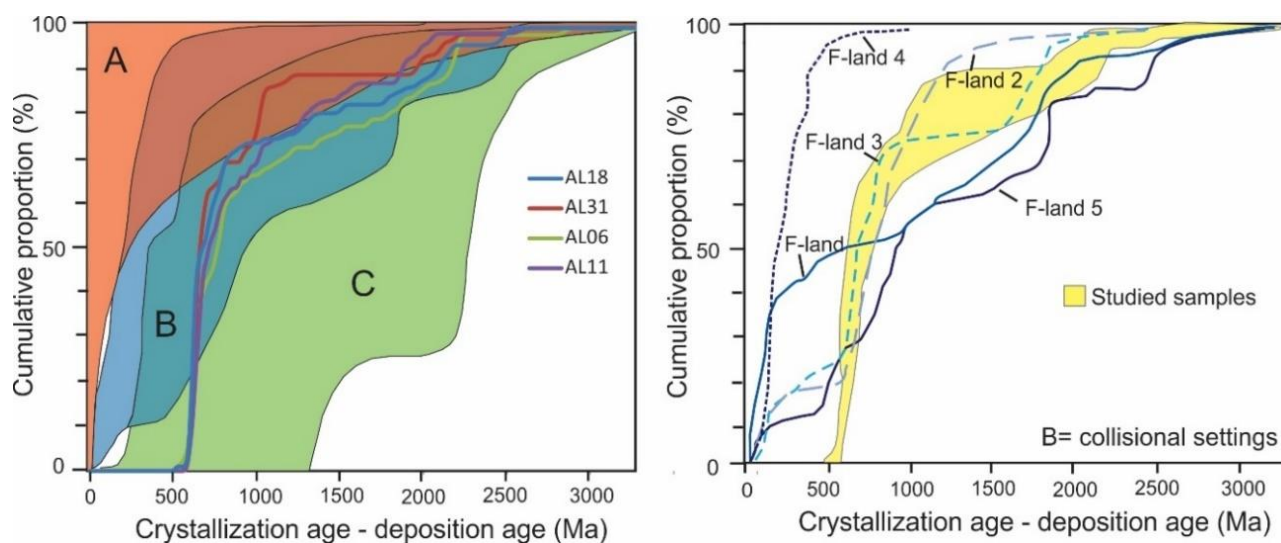


**Figure 5.12** – (A) summary plot of variation of the difference between the measured crystallization age for a detrital zircon grain and the depositional age of the succession in which it occurs, based on cumulative proportion curves of Cawood et al. (2012) for the four samples of this study. A: convergent basins (red field); B: collisional basins (blue field); C: extensional basins (green field); (B) plot of cumulative proportion as function of different curves related to foreland data from five locations established by Cawood et al. (2012).

### 5.5.2. Most probable source areas

The major peak, constrained around 620 Ma, represents a basin sedimentation that evolved in relation to a coeval magmatic arc that lasted active up to ca. 594 Ma. We can account that this period differs from the most likely magmatic source in the regional context, the nearby Goiás Magmatic Arc within the Brasília Belt since it was already fully stabilized at ca. 630 Ma in the center of the Tocantins Province (Della Giustina *et al.*, 2009, 2011). The existence of a younger active magmatic arc continental margin was previously suggested by Leite *et al.* (2021) based on petrological studies of high Ba-Sr granitoids, that intruded the investigated metasedimentary strata. The generation of the appinitic suite at ca. 555 Ma strongly required the existence of a subduction stage around 590 Ma in the studied area (Leite *et al.*, 2021).

To the north, in the Araguaia Belt, the Porangatu Granulite Complex is dated at  $580 \pm 7$  Ma and also indicates a younger orogenic evolution in the center of the Tocantins Province (Gorayeb *et al.*, 2017). Soares *et al.* (2006) postulated from seismic refraction features that the Porangatu metamorphic region corresponds to an active seismic portion associated with a Neoproterozoic mantle in central Brazil. Our U-Pb zircon detrital data corroborate these interpretations and constrain a syn-collisional sedimentation event related to an arc-related activity, developed after ca. 620 Ma, the end of which took place approximately at ca. 594 Ma (e.g. Figure 5.11). Thus, it is possible to indicate that the zircon grains dated after the stabilization of the Goiás Magmatic Arc at ca. 620 Ma were most likely derived from the rocks generated from the advance of this active margin. The remaining elements that record this young magmatic arc margin may be hidden by the Phanerozoic cover and/or possibly have been carried below the orogenic wedge.

The subordinate zircon grains sourced in Cryogenian and Tonian terrains may have been eroded from the supracrustal formations, igneous and meta-igneous stabilized terrains within the Brasília, Araguaia and Paraguay fold belts (Pimentel *et al.*, 1996, 1999, 2003; Laux *et al.*, 2004; Matteini *et al.*, 2010). The remaining older zircon grains with ages between Neoproterozoic (2.5 - 2.8 Ga) and Meso- to Paleoproterozoic ages represent 26% of the concordant ages, and the most appropriate candidates for their source area are the adjacent provinces of the Amazonian Craton (1.3 to 2.5 Ga; Tassinari and Macambira, 1999). The oldest zircon could be correlated to the terranes of Carajás Province (>2.3 Ga), such as the Plaquê Intrusive Suite (2700 Ma, Araujo *et al.*, 1988), emplaced in the Carajás-Iricoumé Block, Central Amazon Province.

The Paleoproterozoic-Archean allochthonous cratonic fragments within the Brasília Belt constitute the Goiás Massif Terrane (Tomazzoli, 1992; Jost *et al.*, 2013) and could be also considered as a possible ancient source. In same reasoning, the Paleoproterozoic layered mafic-

ultramafic complexes at the boundary of Araguaia and Brasília belts may also be pointed out as a possible sources (Gorayeb *et al.*, 2000). The more distant ancient terrains are not considered as likely sources. The cratonic terrains located in the east of the Brasília Belt, as the São Francisco Craton and/or the Paranapanema Block, are less likely to be taken as a possible source, since the debris coming from the east tend to be deposited in the large and in the then still open Goiás-Pharusian Ocean (Cordani *et al.*, 2009, 2013).

The Neodymium isotopic signature attested by the  $T_{DM}$  ages (1.37 to 1.76 Ma) suggest that the basin was filled by combinations between reworked older material (Archean and/or Paleo- to Mesoproterozoic) and younger (Neoproterozoic) sedimentary debris. The most natural candidate for the Cuiabá Group would be the Amazonian Craton, however, to explain such a young  $T_{DM}$ , a contribution from a younger source is required. The negative  $\epsilon_{Nd}$  (-3.37 to -9.33) values are most likely to be compared to some units of the Goiás Magmatic Arc, the Araguaia Belt and to the Paraguay Belt itself (see Figure 5.9). Few zircon grains that display low Th/U ratios (0.003 to 0.027) in their rims record the  $^{206}U/^{238}Pb$  ages between 610 and 646 Ma (see Figure 5.6). When associated to the similar Sm-Nd signature (see Figure 5.9), these features could point to the Neoproterozoic high-grade mafic-ultramafic complexes of the Brasília Belt (Piuzana *et al.*, 2003; Della Giustina *et al.*, 2009, 2011) as a possible source area.

### 5.5.3. *Record of thermal conditions*

The plateau ages of the micas from the calc-alkaline granodiorite pluton and its host low-grade metamorphic schists record robust evidence of low-to-intermediate P/T metamorphic conditions in the investigated area. The mineral ages acquired from argon isotopic data are interpreted as the record of the last cooling event through each mineral closure temperature



relatively to the cumulative  $^{39}\text{Ar}$  release. Based on the model of Dodson (1973), the Ar diffusion parameters for biotite and muscovite are traditionally determined from the experiments of Harrison *et al.* (1985, 2009), respectively. The stipulated nominal Ar closure temperatures of 300°C and 400°C, respectively, are used to define the approximate cooling path for these minerals.

#### 5.5.3.1. Constraining an igneous cooling

The  $^{40}\text{Ar}/^{39}\text{Ar}$  step-heating data of the oriented biotite from a late-tectonic granodiorite yielded a plateau age of  $549.2 \pm 3.9$  Ma (Figure 5.10A) that can be compared to the U-Pb zircon age of  $554.0 \pm 2.9$  Ma (Leite *et al.*, 2021) of the pluton interpreted as a crystallization age associated with the syn- to late-kinematic igneous emplacement of the pluton. The local occurrence of a contact aureole with sillimanite-cordierite-bearing assemblages (Figure 5.4E) suggests that this emplacement took place under a MT-LP gradient ( $P < 4$  kbar,  $550 < T < 600^\circ\text{C}$ ; Harte and Hudson, 1979; Hodges and Crowley, 1985; Jamieson *et al.*, 1998).

The low-pressure mineral paragenesis of the contact aureole suggests heat transference in the middle/upper transitional crust, pointing to a middle metamorphic grade event at shallow crustal level. The U-Pb and  $^{40}\text{Ar}/^{39}\text{Ar}$  data indicate very rapid magmatic heat dissipation, recording cooling from about 600°C to 320°C (i.e. the closure temperature for argon in biotite, Harrison *et al.*, 1985) in a mean time interval of 5 Ma (Figure 5.13). Considering the error margins on the ages, it is possible to suggest a minimum cooling rate of ca. 25°C/Myr for the 554-549 Ma period.

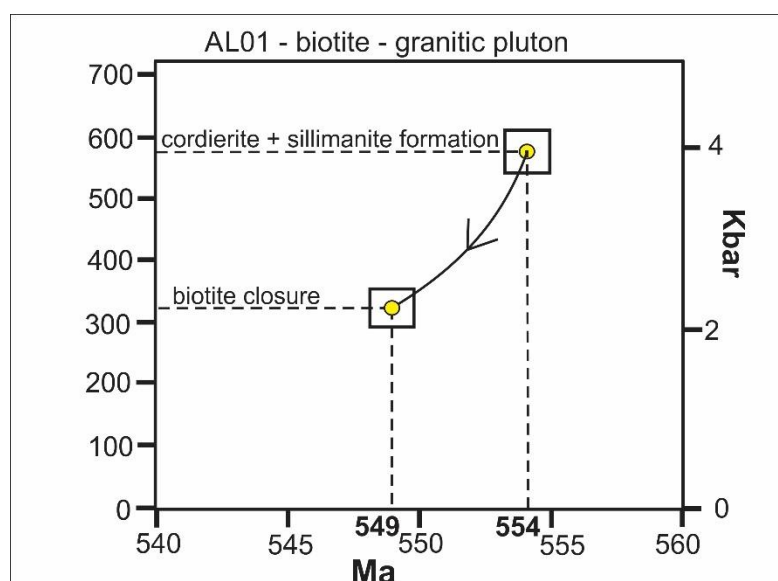


**Figure 5.13** - P-T-t schematic illustration of the cooling path evolution of sample AL01 (granodiorite pluton).

The rapid cooling rate recorded in the analyzed pluton indicates that the magma unroofing occurred almost simultaneously with its crystallization. According to Leite *et al.* (2021), the granodiorite is petrogenetically associated to the less evolved appinitic rocks by fractional crystallization processes. This magmatic suite developed in relation to the Transbrasiliano Lineament strike-slip faults (Leite *et al.*, 2021), which have provided a pathway for ascent of the appinitic magma and a mechanism of emplacement at higher crustal levels (Hutton and Reavy, 1992; Murphy, 2013; Leite *et al.*, 2021). The fast-cooling rate obtained for the pluton can be used to demonstrate that the area has undergone a rapid uplift event up to the end of the Ediacaran. The syn-orogenic depositional character highlighted by the distribution of the U-Pb ages requires that the unroofing of the orogen must have occurred just after or almost concomitantly with the sedimentation period.

This interpretation is consistent with the fast cooling-fast uplift model proposed for the syn-to late granitic-appinitic suites in the Scottish Caledonides, which has been related specifically to the closure of the Iapetus Ocean crust through strike-slip weakness zones during

the subduction beneath Laurentia (Fowler and Henney, 1996; Atherton and Ghani, 2002; Murphy *et al.*, 2019). In such context, between the converging plates, the Caledonian terranes were accreted, and deformed together with the forelands (Hutton and Reavy, 1992).

#### 5.5.3.2. Country rocks metamorphic evolution

The argon closure temperature of muscovite (~400°C; Harrison *et al.*, 2009) is analogous to the metamorphic temperature experienced by the metasedimentary country rocks of the plutons, which record regional greenschist facies conditions (biotite zone; Figure 5.4C). The  $^{40}\text{Ar}/^{39}\text{Ar}$  muscovite age at 536.3±4.1 Ma (Figure 5.10B) reported in this study would suggest that the metasedimentary rocks remained at ~400°C for approximately 10 to 25 m.y. after the metamorphic and/or collisional peak in the region, which is recorded by the late-kinematic pluton age at 554.0±2.9 Ma (Leite *et al.*, 2021).

We assume that the Ar-Ar step-heating plateau age from the country rocks represent the last thermal record in the study area. This age can also indicate the presence of an unknown late-to post-orogenic plutons in the area, that is not exposed but could have heat the country rocks. It is noteworthy that the age spectrum of the dated muscovite displays older ages of ca. 546 Ma at the end of degassing (Figure 5.10B), that are similar to the biotite age of the late-kinematic pluton and that can suggest a continuum of dissolution-recrystallization effects over 10 Ma since the first episode of deformation. Thus, the orogenic activity could have lasted more than previously thought in the internal zone of the Paraguay Belt.

The presented  $^{40}\text{Ar}/^{39}\text{Ar}$  plateau ages are compatible with the early Cambrian/late Ediacaran  $^{40}\text{Ar}/^{39}\text{Ar}$  ages previously recorded in the corridor of the Araguaia, Paraguay and Pampean belts (Table 4; Rapela *et al.*, 1993, 2007; Geraldés *et al.*, 2008, 2010; Tohver *et al.*,

2010, 2012; Piacentini *et al.*, 2013; McGee *et al.*, 2014, 2015). They corroborate several models proposing a large oceanic corridor that only closed in Cambrian times.

**Table 5.4** – Summary of  $^{40}\text{Ar}/^{39}\text{Ar}$ , K-Ar and U-Pb data available in the Araguaia, Paraguay and Pampean belts, along the Clymene Ocean corridor.

| Mobile belt   | Unit/Region                                     | Author                          | Metamorphic ages (Ma) | Mineral/Method              |
|---------------|---|---------------------------------|-----------------------|-----------------------------|
| Araguaia Belt | Estrondo Group                                  | Macambira (1983)                | 553±17                | biotite (mica schists)/K-Ar |
|               | Xambioá Formation                               | Pinheiro (2016)                 | 504 ± 6               | amphibole/Ar-Ar             |
| Pampean belts | Puncoviscana Formation                          | Adams <i>et al.</i> (1990)      | 535-540               | mica schists/K-Ar           |
|               | metaluminous calc-alkaline magmatism            | Rapela <i>et al.</i> (1998)     | 525 to 515            | metamorphic zircon/U-Pb     |
| Paraguay Belt | Nova Xavantina Metavolcano-sedimentary Sequence | Geraldes <i>et al.</i> (2008)   | 541 to 531            | biotite/Ar-Ar               |
|               | Alto Paraguay Group/Northern portion            | McGee <i>et al.</i> (2015)      | 544±7                 | muscovite (detrital)/Ar-Ar  |
|               | Urucum banded iron formation/ Southern portion  | Piacentini <i>et al.</i> (2013) | 547 to 513±3          | braunite/Ar-Ar              |
|               | Cuiabá Group/São Vicente region                 | Tohver <i>et al.</i> (2010)     | 496 to 500            | Illite/Ar-Ar                |

#### 5.5.4. *Evolution of the Paraguay Belt*

The internal zone of the Paraguay Belt is basically composed of a set of metasedimentary sequences traditionally taken as deposited on a passive margin setting and attributed to glacio-marine deposits grading upwards into turbidites and mud flows (Alvarenga, 1990; Alvarenga and Trompette, 1993; Alvarenga and Saes, 1992). The Cuiabá Group exposed in the Region 1 (Figure 5.1C) exhibits Mesoproterozoic maximum depositional age, with sedimentary provenance typically coming from the Amazonian Craton – 1.2 to 2.5 Ma and deposited on a continental margin (Figure 14A; Dantas *et al.*, 2009; Batalha, 2016; Babinski *et al.*, 2018). However, our U-Pb isotopic data of detrital zircon grains appear to demonstrate an evident provenance shift in detrital input of the Cuiabá Group, varying from Paleo- and Mesoproterozoic cratonic sources to Neoproterozoic magmatic arc terrains, especially from Ediacaran-Cryogenian sources (Figure 5.14C).

The presented clear unimodal provenance spectrum of detrital zircon is very close to the data obtained in the center-southern Paraguay Belt, which show maximum depositional age of  $602\pm 13$  Ma (Pelosi, 2017) and  $523\pm 5$  Ma (Vasconcelos, 2018), with also dominantly Neoproterozoic sources. The combination of these data with the study area features constrains an important geodynamic change from passive margin to compressional setting in the eastern Paraguay Belt. We establish that the typical record of oversized clasts such as dropstone or ice-rafted debris typically described in the Cuiabá Group is replaced by a syn-orogenic sedimentation. The investigated debris are more likely to be deposited in a relatively calm marine sedimentation, which comes particularly from an associated uplifted mountain belt.

The external zone of the Paraguay Belt shows the same sedimentary dynamic of evident basin inversion toward the upper Alto Paraguay Group units (Bandeira *et al.*, 2012; McGee *et al.*, 2014). The investigated rocks show maximum depositional age similar to the upper Alto

Paraguay Group, constrained at  $541\pm 7$  Ma and deposited in a foreland basin (McGee *et al.*, 2014). Then, it is possible to infer that the studied rocks and the upper Alto Paraguay Group are contemporary, and these sedimentary records may represent the event of final evolution phase of the Paraguay Belt in Cambrian times. Recently, based on high resolution airborne geophysical data in the Nova Xavantina region, to the north of the study area, Silva *et al.* (2020) stated that the Amazonian Craton served as backstop for the formation of a foreland basin in response to the flexural subsidence due to the tectonic inversion of the basin.

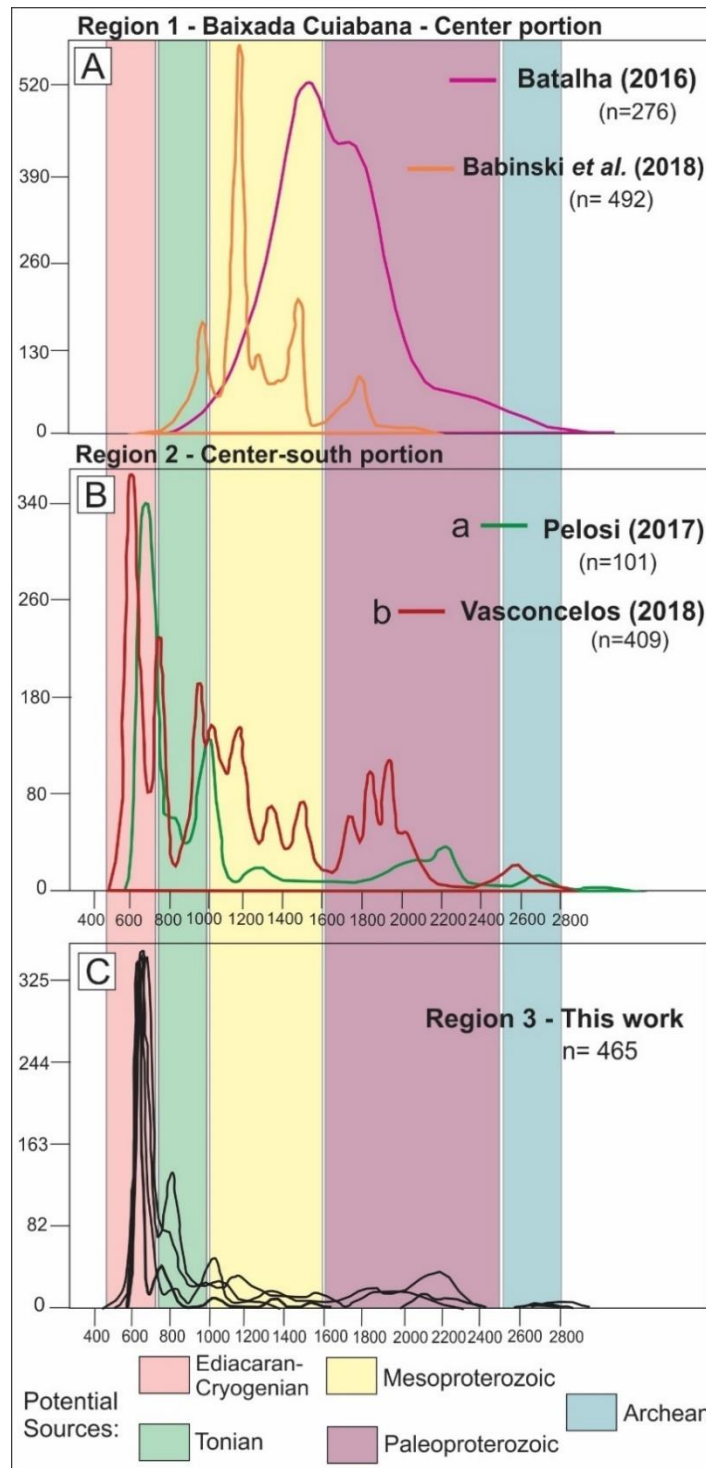


**Figure 5.14** – Histogram illustrating the probability density of detrital zircon ages in the three different regions of the Cuiabá Group, Paraguay Belt: (A) provenance age pattern of rocks considered as typical Cuiabá Group in the core of the Paraguay Belt (Region 1 - Baixada Cuiabana); (B) provenance age pattern of the center-southern sector (Region 2) of the Cuiabá Group; (C) provenance age pattern of the eastern sector of the Paraguay Belt (Region 3).

The investigated lithofacies are restricted to interbedded pelagic sediments with minor micaceous sandstone, which is likely to be compared to the fans generated typically from deposition of debris in deep water (Moiola and Shanmugam, 1984; Ingersoll *et al.*, 2003). The submarine fans that represent from passive margin to collisional stage are commonly described in large accumulations of sediments on Earth, which are subsequently deformed and incorporated into the orogenic belts as collisional foreland basin (Ingersoll *et al.*, 1995, 2003). It is known that during the active thrusting processes and crustal thickening processes, the initial load of the growing orogenic wedge could have promoted subsidence in the foreland setting, accommodating early pelagic foredeep deposits by gravity flow (Covey, 1986; Catuneanu, 2001, 2004; Mutti *et al.*, 1992). The considerable amount of K-feldspar and plagioclase reveals the low maturity of the sedimentary rock and the accelerated rate of erosion, also pointing to a deposition period during a proximal orogenic unroofing (Haughton *et al.*, 1991; Dickinson and Szcek, 1979). Further studies based on sequence stratigraphy are needed to better constrain and perhaps separate the studied lithologies from the set of Cuiabá Group passive margin formations.

The available structural data of the typical Cuiabá Group (Region 1) show greater structural complexity that is not recorded in the investigated rocks, presenting recumbent and close to isoclinal folds (D1) as the primary deformation phase (Barboza, 2008; Vasconcelos *et al.*, 2015). The investigated area registers essentially a scenario of slight compressional thrusts with open folds and a set of brittle-ductile components related to dextral transcurrent faults of the Transbrasiliano Lineament. The syn-orogenic turbidite deposition is often influenced by a transcontinental transform fault system at the end of the tectonic activity (Mutti *et al.* 1999), which could also allow the last pulse of sedimentation in a late compressional effort. We assume that the internal accommodation of the strike-slip fault system in the region becomes essential



to the maintenance of the collisional attempt and the continuous sedimentary deposition up to the Late Ediacaran.

### 5.5.5. *West Gondwana assembly at Cambrian times*

The combination of evidence from our new U-Pb and  $^{40}\text{Ar}/^{39}\text{Ar}$  data from the easternmost region of the Paraguay Belt agree with a tectonic scenario that accommodate continuous deposition in a foreland basin, that developed contemporaneously with the deformation, metamorphism and magmatism during the late Ediacaran (Leite *et al.*, 2021). The main point assumed in this work is that the final evolution of the Paraguay Belt is not linked to the closure of the Goiás-Pharusian ocean, since the terrains that registered this older ocean closure were already built up and uplifted around 620 Ma (Cordani *et al.*, 2009, 2013; Della Giustina *et al.*, 2009, 2011). The tectonic model proposed by McGee *et al.* (2014) for the northern Paraguay Belt and McGee *et al.* (2018) for the southern part point to a hypothesis of a late collisional event related to the closure of the Clymene Ocean in West Gondwana. The presented data also support an indicative of a late orogenic evolution. Moreover, this statement has been previously supported by other lines of evidence in the northern and southern Paraguay Belt (Table 5.5).

**Table 5.5** – Evidence of Clymene Ocean existence and/or closure in the Paraguay Belt.

| Author                        | Unit/portion of the belt | Obtained data  | Interpretations                                 |
|-------------------------------|--------------------------|--|---|
| Nogueira <i>et al.</i> (2007) | Araras Group/northern    | carbon and strontium isotopes in carbonate plataform | paleoenvironmental changes and paleocenographic |

|                               |   |   |  |  |
|-------------------------------|---|---|--|--|
|                               |   |   |  | evolution at the Neoproterozoic end  |
|                               |   |   |  | change in sedimentary  |
| Dantas <i>et al.</i> (2009)   | Cuiabá Group and carbonate units/northern                         | Nd isotopes of overall belt   |  | provenance from an Amazonian source to a source from within the belt itself for the upper carbonate successions  |
|                               |   |   |  | metamorphic peak between 496 and 484   |
| Tohver <i>et al.</i> (2010)   | Cuiabá Group/northern   | Paleomagnetic and geochronological data                               |  | Ma and 90° clockwise rotation of the east-west limb after ca. 528 Ma   |
|                               |   |   |  | metamorphic peak between 496 and 484   |
| Bandeira <i>et al.</i> (2012) | Diamantino and Sepotuba formations – Alto Paraguay Group/northern | U-Pb ages of detrital zircon grains younger than 541 Ma               |  | last marine deposits representing the final basin and restricted sea associated to progradation of deltaic lobes |
| McGee <i>et al.</i> (2012)    | São Vicente Granite/northern                                      | crystallization age of post-tectonic granite at 518 Ma                |  | minimum age of contractional deformation   |
| McGee <i>et al.</i> (2015)    | Diamantino Formation – Alto Paraguay Group/northern               | $^{40}\text{Ar}$ - $^{39}\text{Ar}$ of 544 Ma from detrital muscovite |  | Cambrian metamorphic age for orogenesis within the Paraguay Belt   |
|                               |   |   |  | youngest U-Pb ages of final sedimentation  |
| McGee <i>et al.</i> (2018)    | Jacadigo and Corumbá groups/southern                              | detrital zircon grains between 566 and 543 Ma                         |  | record transition from passive margin  |

---

environment to a  
collisional setting

---

The first model of the Clymene Ocean was proposed by Trindade *et al.* (2003, 2006), who argued that the Amazonian Craton was separated from the proto-Gondwana (eastern terrains/cratons) by a younger ocean up until the Cambrian and its closure gave rise to the NNE-SSW belt corridor in the West Gondwana. In the context of the Tocantins Province, we propose that the length of Clymene Ocean is restricted roughly along the Transbrasiliano Lineament shear zone corridor, where the exposed rocks record a late Ediacaran/early Cambrian evolution. It is known that the final evolution phase of the Araguaia and Paraguay belts is constrained by ca. 550 Ma syn-to late tectonic granitoids, emplaced near or along the Transbrasiliano Lineament (Alves *et al.*, 2019; Arcanjo *et al.*, 2013; Goyareb *et al.*, 2013; Leite *et al.*, 2021). Such late-tectonic magmatic rocks that intruded the investigated metasedimentary rocks evolved associated to the transcurrent strike-slip system and may also record the consumption of an oceanic lithosphere after 590 Ma between the Amazonian Craton and the western Goiás Magmatic Arc (Leite *et al.*, 2021).

The Gondwana agglutination during the Neoproterozoic represents a stepping stone on the path from Rodinia breakup to Pangea assembly (Cawood *et al.*, 2021). The later consumption of oceans during the Gondwana amalgamation reflects a common event in the final process of assembly, also registered in the largest worldwide orogeneses (Kennedy, 1964; Collins and Pisarevsky, 2005; Merdith *et al.*, 2017). The existence of the Clymene Ocean between Rodinia and proto-Gondwana was also suggested by further isotopic, geophysical and paleomagnetic data (Trindade *et al.*, 2003, 2006; Rapela *et al.*, 2007; Geraldés *et al.*, 2008; Tohver *et al.*, 2010, 2012; Tohver and Trindade, 2014; Schmitt *et al.*, 2018; McGee *et al.*, 2018; Wen *et al.*, 2020), in contrast with the view of a united and synchronous West Gondwana (Cordani *et al.*, 2009, 2013).

Within that tectonic context, our data provide a key scenario in the Tocantins Province that evolved from the Rodinia-Gondwana supercontinental transition, after final Rodinia breakup (Laurentia separating from Baltica and Amazonia) and prior to Gondwana amalgamation (Tohver *et al.*, 2012). Therefore, we propose that West Gondwana was completely assembled only in the end of Ediacaran (590 Ma), when the Amazonian Craton collided with its eastern terrains/cratons neighbors (Brasília Belt, Parapanapena Block, São Francisco and Rio de la Plata cratons).

## 5.6.CONCLUSION

Based on field, U-Pb, Sm-Nd and  $^{40}\text{Ar}/^{39}\text{Ar}$  data, it is possible to conclude that the easternmost metasedimentary rocks of the Paraguay Belt show very distinct provenance and tectonic signatures when compared to the typical Cuiabá Group exposed in the central portion of the belt. Further structural and stratigraphic detailed investigations will be crucial, in the future, to support more enhanced discussion of this sedimentary record.

Specifically, the main contributions are:

- (1) The new obtained U-Pb detrital zircon data highlight that the rocks previously interpreted as being part of the Mesoproterozoic passive margin succession of the Cuiabá Group (Seer, 1987) are actually part of a syn-orogenic basin, with maximum depositional age constrained at ca. 594 Ma.
- (2) Approximately 60% of the analyzed detrital zircon grains are sourced in Ediacaran-Cryogenian terrains with the major peak around 620 Ma, indicating a syn-orogenic sedimentation character. The distribution pattern of detrital zircon indicates that the accumulation of sediments is directly linked to the continuous growth of an adjoining

coeval magmatic arc within an active orogenic system. We infer that the basin was filled coevally with the Brasiliano granitoids generation, in a context of final compressional effort.

- (3) The syn-collisional deposition developed associated to extremely fast erosion of sources associated to a nearby mountain belt. The rapid unroofing and orogenic character of the area is confirmed by the  $^{40}\text{Ar}/^{39}\text{Ar}$  age of biotite from the granodiorite pluton, pointing to a rapid maximum cooling rate of ca.  $25^\circ\text{C}/\text{Myr}$ . The studied area is overprinted by the Transbrasiliano Lineament, which could have worked as a corridor of accommodation within the active margin. The collisional phase occurred contemporary or immediately after deposition.
- (4) The investigated rocks are classified as a syn-orogenic succession deposited in a foreland basin, which was probably being simultaneously thrust over the Amazonian Craton during the last orogenic phase registered in West Gondwana.
- (5) The model outlined in this work precludes the notion of a united West Gondwana at ca. 620 Ma and strongly suggests that the Amazonian Craton was separated from the proto-Gondwana (eastern terrains/cratons) up to the end of Ediacaran by the Clymene Ocean, as the presented data record a late sedimentary and orogenic effort in West Gondwana.

### **Acknowledgments**

This study was financed in part by the *Coordenação de Aperfeiçoamento de Pessoal de Nível Superior* (CAPES) – Finance Code 001. The authors wish to thank *Instituto Nacional de Ciência e Tecnologia – Estudos Tectônicos* (INCT-ET, CNPq grant 46.5613/2014-4, FAPDF grant 193.001.263/2017) for financial support, and once again CAPES (grant 88887.137872/2017-00) for the PhD scholarship granted to the first author Leite, A.F.G.D. The first author also acknowledges the support of the Laboratory of Geochronology of *Universidade*

de Brasília and the Noble Gas Laboratory of *Géosciences Montpellier*. RAF, ELD and ASR are grateful to CNPq for research fellowships.

## REFERENCE

- Adams, C., Miller, H. & Toselli, A. J., 1990. Nuevas edades de metamorfismo por el método K-At de la Formación Puncoviscana y equivalentes, NW de Argentina. In: ACENOLAZA et al. q.v., 209-219.
- Andersen, T., Elburg., M.A., Lagwaza, B.N. 2019. Sources of bias in detrital zircon geochronology: Discordance, concealed lead loss and common lead correction. *Earth Science Review* 197 (102899).
- Albarède, F., Telouk P., Blichert-Toft, J., Boyet, M., Agraniér, A., Nelson, B., 2004. Precise and accurate isotopic measurements using multiple collector ICPMS. *Geochimica et Cosmochimica Acta* 68, 2725-2744.
- Almeida, F.F.M., 1984. Província Tocantins, setor sudoeste. In: Almeida, F.F.M. de, Hasui, Y., 1984. *O Pré-Cambriano do Brasil*. São Paulo, Edgard Blücher 265-281.
- Alvarenga C.J.S., 1990. Phénomènes sédimentaires, structuraux et circulation de fluides développés à la transition chaîne-craton: exemple de la chaîne Paraguay d'âge protérozoïque supérieur, Mato Grosso, Brésil. PhD thesis, University of Marseille.
- Alvarenga, C. J. S., Saes, G. S., 1992. Estratigrafia e sedimentologia do Proterozóico Médio e Superior da região sudeste do Cráton Amazônico. *Revista Brasileira de Geociências*, São Paulo, 22, 493-499.
- Alvarenga, C.J.S., Trompette R., 1993. Evolução Tectônica Brasileira da Faixa Paraguay : a estruturação da região de Cuiabá. *Revista Brasileira de Geociências* 23, 18-30.
- Alves, P.V.F.S., Botelho, N.F., Dantas, E.L., Cuadros, F.A. 2019. The Cambrian peraluminous Santa Luzia granite suite in the Araguaia Belt, central Brazil: Evidence for closure of

- the Clymene Ocean based on zircon and monazite U-Pb data. *Journal of South American Earth Sciences* 92, 116-133.
- Atherton, M.P., Ghani, A.A., 2002. Slab breakoff: a model for Caledonian, Late Granite syn-collisional magmatism in the orthotectonic (metamorphic) zone of Scotland and Donegal, Ireland. *Lithos* 62, 65–85.
- Araújo, O.J.B., Maia, R., Jorge João, X.S., Costa, J.B.S., 1988. A Megaestruturação arqueana da Folha Serra dos Carajás. VII Congresso Latino Americano De Geologia, Extended Abstracts. Anais, 324-333.
- Arcanjo, S.H.S., Abreu, F.A.M., Moura, C.A.V., 2013. Evolução geológica das sequências do embasamento do Cinturão Araguaia na região de Paraíso do Tocantins (TO), Brasil. *Brazilian Journal of Geology, São Paulo*. 43 (3), 501–514.
- Assumpção, M., Sacek, V., 2013. Intra-plate seismicity and flexural stresses in central Brazil. *Geophysical Research Letters*, 40, 487- 491.
- Brito Neves, B.B., Fuck, R.A., 2013. Neoproterozoic evolution of the basement of the South-American platform. *Journal of South American Earth Sciences* 47, 72-89.
- Babinski, M., McGee B., Tokashiki, C.C., Tassinari, C.C.G., Saes, G.S., Pinho, F.E.C., 2018. Comparing two arms of an orogenic belt during Gondwana amalgamation: Age and provenance of the Cuiabá Group, northern Paraguay Belt, Brazil. *Journal of South American Earth Sciences*, 85 (2018) 6–42.
- Bandeira, J., McGee B., Nogueira A.C.R., Collins A.S., Trindade R., 2012. Sedimentological and provenance response to Cambrian closure of the Clymene Ocean: the upper Alto Paraguay Group, Paraguay belt, Brazil. *Gondwana*, 21, 324-340.
- Batalha, R.S., 2016. Estudo de Minerais Pesados, Análise Morfológica e Datação U-Pb por ICPMS-LA de Zircão Detrítico - Proveniência dos Metassedimentos do Grupo Cuiabá,

- Faixa Paraguay Norte-MT. Dissertação de mestrado, Universidade Federal de Mato Grosso, Cuiabá.
- Bologna, M. S., Nunes, H. O., Padilha, A. L., Vitorello, I., and Pádua, M. B., 2013. Anomalous electrical structure in the northwestern Paraná Basin, Brazil, observed with broadband magnetotellurics. *Journal of South American Earth Sciences*, 42, 74–82.
- Cawood, P.A., Hawkesworth, C.J., Dhuime, B., 2012. Detrital zircon record and tectonic setting. *Geology*, 40, 875-878.
- Cawood, P.A., Martin, E.L., Murphy, J.B., Pisarevsky, S.A. 2021. Gondwana’s interlinked peripheral orogens. *Earth and Planetary Science Letters*, 568, 117057.
- Collins, A.S, Pisarevsky, S.A. 2005. Amalgamating eastern Gondwana: the evolution of the Circum-Indian Orogens. *Earth-Sci Rev* 71: 229–270.
- Catuneanu, O., 2001. Flexural partitioning of the Late Archaean Witwatersrand foreland system, South Africa. *Sed. Geol.* 141–142, 95–112.
- Catuneanu, O., 2004. Retroarc foreland systems - evolution through time. *J. Afr. Earth Sc.* 38, 225–242.
- Cordani U. G., Teixeira W., D’Agrella-Filho M. S., Trindade R. I., 2009. The position of the Amazonian Craton in supercontinents. *Gondwana Research*, 15, 396–407.
- Cordani, U. G., Pimentel, M. M., De Araujo, C. E., Basei, M. a. S., Fuck, R. A., Girardi, V. A. V., 2013. Was there an Ediacaran Clymene Ocean in central South America? *American Journal of Science* 313, 517-539.
- Corfu, F., Hancher, J.M., Hoskin, P.W.O., Kinny, P., 2003. Atlas of zircon textures. *Rev. Mineral. Geochem.* 53, 469–500.
- Covey, M., 1986. The evolution of foreland basins to steady state: evidence from the Western Taiwan foreland basin. In: Allen, P.A., Homewood, P. (Eds.), *Foreland Basins*, vol. 8. International Association of Sedimentologists, pp. 77–90.



- Curto, J.B., Vidotti R.M., Fuck, R.A., Blakely, R.J., 2014. The tectonic evolution of the Transbrasiliano Lineament in northern Paraná Basin, Brazil, as inferred from aeromagnetic data. *J. Geophys. Res.* 119, 1544–1562.
- Curto, J., Vidotti R.M., Blakely, R.J., Fuck, R.A. 2015. Crustal framework of the northwest Paraná Basin, Brazil: insights from joint modeling of magnetic and gravity data. *Tectonophysics* 655, 58-72.
- Coutts, D.S., Matthews, W.A., Hubbard, S.M. 2019. Assessment of widely used methods to derive depositional ages from detrital zircon populations. *Geosciences Frontiers* 10, 1421-1435.
- Dantas, E.L., Armstrong, R., Pimentel, M.M., Fuck, R.A., Martinelli, C.D., Silva, M.F., Laux, J.H., 2007. 800 Ma rifting in the Paraguay Belt, central Brazil: U-Pb SHRIMP age determination, Rodinia break-up and implications for a connection with Avalonian Peri-Gondwana Terranes. Geological Society of America Annual Meeting.
- Dantas, E.L., Alvarenga, C.J.S. de, Santos, R.V., Pimentel, M.M., 2009. Using Nd isotopes to understand the provenance of sedimentary rocks from a continental margin to a foreland basin in the Neoproterozoic Paraguay belt, Central Brazil. *Precambrian Research* 170, 1-12.
- D'Agrella Filho M.S., Trindade R.I.F., Siqueira R., Ponte-Neto C.F., Pacca I.I.G., 1998. Paleomagnetic Constraints on the Rodinia Supercontinent: Implications for the Neoproterozoic Break-up and the formation of Gondwana. *International Geology Review*, 40, 171-188.
- Della Giustina, M. E. S., Oliveira, C. G., Pimentel, M. M., and Buhn, B., 2009. Neoproterozoic magmatism and high-grade metamorphism in the Goiás Massif: new LA-MC-ICMPS U-Pb and Sm-Nd data and implications for collisional history of the Brasília Belt. *Precambrian Research*, 172, 67–79.)

- Della Giustina, M.E.S., Pimentel, M.M., Ferreira Filho, C.F., Holanda, M.H.B.H., 2011. Dating coeval mafic magmatism and ultrahigh temperature metamorphism in the Anápolis Itaucú Complex, central Brazil. *Lithos*, 124, 82-201.
- DePaolo, D.J., 1981. A neodymium and strontium isotopic study of the Mesozoic calc-alkaline granitic batholiths of the Sierra Nevada and Peninsular Ranges, California. *Journal Geophysical Research*, 86, 10470-10488.
- Dickinson, W.R., Gehrels, G.E., 2009. Use of U–Pb ages of detrital zircons to infer maximum depositional ages of strata: A test against a Colorado Plateau Mesozoic database. *Earth and Planetary Science Letters* 288, 115–125.
- Dickinson, W.R., Suczek, C.A., 1979. Plate tectonics and sandstone composition. *Am. Assoc. Pet. Geol. Bull.* 63, 2164–2172.
- Dodson, M.H., 1973. Closure temperature in cooling geochronological and petrological systems. *Contrib. Miner. Petrol.* 40 (3), 259–274.
- Fowler, M.B., Henney, P.J., 1996. Mixed Caledonian appinite magmas: implications for lamprophyre fractionation and high Ba–Sr granite genesis. *Contributions to Mineralogy and Petrology* 126, 199–215.
- Fuck R. A., Brito Neves B.B., Schobbenhaus C., 2008. Rodinia descendants in South America. *Precambrian Research* 160, 108-126.
- Geraldes, M. C., Tassinari, C. C.G., Babinski, M., Martinelli, C. D., Iyer, S. S., Barboza, E. S., Pinho, F. E.C., Onoe, A. T., 2008. Isotopic Evidence for the Late Brasiliano (500-550 Ma) Ore-Forming Mineralization of the Araés Gold Deposit, Brazil. *International Geology Review* 50, 177–90.
- Gioia, S.M.C.L., Pimentel, M.M., 2000. The Sm–Nd isotopic method in the Geochronology Laboratory of the University of Brasília. *Anais Academia Brasileira de Ciências* 72, 219–245.

- Godoy, A. M., Pinho, F. E. C., Manzano, J. C., de Araújo, L. M. B., da Silva, J. A., Figueiredo, M., 2010. Estudos isotópicos das rochas granitóides neoproterozoicas da Faixa de Dobramento Paraguay . *Revista Brasileira de Geociências* 40, 380–391.
- Gorayeb, P.S.S., Chaves, C.L., Moura, C.A.V., Lobo, R.L.S. 2013. Neoproterozoic granites of the Lajeado intrusive suite, north-center Brazil: a late Ediacaran remelting of a Paleoproterozoic crust. *Journal of South American Earth Science*, 45, 278–292.
- Gorayeb, P.S.S., Costa, J.R.C., Cruz, D.J.N., 2017. A Suíte Máfica Conceição-Santana do Araguaia (feixe de diques de diabásios e gabros), fronteira Pará – Tocantins. In: SBG-NO, Anais XV Simpósio de Geologia da Amazônia, Belém, pp. 292–296.
- Gorayeb, P.S.S., Cordani, U.G., Silva Neto, J.J.A., Sato, K., Maurer, V.C. 2020. U–Pb SHRIMP zircon ages of Ediacaran-Cambrian granitic bodies in central Brazil: Implications for the tectonic evolution of the Araguaia belt. *Journal of South American Earth Sciences*, 104, 102804.
- Gorayeb P.S.S., Moura C.A.V., Barros G.R. 2000. Pb-Pb zircon ages of the Porto Nacional high-grade metamorphic terrain, northern portion of the Goiás Massif, Central Brazil. *Revista Brasileira de Geociências*, 30:190-194
- Graham, S. A., Dickinson, W. R., and Ingersoll, R. V., 1975, Himalayan- Bengal model for flysch dispersal in Appalachian-Ouachita system. *Geological Society of America Bulletin* 86, 273-286.
- Guimarães, S. B., Moura, M. A., Dantas, E. L., 2012. Petrology and geochronology of the Bom Jardim de Goiás copper deposit (GO). *Revista Brasileira de Geologia* 42, 841-862.
- Hanchar, J.M., and Rudnick, R.L. 1995. Revealing hidden structures: the application of cathodoluminescence and back-scattered electron imaging to dating zircons from lower crustal xenoliths. *Lithos*, 36, 289–303.

- Harrison, T.M., Duncan, I., McDougall, I., 1985. Diffusion of  $^{40}\text{Ar}$  in biotite: temperature, pressure and compositional effects. *Geochim. Cosmochim. Acta* 49 (11), 2461–2468.
- Harrison, T.M., Célérier, J., Aukman, J.H., Heizler, M.T., 2009. Diffusion of  $^{40}\text{Ar}$  in muscovite. *Geochimiar et Cosmochimica Acta* 73, 1038-1051.
- Harte, B. & Hudson, N. F. C, 1979. Pelite facies series and the temperature and pressures of Dalradian metamorphism in E Scotland. In: Harris, A. L., Holland, C. H. & Lealce, B. E. (eds) *The Caledonids of the British Isles: Reviewed*. Geological Society of London Special Publication 8, 323-33.
- Houghton, P. D. W., Todd, S. P., Morton, A. C. 1991. Geological Society, London, Special Publications, 57, 1-11.
- Hawkesworth, C., Cawood, P., Kemp, T., Storey, C., and Dhuime, B., 2009. A matter of preservation. *Science* 323, 49–50.
- Hodges, K. V. & Crowley, P. D., 1985. Error estimation and empirical geothermobarometry for pelitic systems. *American Mineralogist* 70, 702-709.
- Hutton, D.H.W., Reavy, R.J. 1992. Strike-slip tectonics and granite petrogenesis. *Tectonics*, 11, 5, 960-967.
- Ingersoll, R.V., Graham, A., Dickinson, W.R., 1995. Remnant ocean basins. In: Busby, C., Ingersoll, R.V. (Eds.), *Tectonics of Sedimentar Basins*. Blackwell Science, Oxford, pp. 363–391.
- Ingersoll, R.V., Dickinson, W.R., Graham, A., 2003. Remnant-ocean submarine fans: Largest sedimentary system on Earth. In: Chan, M.A., Archer, A.W. (Eds.), *Extreme Depositional Environments: Mega End Members in Geologic Time*. Geological Society of America Special Paper 370, 191–208.

- Ingersoll, R.V., 2012. Tectonics of sedimentary basins, with revised nomenclature. In: Busby, C., Azor, A. (Eds.), *Tectonics of Sedimentary Basins: Recent Advances*. Blackwell, Oxford, pp. 3–43.
- Jamieson, R.A., Beaumont, C., Fullsack, P., Lee, B., 1998. [Barrovian regional metamorphism: Where's the heat?](#) Geological Society, London, Special Publications 138 (1), 23-51.
- Jackson, S.E., Pearson, N.J., Griffin, W.L., Belousova, E.A., 2004. The application of laser ablation-inductively coupled plasma-mass spectrometry to in situ U-Pb zircon geochronology. *Chemical Geology* 211, 47-69.
- Kennedy, W. Q. 1964. The structural differentiation of Africa in the Pan-African ( $\pm 500$  m.y.) tectonic episode. Research Institute Afr. Geol. University of Leeds, 48-49.
- Koppers, A.A.P., 2002. ArArCALC- software for  $^{40}\text{Ar}/^{39}\text{Ar}$  age calculations. *Computer and Geosciences*, 28, 605-619.
- Lacerda Filho, J. V. Filho, W. A., Valente, C. R., Oliveira, C. C., Albuquerque, M. C. 2004. *Geologia e Recursos Minerais do Estado de Mato Grosso. Programa Integração, Atualização e Difusão de Dados da Geologia. Goiânia. Escala 1:1.000.000.: CPRM. 200p.*
- Laux, J.H., Pimentel, M.M., Dantas, E.L., Armstrong, R., Junges, S.L., 2005. Two Neoproterozoic crustal accretion events in the Brasília Belt, Central Brazil. *Journal of South American Earth Sciences* 18, 183–198.
- Leite, F.G.D.L., Fuck, R.A., Dantas, E.L., Ruiz, A.S., 2021. Aluminic and high Ba-Sr magmatism in central Brazil: insights into the late accretion stage of West Gondwana. *Lithos*, 398-399, 106333.
- Lo, C.H, Onstott, T.C. 1989.  $^{39}\text{Ar}$  recoil artefacts in chloritized biotite. *Geochim Cosmochim Acta* 53:2697–2711.

- Ludwig, K.R., 2012. User's Manual for Isoplot 3.75. A Geochronological Toolkit for Microsoft Excel. Berkeley Geochronology Center Special Publication, 5, 75.
- Luz J.S.; Oliveira A.M.; Souza J.O.; Motta J.F.M.; Tanno L.C.; Carmo L.S.; Souza N.B., 1980. Projeto Coxipó. Relatório Final. Goiânia, DNPM/CPRM, 1, 136.
- Macambira, J.B., 1983. Geologia e ocorrências minerais da braquianticlinal do Lontra (GO). Master Dissertation. Universidade Federal do Pará.
- Matteini, M., Junges, S.L., Dantas, E.L., Pimentel, M.M., Buhn, B., 2010. In situ zircon U–Pb and Lu–Hf isotope systematic on magmatic rocks: insights on the crustal evolution of the Neoproterozoic Goiás Magmatic Arc, Brasília belt, Central Brazil. *Gondwana Research* 17 (1), 1–12.
- Manoel, T.N., Selby, D., Galvez, M.E., Leite, J.A.D., Figueiredo, L.N. 2020. A pre-Sturtian depositional age of the lower Paraguay Belt, western Brazil, and its relationship to western Gondwana magmatism. *Gondwana Research* 89, 238-246.
- McGee, B., Collins, A. S., Trindade, R. I. F. 2012. G'day Gondwana, the final accretion of a supercontinent: U/Pb ages for the post-orogenic São Vicente Granite, northern Paraguay Belt, Brazil. *Gondwana Research*, 21, 316–322.
- McGee, B., Collins, A.S., Trindade, R.I.F., Payne, J. 2014. Age and provenance of the Cryogenian to Cambrian passive margin to foreland basin sequence of the northern Paraguay Belt, Brazil. *GSA Bulletin*, 127, 76-86.
- McGee, B., Collins, A.S., Trindade, R.I.F., Jourdan, F., 2015. Investigating mid-Ediacaran aciation and final Gondwana amalgamation using coupled sedimentology and  $^{40}\text{Ar}/^{39}\text{Ar}$  detrital muscovite provenance from the Paraguay Belt, Brazil. *Sedimentology* 62, 130–154.

- McGee, B., Babinski, M., Trindade, R., Collins, A.S., 2018. Tracing final Gondwana assembly: Age and provenance of key stratigraphic units in the southern Paraguay Belt, Brazil. *Precambrian Research* 307, 1-33.
- Merdith, A.S., Williams, S.E., Müller, R.D., Collins, A.S. 2017. Kinematic constraints on the Rodinia to Gondwana transition. *Precambrian Research* 299, 132–150.
- Moiola, R.J., Shanmugam, G., 1984. Submarine fan sedimentation, Ouachita Mountains, Arkansas and Oklahoma. *AAPG Database, Gulf Coast Association of Geological Societies Transactions* 34, 175–182.
- Moura, C.A.V., Macambira, M.J.B., Armstrong, R., 2008. U-Pb Shrimp zircon age of the Santa Luzia Granite: constraints on the age of metamorphism of the Araguaia belt, Brazil. In: VI South American Symposium on Isotope Geology, San Carlos de Bariloche. Book of Abstracts CD-ROM, Buenos Aires.
- Mutti, E., 1992. Turbidite sandstone. San Donato Milanese, AGIP, Instituto di Geologia, Università di Parma (275 p.).
- Murphy, J.B., Nance, R.D., Gabler, L.B., Martell, A., Archibald., 2019. Age, Geochemistry and Origin of the Ardara Appinite Plutons, Northwest Donegal, Ireland. *Geosciences Canada* 46, 1, 31–48.
- Murphy, J.B. 2019. Appinites suites and their genetic relationship with coeval voluminous granitoid batholiths. *Int. Geol. Rev.* 65, 683–713.
- Mutti, E., Tinterri, R., Remacha, E., Mavilla, N., Angella, S., Fava, L., 1999. An introduction to the analysis of Ancient Turbidite Basins from an outcrop perspective. *AAPG Continuing Education Course Note*, 39 (74 p.).
- Mutti, E., Bernoulli, D., Lucchi, F.R., Tinterri, R. 2009. Turbidites and turbidity currents from Alpine ‘flysch’ to the exploration of continental margins. *Sedimentology*, 56, 267-318.

- Nogueira A.C.R., Riccomini C., 2007. O Grupo Araras (Neoproterozoico) na parte norte da Faixa Paraguai e Sul do Cráton Amazônico, Brasil. *Revista Brasileira de Geociências*, 36, 576-587.
- Pelosi, G. F. F. 2017. Age, Provenance and Tectonic Setting from Southern Portion of the Cuiabá Group: Implications for the Evolution of the Paraguai Belt. Master Dissertation. University of Mato Grosso.
- Perarnau, M., Gilbert, H., Alvarado, P., Martino, R., and Anderson, M., 2012. Crustal structure of the Eastern Sierras Pampeanas of Argentina using high frequency local receiver functions. *Tectonophysics*, 580, 208–217.
- Piacentini, T., Boggiani, P., Yamamoto, J. K., Freitas, B. T., Campanha, G. A. C. 2017. Formação ferrífera bandada associada à sedimentação glaciogênica da formação Puga (Marinoano) na Serra da Bodoquena, MS. *Revista Brasileira de Geociências*, v. 37, p. 530-541.
- Pimentel, M.M., Fuck, R.A., Alvarenga, C.J.S., 1996. Post-Brasiliano (Pan African) high-K granitic magmatism in central Brazil: the role of late Precambrian/early Paleozoic extension. *Precambrian Research*, 80, 217–238.
- Pimentel, M.M., Fuck, R.A., Botelho, N.F., 1999. Granites and the geodynamic history of the neoproterozoic Brasília belt, Central Brazil: a review. *Lithos* 46: 463-483.
- Pimentel, M.M., Dantas, E.L., Fuck, R.A., Armstrong, R. A., 2003. Shrimp and conventional U-Pb age, Sm-Nd isotopic characteristics and tectonic significance of the k-rich Itapuranga Suite in Goiás, Central Brazil. *Annals of the Brazilian Academy of Sciences*. 75, 97-108.
- Pinho, M. A. S. B., 2001. Petrografia geoquímica e geocronologia do Magmatismo Bimodal paleoproterozóico ocorrente no Norte do Estado de Mato Grosso. Tese (Doutorado em



- Geociências) – Instituto de Geociências, Universidade Federal do Rio Grande Do Sul. Porto Alegre. p. 162.
- Pinheiro, B.L.S., Moura, C.A.V., Gorayeb, P.S.S. 2011. Proveniência das rochas meta-sedimentares do Cinturão Araguaia com base em datações Pb-Pb em zircão e idades-modelo Sm-Nd. *Rev. Bras. Geociencias* 41, 304–318.
- Piuzana, D., Pimentel, M.M., Fuck, R.A., Armstrong, R., 2003a. Neoproterozoic granulite facies metamorphism and coeval granitic magmatism in the Brasília Belt, Central Brazil: regional implications of new SHRIMP U–Pb and Sm–Nd data. *Precambrian Research* 125, 245–273.
- Pupin, J.P., 1980. Zircon and granite petrology. *Contrib. Mineral. Petrol.* 73, 207–220.
- Rapela, C. W., Pankhurst, R. J., Casquet, C., Baldo, E., Saavedra, J., Galindo, C., and Fanning, C. M., 1998. The Pampean Orogeny of the southern proto-Andes: Cambrian continental collision in the Sierras de Córdoba, in Pankhurst, R. J., and Rapela, C. W., editors, *The Proto-Andean Margin of Gondwana: Geological Society, London, Special Publications*, 142, 181–217.
- Rapela, C.W., Pankhurst, R.J., Casquet, C., Fanning, C.M., Baldo, E.G., González-Casado, J.M., Galindo, C., Dahlquist, J., 2007. The Río de la Plata craton and the assembly of SW Gondwana. *Earth-Science Reviews* 83, 49–82.
- Rogers, J.J.W., 1996. A history of the continents in the past three billion years. *Journal of Geology* 104, 91–107.
- Rubatto, D. 2017. *Zircon: The Metamorphic Mineral: Methods and Applications. Petrochronology*
- Schmitt, R.S., Fragoso, R.A., Collins, A.S. 2018. *Suturing Gondwana in the Cambrian: Orogenic Events of the Final Amalgamation. Springer International Publishing AG, part*

- of Springer Nature 2018 S. Siegesmund et al. (eds.), *Geology of Southwest Gondwana, Regional Geology Reviews*.
- Seer H.J., 1985. *Geologia, deformação e mineralização de cobre no complexo vulcano-sedimentar de Bom Jardim de Golás*. MSc Dissertation, UnB, Brasília, 190 p.
- Silva, M.F., 2018. *Evolução Tectônica de Rift para Margem Passiva da Faixa Paraguay -Mato Grosso, Brasil Central*. Instituto de Geociências. Universidade de Brasília. Tese de Doutorado 144 (1v), 198p.
- Silva, M.F., Dantas, E.L., Vidotti, R.M. Shortening history of the Neoproterozoic oroclinal bending in Paraguay belt, Central Brazil, based on structural interpretation of field work and high resolution aerogeophysical data. *Journal of South American Earth Sciences* 103, 103043, 2020.
- Soares, J. E., Berrocal, J., Fuck, R. A., Mooney, W. D., Ventura, D. B. R., 2006. Seismic characteristics of central Brazil crust and upper mantle: A deep seismic refraction study. *Journal of Geophysical Research, Solid Earth*, 111, 12302.
- Stern, R.J. 1994. Arc-assembly and continental collision in the Neoproterozoic African orogen: implications for the consolidation of Gondwanaland. *Annu. Rev. Earth Planet Sci.* 22, 319–351.
- Suriano, J., Limarino, C.O., Tedesco, A.M., Alonso, M.S. 2014. Sedimentation model of piggyback basins: cenozoic examples of san juan precordillera, Argentina. *Geological Society of London Special Publications* 399, 221–244.
- Tassinari, C.C.G., Macambira, M.J.B., 1999. Geochronological provinces of the Amazonian Craton. *Episodes* 22,174-182.
- Tohver, E., D’Agrella-Filho, M.S., Trindade, R.I.F., 2006. Paleomagnetic record of Africa and South America for the 1200–500 Ma interval, and evaluation of Rodinia and Gondwana assemblies. *Precambrian Research* 147, 193–222.

- Tohver, E., Trindade, R. I. F., Solum, J. G., Hall, C. M., Riccomini, C., and Nogueira, A. C., 2010. Closing the Clymene Ocean and Bending a Brasiliano belt: Evidence for the Cambrian formation of Gondwana from southeast Amazon Craton. *Geology*, 38, 267–270.
- Tohver, E., Cawood, P. A., Rossello, E. A., and Jourdan, F., 2012. Closure of the Clymene Ocean and formation of West Gondwana in the Cambrian: Evidence from the Sierras Australes of the southernmost Rio de la Plata Craton, Argentina. *Gondwana Research*, 21, 394–405.
- Tohver E., Trindade R.I.F., 2014. Comment on "Was there na Ediacaran Clymene Ocean in central South America?" By Umberto Giuseppe Cordani, Marcio Martins Pimentel, Carlos Eduardo Ganade de Araújo, Miguel Angelo Stipp Basei, Reinhardt Adolfo Fuck, and Vicente Antonio Vítório Girardi. *American Journal of Science*, 313, 517-539.
- Trindade, R. I. F., Font, E., D'Agrella-Filho, M. S., Nogueira, A. C. R., and Riccomini, C., 2003. Low-latitude and multiple geomagnetic reversals in the Neoproterozoic Puga cap carbonate, Amazon Craton. *Terra Nova*, 15, 441–446.
- Trindade, R. I. F., D'Agrella-Filho, M. S., Epof, I., and Brito Neves, B. B., 2006. Paleomagnetism of Early Cambrian Itabaiana mafic dikes (NE Brazil) and the final assembly of Gondwana. *Earth and Planetary Science Letters*, 244, 361–377.
- Tokashiki, C. C. & Saes, G. S. 2008. Revisão estratigráfica e faciologia do Grupo Cuiabá no alinhamento Cangas-Poconé, baixada Cuiabana, Mato Grosso. *Revista Brasileira de Geociências* 38, 661-675.
- Vasconcelos, B.R. 2018. Proveniência sedimentar do Grupo Cuiabá na Faixa Paraguay meridional. Dissertação de doutorado. Instituto de Geociências. Universidade de Brasília.

Wen, B., Evans, D.A.D., Anderson, R.P., McCausland, P.J.A., 2020. Late Ediacaran paleogeography of Avalonia and the Cambrian assembly of West Gondwana. *Earth Planet. Sci. Lett.* 552, 116591.

Wiedenbeck, M., Hanchar, J.M., Peck, W.H., Sylvester, P., Valley, J., Whitehouse, M., Kronz, A., Morishita, Y., Nasdala, L., Fiebig, J., Franchi, I., Girard, J.P., Greenwood, R.C., Hinton, R., Kita, N., Mason, P.R.D., Norman, M., Ogasawara, M., Piccoli, P.M., Rhede, D., Satoh, H., Schulz-Dobrick, B., Skår, O., Spicuzza, M.J., Terada, K., Tindle, A., Togashi, S., Vennemann, T., Xie, Q., Zheng, Y.F., 2004. Further characterisation of the 91500 zircon crystal. *Geostandards and Geoanalytical Research* 28, 9–39.

Wilson, J.T., 1966. Did the Atlantic close and reopen? *Nature* 211 (81), 254–271, 676.

## ANEXOS ARTIGO 2

**Supplementary Table 5.1** – U-Pb general conditions at Laboratory of Geochronology and Isotope Geochemistry of the Universidade de Brasília - UnB.

| <b>Laboratory and Sample Preparation</b> |  |
|--|--|
| Laboratory name                          | Laboratory of Geochronology and Isotope Geochemistry of the Brasilia University-UnB. |
| Sample type/mineral                      | Zircon   |
| Sample preparation                       | Conventional mineral separation, 0.5 cm resin mount, 1 µm polish to finish           |
| Imaging                                  | BSE, FEI Quanta 450, 10 nA, 20kV, 13.8 mm working distance                           |
| <b>Laser ablation system</b>             |  |
| Make, Model and type                     | ESI/New Wave Research, UP-213, Nd:YAG  |

|  |  |
|--|--|
| Ablation cell and volume                           | Low volume cell, ca. 4 cm <sup>3</sup>   |
| Laser wavelength (nm)                              | 213 nm   |
| Pulse width (ns)                                   | 3 ns   |
| Fluence (J cm <sup>-2</sup> )                      | 3.0 - 3.5 J cm <sup>-2</sup>   |
| Repetition rate (Hz)                               | 10 Hz (U-Pb) and 7 Hz (Lu-Hf)  |
| Spot size  | 25 µm (U-Pb), 40 µm (Lu-Hf)  |
| Sampling mode / pattern                            | single spot analyses   |
| Carrier gas  | 100% He, Ar make-up gas combined using a Y-piece along the sample transport line close to the torch.   |
| Pre-ablation laser warm-up (background collection) | 10 s   |
| Ablation duration (s)                              | 40 s   |
| Wash-out delay                                     | 20 s   |
| Ablation pit depth / ablation rate                 | ~10 µm pit depth   |
| Cell carrier gas flow (l min <sup>-1</sup> )       | 0.40 l min <sup>-1</sup> He  |
| <b>ICP-MS Instrument</b>                           |  |
| Make, Model and type                               | Thermo-Fischer, Neptune, MC-ICP-MS   |
| Sample introduction                                | Ablation aerosol   |
| RF power (W)                                       | 1050 W   |
| Make-up gas flow (l min <sup>-1</sup> )            | 0.7 l min <sup>-1</sup>  |
| Detection system                                   | mixed Faraday cups and multiple ion counting (MIC) array   |
| Masses measured for U-Pb                           | Faraday <sup>232</sup> Th, <sup>238</sup> U and <sup>206</sup> Pb; MIC <sup>202</sup> Hg, <sup>204</sup> Pb, <sup>207</sup> Pb and <sup>208</sup> Pb |
| Masses measured for Lu-hf methodology              | Faraday 171, 173, 175, 176, 177, 178, 179, 180   |

|   |   |
|---|---|
| Integration time per peak/dwell times (ms); quadrupole settling time between mass jumps | #N.A.   |
| Total integration time per output data point (s)  | 1.049 s   |
| Dead time (ns)  | #N.A.   |
| <b>Data Processing</b>  |   |
| Gas blank   | 20 s  |
| Calibration strategy  | GJ1 used as primary reference material, TEMORA used as secondary/validation   |
| Reference Material info   | GJ1 (Jackson <i>et al.</i> 2004, Horstwood <i>et al.</i> 2016)<br>Wiedenbeck <i>et al.</i> , 1995, 2004   |
| Data processing package used / Correction for LIEF                                      | Inhouse U-Pb table (Buhn <i>et al.</i> , 2009) and Lu-Hf table (Matteini <i>et al.</i> , 2010)  |
| Mass discrimination   | Standard-sample bracketing with $^{207}\text{Pb}/^{206}\text{Pb}$ and $^{206}\text{Pb}/^{238}\text{U}$ ratios normalized to reference material GJ1                |
| Common-Pb correction, composition and uncertainty                                       | none  |
| Uncertainty level and propagation   | Ages are quoted at 2s absolute, propagation is by quadratic addition. Excess variance and age uncertainty of reference material are propagated where appropriate. |

**Supplementary Table 2** -  $^{40}\text{Ar}/^{39}\text{Ar}$  step-heating analytical results of biotite and muscovite separates from samples AL01 and AL19, respectively.

**Sample AL01- biotite**

(*J Value* =  $0.00204249 \pm 0.07$ )

| Step | Cum.               |  |  |   |   |  |                        |                      |   |                   |  |  |  |
|------|--------------------|--|--|---|---|--|------------------------|----------------------|---|-------------------|--|--|--|
|      | $\%^{39}\text{Ar}$ | $^{40}\text{Ar}^*$ (fA $\pm$ %1 $\sigma$ ) | $^{39}\text{Ar}_k$ (fA $\pm$ %1 $\sigma$ ) | $^{38}\text{Ar}_{cl}$ (fA $\pm$ %1 $\sigma$ ) | $^{37}\text{Ar}_{ca}$ (fA $\pm$ %1 $\sigma$ ) | $^{36}\text{Ar}_{atm}$ (fA $\pm$ %1 $\sigma$ ) | K/Ca ( $\pm 2\sigma$ ) | $\%^{40}\text{Ar}^*$ | $^{40}\text{Ar}^*/^{39}\text{Ar}$ ( $\pm 2\sigma$ ) | Age $\pm 2\sigma$ |  |  |  |
|      | r                  |  |  |   |   |  |                        |                      |   | (Ma)              |  |  |  |
| 1    | 4.15               | 977.358 $\pm$ 0.02                         | 7.159 $\pm$ 0.29                           | 0.500 $\pm$ 3.62                              | 0.0035 $\pm$ >100%                            | 0.0455 $\pm$ 1.12                              | 1071 $\pm$ >100%       | 98.62                | 136.504 $\pm$ 0.801                                 | 444.68 $\pm$ 2.32 |  |  |  |
| 2    | 9.53               | 2740.071 $\pm$ 0.01                        | 16.458 $\pm$ 0.11                          | 1.204 $\pm$ 1.95                              | 0.0026 $\pm$ >100%                            | 0.0189 $\pm$ 2.77                              | 3256 $\pm$ >100%       | 99.79                | 166.485 $\pm$ 0.378                                 | 529.25 $\pm$ 1.04 |  |  |  |
| 3    | 3.60               | 969.277 $\pm$ 0.34                         | 6.213 $\pm$ 0.74                           | 0.526 $\pm$ 3.83                              | 0.0982 $\pm$ 30.76                            | 6.2778 $\pm$ 0.13                              | 34 $\pm$ 21            | 34.09                | 156.006 $\pm$ 2.527                                 | 500.14 $\pm$ 7.08 |  |  |  |
| 4    | 4.82               | 1421.283 $\pm$ 0.12                        | 8.322 $\pm$ 0.51                           | 0.631 $\pm$ 4.50                              | 0.0259 $\pm$ >100%                            | 1.1814 $\pm$ 0.39                              | 170 $\pm$ >100%        | 80.11                | 170.785 $\pm$ 1.798                                 | 541.06 $\pm$ 4.93 |  |  |  |
| 5    | 5.53               | 1642.938 $\pm$ 0.07                        | 9.555 $\pm$ 0.44                           | 0.683 $\pm$ 2.85                              | 0.0000 $\pm$ 0.00                             | 0.6429 $\pm$ 0.45                              | / $\pm$ /              | 89.53                | 171.934 $\pm$ 1.527                                 | 544.21 $\pm$ 4.17 |  |  |  |
| 6    | 9.52               | 2858.894 $\pm$ 0.04                        | 16.439 $\pm$ 0.26                          | 1.229 $\pm$ 2.33                              | 0.0000 $\pm$ 0.00                             | 0.4639 $\pm$ 0.64                              | / $\pm$ /              | 95.37                | 173.905 $\pm$ 0.906                                 | 549.59 $\pm$ 2.47 |  |  |  |
| 7    | 6.19               | 1862.706 $\pm$ 0.06                        | 10.694 $\pm$ 0.40                          | 0.782 $\pm$ 2.83                              | 0.0000 $\pm$ 0.00                             | 0.1192 $\pm$ 2.15                              | / $\pm$ /              | 98.12                | 174.166 $\pm$ 1.398                                 | 550.30 $\pm$ 3.81 |  |  |  |
| 8    | 8.93               | 2667.023 $\pm$ 0.04                        | 15.423 $\pm$ 0.28                          | 1.090 $\pm$ 2.26                              | 0.0000 $\pm$ 0.00                             | 0.1146 $\pm$ 2.231                             | / $\pm$ /              | 98.73                | 172.915 $\pm$ 0.966                                 | 546.89 $\pm$ 2.64 |  |  |  |
| 9    | 13.68              | 4138.081 $\pm$ 0.03                        | 23.632 $\pm$ 0.19                          | 1.734 $\pm$ 1.72                              | 0.0000 $\pm$ 0.00                             | 0.1116 $\pm$ 2.38                              | / $\pm$ /              | 99.19                | 173.681 $\pm$ 0.655                                 | 548.98 $\pm$ 1.79 |  |  |  |

|    |       |                 |               |               |                |                |               |             |                  |                 |               |
|----|-------|-----------------|---------------|---------------|----------------|----------------|---------------|-------------|------------------|-----------------|---------------|
| 10 | 12.69 | 3813.823 ± 0.02 | 21.92 ± 0.11  | 1.586 ± 1.70  | 0.0242 ± 0     | 71.04 ± 1.98   | 0.0878 ± 1.98 | 479 ± >100% | 99.31            | 173.955 ± 0.383 | 549.72 ± 1.04 |
| 11 | 9.68  | 2884.097 ± 0.02 | 16.721 ± 0.15 | 1.209 ± 1.97  | 0.0000 ± >100% | 0.0337 ± 4.79  | / ± /2        | 99.65       | 172.475 ± 0.522  | 545.69 ± 1.43   |               |
| 12 | 3.88  | 1148.879 ± 0.05 | 6.703 ± 0.33  | 0.444 ± 4.57  | 0.0646 ± 22.40 | 0.0135 ± 12.44 | 55 ± 25       | 99.65       | 171.394 ± 1.140  | 542.73 ± 3.12   |               |
| 13 | 6.67  | 1971.451 ± 0.03 | 11.524 ± 0.21 | 0.799 ± 2.87  | 0.0449 ± 36.16 | 0.0179 ± 9.09  | 136 ± 98      | 99.72       | 171.070 ± 0.709  | 541.84 ± 1.94   |               |
| 14 | 0.93  | 282.834 ± 0.20  | 1.606 ± 1.42  | 0.103 ± 13.56 | 0.0146 ± 98.32 | 0.0041 ± 38.03 | 58 ± >100%    | 99.56       | 176.049 ± 5.029  | 555.42 ± 13.66  |               |
| 15 | 0.20  | 51.494 ± 1.07   | 0.350 ± 7.03  | 0.000 ± 00.00 | 0.0532 ± 26.92 | 0.0002 ± >100% | 3 ± 2         | 99.87       | 147.022 ± 20.920 | 474.80 ± 59.42  |               |

**Sample AL19 – muscovite**

(*J Value = 0.00185630 ± 0.00000297*)

Cum.

| Step | % <sup>39</sup> A | <sup>40</sup> Ar* (fA ± %1σ) | <sup>39</sup> Ar <sub>k</sub> (fA ± %1σ) | <sup>38</sup> Ar <sub>cl</sub> (fA ± %1σ) | <sup>37</sup> Ar <sub>ca</sub> (fA ± %1σ) | <sup>36</sup> Ar <sub>atm</sub> (fA ± %1σ) | K/Ca (±2σ)   | % <sup>40</sup> Ar*                       | Age ± 2σ         |                |
|------|-------------------|------------------------------|--|---|---|--|--------------|---|------------------|----------------|
|      | r                 |                              |  |   |   |  |              | <sup>40</sup> Ar*/ <sup>39</sup> Ar (±2σ) | (Ma)             |                |
| 1    | 0.92              | 124.141 ± 0.26               | 0.618 ± 3.21                             | 0.000 ± 0.00                              | 0.0000 ± 0.00                             | 0.0977 ± 1.04                              | / ± /        | 80.96                                     | 200.657 ± 12.923 | 572.50 ± 31.61 |
| 2    | 46.40             | 5823.883 ± 0.01              | 31.313 ± 0.10                            | 0.000 ± 0.00                              | 0.2006 ± >100%                            | 0.1859 ± 0.59                              | 82.7 ± >100% | 99.05                                     | 185.989 ± 0.385  | 536.26 ± 0.96  |



|    |       |          |        |       |        |       |        |        |         |        |         |      |         |       |         |         |        |         |
|----|-------|----------|--------|-------|--------|-------|--------|--------|---------|--------|---------|------|---------|-------|---------|---------|--------|---------|
| 3  | 10.77 | 1352.571 | ± 0.07 | 7.272 | ± 0.30 | 0.000 | ± 0.00 | 0.0000 | ± 0.00  | 0.0207 | ± 2.13  | /    | ± /     | 99.54 | 186.007 | ± 1.138 | 536.31 | ± 2.84  |
| 4  | 12.31 | 1545.393 | ± 0.06 | 8.307 | ± 0.18 | 0.000 | ± 0.00 | 0.1010 | ± >100% | 0.0189 | ± 3.18  | 43.6 | ± >100% | 99.63 | 186.043 | ± 0.722 | 536.40 | ± 1.80  |
| 5  | 10.21 | 1316.946 | ± 0.07 | 6.890 | ± 0.23 | 0.000 | ± 0.00 | 0.0000 | ± 0.00  | 0.0416 | ± 2.12  | /    | ± /     | 99.06 | 191.132 | ± 0.920 | 549.05 | ± 2.28  |
| 6  | 1.38  | 180.842  | ± 0.52 | 0.929 | ± 1.97 | 0.000 | ± 0.00 | 0.1128 | ± >100% | 0.0019 | ± 22.83 | 4.4  | ± 14.2  | 99.69 | 194.658 | ± 7.930 | 557.77 | ± 19.55 |
| 7  | 3.13  | 393.635  | ± 0.24 | 2.113 | ± 0.68 | 0.000 | ± 0.00 | 0.0982 | ± >100% | 0.0072 | ± 6.11  | 11.4 | ± 31.0  | 99.45 | 186.248 | ± 2.678 | 536.91 | ± 6.68  |
| 8  | 4.81  | 616.227  | ± 0.15 | 3.244 | ± 0.54 | 0.000 | ± 0.00 | 0.0000 | ± 0.00  | 0.0111 | ± 4.93  | /    | ± /     | 99.46 | 189.930 | ± 2.136 | 546.07 | ± 5.30  |
| 9  | 3.03  | 384.426  | ± 0.24 | 2.048 | ± 0.79 | 0.000 | ± 0.00 | 0.0000 | ± 0.00  | 0.0030 | ± 15.13 | /    | ± /     | 99.76 | 187.700 | ± 3.113 | 540.53 | ± 7.75  |
| 10 | 2.66  | 335.920  | ± 0.28 | 1.794 | ± 0.93 | 0.000 | ± 0.00 | 0.1094 | ± >100% | 0.0027 | ± 22.92 | 8.7  | ± 25.5  | 99.75 | 187.159 | ± 3.641 | 539.18 | ± 9.07  |
| 11 | 1.40  | 170.573  | ± 0.55 | 0.945 | ± 2.51 | 0.000 | ± 0.00 | 0.0614 | ± >100% | 0.0014 | ± 41.55 | 8.2  | ± 38.1  | 99.75 | 180.399 | ± 9.263 | 522.26 | ± 23.29 |
| 12 | 2.98  | 381.535  | ± 0.25 | 2.011 | ± 0.75 | 0.000 | ± 0.00 | 0.0226 | ± >100% | 0.0027 | ± 16.69 | 47.1 | ± >100% | 99.78 | 189.715 | ± 2.997 | 545.54 | ± 7.44  |

## 6. CONSIDERAÇÕES FINAIS

A partir da junção dos dados apresentados, é possível sugerir que o ambiente tectônico estabelecido é associado a um novo evento colisional na porção central da Província Tocantins, uma vez que não está ligado ao último evento de fechamento registrado em 620 Ma. Aproximadamente em 555 Ma, tem-se a cristalização da suíte quartzo monzodiorítica(apinítica)/granodiorítica, que apresenta características de magmas tipicamente gerados a partir do fim do evento de subducção (tipo de arco magmático), possibilitando magmatismo derivado do manto litosférico enriquecido por fluidos derivados da placa oceânica descendente. Por volta de 515 Ma, tem-se o alojamento de uma suíte monzogranítica proveniente do processo de delaminação litosférica em contexto de descompressão/colapso do orógeno.

O magma mais jovem representa transição entre um magma shoshonítico (high K) e um magma com afinidade tipo A (intra-placa). As duas suítes não apresentam petrogênese associada, porém ambas se desenvolvem relacionadas ao processo de fusão parcial do manto litosférico enriquecido. O enriquecimento em elementos incompatíveis ocorreu graças ao ambiente de subducção propício para a adição de fluidos derivados da placa descendente. Portanto, o evento tectônico que gerou a suíte mais antiga tem um importante papel em fornecer condições favoráveis de enriquecimento do manto litosférico da região, mesmo após 40 Ma.

As rochas metassedimentares também registram evento colisional pós 600 Ma, quando ocorre a deposição de unidade psamítica sin-orogênica em bacia de *foreland*. O maior pico de idades de zircão ocorre em  $620 \pm 30$  Ma, representando aproximadamente 60% dos grãos analisados. Os sedimentos jovens e abundantes são interpretados como

sendo basicamente provenientes das unidades pertencentes principalmente ao Arco Magmático de Goiás (~610 – 800 Ma; Pimentel *et al.*, 1996, 1999, 2003; Laux *et al.*, 2004; Matteini *et al.*, 2010), complexos granulíticos da Faixa Brasília (630 e 660 Ma; Della Giustina *et al.*, 2009, 2011). A idade máxima de deposição da bacia é definida em 594 Ma, corroborando com o padrão distribuição de zircão detrítico típico de bacia syn-orogênica.

O Lineamento Transbrasiliano desempenha papel muito importante nos processos tectônicos observados na área. O sistema de falhas transcorrentes do LTB possivelmente utilizou a zona de fraqueza da região para a implantação das falhas transcorrentes entre os dois terrenos tardiamente acrescidos. O alojamento da suíte apinitica ocorreu principalmente devido à substituição da zona de subducção/sutura pelo sistema de falhas transformantes, que facilitou a captura tardia de magmas mantélicos em maiores profundidades e a subida do manto subcontinental litosférico enriquecido. A rápida taxa de resfriamento (25°C/Myr) do pluton granodiorítico indica *uplift* associado a zona de fraqueza do LTB, que é descrita localmente como Falha Serra Negra (Curto *et al.*, 2014, 2015). A zona de falhas transcorrentes pode ter atuado também como potencializador do último pulso sedimentar que possibilitou a erosão e sedimentação dos grãos mais jovens obtidos, datados até o fim do Ediacarano (590 Ma), caracterizando a idade máxima de deposição destas rochas.

De maneira sintetizada, concluímos que as rochas magmáticas e metassedimentares investigadas registram suas gêneses em ambiente colisional/orogênico associado ao avanço do consumo do Oceano Clymene. A evidência da existência de um oceano que tem a sua evolução final no fim do Ediacarano se torna mais consistente, podendo-se inferir que se trata de oceano remanescente que foi consumido por volta de 590 Ma em um evento colisional tardio. Portanto, a gênese das

rochas estudadas não ocorre associada ao último evento previamente registrado em 620 Ma. Neste contexto, podemos sugerir que a região de *foreland* do orógeno Paraguai serviu como bacia que recebeu todo o material recém gerado pelo consumo do próprio oceano. Sugere-se um evento tardio de aglutinação após 600 Ma entre o paleo-Arco Magmático de Goiás (ou os terrenos a leste do Cráton Amazônico) e o Craton Amazônico na região central do Gondwana Oriental.

## 7. REFERÊNCIAS

- Almeida, F.F.M., 1984. Província Tocantins, setor sudoeste. In: Almeida, F.F.M. de; Hasui, Y. (Coord.). O Pré-Cambriano do Brasil. São Paulo, Edgard Blücher, 265-281.
- Alvarega, C.J.S., Trompette R., 1993. Evolução Tectônica Brasileira da Faixa Paraguai: a estruturação da região de Cuiabá. *Revista Brasileira de Geociências*, 23, 18-30.
- Arcanjo, S.H.S., 2002. Evolução Geológica das seqüências do Embasamento na porção sul do Cinturão Araguaia–Região de Paraíso do Tocantins. Tese de Doutorado. Instituto de Geociências, Universidade Federal do Pará, Belém, 181 p.
- Arcanjo, S.H.S., Moura, C.A.V., 2000. Geocronologia das rochas do embasamento do setor meridional do Cinturão Araguaia na região de Paraíso do Tocantins (TO). *Revista Brasileira de Geociências* 30, 665-670.
- Boger, S.D., Miller, J.M., 2004. Terminal suturing of Gondwana and the onset of the Ross-Delamerian Orogeny: the cause and effect of an Early Cambrian reconfiguration of plate motions. *Earth Planet Science Lett* 219:35–48.
- Cawood, P.A., McCausland P.J.A. Dunning G.R., 2001. Opening Iapetus: constraints from the Laurentia margin in Newfoundland. *Geol. Soc. Am. Bull.*, 113, 443–453.
- Cawood, P.A., 2005. Terra Australis Orogen: Rodinia breakup and development of the Pacific and Iapetus margins of Gondwana during the Neoproterozoic and Paleozoic. *Earth-Science Review* 69:249–279.
- Cawood, P. A., & Buchan, C., 2007. Linking accretionary orogenesis with supercontinent assembly. *Earth Science Reviews*, 82(3-4), 217-256.
- Collins, A.S., Pisarevsk, S.A., 2005. Amalgamating eastern Gondwana: The Evolution of the Circum-Indian Orogens. *Earth-Science Reviews* 71, 229-270.

- Condie, K.C., 2011. *Earth as an Evolving Planetary System*, Second Edition. Elsevier, Amsterdam. 558 pp.
- Cordani, U. G., Teixeira, W., D'Agrella-Filho, M. S., Trindade, R. I., 2009. The position of the Amazonian Craton in supercontinentes. *Gondwana Research*, 15, 396–407.
- Cordani U.G., Brito Neves B.B., Fuck R. A., Porto R., Thomaz Filho A., Cunha F.M.B., 2010. Estudo preliminar de integração do Pré-Cambriano com os eventos tectônicos das Bacias Sedimentares Brasileiras (Republicação). *Boletim de Geociências da Petrobras*, 17, 137-204
- Cordani, U.G., Pimentel, M.M., Araújo, C.E.G., Fuck R.A., 2013. The significance of the Transbrasiliano-Kandi tectonic corridor for the amalgamation of West Gondwana. *Brazilian Journal of Geology* 43, 583-597.
- CPRM. 2017. Carta Geológica-Geofísica - Folha SE.22-V-B-I Bom Jardim de Goiás. Programa gestão estratégica da geologia, da mineração e da transformação mineral carta Geológica - Geofísica escala 1:100.000.
- Curto, J.B., Vidotti R.M., Fuck, R.A., Blakel, R.J., 2014. The tectonic evolution of the Transbrasiliano Lineament in northern Paraná Basin, Brazil, as inferred from aeromagnetic data. *J. Geophys. Res.* 119, 1544–1562.
- Curto, J., Vidotti R.M., Blakely, R.J., Fuck, R.A., 2015. Crustal framework of the northwest Paraná Basin, Brazil: insights from joint modeling of magnetic and gravity data. *Tectonophysics* 655, 58-72.
- D'agrella Filho M.S., Trindade R.I.F., Siqueira R., Ponte-Neto C.F., Pacca I.I.G., 1998. Paleomagnetic Constraints on the Rodinia Supercontinent: Implications for the Neoproterozoic Break-up and the formation of Gondwana. *International Geology Review*, 40, 171-188.

- Dalziel, I. W. D., 1975. Scotia Arc Tectonics Project, 1969–1975. *Antarct. J. U.S.* 10 70–81.
- Dalziel, I.W.D., 1997. Neoproterozoic – Paleozoic geography and tectonics: Review, hypothesis and environmental speculation. *Bull. Geol. Soc. Am.* 109, 16 – 42.
- Dantas, E. L., Araujo Filho, J. O., Fuck, R., Oliveira, C., Chiarini, M.F., Almeida, T., 2007. O sistema de cisalhamento transcorrente Porangatu, Provincia Tocantins, XI SNET, Natal. p.199-201.
- Dantas, E.L., Alvarenga, C.J.S. de, Santos, R.V., Pimentel, M.M., 2009. Using Nd isotopes to understand the provenance of sedimentary rocks from a continental margin to a foreland basin in the Neoproterozoic Paraguay belt, Central Brazil. *Precambrian Research*, 170, 1-12.
- Dantas, E.L., Fuck, R.A., Vidotti, R.M., Roig, H.L., Almeida, T., 2017. Lineamento Transbrasiliano: A grande cicatriz da Plataforma Sul Americana. In: 15º Simpósio de Geologia da Amazônia, 2017, Belém. Anais. Belém: SBG Núcleo Norte, p. 18-21.
- Della Giustina, M.E., Oliveira, C.G., Pimentel, M.M., Melo, L., V., Fuck, R.A., Dantas, E.L., Buhn, B., 2009. U-Pb and Sm-Nd constraints on the nature of the Campinorte sequence and related Palaeoproterozoic juvenile orthogneisses, Tocantins Province, central Brazil. In: *Palaeoproterozoic Supercontinents and Global Evolution*. Geological Society, London, 323, 255-269.
- Della Giustina, M.E., Pimentel, M.M., Ferreira Filho, C.F., Holanda, M.H.B.H., 2011. Dating coeval mafic magmatism and ultrahigh temperature metamorphism in the Anápolis Itaucú Complex, central Brazil. *Lithos*, 124, 82-201.

- Fairhead, J.D., Maus S., 2003. Champ satellite and terrestrial magnetic data help define the tectonic model for South America and resolve the lingering problem of the pre-break-up fit of the South Atlantic Ocean. *The Leading Edge*, 22, 8, 779-783.
- Faleiros, F.M., Campanha, G.A.C., Martins, L., Vlach, S.R.F., Vasconcelos, P.M., 2011. Ediacaran high-pressure collision metamorphism and tectonics of the southern Ribeira Belt (SE Brazil): evidence for terrane accretion and dispersion during Gondwana assembly. *Precambrian Res* 189:263–291.
- Frimmel, H. E., Frank, W., 1998. Neoproterozoic tectono-thermal evolution of the Gariep Belt and its basement, Namibia and South Africa. *Precambrian Research*, 90, 1–28.
- Frimmel, H.E., Basei, M.S., Gaucher, C., 2011. Neoproterozoic geodynamic evolution of SW-Gondwana: a southern African perspective. *Int J Earth Sci* 100:323–354.
- Fuck, R. A., Dantas, E.L.; Vidotti, R.M., Roig, H. L., Almeida, T., 2013. Deformação intracontinental em sistemas transcorrentes: o caso do Lineamento Transbrasiliano, geometria, idade e significado, In: 140 Simpósio Nacional de Estudos Tectônicos. Chapada dos Guimarães. Sociedade Brasileira de Geologia. p. 1-3.
- Ganade de Araujo, C.E., Weinberg, R.F. Cordani, U.G., 2014. Extruding the Borborema Province (NE-Brazil): a two-stage Neoproterozoic collision process. *Terra Nova*, 26:157 - 168.
- Gastil, G., 1960. Continents and mobile belts in the light of mineral dating. 21st International Geological Convention, Norden, 1960. Proceedings part 9, 162-169.
- Gaucher, C., Boggiani, P. C., Sprechmann, P., Sial, A. N., Fairchild, T., 2003. Integrated correlation of the Vendian to Cambrian Arroyo del Soldado and Corumba groups



- (Uruguay and Brazil): palaeogeographic, palaeoclimatic and palaeobiologic implications. *Precambrian Research*, 120, 241-278.
- Godoy, A. M., Manzano, J. C., Ruiz, A. S., Araújo L. M. B., 2007. Os Granitóides Brasileiros da Faixa de Dobramentos Paraguai, MS e MT. *Geologia USP, Série Científica*, 7, 29–44.
- Godoy, A. M., Pinho, F. E. C., Manzano, J. C., de Araújo, L. M. B., da Silva, J. A., Figueiredo, M., 2010. Estudos isotópicos das rochas granitóides neoproterozoicas da Faixa de Dobramento Paraguai. *Brazilian Journal of Geology*, 40, 380–391.
- Goscombe, B., Gray, D. R., Armstrong, R., Foster, D. A., Vogl, J., 2005. Event geochronology of the Pan-African Kaoko Belt, Namibia. *Precambrian Research*, 140, 1–41.
- Goscombe, B., Gray, D.R., 2007. The Coastal Terrane of the Kaoko Belt, Namibia: outboard arc-terrane and tectonic significance. *Precambrian Res* 155:139–158.
- Goscombe, B., Foster, D.A., Gray, D., Wade, B., Marsellos, A., Titus, J., 2017. Deformation correlations, stress field switches and evolution of an orogenic intersection: the Pan-African Kaoko-Damara orogenic junction. Namibia, *Geosci Front* 8(6):1187–1232.
- Gray, D.R., Foster, D.A., Meert, J.G., Goscombe, B.D., Armstrong, R., Trouw, R.A.J., Passchier, C.W., 2008. A Damara orogen perspective on the assembly of southwestern Gondwana. *Geol Soc Lond (Spec Publ)* 294:257–278.
- Hasui, Y.; Tassinari, C.C.G.; Siga Jr, O.; Teixeira, W.; Almeida, F.F.M.; Kawashita, K., 1980. Idades Rb-Sr e K-Ar do Centro Norte do Brasil e seu significado geológico-geotectônico. *Anais do congresso brasileiro de geologia*. Pg. 2659.
- Hasui, Y., 2010. A grande colisão Pré-cambriana do sudeste brasileiro e a estruturação regional. *Geociências*, São Paulo, v. 29, n. 2, p. 141-169.

- Heilbron, M., Valeriano, C.M., Tassinari, C.C.G., Almeida, J., Tupinambá, M., Siga, O., Trouw, R., 2008. Correlation of Neoproterozoic terranes between the Ribeira Belt, SE Brazil and its African counterpart: comparative tectonic evolution and open questions. *Geological Society of London (Special Publishes)*, 294:211–237.
- Hoffman, P. F., 1991. *Science* 252, 1409–1412.
- Hoffman, P. F., Kaufman, A.J., Halverson, G.P., Schrag, D.P., 1998. A Neoproterozoic Snowball Earth. *Science*, 1342.
- Kennedy, W. Q., 1964. The structural differentiation of Africa in the Pan-African ( $\pm 500$  m.y.) tectonic episode. *Research Institute Afr. Geol. University of Leeds*, 48-49.
- Kröner, A., Cordani, U., 2003. African, southern Indian and South American cratons were not part of the Rodinia supercontinent: evidence from field relationships and geochronology. *Tectonophysics*, 375, 325-352.
- Li, Z.X., Bogdanova, S.V., Collins, A.S., Davidson, A., De Waele, B., Ernst, R.E., Fitzsimons, I.C.W., Fuck, R.A., Gladkochub, D.P., Jacobs, J., Karlstrom, K.E., Lul, S., Natapov, L.M., Pease, V., Pisarevsky, S.A., Thrane, K., Vernikov-sky, V., 2008. Assembly, configuration, and break-up history of Rodinia: A synthesis. *Precambrian Research* 160: 179–210.
- Marini, O J.; Fuck, R. A.; Dardenne, M. A.; Danni, J.C.M., 1984. Província Tocantins-Setores Central e Sudeste. In: Almeida, F.F.M. & Hasui, Y. ed. *O Pré-Cambriano do Brasil*. São Paulo, Edgard Blucher. p. 205-264.
- Martin, H., 1987. Petrogenesis of Archaean trondhjemites, tonalites and granodiorites from eastern Finland: major and trace element geochemistry. *Journal of Petrology* 28 (5), 921-953.
- Martin, H., 1988. Archaean and modern granitoids as indicators of changes in geodynamic processes. *Rev. Bras. Geocienc.* 17, 360– 365.

- Martin, H., 1993. The mechanisms of petrogenesis of the Archaean continental crust comparison with modern processes. *Lithos* 30, 373–388.
- Martin, H., 1999. The adakitic magmas: modern analogues of Archaean granitoids. *Lithos* 46 (3), 411-429.
- Martin, H., Smithies, R.H., Rapp, R., Moyen, J.-F., Champion, D., 2005. An overview of adakite, tonalite-trondhjemite-granodiorite (TTG), and sanukitoid: relationships and some implications for crustal evolution. *Lithos* 79, 1-24.
- Martin, H., Moyen, J.-F., 2002. Secular changes in TTG composition as markers of the progressive cooling of the Earth. *Geology* 30, 319–322.
- McDermott, F., Harris, N.B. W., Hawkesworth, C. J., 2000. Geochemical constraints on the petrogenesis of Pan-African A-type granites in the Damara Belt, Namibia. In: MILLER, R. MCG. (ed.) Henno Martin Commemorative Volume. *Communications of the Geological Survey of Namibia*, 12, 139–148.
- McGee, B., Collins, A.S., Trindade, R.I.F., Payne, J., 2015. Age and provenance of the Cryogenian to Cambrian passive margin to foreland basin sequence of the northern Paraguay Belt, Brazil. *GSA Bulletin*, 127, 76-86.
- McWilliams, M.O., McElhinny, M.W., 1980. Late Precambrian paleomagnetism in Australia in the Adelaide geosyncline. *J. Geol.* 88, 1 – 26.
- McWilliams, M.O., 1981. Palaeomagnetism and Precambrian tectonic evolution of Gondwana. In: Kroöner, A. (Ed.), *Precambrian Plate Tectonics*. Elsevier, Amsterdam, pp. 649– 687.
- Meert, J.G., 1999. Some perspectives on the assembly of Gondwana. *Mem. Geol. Soc. India* 44, 45 – 58.

- Meert, J.G., 2001. Growing Gondwana and rethinking Rodinia: a paleomagnetic perspective. *Gondwana Research* 4, 279–288.
- Meert J.G., 2003. A synopsis of events related to the assembly of eastern Gondwana. *Tectonophysics*, 362, 1-40.
- Meert, J.G., Torsvik, T.H., 2003. The making and unmaking of a supercontinent: Rodinia revisited. *Tectonophysics* 375, 261–288.
- Meert, J.G., Lieberman, B.S., 2008. The Neoproterozoic assembly of Gondwana and its relation to the Ediacaran-Cambrian radiation. *Gondwana Research*. 14 (5-21).
- Medlicott, H. B. and Blandford, W.T., 1879. *A Manual of the Geology of India* (Calcutta, Geol. Survey, India).
- Meira, V.T., Garcia-Casco, A., Juliani, C., Almeida, R.P., Schorscher, J.H.D., 2015. The role of intracontinental deformation in supercontinent assembly: insights from the Ribeira Belt, Southeastern Brazil (Neoproterozoic West Gondwana). *Terra Nova*, Vol 27, No. 3, 206–217.
- Merdith, A.S., Collins, A.S., Williams, S.E., Pisarevsky, S., Foden, J.D., Archibald, D.B., Blades, M.L., Alessio, B.L., Armistead, S., Plavsa, D., Clark, C., Müller, R.D., 2017. A full-plate global reconstruction of the Neoproterozoic. *Gondwana Research* 50:84–134
- Moyen, J.F., Martin, H., 2012. Forty years of TTG research. *Lithos* 148, 312–336.
- Moyen, J.F., Laurent, O., Chelle-Michou, C., Couzinié, S., Vanderhaeghe, O., Zeh, A., Villaros, A. & Gardien, V., 2017. Collision vs. subduction-related magmatism: two contrasting ways of granite formation and implications for crustal growth. *Lithos* 277, 154-177.
- Moyen, J.F., Laurent, O., 2017. Archaean tectonic systems: A view from igneous rocks. *Lithos* 302-303.

- Nance, D.R., Murphy, J.B, Santosh, M., 2014. The supercontinent cycle: A retrospective essay. *Gondwana Research* 25, 54-29.
- Nascimento, D.B., Schmitt, R.S., Ribeiro, A., Trouw, R.A.J., Passchier, C.W., Basei, M.S., 2017. Depositional ages and provenance of the Neoproterozoic Damara Supergroup (northwest Namibia): implications for the Angola-Congo and Kalahari cratons connection. *Gondwana Research* 52:153–171.
- Oriolo, S., Oyhantçabal, P., Wemmer, K., Siegesmund, S., 2017. Contemporaneous assembly of Western Gondwana and final Rodinia break-up: Implications for the supercontinent cycle. *Geoscience Frontiers*. 8 (1431-1445).
- Pastor-Galán, D., Nance, R.D., Murphy, J.B., Spencer, C.J., 2018. Supercontinents: Myths, mysteries and milestones. *Geological Society London Special Publications*, 470.
- Pereira, I., Storey, D.C., Darling, J.R., Moreira, H., Strachan, R.A., Cawood, P., 2021. Detrital rutile tracks the first appearance of subduction zone low T/P paired metamorphism in the Palaeoproterozoic. *Earth and Planetary Sciences Letters* 570, 117069.
- Pimentel, M.M.; Fuck, R.A., 1992. Neoproterozoic crustal accretion in central Brazil. *Geology*, 20:375-379.
- Pirajno, F., 2010. Intracontinental strike-slip faults, associated magmatism, mineral systems and mantle dynamics: examples from NW China and Altay-Sayan (Siberia). *Journal of Geodynamics*, 50:325-346.
- Pisarevsky S. A., Murphy J. B., Cawood P. A., and Collins A. S., 2008. Late Neoproterozoic and Early Cambrian palaeogeography: models and problems, in Pankhurst, R. J., Trouw, R. A. J., de Brito-Neves, Region. *Geological Society, London, Special Publications*, 294, 9–31.

- Ramos V.A., Vujovich G., Martino R., Otamendi J., 2010. Pampia: a large Cratonic block missing in the Rodinia supercontinent. *Journal Geodynamics*. 50, 243-255.
- Rapela, C.W., Pankhurst, R.J., Casquet, C., Baldo, E., Saavedra, J., Galindo, C., Fanning C.M., 1998. The Pampean Orogeny of the southern proto-Andes: Cambrian continental collision in the Sierras de Cordoba. In: Pankhurst R.J., Rapela C.W., (eds.). *The proto-Andean Margin of Gondwana*. Geological Society of London Special Publication, 142, p. 181-217.
- Rapela, C.W., Fanning, C.M., Casquet, C., Pankhurst, R.J., Spalletti, L., Poiré, D., Baldo, E.G., 2011. The Rio de la Plata craton and the adjoining Pan-African/brasiliano terranes: their origins and incorporation into south-west Gondwana. *Gondwana Research*, 20:673–690.
- Rogers, J.J.W., 1996. A history of the continents in the past three billion years. *Journal of Geology* 104, 91–107.
- Schmitt, R.S., Trouw, R.A.J., Van Schmus, W.R., Pimentel, M.M. 2004. Late amalgamation in the central part of West Gondwana: new geochronological data and the characterization of a Cambrian collisional orogeny in the Ribeira Belt (SE Brazil). *Precambrian Research*, 133:29–61.
- Schmitt RS, Silva EA, Collins AS, Reeves C, Fragoso RA, Richetti PC, Fernandes GL de F, Benedek MR, Costa RL, Assis AP., 2016. Gondwana tectonic evolution recounted through the Gondwana map—IGCP-628. In: *Abstracts 35th International Geological Congress*, Cape Town.
- Schmitt, R.S., Fragoso, R.A., Collins, A.S., 2018. Suturing Gondwana in the Cambrian: Orogenic Events of the Final Amalgamation. Springer International Publishing AG, part of Springer Nature 2018 S. Siegesmund et al. (eds.), *Geology of Southwest Gondwana, Regional Geology Reviews*.

- Seer, H.J., Nilson, A. A., 1985. Contribuição à geologia das unidades Pré-Cambrianas da região de Bom Jardim de Goiás. In: Simpósio de Geologia do Centro-Oeste. Goiânia, 1985. SBG. p. 267-281.
- Seifert, Th., 2008. Metallogeny and Petrogenesis of Lamprophyres in the Mid-European Variscides. IOS Press, Amsterdam, 301 pp.
- Shirey, S.B., Hanson, G.N., 1984. Mantle-derived Archaean monzodiorites and trachyandesites. *Nature* 310, 222–224.
- Stern, R.A., Hanson, G.N., 1991. Archaean High-Mg granodiorites: a derivative of light rare earth enriched monzodiorites of mantle origin. *Journal of Petrology* 32, 201–238.
- Stern, R.A., Hanson, G.N., Shirey, S.B., 1989. Petrogenesis of mantle-derived, LILE-enriched Archean monzodiorites and trachyandesites (sanukitoids) in southwestern Superior Province. *Canadian Journal of Earth Sciences* 26, 1688–1712.
- Stern, R.J., 1994. Arc-assembly and continental collision in the Neoproterozoic African orogen: implications for the consolidation of Gondwanaland. *Annu. Rev. Earth Planet Sci.* 22, 319–351.
- Stevenson, R., Henry, P., Gariépy, C., 1999. Assimilation-fractional crystallization origin of Archaean sanukitoid suites: Western Superior Province, Canada. *Precambrian Research* 96, 83–99.
- Tohver, E., Cawood, P. A., Rossello, E. A., Jourdan F., 2012. Closure of the Clymene Ocean and formation of West Gondwana in the Cambrian: Evidence from the Sierras Australes of the southernmost Rio de la Plata Craton, Argentina. *Gondwana Research*, 21, 394-405.
- Tohver, E., Trindade, R. I. F., Solum, J. G., Hall, C. M., Riccomini, C., and Nogueira, A. C., 2010. Closing the Clymene

- Ocean and Bending a Brasiliano belt: Evidence for the Cambrian formation of Gondwana from southeast Amazon Craton. *Geology*, 38, 267–270.
- Tohver, E., Cawood, P. A., Rossello, E. A., and Jourdan, F., 2012. Closure of the Clymene Ocean and formation of West Gondwana in the Cambrian: Evidence from the Sierras Australes of the southernmost Rio de la Plata Craton, Argentina. *Gondwana Research*, 21, 394–405.
- Tohver E., Trindade R.I.F., 2014. Comment on "Was there na Ediacaran Clymene Ocean in central South America?" By Umberto Giuseppe Cordani, Marcio Martins Pimentel, Carlos Eduardo Ganade de Araújo, Miguel Angelo Stipp Basei, Reinhardt Adolfo Fuck, and Vicente Antonio Vitório Girardi. *American Journal of Science*, 313, 517-539.
- Trindade, R. I. F., Font, E., D'Agrella-Filho, M. S., Nogueira, A. C. R., and Riccomini, C., 2003. Low-latitude and multiple geomagnetic reversals in the Neoproterozoic Puga cap carbonate, Amazon Craton. *Terra Nova*, 15, 441–446.
- Trindade, R. I. F., D'Agrella-Filho M. S., Epof I., and Brito Neves B. B., 2006. Paleomagnetism of Early Cambrian Itabaiana mafic dikes (NE Brazil) and the final assembly of Gondwana. *Earth and Planetary Science Letters*, 244, 361–377.
- Unrug, R., 1992. The supercontinental cycle and Gondwanaland assembly: component cratons and the timing of suturing events. *Journal of Geodynamics*, 16, 215–240.
- Valentine, J.W., 2002. Prelude to the Cambrian explosion. *Annual Review of Earth and Planetary Sciences* 30, 285-306.
- Veevers, J.J., 2004. Gondwanaland from 650-500Ma assembly through 320 Ma mergers in Pangea to 185-100 Ma breakup: supercontinental tectonics via stratigraphy and radiometric dating. *Earth Sci Rev* 68: 1-132.
- Wilson, J.T., 1966. Did the Atlantic close and reopen? *Nature* 211 (81), 254–271, 676.



- Windley, B.F., Alexeiev, D., Xiao, W.-J., Kröner, A., Badarch, G., 2007. Tectonic models for accretion of the Central Asian Orogenic Belt. *Journal of the Geological Society of London* 64, 31–47.
- Xiao, W.J., Kusky, T., 2009. Geodynamic processes and metallogenesis of the Central Asia and related orogenic belts. *Gondwana Research* 16, 167–169.
- Zhao, G., Wang, Y., Huang, B., Dong, Y., Li, S., Zhang, G., Yu, S., 2018. Geological reconstruction of the East Asian blocks: From the breakup of Gondinia to assembly of Pangea. *Earth-Science Reviews*.